



Electrical subsystem for Shell eco-marathon urban concept battery powered vehicle

by

Garrett Rose

Thesis submitted in fulfilment of the requirements for the degree

Master in Engineering Technology: Electrical Engineering

in the Faculty of Engineering

at the Cape Peninsula University of Technology

Supervisor: Jacques Wheeler

Co Supervisor: Dr. Marco Adonis

Bellville

July 2018

CPUT copyright information

The dissertation/thesis may not be published either in part (in scholarly, scientific or technical journals), or as a whole (as a monograph), unless permission has been obtained from the University

DECLARATION

I, Garrett Rose, declare that the contents of this dissertation/thesis represent my own unaided work, and that the dissertation/thesis has not previously been submitted for academic examination towards any qualification. Furthermore, it represents my own opinions and not necessarily those of the Cape Peninsula University of Technology.

Signed

Date

ABSTRACT

The purpose of this paper was to design and develop an electrical power train for an Urban Concept electric vehicle geared to complete the Shell Eco-Marathon Africa in 2019. Various technologies which make up the electrical drive train of an electrical vehicle were also reviewed which include the battery pack, the battery management system, the motors, the motor management system and the human interface.

Upon completion of this, the various topologies best suited for this project were selected, designed, constructed and developed. Two motors were re-designed and constructed for this vehicle and the motor drive was also constructed to control these motors. A Lithium-Ion battery pack was constructed and developed to drive the motors and an off-the-shelf battery management system was purchased and developed to suit the requirements for the Shell Eco-Marathon competition rules. A human interface was also developed in order for the driver to see various parameters of the electric vehicle defined by the Shell Eco-Marathon competition rules.

After each component of the drive train was constructed, they underwent various testing procedures to determine the efficiency of each individual component and the overall efficiency for the complete drive train of this electric vehicle was ascertained.

The Product Lifecycle Management Competency Centre group developed the chassis for this vehicle. For this reason, only the electric subsystems were evaluated and a simulation was completed of the complete drive train.

After the complete drive train was constructed and all the individual subsystems evaluated and simulated, a vehicle with an overall efficiency of about sixty percent was expected and the completed drive train should be adequate enough to complete the entire Shell Eco-Marathon Africa circuit.

ACKNOWLEDGEMENTS

I wish to thank:

- God, for providing me with the strength and determination in completing this thesis.
- My fiancé, Tanith Marais, for always motivating me and providing me with support in completing this thesis.
- My parents, Derrick Arthur Rose and Maureen Rose, who as parents defined who I am.
- To Dr Marco Adonis and Mr Jacques Wheeler, my supervisors, who without doubt were always available to assist me with any problems I encountered and guided me throughout this thesis.
- To Mr Ian Robertson, who provided me with support and infrastructure to complete this thesis.

TABLE OF CONTENTS

Table of Contents	v
List of Figures and Tables	ix
List of abbreviations and Terms	xii
Chapter 1: Introduction	
1.1 Statement of research problem	1
1.2 Aims and objectives	2
1.2.1 Research questions	2
1.2.2 Aims	3
1.2.3 Objectives	3
1.3 Thesis structure	4
Chapter 2: Background Study	
2.1 An electric vehicle	5
2.2 Types of electric vehicles	5
2.2.1 Battery electric vehicles	6
2.2.2 Hybrid electric vehicles (HEV's)	6
2.2.2.1 The series type HEV	7
2.2.2.2 The parallel type HEV	7
2.2.2.3 The series-parallel type HEV	8
2.2.3 Fuel cell electric vehicles	8
2.2.4 Power line vehicles	8
2.2.5 Photovoltaic (PV) electric vehicles	8
2.2.6 Super capacitor electric vehicles	8
2.3 Subsystems in electric vehicles	9
2.3.1 Requirements	9
2.3.2 Mechanical requirements of the electric vehicle	10
2.3.3 Forces acting on an EV	11
2.3.3.1 Speed	12
2.3.3.2 Acceleration	12
2.3.3.3 Climbing force	12
2.3.3.4 Aerodynamic force	13
2.3.3.5 Rolling force	13
2.3.3.6 Acceleration force	14
2.3.3.7 Chassis	16
2.3.3.8 Vehicle design	16
2.4 Electrical systems	16
2.4.1 Electric motors	17
2.4.1.1 Permanent magnet motors	17
2.4.1.2 Squirrel cage induction motors	17
2.4.1.3 Reluctance motors	17
2.4.1.4 Motor selection	18
2.4.1.5 Rewinding the motor	19
2.4.2 Motor control options	20
2.4.2.1 Different topologies available in industry	22
2.4.2.2 Control stage options for the motor drive	24
2.4.2.3 FPGA's	25
2.4.2.4 Microcontroller units (MCU)	25

2.4.3	Control strategy	27
2.4.3.1	Voltage source inverter (VSI) control	27
2.4.3.2	Current source inverter (CSI) control	27
2.4.3.3	Voltage frequency (VF) control	27
2.4.3.4	Basic control technique	29
2.4.4	Batteries	30
2.4.5	Battery management system (BMS)	31
2.4.6	Cell Balancing	34
2.4.6.1	Cell balancing techniques	34
2.4.6.2	Bottom balance	34
2.4.6.3	Top balance	34
2.4.6.4	Passive cell balancing	34
2.4.6.5	Active cell balancing	35
2.4.7	Choice selection of BMS	35
2.4.8	The human interface (HMI)	36
Chapter 3: Design specifications		
3.1	The EV motors	38
3.2	The power stage (motor control or inverter) stage	39
3.3	The control stage	39
3.4	The batteries	40
3.5	The battery management system (BMS)	40
3.5.1	Microcontroller (BMS)	40
3.5.2	Communication protocol	40
3.5.3	Sensors	41
3.5.3.1	Current sensors	41
3.5.3.2	Temperature sensors	41
3.5.3.3	Speed sensors	41
3.6	Total expected efficiencies of electrical drive train	42
Chapter 4: The EV motor and the motor control stage design		
4.1	The EV motors	43
4.1.1	Disassembly of the motors	43
4.1.2	Rewiring calculations for the stator windings	49
4.1.3	Rewiring of the stator	50
4.1.3.1	Perspex jig	50
4.1.3.2	Assembly of stator phase windings	51
4.1.3.3	Power connections to stator windings	53
4.1.4	Final machine inspection tests	55
4.1.4.1	Winding resistance	55
4.1.4.2	Insulation resistance	57
4.2	The motor control stage	58
4.2.1	The control stage of the inverter	58
4.2.1.1	Selection of the EV processor	60
4.2.1.2	Dead-time	62
4.2.2	The power stage of the inverter	64
4.2.2.1	MOSFET selection	64
4.2.2.2	Gate resistors	66
4.2.2.3	RC snubber circuit	67
4.2.2.4	Transient voltage suppressors	67
4.2.2.5	Decoupling capacitor	68
4.2.2.6	Power losses in MOSFET's	68
4.2.2.7	Control stage power consumption	70

4.2.2.8	Switch-mode power supply	71
4.2.2.9	Calculation of switch mode power supply values	71
4.2.3	Motor drive testing and results	74
4.2.3.1	Motor drive wave form results from initial testing	76
4.2.4	The gate drivers (line drivers)	81
Chapter 5: The battery pack and battery management system design		
5.1	The battery pack	84
5.1.1	Electrical requirements of the battery pack	84
5.1.2	Lithium polymer pouch cell operating conditions	84
5.1.3	Terminal connections of the battery pack	87
5.1.4	Test results for the battery pack	91
5.1.4.1	Cell balancing	91
5.1.4.2	Battery capacity	93
5.2	The battery management system (BMS)	93
5.2.1	Setup procedure	95
5.2.2	Software configuration initialization	96
5.2.3	Setup of overvoltage and under voltage settings	97
5.2.4	Cell balancing	98
Chapter 6: The EV display panel and user interface design		
6.1	Microcontrollers interface	102
6.1.1	Arduino	102
6.1.2	Raspberry pi	102
6.1.3	Microchip	102
6.1.4	Selection of microcontroller	102
6.1.5	Communication protocol	104
6.1.5.1	Serial communication selection	105
6.1.6	Software flow charts	106
6.1.7	Sensors	107
6.1.7.1	Power monitoring sensors	107
6.1.7.2	Current sensors	108
6.1.7.3	Voltage sensors	110
6.1.7.4	Temperature sensors	111
6.1.7.5	Speed sensors	111
6.2	EV dashboard panel	113
6.3	User Interface	113
Chapter 7: Testing and evaluation of the EV motors and motor drive		
7.1	Power train evaluation	116
7.2	Motor efficiency	117
7.2.1	Motor losses	118
7.2.2	Motor efficiency testing	119
7.3	Motor drive testing and evaluation	124
7.3.1	Initial motor drive testing	124
7.3.1.1	Motor drive testing using a 100 W load	128
7.3.1.2	Motor drive testing using a 600 W load	131
	The Fluke 435B set to 'Volts/Amps/Hertz' display mode	133
	The Fluke 435B set to 'Power and Energy' display mode	135
	The Fluke 435B set to 'Logger' display mode	137
		138

7.3.1.3	Using the Tektronix four channel data logger for power measurements	139
	Motor drive testing using the AC induction motor	
Chapter 8: Testing and evaluation of the EV battery pack, the BMS and the display panel components		
8.1	Evaluation of the battery pack	146
8.2	Evaluation of the BMS	147
8.2.1	Fault finding of the BMS	148
8.2.1.1	Cell voltage measurement	148
8.3	Dashboard metering equipment	150
8.3.1	Ampere hour (Ah) counter	151
8.3.2	Watt hour (Wh) and watt second (Ws) counter	151
8.3.3	Simulation of the race	151
8.4	Drive train system	152
8.4.1	Sprocket size	155
8.4.2	Chain speed	155
8.4.3	Chain pitch	155
Chapter 9: Conclusion and recommendations		
9.1	Simulated race results	156
9.2	Efficiency diagram	158
9.3	Conclusion	159
9.4	Future work	161

References

Appendices

A	Motorelli motor dimension and specifications	186
B	Motor Experimental Results	187
C	Full Circuit Schematic of the Motor Drive	192
D	Bottom and Top Layout of the Control PCB and Power PCB for the Motor Drive	193
E	Data sheet for Eneritech SPB9345136UH1 rechargeable Lithium-ion polymer battery	195
F	The BMS circuit diagram and node schematic	197
G	The Motor Drive test results at various speeds	199
H	Testing and calibrated data for Voltage and Current Sensors for BMS	207
I	Motor Control test results	209
J	Additional BMS Circuit diagrams	215
K	Software code for Arduino Master and Slave	217

LIST OF FIGURES AND TABLES

Figure	Description	Page
2-1	A battery electric vehicle	6
2-2	A hybrid electric vehicle	7
2-3	The series type hybrid electric vehicle	7
2-4	The parallel type hybrid electric vehicle	8
2-5	A super capacitor electric vehicle	9
2-6	The urban concept battery electrical vehicle being designed by the CPUT	10
2-7	A screenshot of the EV chassis design simulation	11
2-8	Forces acting on an EV	12
2-9	Typical block diagram for a battery powered EV	17
2-10	Typical distribution of losses	20
2-11	A typical control system block diagram for an EV controlled by a human interface	21
2-12	A three phase AC induction machine voltage/frequency open loop control	22
2-13	Motor-drive topology flow-chart	23
2-14	Typical torque-speed characteristics of an induction motor	28
2-15	Torque-speed characteristics of an induction motor with VF control	29
2-16	General architecture of a BMS	31
2-17	Battery management IC function loop	33
2-18	A commercial EV dashboard	36
2-19	A human interface block diagram	37
3-1	System block diagram for the CPUT EV	38
3-2	A block diagram of the subsystems affiliated to the BMS	40
3-3	Total system efficiency expected from sub components of the EV drive train	42
4-1	The Motorelli three phase, squirrel cage induction motor	43
4-2	EV motor connections	44
4-3	Stator frame and end covers being marked for alignment	45
4-4	Various components of the rotor	45
4-5	A clean stator after removal of the windings	46
4-6	Original windings laid out for mapping	47
4-7	Layout of the windings removed from the stator	48
4-8	Templates for Perspex jig	50
4-9	Completed Perspex jig	51
4-10	Completed Perspex jig with completed stator winding for one phase	52
4-11	One winding inserted into machine stator	52
4-12	Power entry/exit leads connection	53
4-13	Terminal box connections	54
4-14	Completed machine assembly	55
4-15	Insulation resistance test setup	57
4-16	Voltage/frequency or open loop scalar control	59
4-17	EV motor control processor	61
4-18	PWM signal processing	62
4-19	HI and LO signals with dead-time	62
4-20	Cross conduction due to insufficient dead-time	63
4-21	Minimum circuit connections for the dsPIC30F processor	64
4-22	Semiconductor selection guide	65
4-23	Effect of parallel MOSFET's on gate charge and on-state resistance	66
4-24	The basic power stage of one phase	66
4-25	Gate resistors added to the circuit	67
4-26	A resistive and capacitive (RC) snubber placed across the HI and LO terminals	67
4-27	TVS's inserted from each source gate on each MOSFET	68

4-28	Decoupled capacitors connected from HI to LO terminals	68
4-29	Stepping down stages of voltage from 38 V to 3.3V	71
4-30	EV Switch mode power supply circuit (buck converter)	74
4-31	HI side signal, LO side signal and filtered output of the motor drive	76
4-32	The three phase output waveforms (PWM modulated sine wave)	77
4-33	The three phase output waveforms with a low pass filter added	77
4-34	All three phase signals 120 degrees out of phase from each other	78
4-35	All three phases were set to averaging	78
4-36	Final motor drive control stage	79
4-37	Final motor drive power stage	79
4-38	Final assembled motor drive	79
4-39	Thermal dissipation network	80
4-40	Minimum circuit connection for three phase inverters using three IRS2110 devices to drive six IGBTs	82
5-1	3D model of cell clamping mechanism designed in AutoCad	88
5-2	Assembly of aluminium enclosure for the battery pack	89
5-3	The assembly of one stack of ten cells	89
5-4	The assembled battery pack	90
5-5	The completed battery pack together with fuse protection	90
5-6	Battery pack enclosure	91
5-7	The battery cell voltages before charging and balancing	92
5-8	The battery cell voltages after charging and balancing	92
5-9	The battery capacity and cell voltages during discharging	93
5-10	Hardware connections to the BMS	95
5-11	Interface of addressable registers	97
5-12	A safety overview in standalone mode	98
5-13	The configuration of a cell when balancing with the internal NMOS activated	99
5-14	The configuration of a cell when not balancing with the internal NMOS deactivated	99
5-15	The configuration of a cell with external balancing and the internal NMOS activated	100
5-16	The configuration of a cell with external balancing and the internal NMOS deactivated	100
5-17	Setting up of cell overvoltage and under-voltage threshold limits	101
6-1	Arduino Uno complete connectivity diagram	103
6-2	Arduino Mega complete connectivity diagram	103
6-3	RS232 output pins interface connections	105
6-4	Connections between Arduino Uno and Mega via RS232 cable	106
6-5	Flow chart of software for Arduino Uno	106
6-6	Flow chart for slave device	107
6-7	Block diagram of current sensing	109
6-8	Linearity relationship of calibrated data and standard current value	110
6-9	Data obtained from voltage meter evaluation	110
6-10	Testing the LCD functionality with the microcontroller	114
6-11	LCD configuration adjusted to fit into the EV dashboard	115
6-12	EV dashboard display template	115
7-1	The Zwartskop Raceway track for the South African Shell Eco-marathon	117
7-2	Efficiencies of the original motor (measured) and the new motor (expected)	118
7-3	The EV motor efficiency test block diagram	119
7-4	The EV motor three phase power supply	120
7-5	The eddy current dynamometer/brake and digital scale	120
7-6	The complete test setup for the testing of the EV motor	121
7-7	The re-wound motors torque versus speed curve	123

7-8	The old motor (measured), the new motor (expected), and the new motor (measured) efficiencies and I^2R Losses	123
7-9	Test bench for initial load testing of dsPIC30F2010 motor controller	124
7-10	The input side to the motor drive together with the metering equipment	125
7-11	(a) The Fluke 80i-110s AC/DC current probe (b) The display of the Fluke 43B being setup correctly.	126
7-12	The Fluke 43B and Fluke 435B connections on the output side of the motor drive	126
7-13	The Fluke 435B being set to 10mV/A scale	127
7-14	The resistive, high voltage, element bank used for initial load testing	127
7-15	(a) The load resistance connected in parallel (b) The phase resistances connected in a delta configuration.	128
7-16	Complete test bench for the inverter to measure a 100W load	129
7-17	Measurements of input and output power for the 100W load	130
7-18	Graph of efficiency versus the output power and frequency for the inverter for 100W load.	131
7-19	Test bench for the load testing of dsPIC30F2010 motor controller and Motorelli motor	133
7-20	The 600W load testing of the motor drive measurements and temperature readings	134
7-21	Graph of efficiency versus the output power and frequency for the inverter for 600W load using the Volts/Amps/Hertz display option on the Fluke 435B	135
7-22	Graph of efficiency versus the output power and frequency for the inverter for 600W load using the Power and Energy display option on the Fluke 435B	136
7-23	Maximum cable temperature reached when using the Fluke 435B on the Power and Energy display option	136
7-24	(a) Set of variables selected to be logged on Fluke 435B when in 'Logger' mode (b) The output power being logged by the Fluke 435B when in 'Logger' mode	137
7-25	Graph of efficiency versus the output power and frequency for the inverter for 600W load using the 'Logger' display option on the Fluke 435B	138
7-26	Graph of efficiency versus the output power and frequency for the inverter for the 600W load using the Blondel's four channel digital scope	139
7-27	Block diagram for test bench with AC induction motor incorporated and metering equipment	140
7-28	Complete test bench with AC induction motor incorporated with metering equipment and eddy current brake for loading purposes	140
7-29	Graph of efficiency versus the output power and frequency for the inverter when the AC induction motor and eddy current brake are connected using the Blondel's four channel digital scope	142
7-30	Experimental Exercise 3 data display	143
7-31	Induction motor regenerative power	144
7-32	(a) $2\mu\text{F}$ AC & power capacitors (b) Regenerative power protection	145
8-1	The battery pack voltage and current during charging	146
8-2	The battery cell voltages after charging and balancing	147
8-3	The cell monitoring circuit of the BMS	149
8-4	Calibration procedure of the BMS	150
8-5	Faulty S/H circuit of the BMS	150
8-6	Calibrated data for the Ah counter	151
8-7	Calibrated data for the Wh counter	152
8-8	A shaft and gearbox drive train system	153
8-9	A typical CVT belt system	153
8-10	A typical chain and sprocket drive train	154

9-1	Simulated efficiency results for CPUT EV	156
9-2	Simulated results for forces acting on the EV	157
9-3	Simulated results for the EV completing one track length	157
9-4	A typical power train of a battery EV	158
9-5	Efficiency diagram for the overall system	158

Table	Description	Page
2-1	Design requirements for the vehicle's electrical systems	9
2-2	Motor comparison	18
2-3	FPGA's vs. microcontrollers	26
2-4	Microcontroller options	26
2-5	Primary Lithium-ion battery chemistries and their uses	30
3-1	EV motor characteristics	38
3-2	EV motor drive characteristics	39
4-1	Motor specifications	43
4-2	Winding resistance test results	56
4-3	Insulation resistance test phase-ground results	58
4-4	Insulation resistance test phase-phase results	58
4-5	Measuring equipment for initial testing of motor drive	74
4-6	Bootstrap capacitor values	82
5-1	Comparison of typical Lithium Manganese oxide batteries and the Lithium-ion batteries available at CPUT	85
5-2	Battery pack characteristics	86
5-3	BQ77PL900 addressable registers	96
6-1	Comparison of serial protocols	104
6-2	ACS758 current sensor	108
6-3	Comparison of different temperature sensors	111
6-4	Speed sensing technology comparison	112
8-1	Recovery commands of the BMS	148
8-2	The advantages and disadvantages of a shaft and gearbox; a belt drive and a chain drive	154
9-1	Research questions answered	159
9-2	Aims questions answered	159
9-3	Objective questions answered	160

LIST OF ABBREVIATIONS AND TERMS

Abbreviation	Definition/Explanation
3D	Three dimensional
ABS	Acrylonitrile Butadiene Styrene
AC	Alternating current
AC _{RMS}	Root means square alternating current
ADC	Analogue-to-digital-converter
AFE	Analog front end
Ah	Ampere-hours
BMS	Battery management system
BQ	BQ77PL900
C _d	Aerodynamic drag coefficient
CIR	Centre for Instrumentation Research
COTS	Currently off the shelf
CPUT	Cape Peninsula University of Technology
CSI	Current source inverter
DC	Direct current
DCE	Data communication equipment
DSP	Digital signal processor
DTE	Data terminal equipment
EEPROM	Electrically erasable programmable read-only memory
EMF	Electromotive force
ESR	Equivalent series circuit
EV	Electric vehicle
EVM	Electric vehicle motor
FET	Field effect transistor
FPGA	Field programmable gate array
FSM	Finite state machine
GnD	Ground
HEV's	Hybrid electric vehicle
HI	High
HMI	Human Machine Interface
Hz	Hertz
IC	Internal combustion
I/O's	Inputs or outputs
I ² C	Inter-integrated circuit
IGBT	Insulated gate bipolar transistor
IM	Induction Machine
I _{INL-L}	Input line-to-line current
LEM	Liaisons Electroniques et Mecaniques
LiPO	Lithium-Ion Polymer
L-L	Line-to-Line
LO	Low
MCU	Microcontroller unit
MOSFET	Metal-oxide semiconductor field-effect transistors
OV	Overvoltage
OV CFG	Overvoltage level register
PDU	Power distribution unit
PIC	Programmable Interface Controller

PLMCC	Product Lifecycle Management Competency Centre
PWM	Pulse-width modulation
PV	Photovoltaic
PWM	Pulse width modulation
RAM	Random Access Memory
RC	Resistive and capacitive
RPM	Revolutions per minute
S/H	Sample-and-hold
SOC	State of Charge
SOH	State of Health
SPI	Serial Peripheral Interface
SRAM	Static Random Access Memory
TPS	Throttle position sensor
TTL	Transistor-transistor logic
TVS	Transient voltage suppressors
USA	United States of America
UV	Under-voltage
VF	Voltage frequency
VFD	Variable frequency drive
VCU	Vehicle control unit
Variac	Variable Transformer
Vcc	Positive supply voltage
VFD	Variable frequency drive
$V_{IN\ L-L}$	Input line-to-line voltage
$(V_{I-L\ rms})$	RMS line-to-line output voltage
VoV	Voltage to overvoltage
VSD	Variable speed drive
VSI	Voltage source inverter
VuV	Voltage to under voltage

Term	Definition/Explanation
C-rating	The C-rating is defined as the charge or discharge rate given in terms of capacity of the battery divided by the number of hours for full charge or discharge. The higher the number of hours required for either full charge or discharge, the lower will be the charge/discharge rate. The charge or discharge current for a given C-rating is obtained by dividing the Ah capacity of the battery by the number of hours for full charge or discharge (Solanki, 2011).
Multiplexer	Also known as a data selector. It is a device that selects one of several analogue or digital input signals and forwards the selected input into a single line output (Kumar, 2014)
Photovoltaic	It is the name of a method of converting solar energy into direct current electricity using semiconducting materials that exhibit the photovoltaic effect.
Snubber	They are frequently used in electrical systems with an inductive load where the sudden interruption of current flow leads to a sharp rise in voltage across the current switching device, in accordance with Faraday's law. This transient can be a source of electromagnetic interference (EMI) in other circuits. (Wikipedia, 2017)
State of Charge	This is the capacity of the battery given in a percentage of the total capacity of the battery when it is full (Pop, et al., 2008)
UrbanConcept	It is defined as a fuel economy pure electrical vehicle which will be the closer in appearance and technology to road-going vehicles, addressing current transportation (IIUM research, Innovation & Invention Exhibition 2010 (IRIIE 2010), 2010)

Chapter One

Introduction

In 1939, a wager by Shell oil company employees in Wood River Illinois, United States of America (USA) saw the evolution of the Shell Eco-Marathon. This Shell Eco-Marathon is an international event and has developed over the years in the USA, Europe and recently Asia (Shell Global, 2014). There is now a strong drive to have South Africa partake in the Shell Eco-Marathon.

The Electrical Engineering department, in collaboration with the Mechanical Engineering department, the Product Lifecycle Management Competency Centre (PLMCC) and Centre for Instrumentation Research (CIR) of the Cape Peninsula University of Technology (CPUT) have embarked upon building an UrbanConcept Vehicle to compete in the Shell Eco-Marathon 2019. The purpose of this work was to develop the electrical subsystems to power not only the motors for the vehicle but to also power the auxiliary circuits. The electrical system built is designed to operate at maximum efficiency and will compete with other countries for the most energy efficient vehicle (Shell, 2013).

The chassis and body was designed and developed by the Mechanical Engineering Department (CPUT) and PLMCC. The body of the vehicle was designed to meet the competitions requirements as stipulated in the Shell Eco-Marathon rules (Shell, 2013). After the chassis, vehicle shell and electrical system were completed, the vehicle was assembled and various tests were performed to evaluate the efficiency of the vehicle. All the competition rules and regulations regarding the UrbanConcept vehicle are enforced, and after all the necessary tests have been completed the vehicle will be entered in the Shell Eco-Marathon 2019 (Shell, 2014).

1.1 Statement of research problem

The Shell Eco-marathon is a competition intended to challenge students from across the world in the design of a vehicle within the boundaries stipulated in the rules (Shell, 2013). There are limitations to the competition and this competition is designed for a student to have a “do it yourself” approach in building a vehicle. There are a set standard of rules which must be complied with regarding the vehicles (Shell, 2013) as well as safety standards for teams, individuals and vehicles. Failure to do so will result in a team and/or vehicle being disqualified (Shell, 2014).

Motors for this competition are not readily available. A motor was bought, rewound and then rebuilt to meet the competition requirements. The Shell Eco-marathon does also not permit off the shelf variable speed drives (VSD). An efficient power stage was developed for the motors. An efficient battery pack was also developed as well, and the implementation of an effective battery management system (BMS) was designed (Shell, 2013).

Once this was completed all the peripherals pertaining to the electrical systems and subsystems were investigated and developed to ensure that the vehicle is fully functional.

1.2 Aims and objectives

This research led to the design and development of a battery electric, energy efficient vehicle to compete in the class of UrbanConcept at the Shell Eco-Marathon, Africa 2019. The vehicle will meet all race specifications in terms of design, safety and operation. It will be the first time that the CPUT will compete in this competition (Shell, 2014).

Before any aims or objectives could be considered, it was necessary to have direction with a few research questions.

1.2.1 Research questions

The following research questions needed to be reviewed and form the main focus areas:

- Can an effective power train be developed for this car?
 - The motor needs to be rebuilt to comply with the Shell-eco rules without sacrificing efficiency.
 - An effective motor drive needs to be developed.
- Can an effective power source be developed for this vehicle?
 - The battery needs to be sized to complete the race.
 - The BMS needs to comply with the competition rules.
- Will the total system:
 - Allow the vehicle to complete the race?

With the above taken into consideration, the following aims and objectives were required to ensure that the vehicle met all the requirements.

1.2.2 Aims

The EV that was developed was for competing in the Africa Shell Eco-Marathon 2019. Taking this into consideration, the EV was designed having the following aims:

- The EV must be able to complete a complete single track length of 2.40 km (for the Zwartkops Raceway) without stopping.
- As the EV developed is a battery electric vehicle, it must produce at least 60 km/kWh in completing a single track length.
- The overall efficiency of the electric drive train was expected to be above 60%.

1.2.3 Objectives

For the Shell Eco-Marathon, UrbanConcept vehicle there were a few objectives in designing and building the vehicle. The main objectives are listed as follows:

- Two “currently off the shelf” (COTS) motors will be taken apart and reconstructed to deliver 750 W of mechanical power at 23 V AC. Calculations to carry 50 A for the motor wiring thicknesses, will be performed.
- A battery pack containing Lithium-Ion batteries providing at least 40 A at 38 V DC (nominal), will be developed together with an effective BMS for this EV.
- A 23 V AC motor drive for the vehicle will be developed. This motor drive will produce an output power of 1200W electrical power and a minimum of 30 A AC.
- The efficiency of the power train will be above 60 %.
- The vehicle electrical subsystems will be designed and developed.
- Monitoring and measurement parameters will be implemented to ensure that the objectives are met.
- All electrical peripherals will be installed and comply with the competition rules.

In constructing this EV drive train, the motors will firstly be developed and evaluated. Thereafter the motor drive will be developed and tested. The battery pack will also be constructed followed by a battery management system. All these components to the drive train will be individually tested and evaluated. A completed drive train will be assembled and the overall testing and evaluation of this drive train will be completed.

Benefits of this research will include developing an effective electric motor and motor drive for this EV. An effective battery pack and efficient battery management system will also be developed. As this EV is the first prototype developed by the CPUT, it will allow for future research and improvements in developing an EV for the CPUT.

1.3 Thesis structure

The layout of the remaining part of this thesis is as follows:

- Chapter 2: This chapter looked at different topologies implemented and related to the UrbanConcept battery powered electrical vehicle in terms of battery technologies used, motor technologies, basic BMS systems, various batteries considered and various power trains utilised. This chapter also considered the various forces that act on an EV and other factors that influenced the efficiency of the EV drive train.
- Chapter 3: Looked at the electrical design specifications of the electric vehicle. A functional description of all the electrical parts is described, together with the electrical specifications and a system block diagram was designed. An investigation into the efficiency targets was also considered.
- Chapter 4: This chapter looked specifically at the design of the electric motors and motor drive developed for the electric vehicle (EV) for the Shell Eco-Marathon UrbanConcept vehicle. Each component is described in detail.
- Chapter 5: This chapter looked specifically at the design of the battery pack and battery management system (BMS) developed for the electric vehicle (EV) for the Shell Eco-Marathon UrbanConcept vehicle. Each component is described in detail.
- Chapter 6: This chapter looked specifically at the design of the EV display panel and user interface developed for the electric vehicle (EV) for the Shell Eco-Marathon UrbanConcept vehicle. Each component is described in detail.
- Chapter 7: Testing and the evaluation of the EV motors and motor drive were covered in this chapter.
- Chapter 8: Testing and the evaluation of the battery pack and BMS were covered in this chapter.
- Chapter 9: Integration of the various components related to the power train was covered and testing of the entire system was completed.
- Chapter 10: Results on the systems and subsystems are analysed and described in this chapter. Final testing of all electrical subsystems was completed and conclusions of the study were drawn here. Recommendations are made for the system for future studies and a summary of all the findings are also completed.

Chapter Two

Background study

2.1 An electric vehicle

In the 1780's, the discovery of the battery by Alessandro Volta, an Italian inventor and chemist led to the development of the electric vehicle (Ellyard, 2005). The earliest electric vehicle was dated back to between 1890 and 1920, with England and France being the first nations to experiment in this field. The first commercial electric vehicle fleet was launched in the United States of America (USA) as New York Taxicabs in 1897 (Emadi, 2015). These electric vehicles however had a short range and initially a high cost. However, with the development of the combustion engine being able to commute over greater distances saw the decline in sales of electric vehicles.

In the more modern day, with the depletion of fossil resources, there have been some new developments in the electric vehicle industry with companies such as Toyota, Nissan and Chevrolet developing the electric cars such as the Prius, the Leaf and the Volt (Inderwildi & King, 2012)

2.2 Types of electric vehicles

There are two types of electric vehicles, namely:

- Pure electric EV's
- Hybrid electric EV's

The following six types of electric vehicles would fall into either the pure electric EV or the hybrid electric EV category.

- Battery powered electric vehicles.
- Hybrid electric vehicles (which utilises a combination of a battery and an internal combustion (IC) engine).
- Fuel cell vehicle (which use replaceable fuel as a source of energy).
- Vehicles powered by power lines.
- Vehicles that utilise photovoltaic (PV) cells.
- Vehicles that use super capacitors (to store energy).

Each type of electric vehicle has specific technologies in supplying energy and powering the electric vehicle. The following section briefly describes each technology used and the typical type of systems found in industry.

2.2.1 Battery electric vehicles

A battery electric vehicle comprises of two main components, namely a battery pack and an electric drivetrain. This would include a battery pack, a battery charger, an inverter to vary the current required for the electric vehicle (EV), a vehicle control unit (VCU), a power distribution unit (PDU) and a DC\DC inverter to allow for 12 V used on the various vehicle peripheral (Bakker, 2010). Battery electric vehicles also incorporate various batteries such as Lead Acid, Nickel Metal Hydride, Lithium-Ion, Sodium Nickel Chloride and many more. This will be more extensively covered in chapter 5 (Scrosati, et al., 2015).

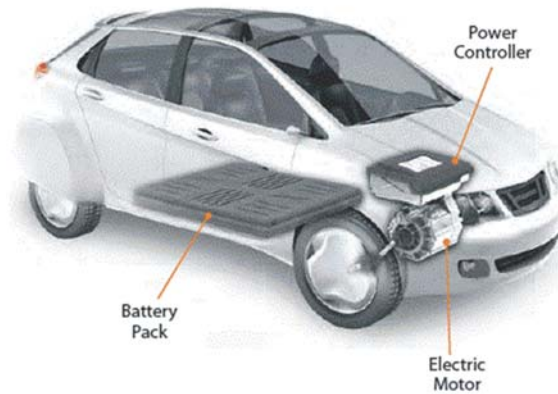


Figure 2-1: A battery electric vehicle (Union of Concerned Scientists, 2016)

2.2.2 Hybrid electric vehicles (HEV's)

The first hybrid electric vehicle (HEV) was built in 1898 by Dr Ferdinand Porsche. It used a generator that provided power to motors on the hub of the vehicle (Mi, et al., 2011). Hybrid motors generally have two or more power sources. The most common of the hybrid electric motor consists of an internal combustion (IC) engine, with a battery and a generator with an electric motor. The most commonly EV found presently is the hybrid electric vehicle (Larminie & Lowry, 2012).

For a hybrid electric motor that comprises of an IC engine and batteries, two types of load power are produced. One is produced by the IC engine fuel cell and is known as the average (steady) power and it has a constant value. The other load power produced is dynamic power produced by the electric motor. This power has a zero average during the whole driving cycle.

These powers will be covered when considering the different drivetrains implemented (Ehsani, et al., 2007).

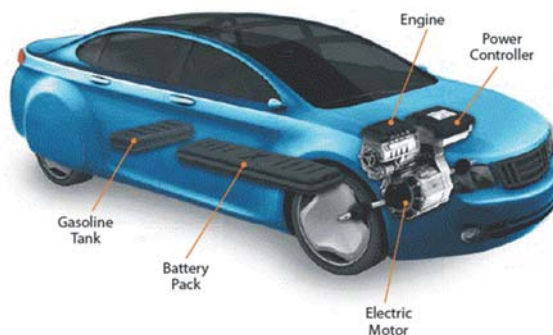


Figure 2-2: A hybrid electric vehicle (Union of Concerned Scientists, 2016)

There are mainly three types of HEV designs. They are namely:

- Series type HEV
- Parallel type HEV
- Series-parallel type HEV

2.2.2.1 The series type HEV

A HEV incorporating a series type system utilises an IC engine to power a generator which, in turn, charges the battery pack. The vehicle is never powered by the engine. The engine rather drives the generator, which powers the battery pack or the electric motor. The electric motor is the only source for powering the vehicle (Erjavec, 2012).

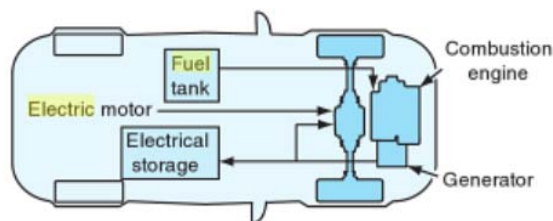


Figure 2-3: The series type hybrid electric vehicle (Erjavec, 2012)

2.2.2.2 The parallel type HEV

A HEV incorporating the parallel type system utilises either a battery pack or a fuel tank via an IC engine to power the vehicle (Erjavec 2012).

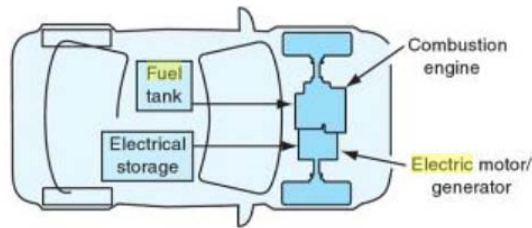


Figure 2-4: The parallel type hybrid electric vehicle (Erjavec, 2012)

2.2.2.3 The series-parallel type HEV

The series-parallel type has the features of both the series and the parallel HEV. It is however a lot more complicated as well as costly. It has an additional mechanical link (for the series hybrid) and an additional generator (for the parallel hybrid) (Chan & Chau, 2001).

2.2.3 Fuel cell electric vehicles

A fuel cell vehicle works similar to an EV except that instead of batteries being the source of energy, fuel cells replace the batteries. An advantage of this is that fuel cells do not need to be recharged. Fuel cells convert chemical energy into electrical energy by combining hydrogen with oxygen. Hydrogen ions combine with oxygen molecules, and water, heat and electricity are the three by-products released (Erjavec, 2012). There are many other types of fuel cells, however, for the Shell Eco-marathon only hydrogen fuel cells are allowed.

2.2.4 Power line vehicles

This type of system can be seen on trams and trolley buses. This type of vehicles received power from overhead lines and a small battery was used on board, when not connected to the power lines (Larminie & Lowry, 2012).

2.2.5 Photovoltaic (PV) electric vehicles

A photovoltaic (PV) electric vehicle is one whereby the vehicle is powered by solar panels mounted on the vehicle. The solar panels capture solar energy, usually on the roof of the vehicle and convert this energy into electrical energy. PV vehicles are not currently used for everyday transportation but were mainly used for demonstration purposes. There is an increase in this technology in assisting a battery electric vehicle (Arsie, et al., 2007).

2.2.6 Super capacitor electric vehicles

In this type of electric vehicle super capacitors are placed in shunt with the battery pack. Super capacitors have the advantage over batteries in that they can supply short bursts of energy and also assist the battery with acceleration as well as regenerative braking. This also allows the battery pack to be more compact (Pay & Baghzouz, 2003).



Figure 2-5: A super capacitor electric vehicle (SAE International, 2016)

2.3 Subsystems in electric vehicles

There are various aspects of the electric vehicle that needed to be considered before developing the vehicle. Factors such as the requirements and rules for the class of UrbanConcept, the mechanical requirements as well as the electrical systems are different aspects taken into consideration. Various subsystems such as different motor technologies, the different batteries available and the battery management system (BMS) are also subsystems that needed to be considered. These subsystems are major contributing factors in developing an efficient electric vehicle (Cabrera, et al., 2015).

2.3.1 Requirements

There are mechanical and electrical requirements for the UrbanConcept vehicle but for the purpose of this research only the electrical requirements were looked at. The checklist in Table 2-1 is a summary of the electrical requirements for the vehicle (Shell, 2013).

Table 2-1: Design requirements for the vehicle's electrical systems (Shell, 2013)

Item No.	Item description	Yes	No
1	The EV motors must be capable of delivering 1.4 kW mechanical power.		
2	The EV must be capable of travelling at a constant speed of 60 km/h.		
3	The motors developed for the EV runs at an AC input voltage of 23 V.		
4	The motors developed must have an efficiency of above 50 %.		
5	The motor drive must deliver a voltage higher than 38 V DC and a current rating higher than 30 A DC.		
6	The motor drive must be able to deliver a power of 1200 W (or higher).		

7	The motor drive must have an efficiency of 80 % (or higher).		
8	Only Lithium type batteries are to be used for this EV with a maximum voltage of 60 V.		
9	The battery management system is expected to produce an efficiency of 80 % (or higher).		
10	The electrical system is protected against overload.		
11	The accessory battery maintains a negative ground.		
12	The capacity of the accessory battery is sufficient to power all the accessory loads with a sufficient safety margin.		
13	Cell overvoltage protection limits are provided for the BMS.		
14	Operation of the cell balancing for the BMS is provided.		
15	The battery operates when over-voltage limits are reached for the BMS are provided.		

2.3.2 Mechanical requirements of the electric vehicle

The vehicle was designed by the PLMCC group and the chassis/frame was constructed by Mechanical Engineering students. A simulation done by the PLMCC team of the car determined that 1.4 kW of mechanical power was required from the electrical motors at a speed of 60 km/h. Figure 2-6 shows a virtual image of the vehicle design.



Figure 2-6: The urban concept battery electrical vehicle being designed by the CPUT

The chassis was also designed in order to achieve optimal aero-dynamic efficiency, while still being rigid and lightweight (in order to comply with the shell eco-marathon strict specifications). Further investigations by the PLMCC found the following values for the EV.

The aerodynamic drag coefficient was found to be $C_d = 0.4$ and the characteristic frontal area was $A = 1.15 \text{ m}^2$ for the CPUT EV. A simulation of this can be seen in Figure 2-7.

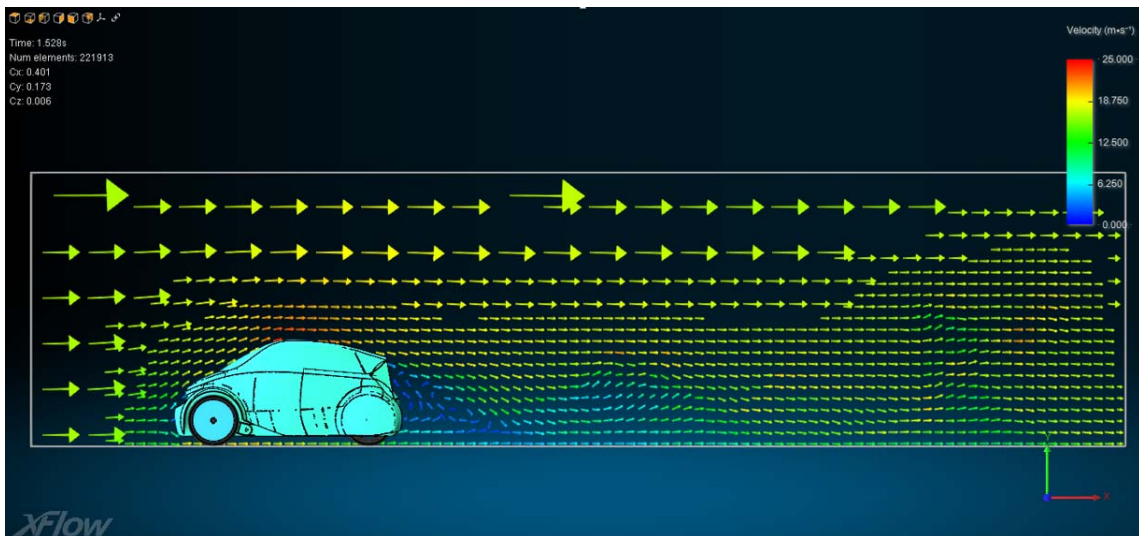


Figure 2-7: A screenshot of the EV chassis design simulation

For the purpose of this research, the focus was on the design of the vehicle's electric system. This included selection, design and development of the motors and motor drives for the vehicle, the batteries and the BMS as well as the auxiliary systems which would include, the lights, indicators, wiper units, measuring equipment, etc.

2.3.3 Forces acting on an EV

There are many factors which influence the efficiency of the EV and in order to calculate the efficiency of the entire drive train, the power and force required to propel the EV needed to be calculated. There were three major forces that we needed to consider before determining the forward motion of the EV, namely aerodynamic drag, rolling resistance and climbing resistance. These forces are illustrated in Figure 2-3 (Strickland, 1993).

Figure 2-8 shows the forces acting on a vehicle in motion, where F_t is the tractive force measured in Newton (N), F_a the aerodynamic drag (N), F_r the rolling resistance force (N), F_g is the climbing resistance force (N) and α is the road angle (measured in radians).

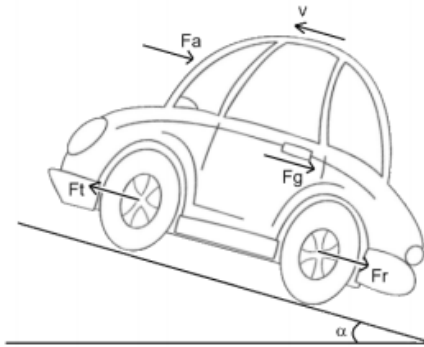


Figure 2-8: Forces acting on an EV (Grunditz & Jansson, 2009)

2.3.3.1 Speed

In order to calculate the speed of the vehicle, it was necessary to know the distance travelled and the time taken to travel this distance (Rae, 2005):

$$Speed = \frac{Distance}{Time} \quad (1)$$

2.3.3.2 Acceleration

To calculate the acceleration of the EV, it is a change in speed divided by the change in time (KirkPatrick & Francis, 2010).

$$Acceleration = \frac{\Delta speed}{\Delta time} \quad (2)$$

2.3.3.3 Climbing force

As a vehicle moves up or down an incline or decline, the weight of the vehicle creates a downward directed force. When travelling up an incline, this force opposes the motion and when travelling down a decline, this force contributes to the motion. The climbing resistance force is given by (Grunditz & Jansson, 2009):

$$F_{climb} = m \times g \times \sin(\alpha) \quad (3)$$

Where:

m = Mass of the vehicle (kg)

g = Gravitational constant (m/s^2)

α = Road angle (rad)

The gravitational constant is $g = 9.807 \text{ m/s}^2$ (Grassmann, 1971).

2.3.3.4 Aerodynamic force

The force which opposes the forward motion of the vehicle as a result of air drag, consists predominantly of shape drag and skin friction. As the vehicle moves, an area of high air pressure at the front of the vehicle and an area of low air pressure at the rear of the vehicle is generated. These two areas will oppose the motion of the vehicle and the resultant force on the vehicle is termed “shape drag”. “Skin friction” is generated due to the fact that air molecules travelling at different speeds produce friction. This means that, because the speed of the air close to the vehicle is nearly equal to the vehicle speed and the air further away from the vehicle is substantially slower, friction will be produced. From the equation below (for drag force) it can be seen that the aerodynamic forces become much more significant as the vehicle speed increases (Giordano, 2009) (Grunditz & Jansson, 2009).

$$F_{drag} = \frac{1}{2} \times \delta \times C_d \times A \times v^2 \quad (4)$$

Where:

δ = Air density (kg/m³)

C_d = Aerodynamic drag coefficient

A = Characteristic frontal area (m²)

v = Velocity of the vehicle (m/s)

Air density at sea level is typically $\delta = 1.225 \text{ kg/m}^3$ (Kreith & Yogi Goswami, 2007); the aerodynamic drag coefficient was found to be $C_d = 0.400$ according to our PLMCC simulation and the characteristic frontal area was $A = 1.150 \text{ m}^2$ as previously mentioned.

2.3.3.5 Rolling force

The biggest contributor to rolling resistance of tyres on a hard surface is hysteresis. When the carcass of a tyre is deformed or degraded, this results in an asymmetrical distribution of ground reaction forces, causing hysteresis to arise. Other factors which may influence the rolling resistance are friction between the tyre and the road, as well as, circulating air in the tyre itself. The rolling resistance force is given by the equation (Benenson, et al., 2000)(Grunditz & Jansson, 2009):

$$F_{roll} = C_r \times m \times g \quad (5)$$

Where:

C_r = Friction constant

The friction constant was calculated to be $C_r = 0.010$. This is the typical value for the tyres used for the CPUT EV. The total mass of the EV was measured at 205 kg with a minimum driver weight of 70 kg, according to the rules of the Shell Eco-marathon (Shell Eco-marathon, 2016).

The friction constant (C_r) is greatly influenced by parameters like tyre material, structure, temperature, and pressure, as well as, tread geometry, road surface roughness, road surface material and the presence or absence of liquids on the road surface (Grunditz & Jansson, 2009).

2.3.3.6 Acceleration force

The acceleration force can be described as the total tractive effort of the vehicle minus the sum of the forces which oppose the vehicles motion. The acceleration force is given by the equation (Benenson, et al., 2000)(Grunditz & Jansson, 2009):

$$F_{acc} = m \times a \quad (6)$$

Where:

a = Acceleration of the vehicle (m/s^2)

The aerodynamic drag, the rolling force, the climbing force and the acceleration force have all been now defined. The power for each can now be calculated based on force and speed. Work equals force times distance as indicated in the equation (Strang, 1991):

$$W = F \times d \quad (7)$$

Where:

W = Work (Nm or J)

F = Force (N)

d = Distance travelled (m)

The equation for power can be written as follows, assuming that the force acts along the direction of travel (Newman, 2008).

$$P = \frac{W}{t} = \frac{F \times d}{t} \quad (8)$$

Where:

P = Power

t = Time taken (s)

The objects speed, v is $\frac{d}{t}$, so the equation becomes (Newman, 2008):

$$P = \frac{W}{t} = \frac{F \times d}{t} = F \times v \quad (9)$$

However, you have to take acceleration into consideration when you apply a force, so the equation must be written in terms of average power and average speed (Newman, 2008).

$$\bar{P} = F \times \bar{v} \quad (10)$$

Where:

\bar{P} = Power (W)

F = Force (N)

\bar{v} = Average speed and can be calculated from the formula (Newman, 2008).

$$\bar{v} = \frac{v_i + v_f}{2} \quad (11)$$

Where:

v_i = Starting speed (m/s)

v_f = Ending speed (m/s)

The ending speed can be calculated from the equation (Newman, 2008).

$$v_f = v_i + at \quad (12)$$

Alternatively, the average power can also be calculated by work divided by time (Newman, 2008).

$$\bar{P} = \frac{W}{t} \quad (13)$$

The work done by the car is the difference in kinetic energy in the beginning and in the end. This is represented by (Newman, 2008):

$$W = KE_f - KE_i \quad (14)$$

Where:

KE_i = Kinetic energy in the beginning (0J)

KE_f = Kinetic energy at the end, which can be calculated for the formula (Newman, 2008):

$$KE_f = \frac{1}{2}mv_f^2 \quad (15)$$

Where:

v_f = Ending speed (m/s)

2.3.3.7 Chassis

There are specific safety regulations for the chassis being constructed for the competition. Aspects such as the roll bar being able to withstand a static load of 700 N applied in a horizontal or perpendicular direction, without deforming is one of the concerns regarding the chassis (Shell, 2013).

2.3.3.8 Vehicle design

Stringent factors such as aerodynamic appendages, vehicle interior, vehicle body and wheels, luggage space, towing hook, mechanical parts, vehicle access, windscreen and wiper(s) requirements will be considered in the design of the Urban Concept vehicle (Shell, 2013).

2.4 Electrical systems

For the purpose of this competition and research a battery electric UrbanConcept vehicle was designed. This battery electric vehicle can only utilize two Lithium-Ion battery packs, one for vehicle propulsion and one for accessories such as safety devices namely lights, wiper(s), horn, etc.

There are also other accessories such as ignition, starter motor, communication systems, GPS system, data loggers and ventilation/cooling of the driver than needs to be developed (Grudic, 2008) but for the purpose of this research only the power train was developed.

There are various components of the EV that needed to be considered, namely the motors being used, the batteries and BMS and the various subsystems. The EV being developed by the CPUT consists of the following main sub-systems; chassis (purely mechanical), electric motor, power stage (motor drive), batteries, a BMS and a control stage (control mechanism for the power stage). Figure 2-9 shows a typical block diagram for an EV.

The main aspects of the EV are the electric motor, the battery bank and the power converter. These are discussed in the sections to follow (Husain, 2011).

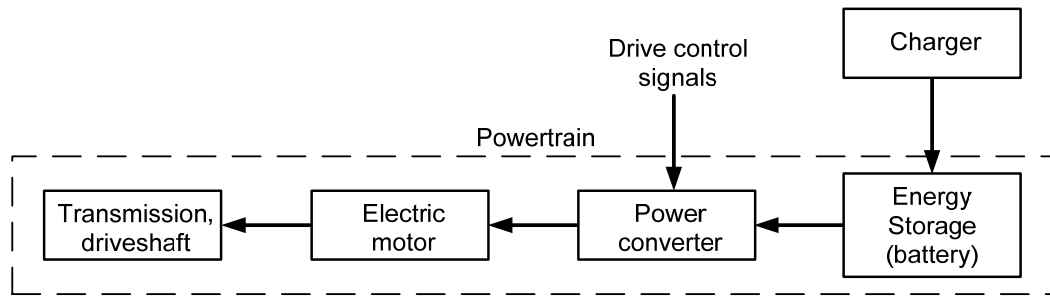


Figure 2-9: Typical block diagram for a battery powered EV (Husain, 2011)

2.4.1 Electric motors

The criterion for the motor is that it must be efficient, reliable and suitably priced in that the motor should be above 60% efficient and cost not more than R1500 (within the project budget). Three motors were considered, namely the permanent magnet, squirrel cage and reluctance motors. Each motor have its own advantages and disadvantages.

2.4.1.1 Permanent magnet motors

Permanent magnet motors are very simple in construction; they have no commutator or slip rings, making for easy maintenance. These motors are high in cost and are moderately reliable. Their small air gap is, however, a huge drawback and the possibility of cracking rotor bars due to hot spots always remains an issue. Compared to synchronous motors these motors also have a higher efficiency (Gieras, 2010).

2.4.1.2 Squirrel cage induction motors

The squirrel cage induction motor is one of the most commonly used motors in industry and is very robust. In these motors, the slots are partially closed and the windings consist of embedded copper bars to which the short circuit rings are brazed, hence leading to the name “squirrel cage motor”. Squirrel cage motors are extremely low cost and very rigid and robust in construction. These motors are able to operate in the harshest of conditions and take much abuse (Rajput, 2005).

2.4.1.3 Reluctance motors

Reluctance motors are unique, in that, their mechanical output power and overall performance is fairly good in comparison to their maintenance and operating costs. Many timing devices, which require a constant speed characteristic, make use of this type of motor (Gupta, 2010).

2.4.1.4 Motor selection

A comparison of the three motors considered is shown in Table 2-2. The selection of the motor was based on the following criteria; must be low priced (within the project budget and not more than R1500), have an efficiency above 60%, good reliability, light weight and must be available in South Africa.

Table 2-2: Motor comparison (Hashernnia & Asaei, 2008)

	Permanent Magnet Motor	Squirrel Cage Motor	Reluctance Motor
Cost	High	<i>Low</i>	Moderate
Efficiency	<i>High</i>	Moderate	Moderate
Power Density	<i>High</i>	Moderate	Moderate
Controllability	Moderate	<i>High</i>	Low
Reliability	Moderate	<i>High</i>	<i>High</i>
Availability	Moderate	<i>Abundant</i>	Rare in RSA

From Table 2-2, it is clear that the permanent magnet motor was the best solution for an economical race with its high efficiency and light weight; however, it is very expensive. The reluctance motor was also a good option, but is not readily available in South Africa, at an affordable price.

The squirrel cage motor was selected as it is readily available, at an affordable price and has a better reliability than the other two. The objective is to complete the race within the allotted time.

A battery voltage of 38 V DC nominal was selected due to limitations of the BMS available at the CPUT. This means a three phase squirrel cage motor needed to work from a 38 V DC power source. A three phase squirrel cage motor with such a low operating voltage was virtually impossible to find. It made sense to use a “currently off the shelf” (COTS) 380 V motor and re-wind it to operate from this low voltage as this motor was within the R1500 budget and produces an efficiency of 70%.

2.4.1.5 Rewinding the motor

In rewinding the motor, the windings were not duplicated, but the number of turns were changed in order to allow the motor to operate on a three phase, 23 V alternating current (AC) voltage.

A method of increasing the motors efficiency is to increase the copper cross-sectional area as much as is possible, as well as, keep the end turns as short as is possible. In some cases, however, the coil extension is crucial for rapid heat dissipation. This means, if it is too short, it may lead to an increase in winding temperature, and thereby increase the copper (I^2R) losses (Electrical Apparatus Service Association, Inc., 2003).

The voltage which is applied to each of the phases (of the motor) is opposed by and nearly equivalent to the back electromotive force (EMF). The back EMF can be described as the induced voltage in a coil, due to the conductors cutting field magnetic lines of flux (Electrical Apparatus Service Association, Inc., 2003).

Back EMF is expressed by the following formula (Electrical Apparatus Service Association, Inc., 2003):

$$E = 4.44 \times f \times N \times F \times Kd \times Kp \quad (16)$$

Where:

E = Back EMF per phase (V)

f = Frequency (Hz)

N = Number of series turns/phase

F = Magnetic flux/pole (Wb)

Kd = Winding distribution factor

Kp = Winding pitch factor (Electrical Apparatus Service Association, Inc., 2003)

This means Kd and Kp must be optimised in order to ensure that fundamental EMF's per coil are maximized and harmonic EMF's minimized (Electrical Apparatus Service Association, Inc., 2003). Efficiency is the measure of how much electrical input energy a motor can convert into useful mechanical work versus how much energy is wasted (due to losses). Losses are wasted energy, most of which is dissipated as heat. Losses comprise of: stator winding losses, stator core losses, rotor losses, and stray-load losses - see Figure 2-10: Typical distribution of losses (Electrical Apparatus Service Association, Inc., 2003).

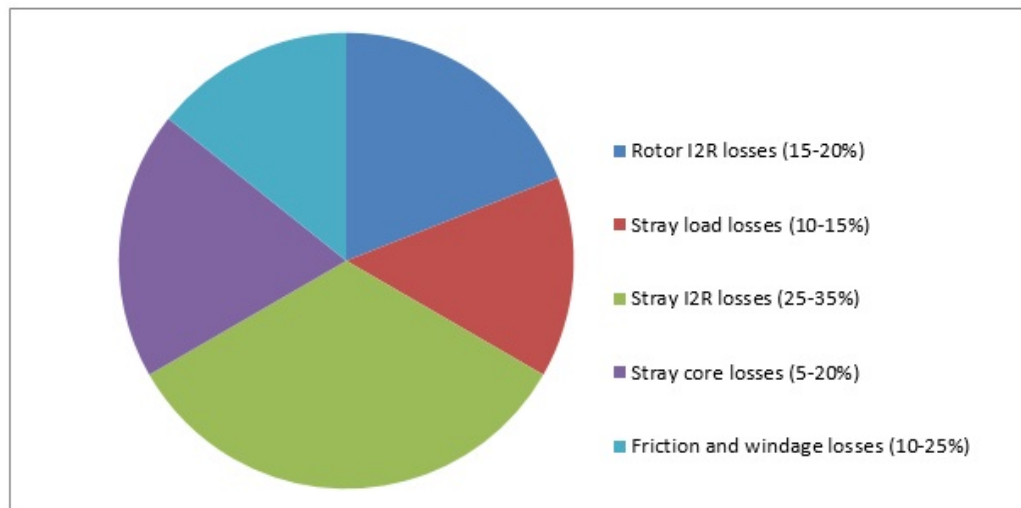


Figure 2-10: Typical distribution of losses (Electrical Apparatus Service Association, Inc., 2003)

Since majority of the wasted energy is dissipated as heat, it is clear that less heat means better efficiency. There are many ways to reduce heat loss in a new motor design, but for rewinding, adding more copper to windings in order to increase slot fill can reduce the copper losses. This change aids in lowering the winding temperature, and hence permits the use of smaller fans. A smaller fan will reduce the amount of power used to drive the fan and therefore increase efficiency. When current flows through a conductor, I^2R losses are incurred (in the form of heat). For the same amount of current, using a larger conductor will generate less heat than a smaller conductor. The amount of copper in a motor is determined by the cross-sectional area of the paralleled conductors. This quantity is based on current density and the unit is termed as amperes per mm^2 . Generally, lower current density results in lower I^2R losses, therefore, where it is practical, it is preferable to use a conductor with less wires and a larger cross-sectional area, instead of more wires and a smaller cross-sectional area (Electrical Apparatus Service Association, Inc., 2003).

2.4.2 Motor control options

Induction motors, when coupled to a mains supply, can only run at their rated (nameplate) speed. With the EV application, as in many other applications, the ability to vary the motor speed was essential (Parekh, 2009).

With growing technology and a reduction in natural resources, an efficient and effective way of driving and controlling motors has become a major concern. In the past inefficient mechanical motor drives and control systems, such as mechanical transmission systems which were mechanically coupled to the motors and differential drives were utilised (Emadi, 2005).

With great technological advancements in semiconductor technology today, these inefficient drives may be replaced with semiconductor based motor drive and control solutions. The electronic motor drive, which is the power stage, is discussed in this section (Parekh, 2009).

A motor-drive, also known as a variable frequency drive (VFD) or a variable speed drive (VSD), is an device used to control the speed and torque of an electric motor by varying the applied voltage and frequency to the motor in a locked or fix ratio. Controlling a motor drive can be anything from a potentiometer to a more advanced foot-pedal which is controlled by a human and/or a control display or dashboard in the EV (Yardley & Stace, 2008).

This form of control is termed “human interface”. By varying the human interface, the control circuit determines “how much power” is required from the user and delivered to the motor(s) via the motor-drive. Figure 2-11 depicts a block diagram of the essential components in an EV, together with the human interface (Brain, 2001).

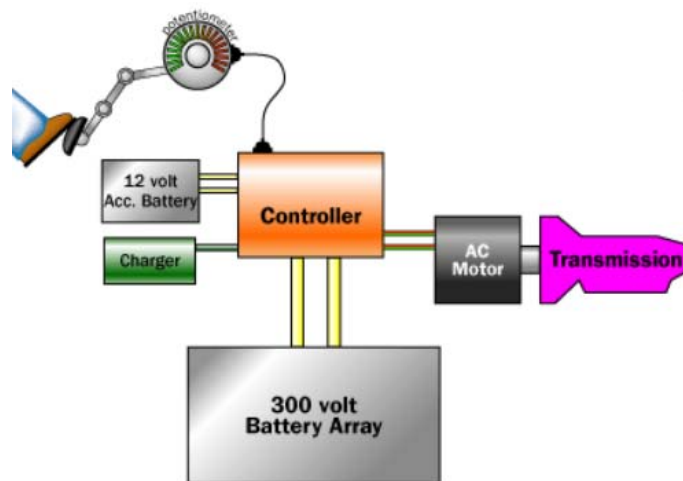


Figure 2-11: A typical control system block diagram for an EV controlled by a human interface (Brain, 2001).

The selection of a motor-drive was determined by the specific needs of the motor(s) to be driven. The motor-drive selection depended on:

- The type of motor(s),
- The amount of motors to be driven,
- Whether a variable speed or constant speed is required, and
- The size or power rating of the motor(s).

A block diagram showing a control stage and a power stage of a motor-drive for a three phase induction machine is illustrated in Figure 2-12 (Freescale, 2016). The purpose of the power stage is to produce a sinusoidal three phase waveform for the three phase motor. The pulse width modulator (PWM) controls the speed of the motor while the micro control unit (MCU) or digital signal controller (DSC) lowers the power consumption used by the motor. The analogue-to-digital convertors convert the sinusoidal analogue signal from the power stage driver to a digital signal and provides feedback.

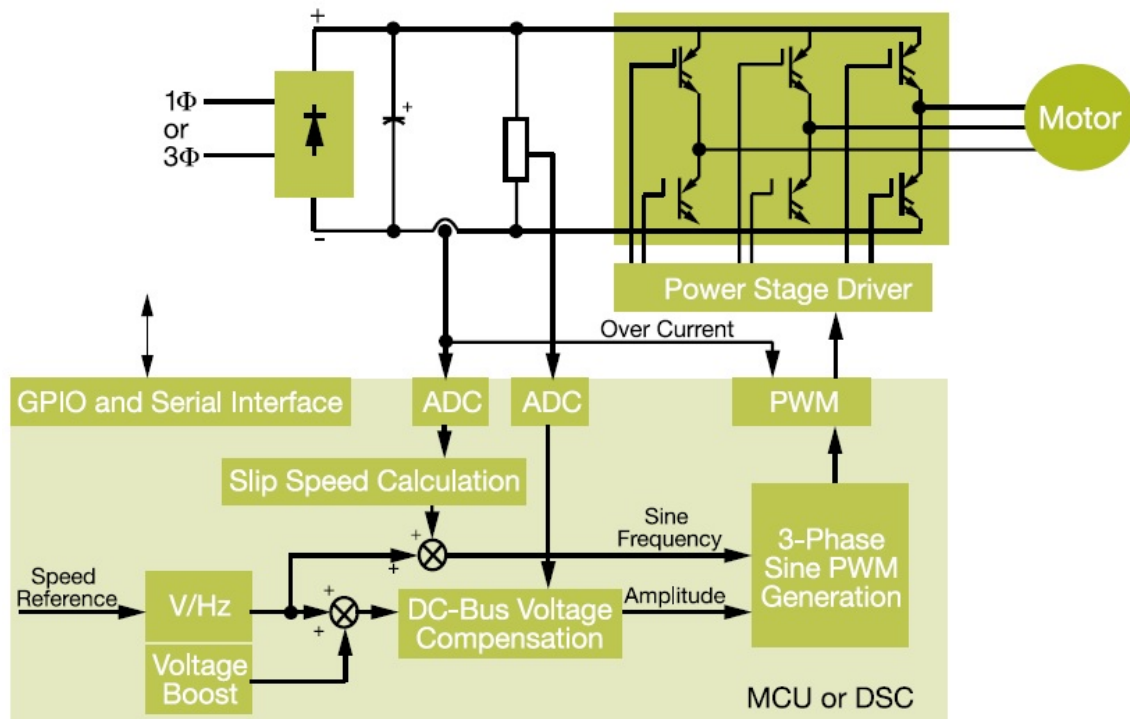


Figure 2-12: A three phase AC induction machine voltage/frequency open loop control (Freescale, 2016)

A typical three phase inverter bridge (variable speed drive) can have an efficiency of between ninety five percent and ninety eight percent. This typical value should be similar for both a designed system and a COTS system (Novak, 2016).

2.4.2.1 Different topologies available in industry

As this research is on a three phase, alternating current (AC) induction machine (IM), direct current (DC) motor-controllers will not be discussed in detail but only mentioned if and when applicable.

According to Rockwell Automation, a leading VFD/VSD manufacturer, if a motor is run at eighty percent of full speed, a saving of up to fifty percent in energy can be made.

This is a major saving regardless of what industry this is implemented in (CMI, 2009). Early motor-control consists of manually changing the pole connection on the motor if a different speed is required; this is very labor intensive and not very practical or economical. The Microchip designs flow-chart (Figure 2-13) has most of the drive topologies that is implemented in industry (Microchip, 2016).

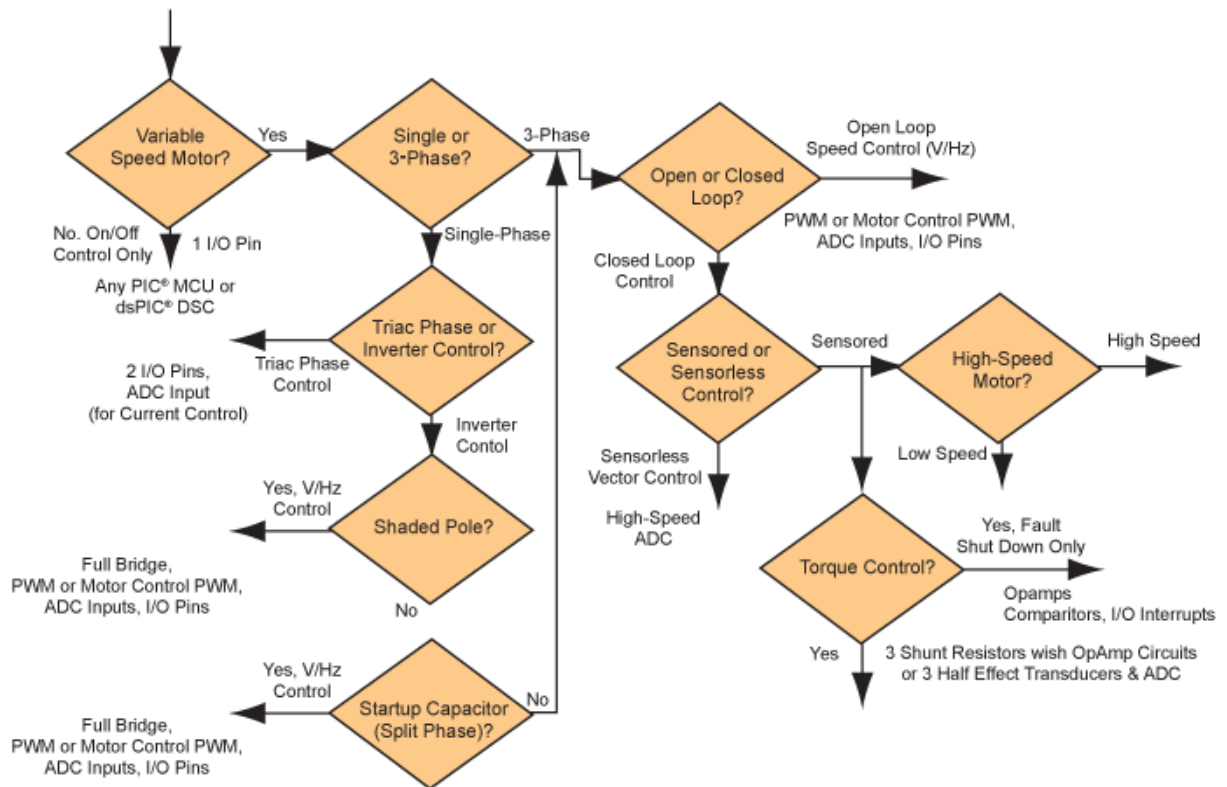


Figure 2-13: Motor-drive topology flow-chart (Microchip, 2016)

Open loop scalar or voltage/frequency control is the most common for cost effective solutions in industry (Rashid, 2011). The voltage and frequency applied to the motor is always in a specific ratio to each other. As the voltage or frequency increases, so does the revolutions per minute (RPM). The problem with this kind of control is that all AC IM have slip, so under hard acceleration or high and sudden torque conditions the motor will have more slip than normal, thus not operating at precisely the speed the controller is instructing it to operate at (ABB Webinar, 2014).

Some of the advantages of this type of control are listed below:

- The motor can be operated in both directions with fast torque response.
- This topology is the most cost effective.

- It is ideal for low speed control.
- It has a high efficiency.
- It has precise speed control.
- It works well on motors with unstable parameters (Freescale semiconductor, 2016).

To overcome the problem of slip; several forms of feedback can be implemented to monitor the actual speed of the rotor, some more accurate than others. A form of feedback in a closed loop system is that there is an encoder on the accessory side of the motor that counts the RPM's of the shaft and compares it to the pre-set value of the human interface. If the controller detects that the shaft has deviated too much from the requested speed it will either increase or decrease the speed (Ranka, et al., 2010).

Other forms of feedback include - hall-effect sensors, rotary encoders, current sensing on two of the phases and velocity sensing. The more sophisticated the feedback function, the more efficient is the drive and subsequently the more expensive it becomes (ABB Webinar, 2014).

Some of the advantages of feedback control are listed below (Freescale semiconductor, 2016).

- It is very accurate and precise speed and torque control.
- This topology is ideal for high end control.
- It has a high efficiency.

For the motor and motor drive requirements of the EV for the Shell Eco-Marathon, the precise rotor position is not critical, thus the more expensive and advanced closed loop topologies will not be implemented. Focus will be set on acquiring a linear torque curve and a form of feedback to reduce the chances of rotor lockup under heavy load.

2.4.2.2 Control stage options for the motor drive

The primary purpose of the control stage is to provide PWM signals to control the six switches of the power stage. At the same time, the control strategy must be implemented, which will allow the speed of the motor to be varied, and subsequently allow the EV to vary its speed. There is an endless amount of platforms which can be used to provide this type of control, but only two, namely field programmable gate array (FPGA's) and microcontrollers are discussed in this section. Additionally, the various control strategy options are also discussed.

2.4.2.3 FPGA's

The FPGA is a semi-conductor device which can be programmed post manufacturing. What makes FPGA's so special is that they can be utilised to implement any logical function that an application specific integrated circuit (IC) can perform, but with the difference that they have the ability to be reprogrammed after implementation (Soni & Shah, 2011).

Modern day FPGA's comprise of various mixes of configurable static random access memory (SRAM), high-speed transceivers, high-speed inputs/outputs (I/O's), logic blocks, and routing. FPGA's contain programmable logic components, namely logic elements, as well as many levels of reconfigurable interconnects that make provision for the physical connection of logic elements. Logic elements can be used to perform any functions from simple logic gates to highly complex combinational functions. In majority of the modern FPGA's, the logic blocks also possess memory elements (Soni & Shah, 2011).

2.4.2.4 Microcontroller unit (MCU)

A MCU is a small computer on a single integrated circuit, which contains a processor core, memory, as well as, programmable I/O peripherals. MCU's are designed for embedded applications, which makes them quite different from the microprocessors used in personal computers or any other general purpose applications (Barry Davies, 2016).

MCU's have many uses, some of which include: engine control systems, implantable medical devices, remote controls, and power tools, etc. MCU's greatly reduce the size and cost, compared to designs using separate microprocessors, memory and I/O devices. They make the digital control of devices and processes extremely economically viable. Many MCU's have analog components incorporated, in order to facilitate the control of non-digital electronic systems (Barry Davies, 2016). An advantage of FPGA's is that they are extremely configurable and the pins are even swappable (StackElectronix, 2016). Table 2-3 shows a table that compares FPGA's and microcontrollers.

Table 2-3: FPGA's vs. microcontrollers (Rajewski, 2017)

FPGA's vs. Microcontrollers		
	FPGA	Microcontroller
Cost	±R6000	±R3000 (incl. Development Board)
Processing power	Excellent	Sufficient (for this application)
Multi-tasking ability	Excellent	Not Possible
Speed	Very Fast	Sufficient (for this application)
Expansion capability	Infinite	Limited
Reconfiguration	Infinite	Limited
Setup	Complicated	Simple

The different microcontroller options are listed and compared in Table 2-4.

Table 2-4: Microcontroller options (Microchip, 2013) (Atmel, 2016) (Texas Instruments, 2017) (Microchip, 2011)

Microcontroller Options				
	PIC16F737	AT90PWM3	TMS320F28232	dsPIC30F2010
Cost	R54 (excluding development board)	R38 (excluding development board)	R240 (excluding development board)	R60 (excluding development board)
Program memory (Bytes)	4096	16000	16000	12000
I/O's	25	19	88	28
SRAM (Bytes)	368	1024	34k	12k
Interrupts	16	4	58	32
SPI	Yes	Yes	Yes	Yes
Timers	3	2	17	3
Comparators	2	2	0	4
Lead Time	6 days	6 days	± 1 week	3 days

Due to the low cost, the amount of I/O's, comparators, and timers, the PIC16F737 was found to be one of the best suited packages for this application. The dsPIC30F2010 was also looked at as a second option in a microcontroller for the EV.

2.4.3 Control strategy

Selecting the correct control strategy was critical, as it controls the motors speed, and has the ability to improve the motors steady state and dynamic characteristics. Additionally, utilizing a good control strategy can even bring down the systems average energy consumption. These characteristics were imperative for the EV application (Parekh, 2009).

2.4.3.1 Voltage source inverter (VSI) control

A few disadvantages associated with VSI control:

- There is a decreasing power factor with decreasing speed.
- It has induced harmonics.
- "Cogging" (jerky start/stop motion) may occur (Singh & Khanchandani, 2007)

These characteristics make this method undesirable for the EV application.

2.4.3.2 Current source inverter (CSI) control

Disadvantages associated with CSI control (Turkel, 2016):

- There are large power harmonics generated back into the power source.
- "Cogging" occurs below 6 Hz due to a square wave output.
- Needs to make use of large and costly inductors.
- There are high voltage spikes to motor windings.
- They are load dependent.
- They have poor input power factor.

Once again, these characteristics make this method undesirable for the EV application.

2.4.3.3 Voltage frequency (VF) control

Voltage frequency (VF) control consists of the generation of a variable frequency supply, which possesses a constant voltage to frequency ratio. VF control is well suited for a variety of motor drive applications, where it is required to vary motor speed and control the motor as efficiently as possible. Additionally, VF control is very simple to implement and at a low cost. After some research, it was found that the PIC16F7X7 series of microcontrollers were ideal for the application of the VF control strategy. Due to the fact that these microcontrollers have three hardware PWM modules, made them quite suitable for three phase motor control applications. For this reason the VF control strategy was chosen (Parekh, 2009).

In this section only the most important points of VF control will be highlighted, as an in depth discussion of induction motor control theory is beyond the scope of this study. The base speed of an induction motor is directly proportional to the frequency of the supply and the motors number of poles. The number of poles for the motor is fixed; therefore the best method of speed variation is to vary the frequency of the supply. The induction motor's torque which is developed is directly proportional to the ratio of the voltage applied and the supply frequency. With the variation of the voltage and frequency (while maintaining a constant ratio between them), the torque developed may be kept at a constant value, throughout the speed range.

This is precisely what the VF control strategy attempts to achieve. The typical torque-speed characteristic curve of an induction motor, which is supplied directly from the mains supply, is shown in Figure 2-14. Figure 2-15 illustrates what the torque-speed characteristic curve looks like with the use of VF control (Parekh, 2009):

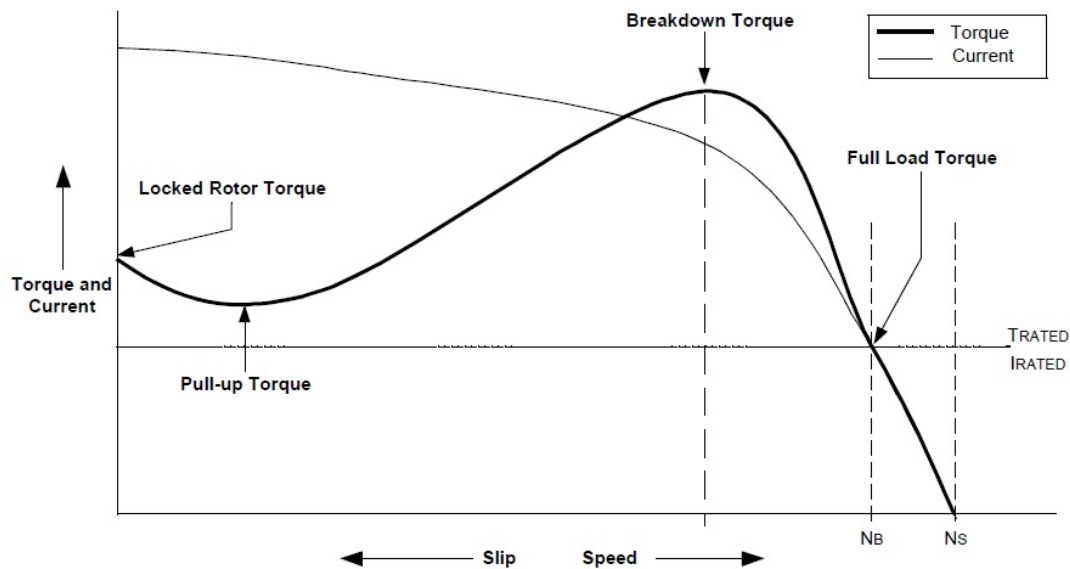


Figure 2-14: Typical torque-speed characteristics of an induction motor (Parekh, 2009)

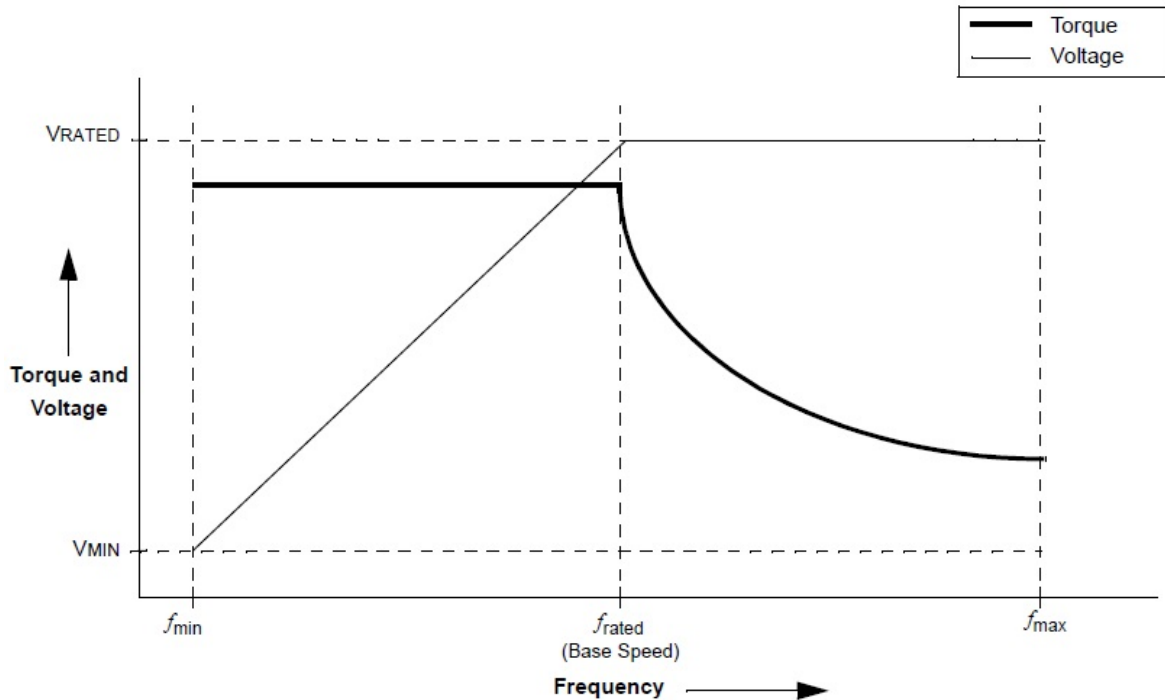


Figure 2-15: Torque-speed characteristics of an induction motor with VF control (Parekh, 2009)

In addition to the variation of speed, the torque-speed characteristics of the induction motor with VF control illustrates the following (Parekh, 2009):

- The required starting current is lower.
- There is an increase in the size of the stable operating region. The motor can run from five percent of the synchronous speed (N_s) up to the base speed (N_B), instead of just running at its base speed. The torque generated can also be kept constant throughout this region.
- The voltage and frequency reach the rated values at the base speed. The motor can be driven beyond this base speed by increasing the frequency. The applied voltage may not, however, be increased beyond the rated voltage level. This means only the frequency is able to be increased, resulting in the reduction of torque.
- By changing the supply frequency, with respect to time, the acceleration and deceleration of the motor can be controlled.

2.4.3.4 Basic control technique

The PIC16F7X7 series of microcontrollers have three 10-bit PWMs in the hardware. The duty cycle of each PWM has the ability to be varied independently in order to generate a three phase AC waveform.

In order to derive a varying three phase AC voltage from the DC bus, the PWM outputs are required to control the six switches of the power stage. This can be achieved by coupling the PWM outputs to the MOSFET gate drivers of the power stage. Of the six signals fed to the gate drivers, there are three pairs (one for each phase); each pair has one signal switching the upper switch and one signal switching the lower switch (Parekh, 2009).

A reference voltage input can be used to vary the motor frequency. The microcontroller then uses the analogue-to-digital-converter (ADC) results to calculate the PWM duty cycle and thus determines the necessary output frequency and amplitude of the supply to the motor (Parekh, 2009),

2.4.4 Batteries

The batteries are a critical part for any off-grid power system. Car batteries are designed for an entirely different purpose. They must be long lasting for a long run. The long-time standard batteries for this project are Lithium-polymer rechargeable batteries. These are approximately 3.7 V (nominal) (see Appendix E).

For the Shell Eco-Marathon rules and regulations; only Lithium type batteries may be used for the main storage system, with a maximum voltage of 60 V (Shell, 2013).

Lithium-Ion batteries use a carbon anode, metal oxide cathode, and a Lithium salt electrolyte solution. They have excellent energy density and capacity. They are also very commonly used in portable consumer electronics, such as cell phones and laptops (Buchmann, 2014) and are mostly used for electric vehicles as a source of energy. The Lithium air battery can be one of the most suitable advanced energy sources for an electric vehicle, as they have a high energy density due to light materials as active materials (Buchmann, 2014).

Table 2-5 below shows the main types of Lithium-Ion batteries with their typical uses and chemistries (Pistoia, 2014).

Table 2-5: Primary Lithium-ion battery chemistries and their uses (Pistoia, 2014)

Chemical Name	Material	Abbreviation	Application
Lithium Cobalt Oxide	LiCoO ₂ (60 % Co)	LCO	Cell Phone, Laptop, Camera
Lithium Manganese Oxide	LiMn ₂ O ₄	LMO	

Lithium-Ion Phosphate	LiFePO4	LFP	Power tools, e-bikes, EV, medical, hobbyist.
Lithium Nickel Manganese Cobalt Oxide	LiNiMnCoO2 (10-20 % Co)	NMC	
Lithium Nickel Cobalt Aluminium Oxide	LiNiCoAlO2	NCA	
Lithium Titanate	Li4Ti5O12	LTO	Gaining importance in electric powertrain and grid storage.

2.4.5 Battery management system (BMS)

The very first BMS introduced was by a company called Albercorp in 1979. Since then research have shed light on how and why batteries fail. Major improvements in BMS's happened during the years. A BMS is used to ensure that the batteries are kept within their operating voltage and temperature range stated by the manufacturer during operation (Alber & Leissle, 2000). A BMS is an electronic system that monitors and protects the battery. It also estimates the state of the battery in order to maximize the batteries performance and reports to the user or an external device (Andrea, 2010). A battery pack built together with a battery management system with an external communication data bus is a smart battery pack (Bergveld, 2001).

The main function of a BMS is to ensure maximum efficiency energy supply to a portable product and the risk damage to be prevented (Pop, et al., 2008).

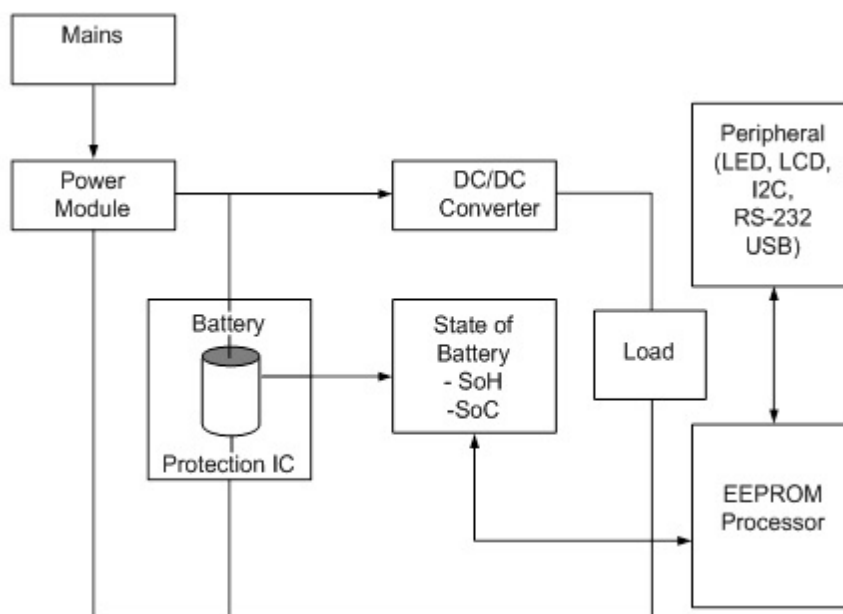


Figure 2-16: General architecture of a BMS (Pop, et al., 2008)

The purpose of the power module is to charge the battery by converting electrical energy from the mains into electrical energy suitable for charging the battery/ A protection integrated circuit (IC) connected in series with the battery is generally needed for Lithium-ion batteries. The reason for this is that battery suppliers are particularly concerned about safety issues due to liability risks. The battery voltage, current and temperature have to be monitored and the protection IC ensures that the battery is never operated under unsafe conditions. The DC/DC converter is used to efficiently condition the unregulated battery voltage for compatibility with stringent load requirements. The task of the load is to convert the electrical energy supplied by the battery into an energy form that will fulfil the load's function, such as mechanical energy, light, sound, heat, EM radiation, etc. The battery status can be indicated in one light emitting diode (LED) or several such diodes. This indicates the battery's state of charge (SOC) and condition. The processor is used to run the battery management software. Communication between the BMS and other devices is another important task of the BMS (Pop, et al., 2008).

In multi-cell battery packs, small differences between cells due to production tolerance or operating tend to be magnified with each other's charge and discharge. Weaker cells become overstressed during charging causing them to become even weaker, until they eventually fail causing premature failure of the battery (Arendarik, 2016).

Cell balancing is a way of compensating for weaker cells by equalizing the charge on all the cells in the chain and thus extending the battery life (Arendarik, 2016). As previously stated, the BMS is the heart and most critical component of the EV. It ensures the power source is operated safely and efficiently for its maximum lifespan. The most important features that the BMS needs to control and monitor are:

- Cell protection - The individual cells in a battery pack must be prevented from operating outside their voltage and current ranges (Andrea, 2010) (Larminie & Lowry, 2012).
- Charge Control - It is important that the cells are not overcharged as this is a definite way to destroy them fast.
- State of Charge (SOC) determination - It is important to know the SOC of the battery at all times. Many applications require it including the human machine interface (HMI) (Andrea, 2010) (Scrosati, et al., 2015).
- Cell Balancing - Small imperfections between the batteries are magnified with each charge and discharge cycle, causing the individual cells in the battery to be at different SOC's. To protect the cells the BMS must switch off charge or discharge when one cell is full or empty.

Thus to achieve maximum battery life it is necessary to regularly balance the individual cell's SOC (Larminie & Lowry, 2012) (Sixto, et al., 2014).

- Communications - These are necessary for reconfiguring the BMS and obtaining the information for the HMI's or system level management. The data collected and calculated can be sent to external devices such as microcontrollers over wireless, serial communications, CAN bus or direct wiring (Sixto, et al., 2014).

The BMS can also provide several other useful but not essential functions such as:

- State of health (SOH) determination - The batteries remaining lifespan can be determined. This will indicate if it can supply its rated power output which is essential for emergency battery backup systems (Andrea, 2010) (Scrosati, et al., 2015).
- History - A log can be kept of the batteries states. It is necessary for accurate SOH determination (Andrea, 2010) (Scrosati, et al., 2015).
- Demand management - The BMS can take an active role in system tasks in order to maximize the battery life. It may also be necessary to switch non-essential components off in order to provide core features for as long as possible (Electropaedia, 2015)
- Thermal management - The operating temperature is a significant parameter that determines the performance of the Lithium cells, likewise the voltage and current. The cell temperatures must be maintained within the safe operation area as appointed by the manufacturer at all times, by the BMS (Gross & Clark, 2011).

To provide all of the above functions several IC's are usually required, as there is no one solution that enables all of these features (Linear Technology, 2016). A loop of the functions required from a BMS by the rest of a typical EV system is shown in Figure 2-17. This requires a combination of analogue measurements and calculations (Plett, 2015).

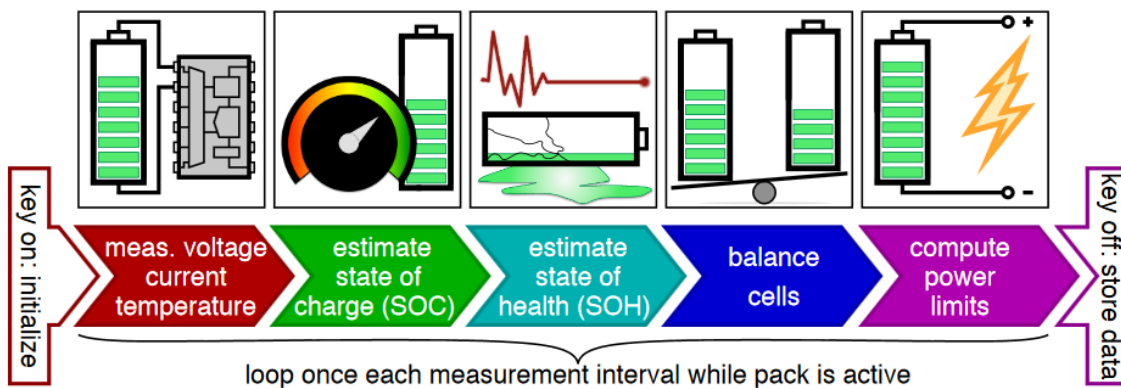


Figure 2-17: Battery management IC function loop (Plett, 2015)

2.4.6 Cell balancing

2.4.6.1 Cell balancing techniques

There are several ways to balance a Lithium-Ion battery pack depending on the charge and discharge profiles.

2.4.6.2 Bottom balance

A bottom balance is useful for applications in which the battery is often discharged to near its empty state. It is also a good idea to regularly perform a bottom balance as it may extend the batteries' useful lifespan (Andrea, 2010). Performing a bottom balance requires monitoring the voltage of every cell in a series while discharging and opening a bypass path around each cell as it reaches its empty state (3.0 V for Lithium-Ion polymer). Once all the cells are stable at 3.0 V normal charging may commence (Andrea, 2010).

2.4.6.3 Top balance

When a set of series cells is charged the cells may charge at different rates depending on their age, the equivalent series circuit (ESR), and total capacity. In order to obtain the maximum available charge levels, the cell's voltage must be equalized at their maximum charge level. This is done by opening a discharge path for individual cells in turn, dissipating some energy through an external resistor when a cell exceeds a defined voltage limit, once it drops below the limit charging resumes until all cells are at the same (maximum) voltage (Plett, 2015). This disadvantage of this balancing method is that it is a waste of energy and it requires high power resistors and thermal management. It may also take a long time depending on how unbalanced the cells are. This may be performed with low power high value resistors; however it will take even longer to reduce a cell's voltage to within acceptable limits to resume charging (Plett, 2015).

This method may also be implemented even more passively by continuously shunting a low current past every cell; however this will drain the battery in a few days if operated continuously and will only balance the cells at a rate of around one percent per hour (Moore & Schneider, 2001).

2.4.6.4 Passive cell balancing

In passive cell balancing, the excess energy of the highest SOC cells is converted into heat energy and dissipated, essentially wasting the excess energy of the highest SOC cell. There are several methods of doing this but the most common method is to use a resistor to convert the energy into heat. The main benefit of passive cell balancing is that it is less expensive than active cell balancing.

However, a disadvantage of this technique is that energy is wasted as it is converted into heat energy. It is also more time consuming dissipating the heat energy (Warner, 2015).

2.4.6.5 Active cell balancing

Active cell balancing is used for overcoming the drawbacks of passive cell balancing. The sample cells voltages are measured and then instead of choosing the lowest cell voltage as the base, the system takes the average of the instantaneous cell voltage (Bajpai & Chandrasekhar, 2016). Once this average is identified, the higher voltage cells are made to drain out their charges which are then transferred to the cells whose cell voltage value is lower than the average voltage value which has been calculated.

This optimization technique is however more complex than the passive cell balancing technique and it uses a lot of power electronic components for switching and regulation processes. However, the power losses involved in active cell balancing are minimal. The only losses would be due to the presence of power electronic switches which, while their switching process produces loss of power in the form of heat. However, if proper zero voltage or zero current switching resonant circuits are implemented it will enable to reduce the switching losses thus making active cell balancing the most optimized technique (Bajpai & Chandrasekhar, 2016).

2.4.7 Choice selection of BMS

The BMS also needed to provide extremely rapid response to changes in the battery condition to protect it from short circuits, or cell failure. Dedicated application specific integrated circuits (ASIC's) are usually employed (NXP Products, 2016). A comparison is made between the BQ77PL900 and other BMS's.

- The BQ77PL900 - This device from Texas Instruments provides five to ten series cell support and has an inter-integrated circuit (I²C) communications interface (FET isolated). It employs Passive cell balancing (Appendix D).
- The MC33771 - This BMS is from Freescale Semiconductor and provides fourteen series cell support and serial peripheral interface (SPI) communications (transformer isolated). Passive cell balancing is also a feature of this BMS (Freescale, 2016).
- LTC3300-1 – It is an active balancing controller from Linear Technologies. This chip provides active balancing capabilities to a stack of up to six series Lithium-Ion cells. It is stackable allowing it to be expanded to support up to 1000 V of series cells. It employs synchronous fly-back balancing using inductors as charge storage elements to shuttle charge between adjacent cells. This IC does not provide full analog front end (AFE) or

battery protection however and thus will require a separate AFE to ensure safe operation. Additionally a large number of external components are required to perform the active balancing, including a field effect transistor (FET) for every cell as well as current sense resistors and snubber circuitry (Linear Technology Corporation, 2014).

For this project the BQ77910AEVM circuit board is used as a BMS. The reason for selecting the BQ77910AEVM is that it allows for a stack of ten series battery cells multiplied by four stacks, which suited the needs of the battery pack developed. It also provides adequate over charge and over discharge, short circuit and overcurrent discharge.

2.4.8 The human interface (HMI)

The user interface, also known as a Human Machine Interface (HMI), consists of a user oriented display, containing information that will provide feedback to the user concerning the performance of the electric car subsystem's throughout the race. Moreover, the system must be simple and must not contain any distracting and irrelevant information to the driver. The HMI must be designed in order to run and stop the EV (motor), as well as control its speed. The HMI must be fully compatible with, and able to interface with the control stage (D.Rozhdestvenskiy, et al., 2015). A typical HMI dashboard can be seen in Figure 2-18 (Digital Trends, 2015).



Figure 2-18: A commercial EV dashboard (Digital Trends, 2015)

HMI's in EV's are preferably implemented into dashboard formats (similar to internal combustion vehicles) with the system reflecting the current state of the vehicle at all times.

These dashboards are generally implemented by means of software with which processed data is obtained from input sources that interfaces with the EV's battery pack, monitoring and protection systems of the BMS. The use of existent technologies such as smartphone's apps, web portals and existent gadgets are also utilized to simplify the associated design (Larminie & Lowry, 2012) (Shahan, 2015). The idea is to use a potentiometer (variable resistor) in order to generate a reference voltage for the control stage speed input. A block diagram illustrating the idea can be seen in **Error! Reference source not found.19**.

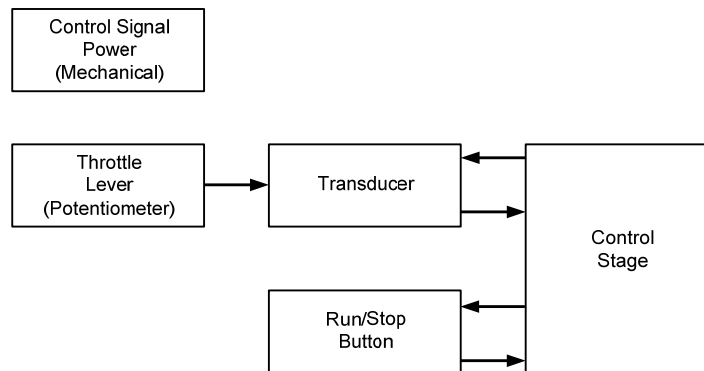


Figure 2-19: A human interface block diagram (Erjavec & Pickerill, 2015)

The circuit operates as follows: The control stage supplies power to the potentiometer, which is mechanically linked to the throttle lever. As the throttle opens and closes, the potentiometer would vary its resistance and hence vary the output voltage signal to the control stage, which in turn varies the EV motor speed (Curtis Instruments, Inc., 2015).

This means that:

- Full throttle = Low Ω = Logic High control signal = full speed
- Zero throttle = High Ω = Logic Low control signal = zero speed

The run/stop button simply makes or breaks a Logic High signal to the control stage, which in turn switches the EV motor on and off. Three points are generally agreed upon as good practice for the overall design of the EV HMI:

- The system is designed to support the driver and should not give rise to a potentially hazardous behavior by the driver or other road users.
- The system is designed in such a way so that the allocation of driver attention to the system displays or controls remain compatible with the attentional demand of the driving situation.
- The system is designed not to distract or visually entertain the driver (European Commission, 2010).

The control system developed for the EV was designed for speed control.

Chapter Three

Design specifications

The design specifications are summarised in this chapter. Aspects of the vehicle such as the electrical specifications will be discussed. Also a block diagram of the entire system is described towards the end of chapter 3.

The EV developed by CPUT consists of the following main electrical sub-systems; the batteries, the battery management system (BMS), an electric motor, a power stage (motor drive), a control stage (control mechanism for the power stage) and a human machine interface (HMI). These sub-systems are shown in Figure 3-1 (Grunditz & Jansson, 2009).

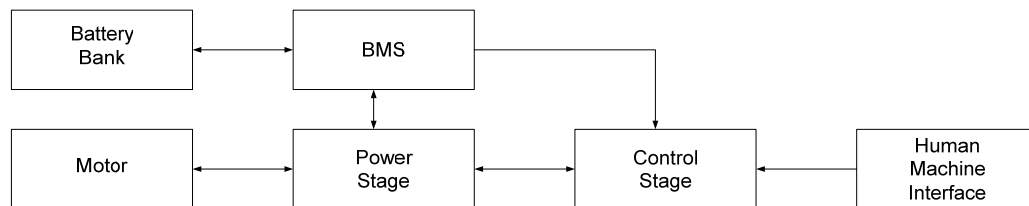


Figure 3-1: System block diagram for the CPUT EV

3.1 The EV motors

Simulation done by the PLMCC team of the car determined that 1.4 kW of mechanical power would be required from the electrical motors to run at a constant speed of 60 km/h. To ensure reliability of the overall system a decision was made to use two three phase, 750 W, AC induction motors. An off the shelf motor could not be bought and used for the competition. The motor purchased was taken apart, calculations completed and the motor was rebuilt to meet the requirements of the competition and also be compatible with the BMS. The motor is driven by a three phase, AC input voltage of 23 V and it produces 750 W of mechanical power to the wheels of the vehicle. The motor was expected to be fifty to sixty percent efficient. The required electrical specification for this motor is summarised in Table 3-1.

Table 3-1: EV motor characteristics

Motor	Rating
Power Output	750 W
Line Current	30 A
Line Voltage	23 V AC RMS
Efficiency	±65 %
Number of Poles	4
Phase Configuration	Star

Each motor required approximately 1200 W of electrical power due to the relatively low efficiency of the induction motor and was the design requirement for the VSD.

3.2 The power (motor control or inverter) stage

The function of the power (motor control or inverter) stage was to generate a three phase AC output voltage from the DC input of the BMS. This three phase output was then used to power the three phase AC induction motor. The power stage consists of six high power switches, which have a current rating higher than 30 A, and a voltage rating higher than 38 V DC. The high and low inputs to the power stage are compatible with the control stage, meaning they are able to be triggered by transistor–transistor logic (TTL) voltage level control signals (i.e. 0 to 5 V DC signals). Ideally, the power stage was rated to power a 1200 W (or higher) load. This is to prevent the inverter from running at more than a hundred percent which could result in damage of the inverter. The power stage efficiency was expected to be above seventy percent.

3.3 The control stage

The primary purpose of the control stage was to provide PWM signals to control the six switches of the power stage. At the same time, it had to implement the control strategy, which allowed the motor to be switched on and off, and subsequently allow the EV to vary its speed. The run/stop and speed control inputs, had to be compatible with the logic voltage level output of the HMI. The six outputs of the control stage are PWM signals at TTL voltage levels i.e. 0 to 15 V DC. Of these six signals, three are fed to ‘HIGH INPUTS 1, 2 and 3’; these control the lower switches of each phase. For the motor drive, based on the motor specifications, the design of the motor drive is finalised as tabulated in Table 3-2.

Table 3-2: EV motor drive characteristics

Motor-Drive Aspect	Rating
Power Output	1200 W
Maximum Current per Line	30 A AC
Supply Voltage	38 V DC
Line Voltage	23 V AC
Efficiency	(High as possible) ± 90 %
Number of Phases	3
Speed Control	Yes
Speed Feedback	No

3.4 The batteries

The batteries selected for the CPUT EV are Lithium-Ion polymer (LiPO) batteries. The LiPO batteries were selected because they have the advantages of being smaller in size and lower in weight. They were also lower in cost and have a high specific energy (in watts per kg) (Fuhs, 2009).

3.5 The battery management system (BMS)

The BMS for the CPUT EV is directly interactive with the following modules as seen in Figure 3-2.

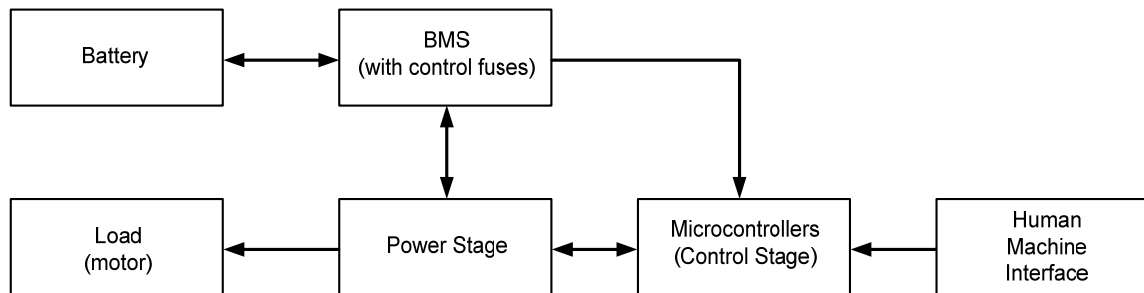


Figure 3-2: A block diagram of the subsystems affiliated to the BMS

The BMS provides at least 40 A at 38 V DC (nominal) to the input of the power stage. Due to competition rules and regulations, the BMS was bought off the shelf and adapted to the CPUT EV. It is for this reason that only the inputs/outputs were of concern for the purpose of this thesis. Designing and developing of the BMS was not part of the scope of this project. For the EV being designed, two BMS's were looked at, namely the Texas Instruments BQ77910AEVM and the B77PL900.

3.5.1 Microcontroller (BMS)

The microcontroller should provide features such as data acquisition, sensor interfacing and facilitate upgrades for the vehicle. Three microcontrollers were looked at, namely Arduino, Raspberry pi and Microchip (Larminie & Lowry, 2012).

3.5.2 Communication protocol

It is standard that communication is established among the EV subsystems. Such exchange should be provided between the microcontrollers that will gather information from the battery and sensors and operate the dashboard of the vehicle. Serial communication was preferred over parallel for this application due the limited amount of I/O pins available from the available microcontrollers.

3.5.3 Sensors

Various sensors were required by the EV such as current sensors, temperature sensors, speed sensors, etc.

3.5.3.1 Current sensors

There are numerous current sensors on the market which are invaluable to an electric vehicle. One of the many current sensors is the Hall Effect sensor. Typically these sensors have an accuracy of one percent. To achieve a high accuracy over a wide range, two current sensors were used measuring the same current. One sensor was to detect the low current and the other sensor for the high current. Their outputs were sent to a processor with an A/D converter, to select the appropriate sensor based on the level of the current measured (Andrea, 2010).

The greatest advantage of Hall Effect current sensors is that they can measure either a DC or an AC current. However, the magnitude of the current that can be measured with the Hall Effect current sensor is less than that of an inductive current sensor (Mohanty, 2015) . They also have the added advantage of providing electrical isolation and they have a high reliability. They however require an external power supply (Hossain, et al., 2012).

3.5.3.2 Temperature sensors

Temperature sensors are important in measuring various temperature aspects of any electric vehicle. Temperature sensors are critical for Lithium-Ion batteries that may not be discharged outside a certain temperature range and more importantly not be charged outside an even tighter range. Temperature sensors are also incorporated as a warning system should any cell within the battery pack become particularly hot due to external or internal reasons. Temperature sensors were also be incorporated to detect whether or not a balancing load was working or not and the temperature of individual cells (Andrea, 2010).

3.5.3.3 Speed sensors

Speed measurement is vital for monitoring the speed of the EV motor. A speed sensor incorporated in the EV was the Hall Effect sensor.

3.6 Total expected efficiencies of electrical drive train

Figure 3-3 is a block diagram of the expected efficiencies of the various parts of the EV drive train.

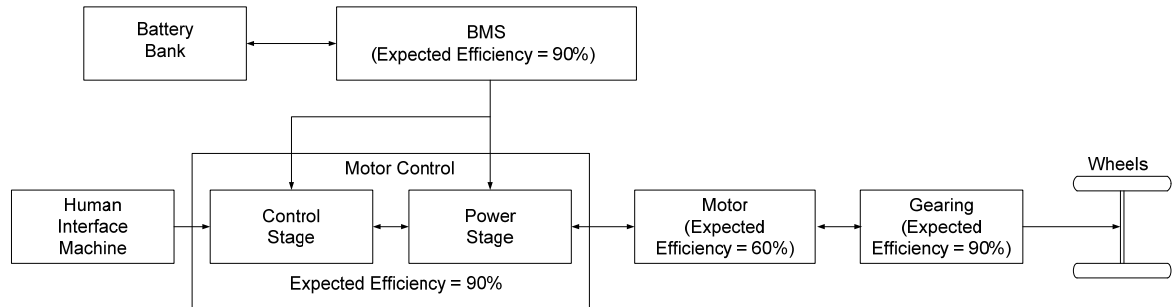


Figure 3-3: Total system efficiency from sub components of the EV drive train.

As seen in Figure 3.3, the expected efficiency of the BMS is 90 %, the expected efficiency of the motor controller 90 %, the expected efficiency of the motor 60 % and the expected efficiency of the gearing 90 %.The overall efficiency of the overall drive train is expected to be above 43% as opposed to an expected efficiency of above 60%, as stipulated in Chapter 1.

Chapter Four

The EV motor and the motor control stage design

4.1 The EV motors

As previously mentioned, the motor selection for the EV was based on many factors such as cost, reliability, durability and efficiency. The squirrel cage, three phase induction motor was found to be the most cost effective motor to suit the purpose of the EV. Two Motorelli 750 W three phase, squirrel cage induction motors were purchased. One of these motors can be seen in Figure 4-1. The motor dimensions and original specifications can be viewed in Appendix A.



Figure 4-1: The Motorelli three-phase, squirrel cage induction motor

4.1.1 Disassembly of the motors

Before any work could be completed on the motor, it was essential to record all the information about the motor before taking it apart. Information such as the frame type, current, voltage, power rating, torque and weight were recorded. This information was collected from the nameplate of the motor and is tabulated in Table 4-1.

Table 4-1: Motor specifications

Frame	P (kW)	Efficiency (%)	PF	Volts (V)	f (Hz)	Current (A)	Connection	Speed (RPM)	Torque (Nm)	Weight (kg)
1E802-4	0.75	74.4	0.7	230/ 400	50	3.4/2.0	Delta or Star	1380	5	16

The next step taken in the disassembly of the motor was to record the layout of the terminal box, how the end covers of the motors were attached to the main frame of the motor, the positioning of the various nut and bolts and the orientation of the covers. Figure 4-2 illustrates the terminal connections of the motor for both the star and delta connections of the motor.

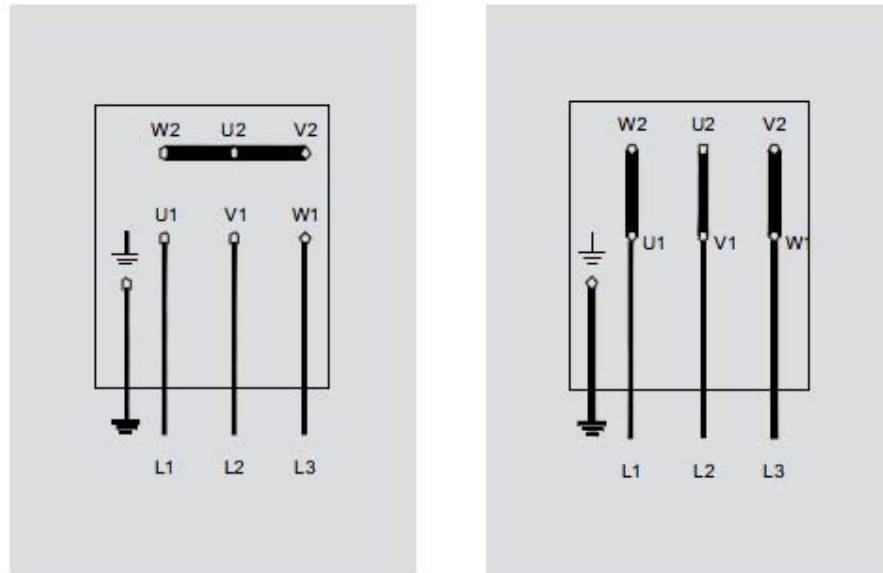


Figure 4-2: EV motor connections

Once this was completed it was necessary to mark the orientation of the end covers. This was very necessary as the axle of the rotor rotates on bearings which are located inside these end covers. Misalignment of these covers could cause the rotor to run uneven which in turn could cause the rotor to shave against the stator. This could cause the motor to cease (Hill Publishing Company, 1945).

Marking of the stator housing and the end covers is seen in Figure 4-3. This was done with a center punch and a small pilot hole being drilled for both end covers.

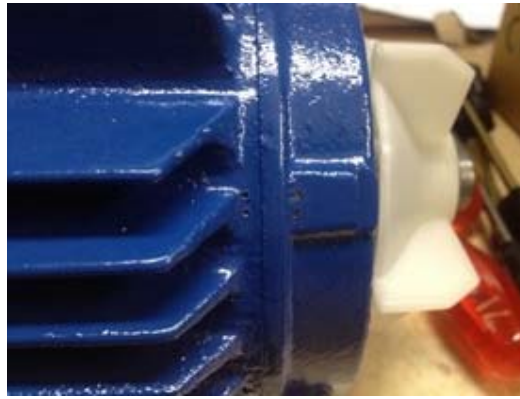


Figure 4-3: Stator frame and end covers being marked for alignment

The end covers were then removed. To remove the “O-ring” from the fan, a combination ring pliers was used and a pulley-puller was used in order to remove the fan. After removing the fan, the stator could easily be removed from the rotor. Care however was taken in removing the rotor as any nick in the rotor from the stator housing could adversely affect the performance of the motor when reassembled. After removing the rotor from the stator housing it was necessary to start mapping the orientation of the windings of the stator and then removal of the windings from the slots of the stator. The following steps were taken in removing the windings from the stator slots.

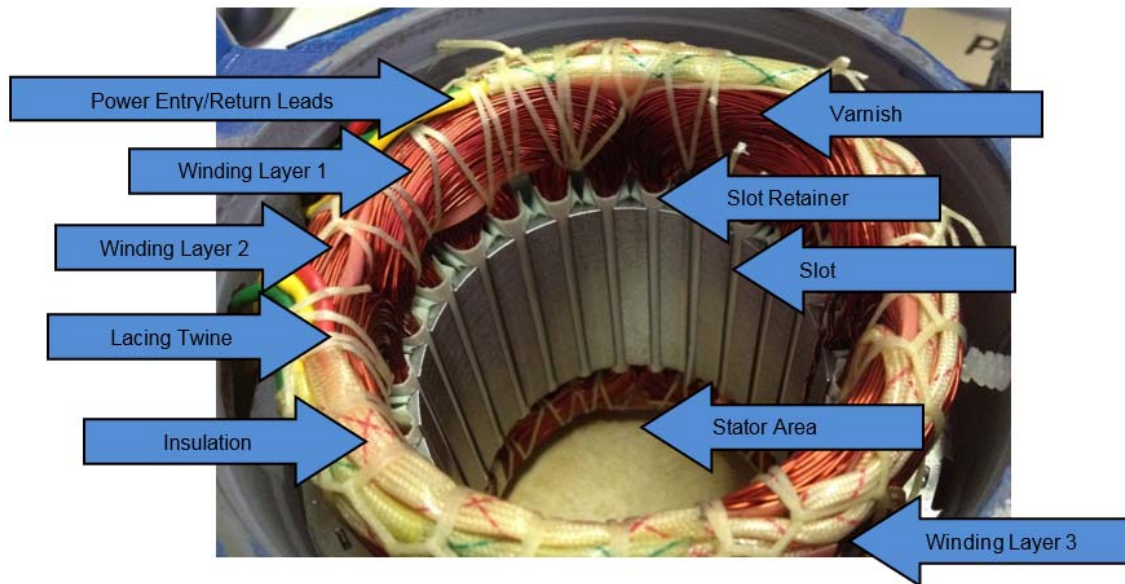


Figure 4-4: Various components of the stator

1. The twenty-four slots within the stator were firstly marked with a permanent marker. This was done as a reference point when rewiring the slots.
2. The lacing twine and the insulation were removed by means of side cutters.

3. The plastic slot retainers were carefully removed using long nose pliers.
4. With the windings now slightly loose within the slots and the windings also not being heavily varnished, they were individually and carefully removed. The very first layer of windings was removed and the individual coils were labeled with regards to entry and exit points on the twenty-four stator slots.
5. Once all the coils were removed for a single “phase”, the entry and return leads were labeled and then cut using side cutters.
6. This process was repeated in removing each winding for the remaining two “phases”.
7. In completing the removal of the three phase windings from the stator a scalpel was used to remove any remaining debris. Pure alcohol was also used to ensure that the entire stator was clean.



Figure 4-5: A clean stator after removal of the windings

The windings were then laid out according to their labels. This was done to make mapping of the windings easier. Figure 4-6 illustrates this.



Figure 4-6: Original windings laid out for mapping

The drawing in Figure 4-7 better illustrates the connections and the mapping of the windings. It also illustrates the entry and exit points of the various coils in the slots.

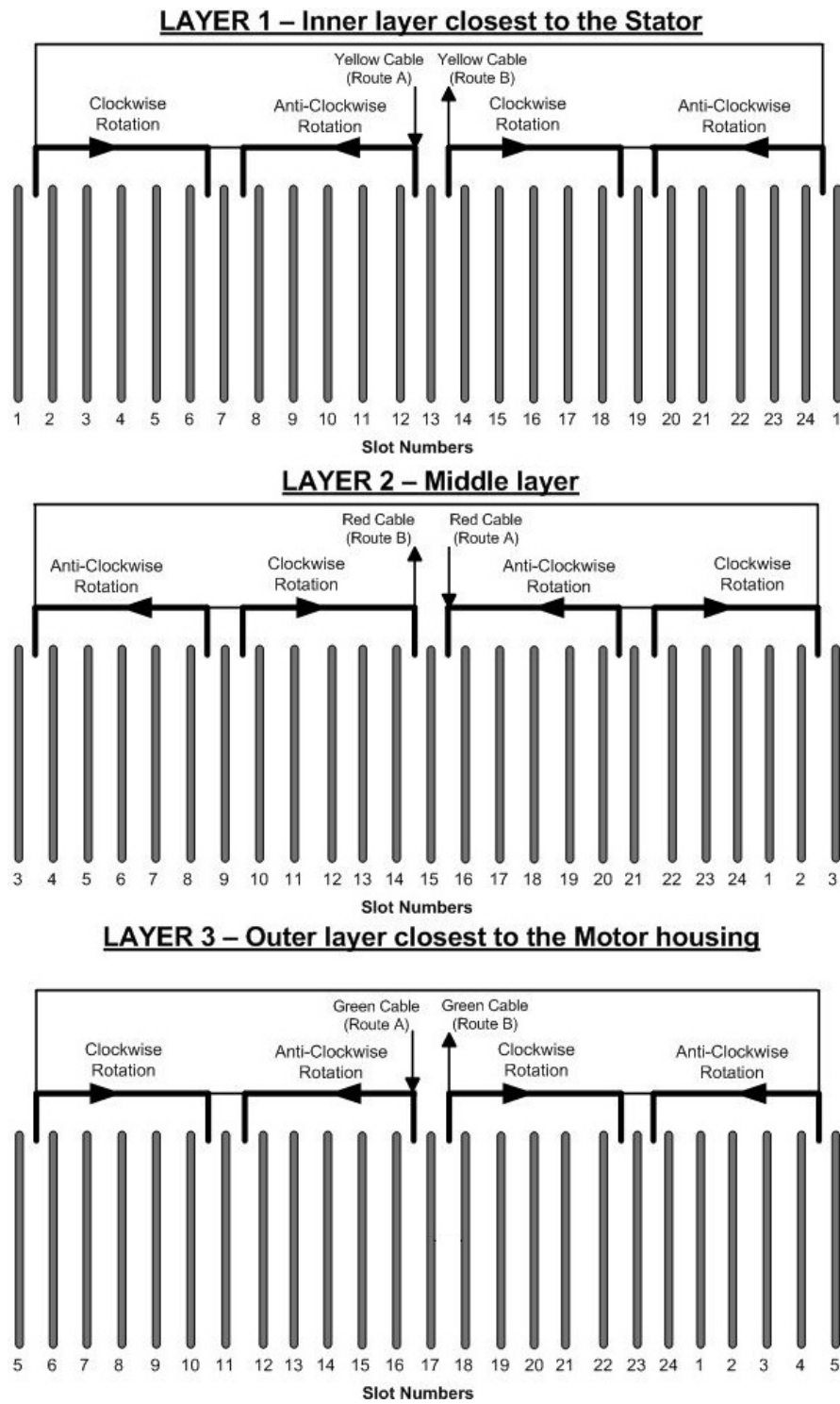


Figure 4-7: Layout of the windings removed from the stator

From the layout of the windings it can be seen that there are three layers of windings which is indicative of three phases. These windings also spread over twenty four slots and there are four poles in the stator.

Each winding had 128 turns (coils) and the coil pitch extended over five slot pitches. The thickness of the conductors in each coil was 0.57 mm in diameter and had a cross sectional area of 0.26 mm².

4.1.2 Rewiring calculations for the stator windings

For the new windings, the motor input voltage, the number of turns, the rated current and the cross-sectional area of the conductor to be used, needed to be calculated. In order to determine the new input voltage of the motor, the RMS line-line Output Voltage (V_{l-rms}) from the power stage had to first be calculated based on a DC supply voltage (V_{DC}) of 38V (Siddiqui, et al., 2015).

$$V_{l-rms} = \sqrt{\frac{3}{2}} \times \frac{V_{DC}}{2} = 0.612 \times V_{DC} \quad (17)$$

Therefore: $V_{l-rms} = 0.612 \times 38V = 23.271V$

The number of turns for the new motor could then be determined (Bird, 1995):

$$\frac{N_1}{N_2} = \frac{V_1}{V_2} \quad (18)$$

Therefore: $N_2 = \frac{N_1 V_2}{V_1} = \frac{(128)(23.271V)}{400V} = 7.446 \text{ Turns}$

The new rated current could be determined (Bird, 1995):

$$\frac{I_2}{I_1} = \frac{V_1}{V_2} \quad (19)$$

Therefore: $I_2 = \frac{V_1 I_1}{V_2} = \frac{(400V)(2A)}{23.271V} = 34.378A$

Similarly, the new conductor cross-sectional area could be determined (Pappano & Wier, 2013):

$$\frac{A_2}{A_1} = \frac{I_2}{I_1} \quad (20)$$

Therefore: $A_2 = \frac{I_2}{I_1} \times A_1 = \frac{400}{23.271} \times 0.26 = 4.469 \text{ mm}^2$

Therefore, the new conductor diameter:

$$d_2 = 2.385 \text{ mm}$$

Due to the small size of the slot entries, the following size conductor was used.

- 4 x 1 mm diameter conductor each with a cross-sectional area of 0.79 mm² - (connected in parallel).
- This resulted in a total cross-sectional area of 3.14 mm² less than required, however (Pappano & Wier, 2013),(Sengpiel, 2014),
- The total current carrying capacity was 4 x 16 A = 64 A (Lund, 2016)

This meant that the total amount of copper would be less than the ideal 4.469 mm², but it should still be able to operate sufficiently. Unfortunately, due to the small size of the slot entries, not much could be done about this, unless another motor was used. The total current carrying capacity was, however, more than sufficient and as a result of the reduced area an increased stator resistance was expected, unfortunately resulting in a reduction of the motor efficiency.

4.1.3 Rewiring of the stator

The next task at hand was to rewire the stator windings. In order to do so a Perspex jig had to first be assembled so that an even number of stator turns could be completed for each stator winding.

4.1.3.1 Perspex jig

In order to rewire the stator, a winding template (jig) had to be constructed. The jig was made from Perspex so that one could clearly see the wiring configuration as well as the number of turns during the rebuilding phase of the stator windings. The following Perspex templates were constructed with the following dimensions:

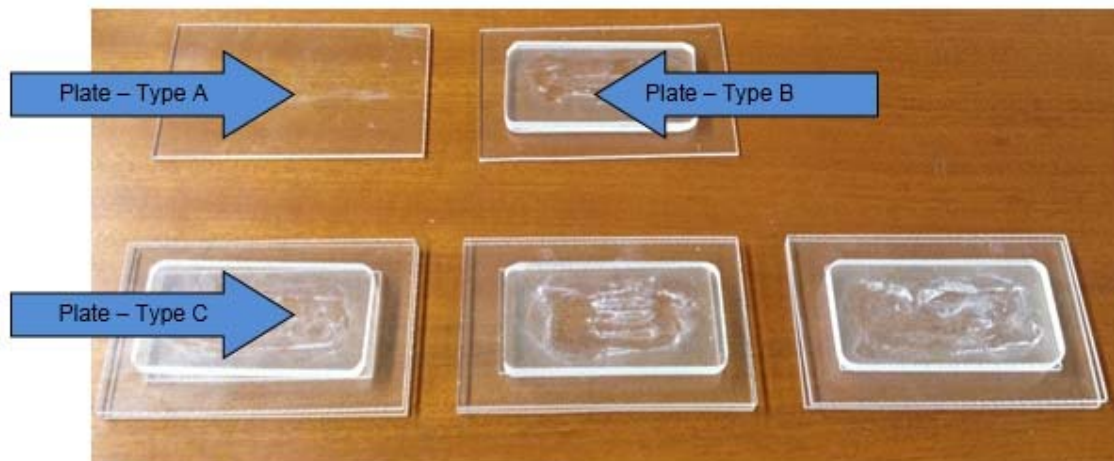


Figure 4-8: Templates for Perspex jig

- Plate Type A: 1 x (75 mm x 120 mm)
- Plate Type B: 1 x (75 mm x 120 mm) + 3 x (50 mm x 95 mm)
- Plate Type C: 1 x (75 mm x 120 mm) + 1 x (50 mm x 95 mm) +
1 x (75 mm x 120 mm) + 3 x (50 mm x 95 mm)

Once all the Perspex templates were built, they were clamped together, drilled on opposite corners and 2 x M5 bolts and nuts kept them together and in place. Thereafter an 8 mm hole was drilled right through the centre of the jig. This was done to assist rotation on the jig when winding the copper using a winding machine. Figure 4-9 shows the complete assembly of the jig.

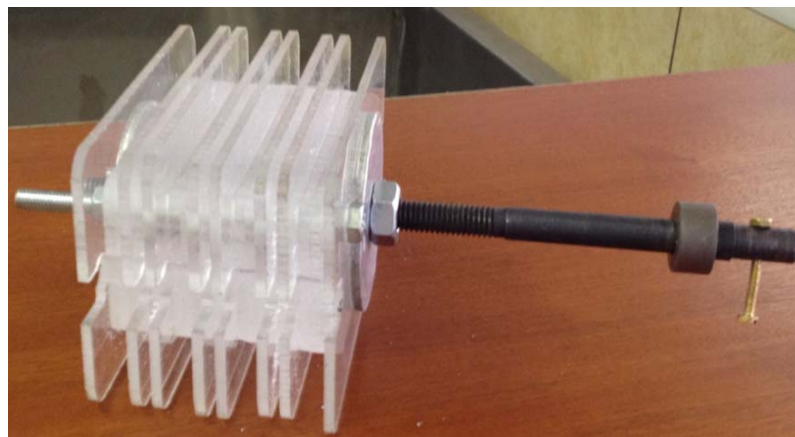


Figure 4-9: Completed Perspex jig

4.1.3.2 Assembly of stator phase windings

After completion of the Perspex jig, a winding machine was used to wind the copper coils with the exact number of turns. Four parallel conductors were used, each 1 mm thick in diameter. Each coil was wound to have seven turns. The turns gauge on the winding machine accurately measures the amount of turns, making winding really simple. This winding process was repeated for all three layers. The end product is seen in Figure 4-10.



Figure 4-10: Completed Perspex jig with completed stator winding for one phase

All three windings of the stator were completed for the three phases of the machine. Thereafter, one phase winding was inserted into the stator. This can be seen in Figure 4-11.

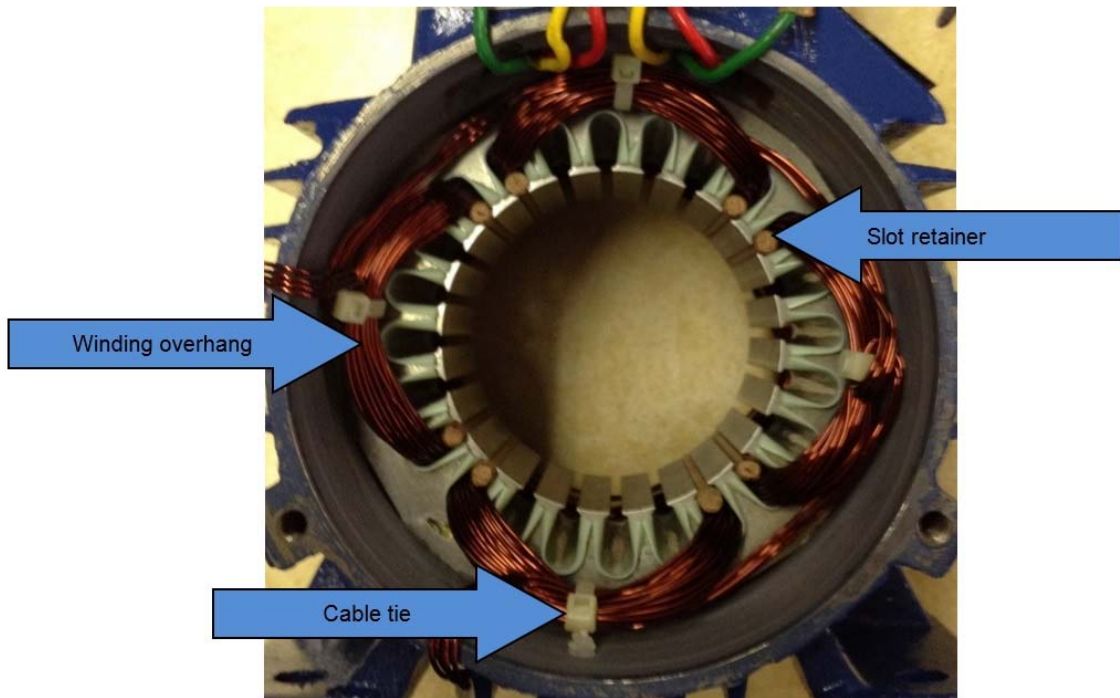


Figure 4-11: One winding inserted into machine stator

The following guidelines are important to note when rewiring the stator with the windings.

- Inserted one completed winding at a time.
- Started with the last winding first, then the second phase winding and finished off with the last/inner most phase winding.
- After each winding was fitted, inserted a slot retainer in each slot so that the windings did not come out of the slots.
- After each winding was inserted, the “overhang” was pushed outward towards the motor enclosure, to provide more space for the next winding. This was also to ensure that both the end covers fitted the machine once all the windings were inserted into the stator slots.
- Did not remove the cable ties until all three windings were inserted and all the slot retainers were inserted as well.

The slot retainers used for these machines were 5 mm wooden dowels cut to the stator teeth length. Some of the dowels had to be trimmed to ensure correct fitment into the slot.

4.1.3.3 Power connections to stator windings

The first step of the reassembly process, after the phase windings and slot retainers were inserted, was to connect the power entry/exit leads to the terminal box (Figure 4-12).

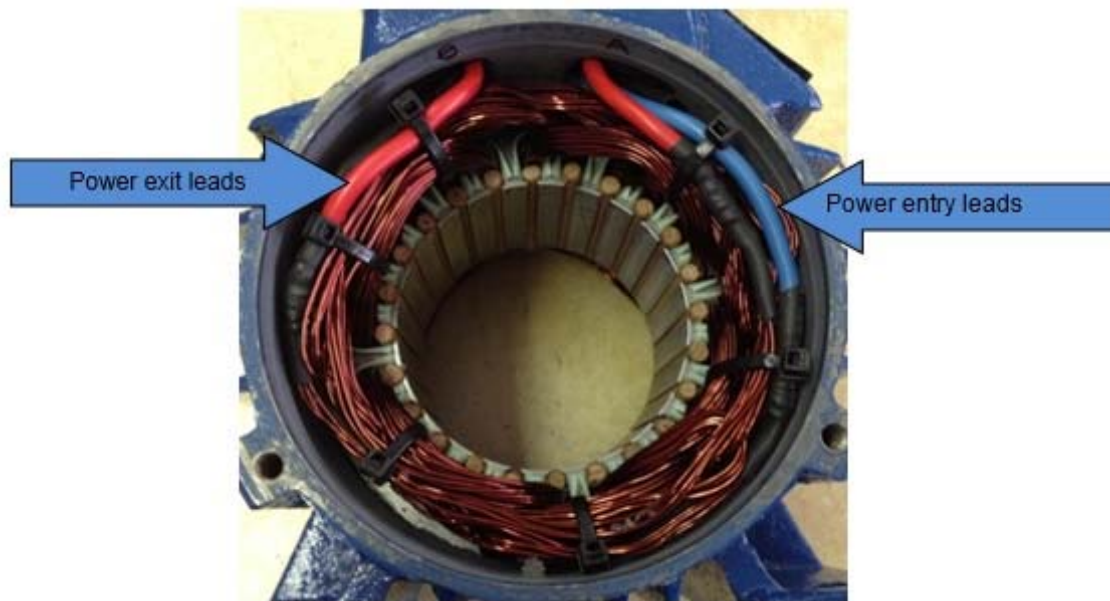


Figure 4-12: Power entry/exit leads connection

The cable used was selected to handle 35 A or more. The following cable was selected based on the current requirements per phase winding.

- 4 mm diameter (\approx 6 AWG) stranded copper cable
- Voltage (insulation) rating – 500 V DC
- Current rating – 101 A (Lund, 2016)

These cable characteristics make the selection of the cable optimal for this application. The power entry/exit leads were spliced to the windings according to IPC/WHMA-A-620 (Wiring Harness Manufacturers Assoc., 2010) and connected as follows.

- Six 20 cm length cables were cut; namely two red, two white and two blue cables.
- 8 mm of cable insulation was stripped off on one end.
- Each cable was then lined up with the respective winding termination point and one strand of copper was wrapped around the two points (to hold them in place).
- These points were then soldered together.
- Heatshrink of 4 cm long and 4-8 mm in thickness was slid over the termination points and then shrunk with a heat-gun.
- The non-terminated ends were then routed to the terminal box.

After completion of this the wiring of the terminal box wiring commenced. The final step in assembling the machine was to wire up the terminal box (Figure 4.13). The following steps were followed in completing this procedure.

- All 6 cables were crimped using yellow ring lugs (according to IPC/WHMA-A-620) (Wiring Harness Manufacturers Assoc., 2010).
- The power exit leads were connected to the star point.
- The power entry leads were connected to the power input terminals.

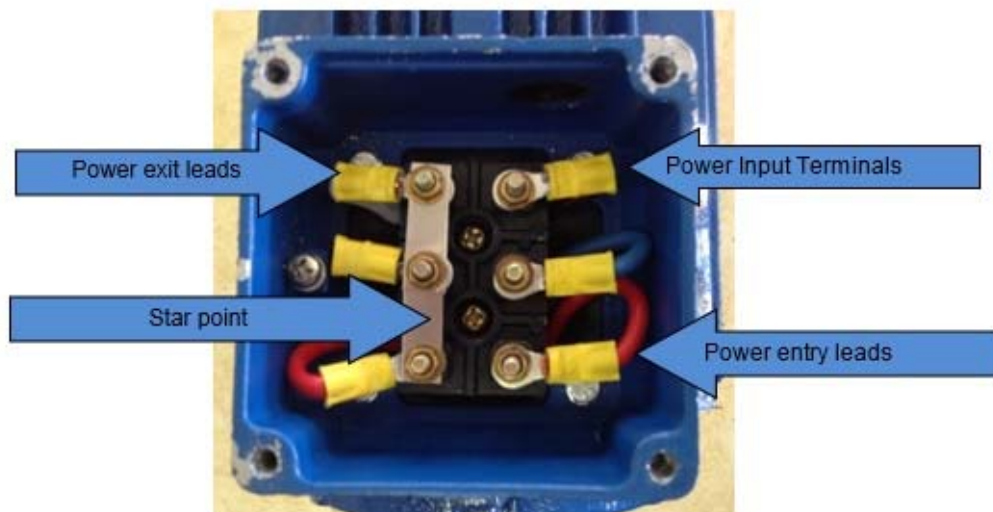


Figure 4-13: Terminal box connections

After completion of the assembly of the terminal box, the re-assembly of the entire machine could commence. This involved the following procedures.

- The rotor was inserted into the stator. This was done very carefully, to avoid damaging either one.
- The bearing caps were fitted next. All the punched markings were lined up, to ensure correct orientation of the bearing caps.
- The next step was to fit the fan onto the rotor and then the fan covers.
- Lastly the terminal box cover was replaced.

The complete assembly (without terminal box cover) can be seen in Figure 4-14.

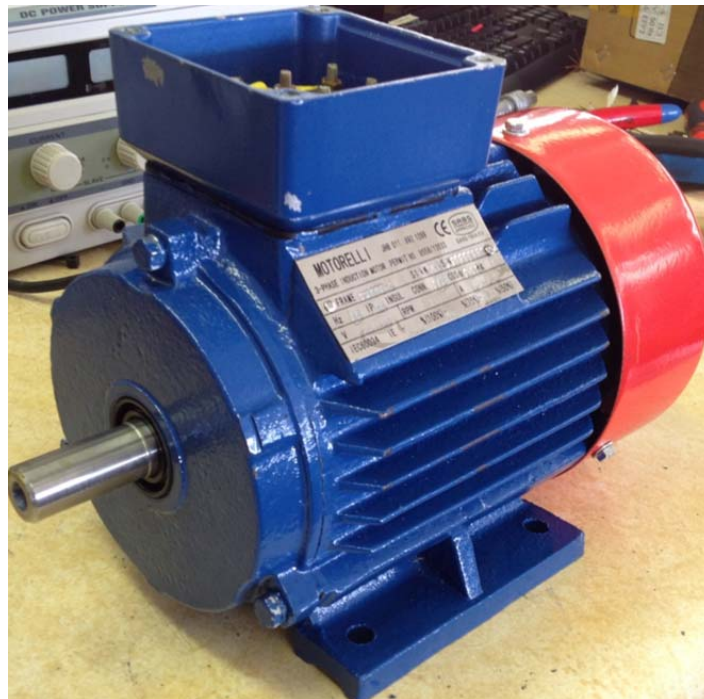


Figure 4-14: Completed machine assembly

4.1.4 Final machine inspection tests

After the motor was completely assembled various tests had to be completed on the motor.

4.1.4.1 Winding resistance

The purpose of this test was to ensure that the machine windings were not damaged. Possible damage that could have occurred could be a complete break in winding conductor (open circuit), or a high winding resistance, which would create huge copper losses, and an unbalanced motor.

The approximate length of winding is as follows:

$$Total\ Length = [(Turn\ Length \times 2) + (Turn\ Width \times 2)] \times Number\ Turns \times Number\ poles$$

$$Total\ Length = [(120\ mm \times 2) + (70\ mm \times 2)] \times 7 \times 4$$

$$Total\ Length = 10640\ mm = 10.64\ m$$

Since the resistance per meter of the copper conductor = 0.001295928 Ω/m (Lund, 2016).

$$Total\ Winding\ Resistance = 10.64\ m \times 0.001295928\ \Omega/m = 0.014\ \Omega$$

Since four parallel conductors were used, the total winding resistance is:

$$Total\ Winding\ Resistance = \frac{0.014}{4} = 0.004\ \Omega$$

Therefore a winding resistance between 1 mΩ - 100m Ω was acceptable (Electrical Engineering portal, 2012). Once this was completed an insulation test using a MEGGAR meter was completed. The procedure in completing this test was as follows.

- Connected the insulation tester (MEGGAR meter) to both ends of a winding.
- Set the insulation tester to resistance measurement.
- Pressed the “press to test” button and locked it into position.
- Monitored the measured resistance for one minute.
- Recorded the maximum resistance reading in that period.
- Repeated this test for all three windings or phases.

The results of the measurements can be seen in Table 4-2.

Table 4-2: Winding resistance test results

Winding resistance		
Winding	Measured resistance	Pass/Fail
Yellow (Layer 1)	±80 mΩ	Pass
Red (Layer 2)	±80 mΩ	Pass
Green (Layer 3)	±80 mΩ	Pass

From this table, it can be seen that all the measurements are within specification, and the test was therefore successful. A value of 3 m Ω was expected from the measurement; however, there was a balanced outcome of approximately 100 m Ω . This was due to the Meggar meter having an analogue scale. This resulted in a balanced motor even though the winding resistance is a bit higher than expected.

4.1.4.2 Insulation resistance

The purpose of this test was to ensure that the winding insulation was not damaged i.e. to ensure that there were no short circuits between windings and from windings to ground. The winding resistance with an insulation resistance greater than 1 M Ω was sufficient. A picture of the test setup can be seen in Figure 4-15.

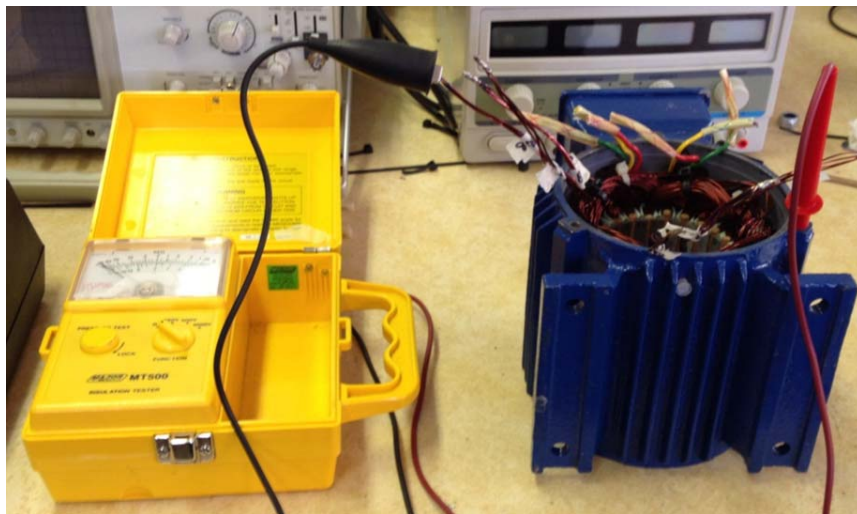


Figure 4-15: Insulation Resistance Test Setup

Procedure:

1. Connected the insulation tester to one end of a winding and to ground.
2. Set the insulation tester to 500 V.
3. Pushed and locked the “press to test” button.
4. Monitored the meter for one minute.
5. Recorded the maximum reading for that period.
6. Repeated the above steps for all three layers/windings.
7. Connected the insulation tester to one end of Layer 1 and one end of Layer 2.
8. Pushed and locked the “press to test” button.
9. Monitored the meter for one minute.
10. Recorded the maximum reading for that period
11. Repeated the same process for Layer 1-3 and Layer 2-3.

The results of the measurements can be seen in Table 4-3 and Table 4-4.

Table 4-3: Insulation resistance test phase-ground results

Insulation resistance - Phase to Ground		
Winding	Measured resistance	Pass/Fail
Yellow (Layer 1)	∞	Pass
Red (Layer 2)	∞	Pass
Green (Layer 3)	∞	Pass

Table 4-4: Insulation resistance test phase-phase results

Insulation resistance - Phase to Phase		
Windings	Measured resistance	Pass/Fail
Yellow (Layer 1) - Red (Layer 2)	∞	Pass
Yellow (Layer 1) - Green (Layer 3)	∞	Pass
Green (Layer 3) - Red (Layer 2)	∞	Pass

From these tables, it can be seen that all the measurements are within specification, and the test was therefore passed. The maximum deflection on the analogue Meggar meter was at ∞ and the scale below this was at 100 M Ω . When the insulation test was completed the needle did not deflect at all showing that the resistance of the insulation was above 100 M Ω .

4.2 The motor control stage

A suitable motor control stage or inverter was required to control the motors for the EV. This was necessary to convert the incoming DC to a suitable three phase AC required to power the motor. In order to do so, it was necessary to design an inverter which had three elements in it. These elements are namely a control stage, a power stage and the integration of the two stages for the inverter.

4.2.1 The control stage of the inverter

For the control stage, voltage/frequency or open loop scalar control was selected due to the motor which would have some unstable parameters and was operating at a very low voltage, when being driven.

The open loop scalar controls an AC induction motor's speed and torque by varying the supplied voltage and frequency to it. The voltage and frequency is always in a constant ratio to one another, hence the alternative name of voltage/frequency.

In Figure 4-16, it is evident that if a constant torque is desired over the full speed range (or follows the indicating red line as close as possible) and that the applied voltage and frequency will have to change proportionally. If half the speed is required, half the voltage and half the frequency are required and if a quarter of the speed is required then quarter of the voltage and frequency is required (Microchip, 2007).

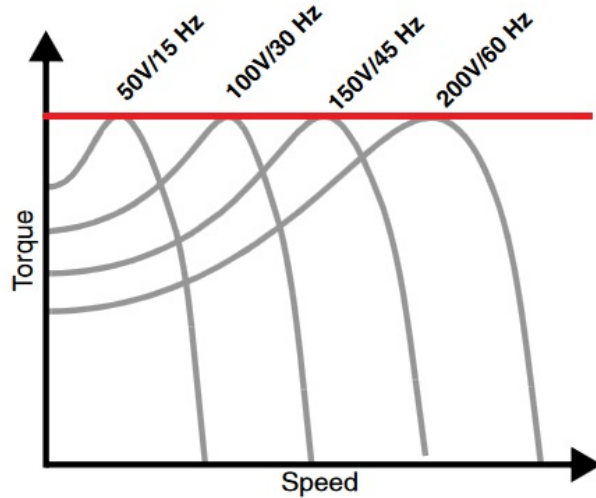


Figure 4-16: Voltage/frequency or open loop scalar control (Microchip, 2007)

The voltage and speed changes proportionally where torque and current change proportionally. To calculate a constant for the relationship between the voltage and the frequency, the following formula was used.

$$K = \frac{\text{Applied voltage}}{\text{Applied frequency}} \quad (21)$$

$$K = \frac{42}{60}$$

$$\therefore K = 0.7$$

Now that the constant was calculated, the applied voltage was calculated for a specific frequency from equation (21) (Grunditz & Jansson, 2009).

$$\text{Voltage} = K \times \text{Frequency} \quad (21)$$

4.2.1.1 Selection of the EV processor

After some research, it was decided that using a Microchip motor drive, one of their solutions will be adequate for this application.

Initially the processor chosen was the PIC16F7X7 from Microchip. This processor was used in conjunction with a power stage to power the electric motor. The package initially selected for the power stage was by International Rectifier and was the IRAM 136-3023B.

However, after considerable testing and evaluation of this microprocessor and the power stage IC, it was found that the power stage IC was unsuitable for our research. The IRAM 136-3023B could only maintain an efficiency of around seventy percent up to an output of 600 W. Above this, the inverter IC went into thermal shutdown and therefore produced no output. This undesirable result is due to the huge amount of I^2R losses in the MOSFET's. These switching losses generated a huge amount of heat, which caused the inverter IC to go into thermal shutdown. Even after a much bigger heat sink was used, adequate heat could still not be dissipated. Thus, it can be concluded that even though the power stage (for the three phase motor drive) developed was as efficient as expected, the tendency to go into thermal shutdown (due to inadequate heat dissipation) made it undesirable to use for the application. The PIC16F7X7 solution was abandoned.

The other option of a microcontroller selected for the EV was a single chip, namely the dsPIC30F2010, from Microchip. It has the control characteristics of a sixteen-bit single chip microcontroller unit (MCU) and the merits of a high speed digital signal processor (DSP), creating the optimum single-chip solution for embedded control of three-phase induction motor.

Other features of this single chip include (Liu, et al., 2015):

- It simplifies the control of software and external hardware.
- The software can generate PWM waveform.
- It can generate a three phase, six channel pulse width modulation (PWM) signal (by means of programming).
- Each PWM output pin drives a current of approximately 25 mA.

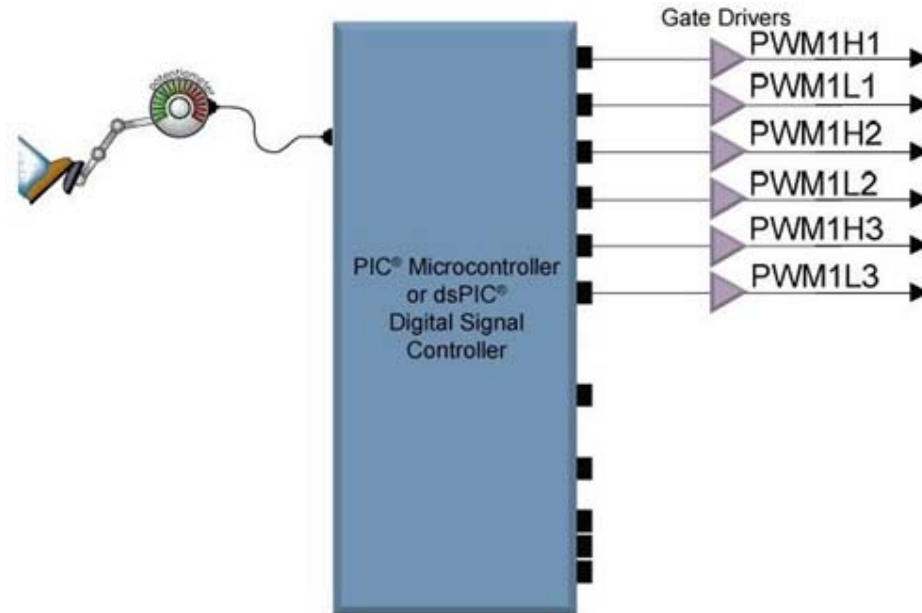


Figure 4-17: EV Motor control processor (Microchip, 2016)

The dsPIC reads an analogue signal from a foot pedal or a potentiometer at 500 Hz or every 2 ms. It determines the value and sends it through the analogue to digital converter (ADC). The digital value then uses a sixty-four entry sine wave look-up table that contains all the points of a sine wave; the sine values are read periodically and then written to the duty cycle registers. The switching frequency was selected just above the audible range of 16 kHz. By keeping the switching frequency low, the switching losses could be kept to a minimum and the efficiency was improved. Determining the sine wave look-up table size was done by using the following calculation (Microchip, 2007).

$$\begin{aligned}
 \text{Number of Table values} &= \frac{\text{Frequency}_{PWM}}{F_{MOD} - F_{MAX}} & (22) \\
 &= \frac{16000}{60} \\
 &= 267
 \end{aligned}$$

In this case a two hundred and fifty six entry table sufficed, but in practice a quarter sine wave needed is more than enough to get the modulated sine wave we required. The duty cycle registers determined the allowable PWM signals and six separate signals were generated from the dsPIC. They are grouped as follows in Figure 4-18.

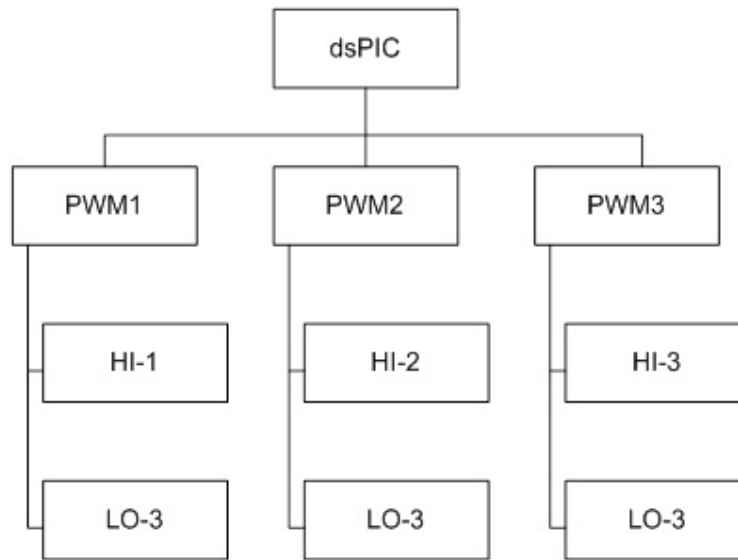


Figure 4-18: PWM signal processing (Microchip, 2007).

The high (HI) and low (LO) signals were used to drive the high and low side of the three single phase arms in the power stage.

4.2.1.2 Dead-time

One very important factor that needed to be considered with the PWM signals is dead time. Dead time is a time delay between one signal switching off and the next switching on. Figure 4-19 shows both the active and inactive dead-time between the HI and LO signals (Rashid, 2011).

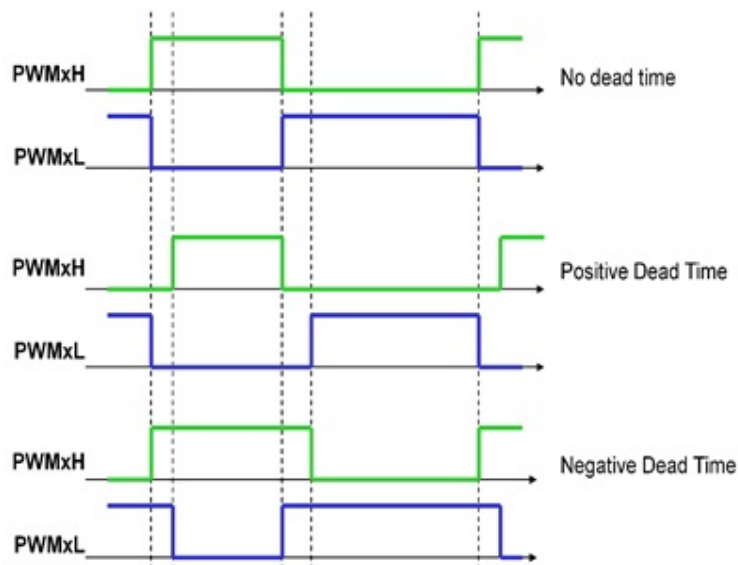


Figure 4-19: HI and LO signals with dead-time (Microchip, 2016)

If insufficient dead-time was implemented and it did occur that a HI signal was still busy switching off while a LO signal already started to switch on, cross-conduction could have occurred.

This meant that the DC bus would have short-circuited across the metal-oxide semiconductor field-effect transistors (MOSFET's) and it would have destructive results, such as blowing them up (Microchip, 2007).

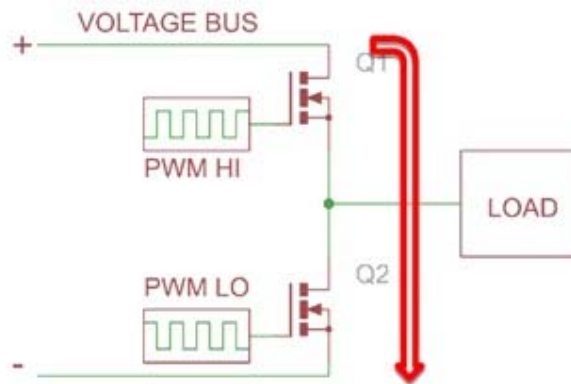


Figure 4-20: Cross Conduction due to insufficient dead-time (Microchip, 2007)

Due to this, a 2 μ s delay was implemented in the code of the dsPIC. This was easily adjustable if it became evident that cross conduction occurred. With the current setup the resolution for the modulation frequency or operating frequency had to be calculated (Microchip, 2007).

$$\begin{aligned}
 \text{Modulation frequency resolution} &= \frac{\text{Frequency}_{PWM}}{2^{16}} & (23) \\
 &= 0.255 \frac{\text{Hz}}{\text{bit}}
 \end{aligned}$$

The minimum circuit connections for the dsPIC pic were made, and the code was programmed onto the chip using MPLAB X IDE and a Microstick 2 development board (Microchip, 2011). Figure 4-21 shows the dsPIC30F with all the necessary components.

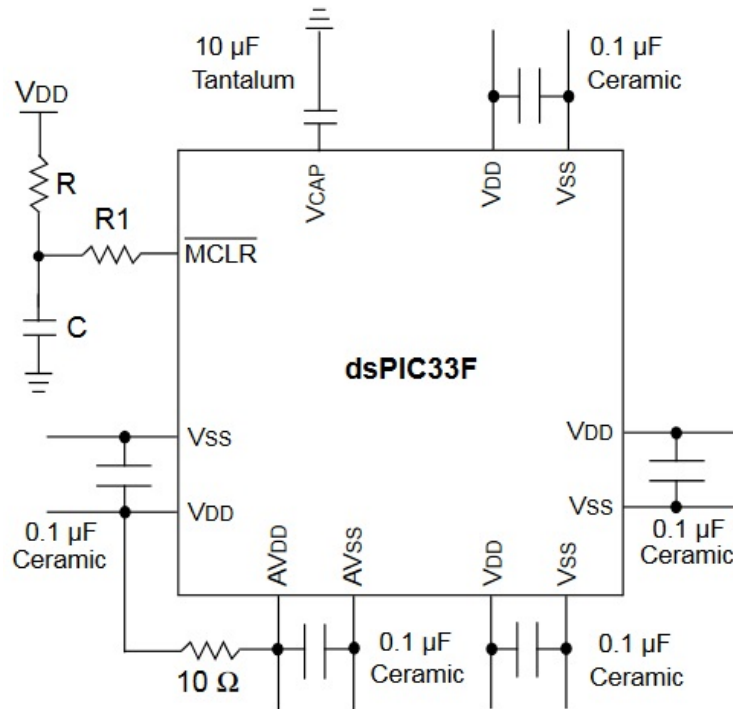


Figure 4-21: Minimum circuit connections for the dsPIC30Fprocessor (Microchip, 2011)

4.2.2 The power stage of the inverter

For the power stage of the inverter, a bridge arrangement was chosen. The minimum requirement for this arrangement to work was to have six PWM signals from the control stage, six field effect transistors (FET's) arranged in a bridge, a direct current (DC) voltage bus and an AC IM motor (International Rectifier, 2016). In order to do so, it was necessary to firstly select FET's which would be appropriate for our application.

4.2.2.1 MOSFET selection

In order to select the correct FET's we firstly needed the following information.

Operating frequency:	F	= 16 kHz
RMS Current:	I_{RMS}	= 30 A
Max Voltage:	V_{MAX}	= 38 V DC

With these values and the operating frequencies required taken into consideration, and the voltages and currents as seen in Figure 4.22, it was evident that MOSFET's or IGBT's were the ideal semiconductor switch for our application needs. However the MOSFET provided a better efficiency at low voltages compared to the IGBT (Kazanbas, 2014).

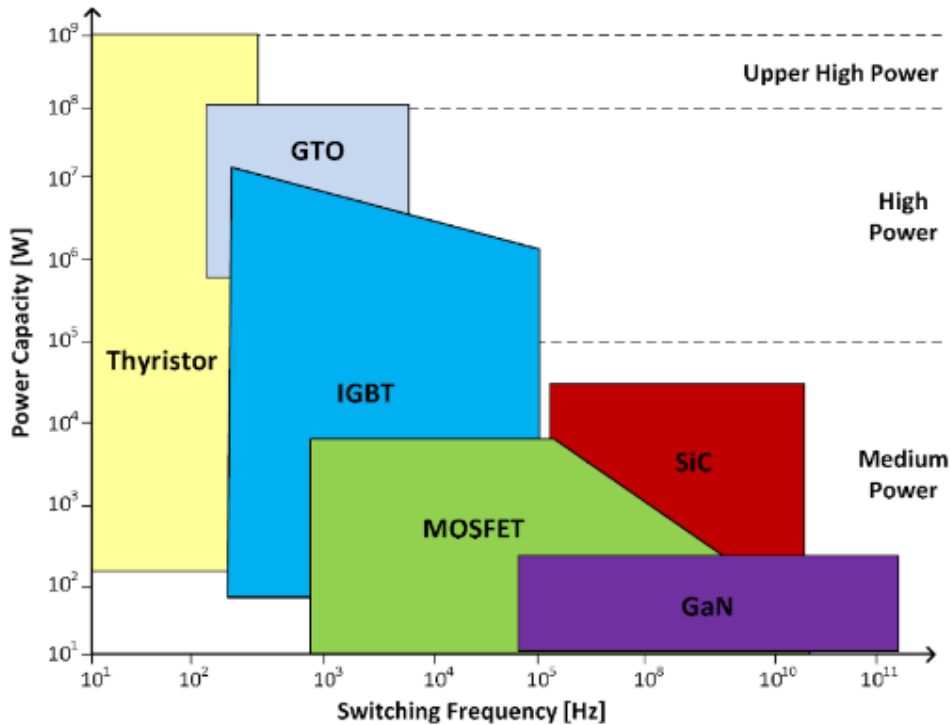


Figure 4-22: Semiconductor selection guide (Kazanbas, 2014)

Fairchild Semiconductor FDP3632 MOSFET's were chosen due to their extremely low "on-state" resistance and high current capability with more that reasonable voltage rating. It is common practice to use MOSFET's in parallel with each other to reduce the "on-state" resistance. By reducing the "on-state" resistance the conduction is reduced and the efficiency is increased. The more MOSFET's that are placed in parallel results in a lower on-state resistance (Fairchild, 2016). However, the negative effect of placing MOSFET's in parallel is that the gate charge capacitance is increased. This means that the line drivers will have to use more current to ensure the gate capacitors are charged and discharged in the same time frame. This decreases the efficiency of the control stage (Fairchild, 2016). A good midpoint needed to be selected, due to the relatively low switching frequency; a high gate charge will not be too intrusive. The amount of FET's chosen was based more on the current handling capabilities. Two FDP3632 for each section was chosen, leaving the total MOSFETs for the three single phase arms at twelve (Fairchild, 2016).

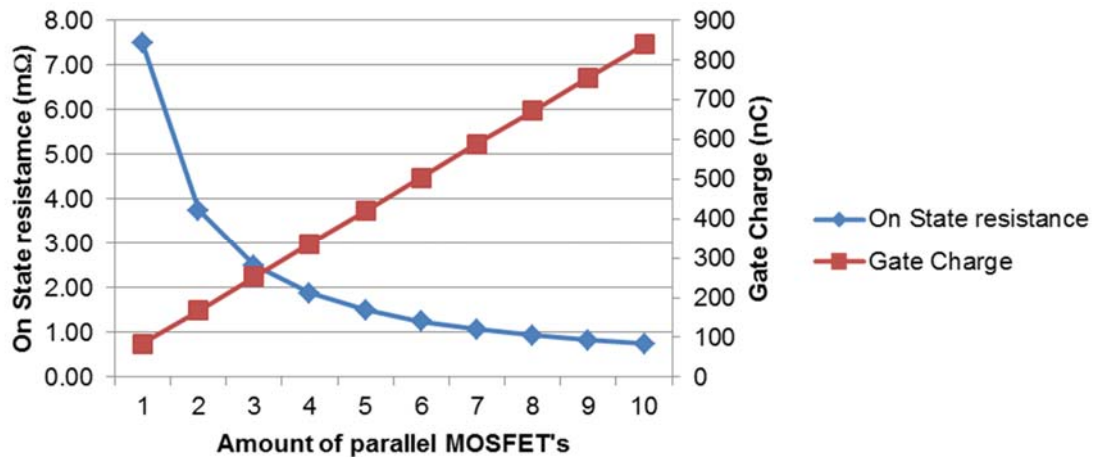


Figure 4-23: Effect of parallel MOSFET's on gate charge and on-state resistance

Once the basic circuit design was completed, a further investigation into prohibiting the switching noise and the node ringing commenced.

The basic design of a single power stage in Figure 4-24 is an indication of the minimum requirement in reducing noise and node ringing reduction. Circuit protection and noise reduction were also implemented in the following ways.

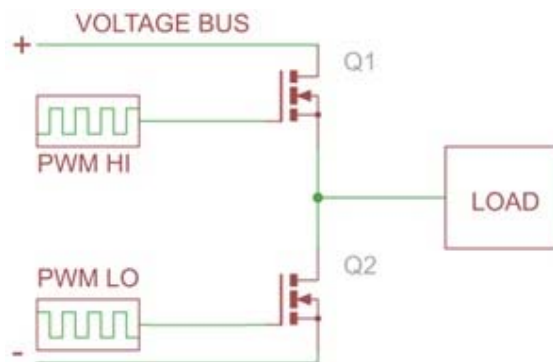


Figure 4-24: The basic power stage of one phase (Microchip, 2007).

In order to reduce the noise and node ringing the following aspects of the power stage on the inverter needed to be looked at.

4.2.2.2 Gate resistors

Small 15 Ω resistors were placed on each MOSFET gate to reduce node ringing by slowing down the gate pulses. This increases the current draw from the line drivers. A small enough value was used to reduce the negative effect (Microchip, 2007).

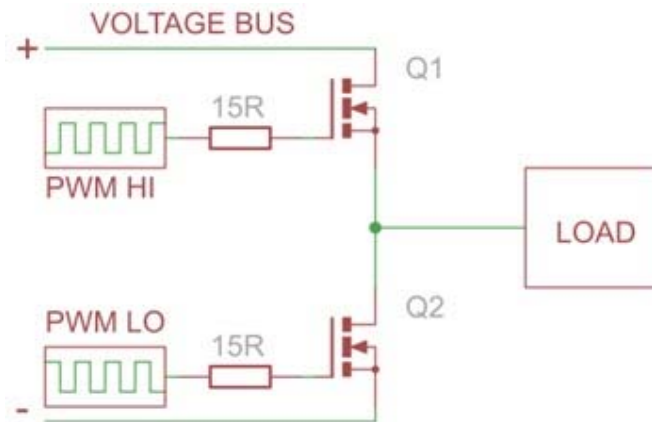


Figure 4-25: Gate resistors added to the circuit (Microchip, 2007).

4.2.2.3 RC snubber circuit

Snubber's were also placed across each side of the HI and LO terminals. This arrangement breaks down any high $\frac{dv}{dt}$ surges that might occur due to the inductive load (Microchip, 2007).

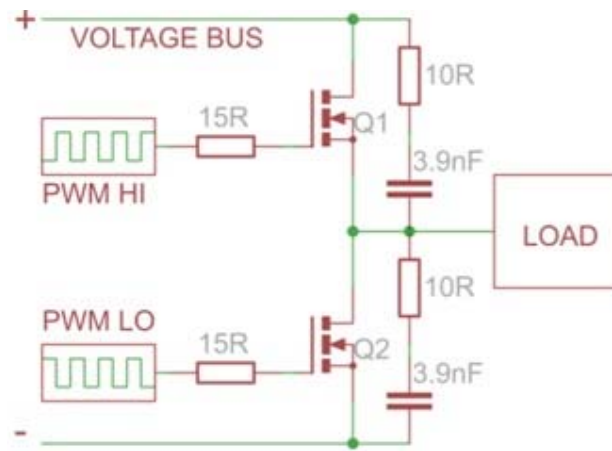


Figure 4-26: A resistive and capacitive (RC) snubber placed across the HI and LO terminals (Microchip, 2007).

4.2.2.4 Transient voltage suppressors

The main cause of MOSFET failure is a high $\frac{dv}{dt}$ surge from switching an inductive load such as an AC IM. To further help the breakdown of these transient voltages, transient voltage suppressors (TVS's) were inserted from each source to the gate on each MOSFET (Microchip, 2007).

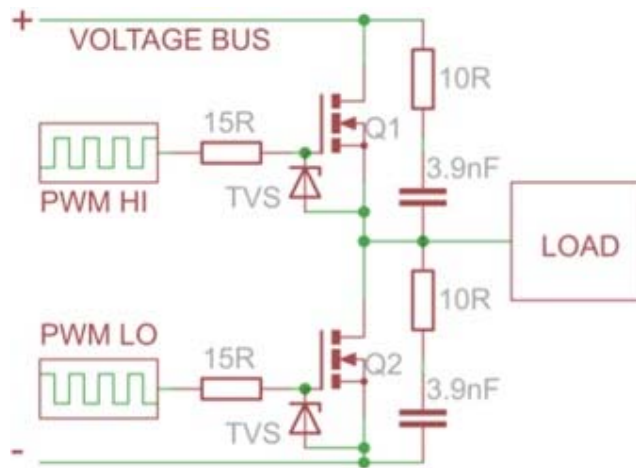


Figure 4-27: TVS's inserted from each source gate on each MOSFET (Microchip, 2007).

4.2.2.5 Decoupling capacitor

Lastly, decoupling capacitors were placed across each side of the HI and LO terminals to break down any transient current ripple that would have been induced from high frequency high current switching (Microchip, 2007).

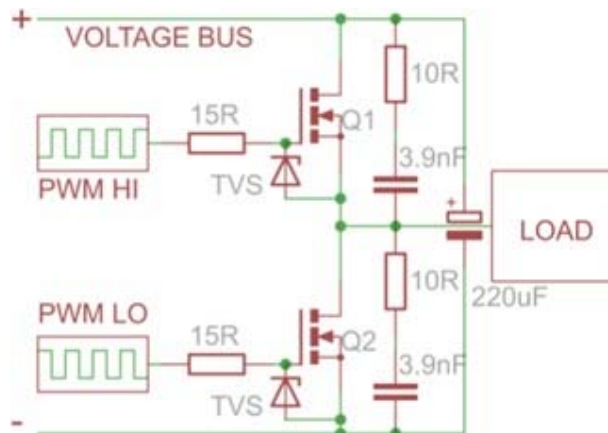


Figure 4-28: Decoupled capacitors connected from HI to LO terminals (Microchip, 2007).

4.2.2.6 Power losses in MOSFET's

The focus for the power losses of the EV motor controller power stage are categorised into two losses, namely conduction losses and switching losses. Both were reviewed and the total efficiency of the motor drive was calculated. Conduction losses ($P_{CONDUCTION}$) are the power loss due to the on-state resistance and the MOSFET RMS current. Usually the HI and LO outputs are calculated separately, but in this case the exact same FET was used for both the HI and LO side (Dobkin & Williams, 2013) (Texas Instruments, 2016)

High on-state resistance :	$H_{SRDS_{ON}}$	=	4.5 m Ω
MOSFET RMS current:	$I_{OUT_{RMS}}$	=	20 A
Low on-state resistance:	$L_{SRDS_{ON}}$	=	4.5 m Ω

$$P_{CONDUCTION} = (H_{SRDS_{ON}} \times I_{OUT_{RMS}}^2) + (L_{SRDS_{ON}} \times I_{OUT_{RMS}}^2) \quad (35)$$

$$\therefore P_{CONDUCTION} = 3.6 \text{ W}$$

It is important to notice that the MOSFET used has a maximum $R_{RDS_{ON}}$ value of 9 m Ω and the maximum current (I_{OUT}) was taken to be 40 A RMS. As the two MOSFET's are used in parallel, the resistance halves and so does the current. The total maximum power loss in one stage was therefore 3.6 W (Texas Instruments, 2016).

In calculating the total conduction losses, the total power losses in one stage needed only to be multiplied by three.

$$P_{CONDUCTION \text{ TOTAL}} = 3.6 \text{ W} \times 3$$

$$\therefore P_{CONDUCTION \text{ TOTAL}} = 10.8 \text{ W}$$

It takes a finite time for a MOSFET to turn on and off. During the "ON" and "OFF" transitions, due to the LO side clamping effects, the HI side device is affected by both high current and high voltage at the same time, which induces switching losses. This calculation for the switching losses ($P_{SW-RISE}$) and ($P_{SW-FALL}$) is dependent on the rise and fall time, the supply voltage and current, and lastly the switching frequency (Dobkin & Williams, 2013).

Input voltage:	V_{IN}	=	38 V
Output current:	I_{OUT}	=	40 A
Rise time:	t_R	=	39 ns
Switching Frequency:	f_{SW}	=	16 kHz

$$P_{SW-RISE} = \frac{1}{2} \times V_{IN} \times I_{OUT} \times t_R \times f_{SW} \quad (36)$$

$$P_{SW-RISE} = 0.474 \text{ W}$$

Input voltage:	V_{IN}	=	38 V
Output current:	I_{OUT}	=	40 A

$$\begin{aligned}
\text{Fall time:} & \quad t_F & = & \quad 46 \text{ ns} \\
\text{Switching Frequency:} & \quad f_{SW} & = & \quad 16 \text{ kHz}
\end{aligned}$$

$$\begin{aligned}
P_{SW-FALL} &= \frac{1}{2} \times V_{IN} \times I_{OUT} \times t_F \times F_{SW} & (37) \\
P_{SW-FALL} &= 0.559 \text{ W}
\end{aligned}$$

The total switching losses for one FET ($P_{SW-TOTAL}$) was:

$$P_{SW-TOTAL} = P_{SW-RISE} + P_{SW-FALL} = 1.033 \text{ W}$$

If the total switching losses was 1.033 W in one FET, then the total losses ($P_{SW-TOTAL}$) was 12.396 W for the total of twelve FET's.

$$P_{SW-TOTAL} = 12.396 \text{ W for twelve FET's}$$

$$\begin{aligned}
P_{MOSFET} &= P_{SW-TOTAL} + P_{CONDUCTION TOTAL} \\
P_{MOSFET} &= 23.196 \text{ W}
\end{aligned}$$

The total power-stage losses are included in the losses of the LT1074 as well.

$$\begin{aligned}
\text{Total switching losses for the twelve MOSFETS:} & \quad P_{MOSFET} & = & \quad 23.196 \text{ W} \\
\text{Total power losses of the buck converter:} & \quad P_{TOTAL BUCK} & = & \quad 7.641 \text{ W}
\end{aligned}$$

$$\begin{aligned}
P_{TOTAL} &= P_{MOSFET} + P_{TOTAL BUCK} & (38) \\
\therefore P_{TOTAL} &= 30.887 \text{ W}
\end{aligned}$$

4.2.2.7 Control stage power consumption

The last calculation to perform for the control stage was the power consumption, or power loss. This and the power loss in the power stage were used to calculate the drive efficiency. The calculation was as follows (International Rectifier, 2016):

$$\begin{aligned}
P_G &= 2[V \times Q_g \times F_s] & (27) \\
\therefore P_G &= 2[15 \times (110 \times 10^{-12}) \times (16 \times 10^3)] \\
\therefore P_G &= 15 \text{ mW (for one driver)}
\end{aligned}$$

4.2.2.8 Switch-mode power supply

As there are several sensitive electronic components on the control stage, the higher voltage and high switching current were kept completely separate from them. The dsPIC required no more than 3.3 V DC to operate. The logic side of the IR2110 can also operate from this but needs approximately 15 V DC for switching the gates. This meant that 38 V had to be reduced to 15 V and then to 3.3 V.

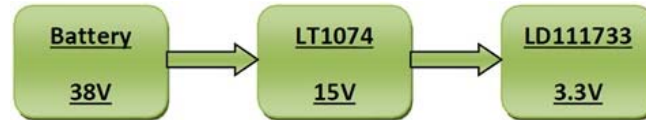


Figure 4-29: Stepping down stages of voltage from 38 V to 3.3 V

The design specifications for the switch mode power supply regulator are as follows. The input voltage is $V_{IN} = 38 \text{ V}$ and the output voltage is $V_{OUT} = 15 \text{ V}$.

4.2.2.9 Calculation of switch mode power supply values

The following parameters had to be calculated for the switch mode power supply. This included the duty cycle of the circuit, the output current, the power diode consumption, the output divider of the supply, the power losses and efficiency of the supply and the inductor inductances.

The duty cycle of the regulator was calculated as follows (Dobkin & Williams, 2013):

Output voltage:	V_{OUT}	=	15 V
Forward voltage of the catch diode:	V_f	=	0.5 V
Input Voltage:	V_{IN}	=	38 V
Voltage loss across "on" switch:	V_{SW}	=	2.0 V

$$DUTY \ CYCLE = \frac{V_{OUT} + V_f}{V_{IN} - V_{SW}} \quad (28)$$

$$\therefore DUTY \ CYCLE = 43.056 \%$$

The output current $I_O(CRIT)$ - load current, of the buck converter, changed from a continuous to discontinuous mode, was calculated as follows (Dobkin & Williams, 2013).

Output voltage:	V_{OUT}	=	15 V
Input voltage:	V_{IN}	=	38 V
Operating frequency:	f	=	100 kHz
Chosen inductance value:	L	=	50 μF

$$I_O(CRIT) = \frac{V_{OUT} \times (V_{IN} - V_{OUT})}{(2 \times V_{IN} \times f \times L)} \quad (29)$$

$$\therefore I_O(CRIT) = 0.908 \text{ A}$$

The maximum output current ($I_{OUT(MAX)}$) of the buck converter used was given as follows (Dobkin & Williams, 2013).

Output voltage:	V_{OUT}	=	15 V
Input voltage:	V_{IN}	=	38 V
Operating frequency:	f	=	100 kHz
Chosen inductance value:	L	=	50 μ H
Maximum switch current:	I_M	=	5.5 A (for the LT1074)

$$I_{OUT(MAX)} = I_M - \frac{V_{OUT} \times (V_{IN} - V_{OUT})}{(2 \times V_{IN} \times f \times L)} \quad (30)$$

$$\therefore I_{OUT(MAX)} = 4.592 \text{ A}$$

The diode power consumption/dissipation (P_{DIODE}) was calculated as follows (Dobkin & Williams, 2013).

Maximum output current:	$(I_{OUT(MAX)})$	=	4.592 A
Output voltage:	V_{OUT}	=	15 V
Input voltage:	V_{IN}	=	38 V
Forward voltage of the catch diode:	V_f	=	0.5 V

$$P_{DIODE} = I_{OUT(MAX)} \times \frac{V_{IN} - V_{OUT}}{V_{IN}} \times V_f \quad (31)$$

$$\therefore P_{DIODE} = 1.39 \text{ W}$$

For the output divider, the DC output voltage was set by R_1 and R_2 . R_2 was set at 2.21 k Ω (a standard 1 % value) to match the LT1074 reference voltage of 2.21 V. Giving a divider current of 1 mA, R_1 was then calculated to be (Dobkin & Williams, 2013).

Output voltage:	V_{OUT}	=	15 V
Reference voltage:	V_{REF}	=	2.21 V

$$\text{Standard resistance value for } R_2: \quad R_2 = 2.21 \text{ k}\Omega$$

$$R_1 = R_2 \times \frac{V_{OUT} - V_{REF}}{V_{REF}} \quad (32)$$

$$\therefore R_1 = 12.790 \text{ k}\Omega$$

The power losses of the buck converter ($P_{TOTAL\ BUCK}$) was calculated as follows (Dobkin & Williams, 2013).

$$P_{TOTAL} = 38 \times \left[\underbrace{((7 \times 10^{-3}) + (5 \times 10^{-3} \times 0.407))}_{\text{Supply current losses}} + \underbrace{(2 \times 5 \times (65 \times 10^{-9}) \times (100 \times 10^3))}_{\text{Dynamic switching losses}} \right] + \underbrace{\left((0.407) \times ((5 \times 1.8) + (0.1 \times 5^2)) \right)}_{\text{Switching conduction losses}}$$

$$\therefore P_{TOTAL\ BUCK} = 0.362 \text{ W} + 2.6 \text{ W} + 4.68 \text{ W}$$

$$\therefore P_{TOTAL\ BUCK} = 7.641 \text{ W}$$

In calculating the efficiency (η) of the buck converter (Dobkin & Williams, 2013).

Maximum output current:	$(I_{OUT(MAX)})$	=	4.592 A
Output voltage:	V_{OUT}	=	15 V
Forward voltage of the catch diode:	V_f	=	0.5 V
Total regulator loss:	ΣP_L	=	4.16 W

$$\eta = \frac{I_{OUT(MAX)} \times V_{OUT}}{I_{OUT(MAX)} \times V_{OUT} + \Sigma P_L} \quad (33)$$

$$\eta = 94.304 \%$$

Figure 4-30 is a completed design of the buck converter that was built and used for our application (Microchip, 2007).

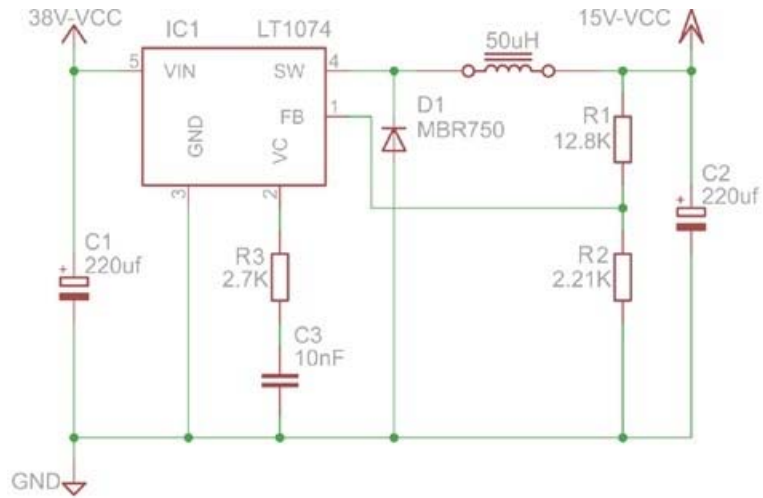
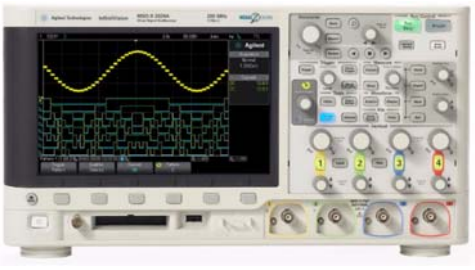
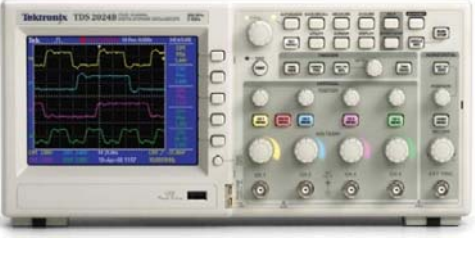


Figure 4-30: EV Switch mode power supply circuit (buck converter) (Microchip, 2007).

4.2.3 Motor drive testing and results

After completion of the motor testing, the next testing to be completed was on the motor drive. This needed to be completed in order to ensure that each component of the EV was tested before testing of the completed system could commence. This was also done to ensure compatibility with the motor and motor drive and to also test the modular design set out from the beginning. The test equipment used for testing the motor drive can be seen in Table 4-5.

Table 4-5: Measuring equipment for initial testing of motor drive

Equipment Name and Model	Equipment picture
Agilent InfiniiVision DSO-X 2024A Digital Storage Scope	
Tektronix TDS 2024B Digital Storage Scope	

YF-3503 Multimeter



DF17315B, Variable Power Supply (5 A)



Delta Elektronika SM 120-25D Variable Power Supply



Fluke 43 Power Quality Analyzer



DT-2236 Tachometer



4.2.3.1 Motor drive wave form results from initial testing

After completion of building the motor drive, the HI and LO signals from the line drivers were the first measurement to be taken. Figure 4-31 shows the HI side signal (in orange), the LO side signal (in green) and then the output signal passed through a low pass filter (in blue), mentioned in the order from top to bottom.

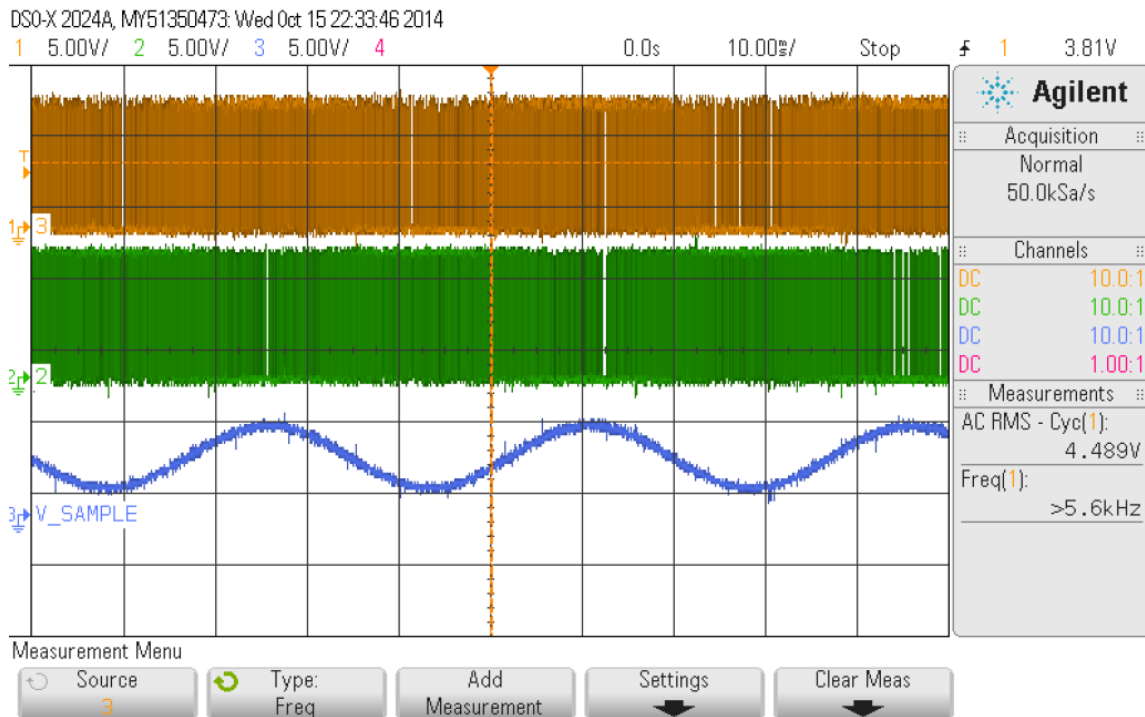


Figure 4-31: HI side signal, LO side signal and filtered output of the motor drive

At this point the gate signals appeared not to be clear. The outputs were then measured with each phase measured with respect to ground. The outputs were then zoomed into and the waveforms in Figure 4-32 were captured showing the fundamental frequency, which just about appeared.

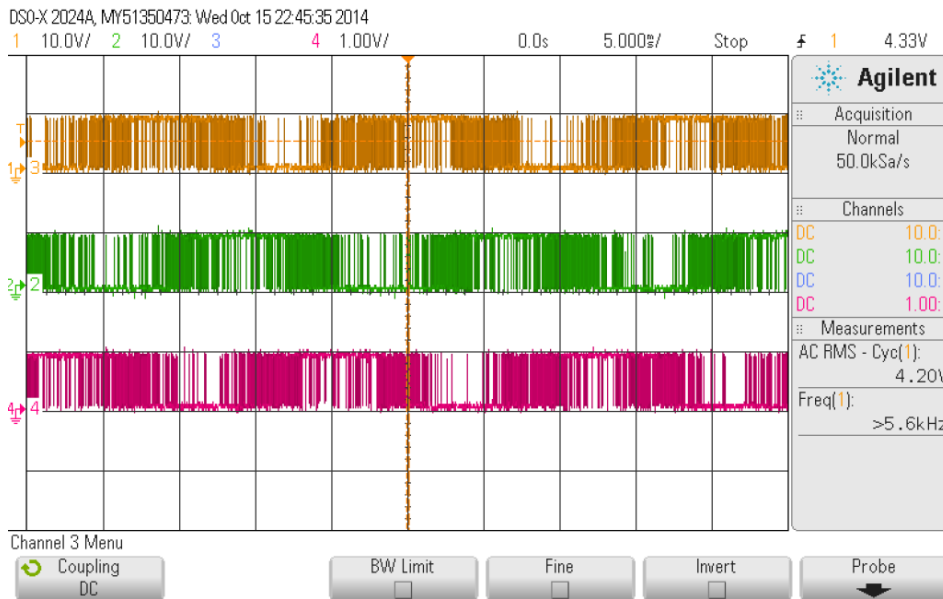


Figure 4-32: The three phase output waveforms (PWM modulated sine wave)

The outputs were then passed through a low pass filter and produced three phase shifted sine waves as seen in Figure 4-33.

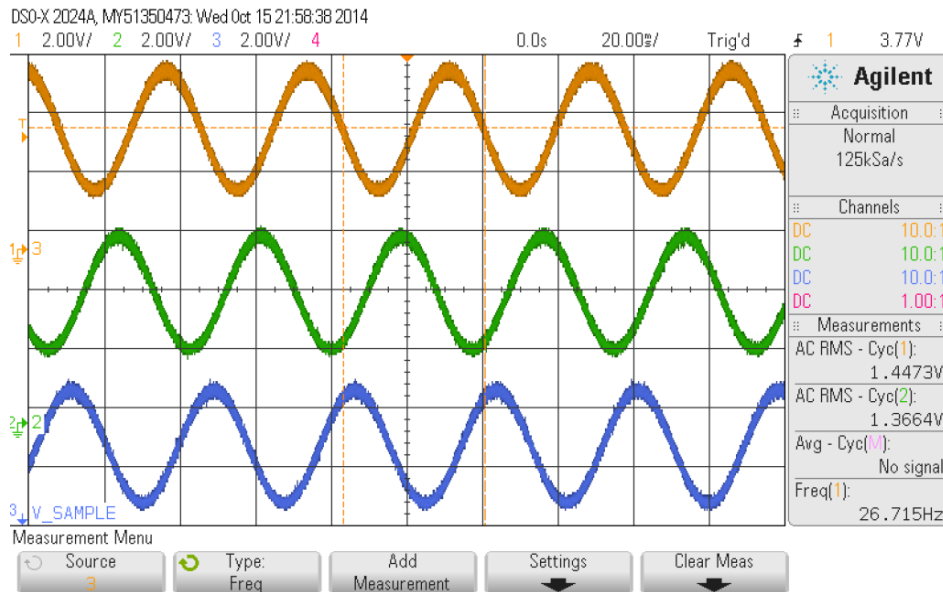


Figure 4-33: The three phase output waveforms with a low pass filter added

By placing the three phases on top of each other and keeping the low pass filter, it was clear that all three phases were exactly a hundred and twenty degrees out of phase with one another, as can be seen in Figure 4-34.

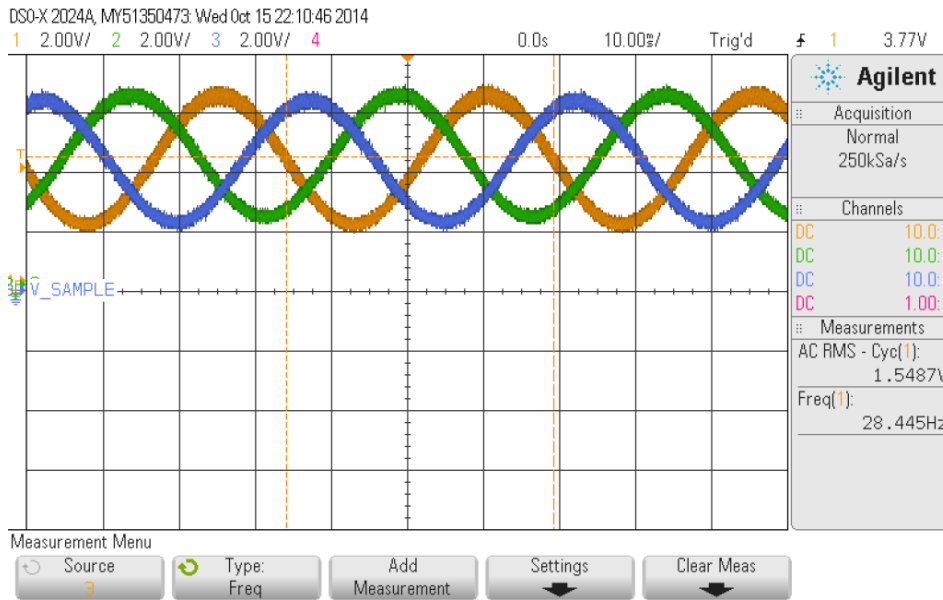


Figure 4-34: All three phase signals 120 degrees out of phase from each other

The advantage of using the Agilent digital storage scope is that the trigger can be set to averaging and it “locks” onto the fundamental frequency. The scopes trigger was set to averaging and all three phases were measured.

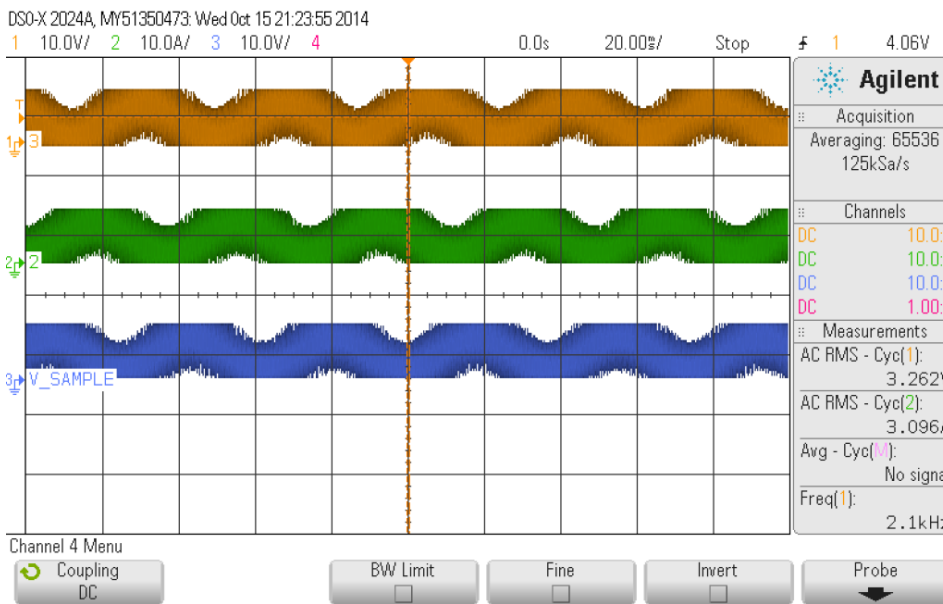


Figure 4-35: All three phases were set to averaging

Now the fundamental frequency was clearer, at this point the results were more that convincing to move on the load testing. The extent of the load testing is completed in the following chapter.

Figure 4-36 and Figure 4-37 are pictures of the completed final control stage and the power stage of the motor drive. These boards were assembled according to the design specifications stipulated before undergoing the initial testing described.

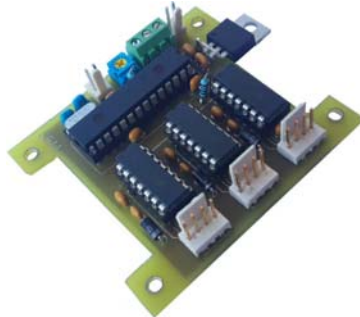


Figure 4-36: Final motor drive control stage

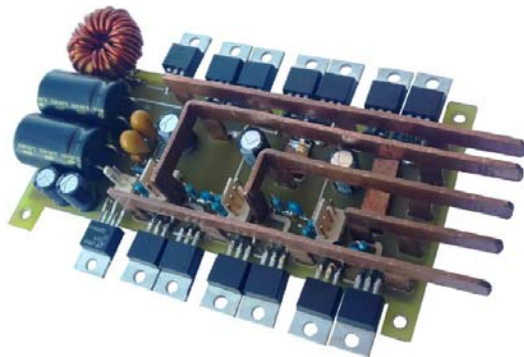


Figure 4-37: Final motor drive power stage

A completed picture of the assembled motor drive is seen in Figure 4-38.



Figure 4-38: Final assembled motor drive

The integration of the power and control stage was the final step in the design of the motor controller. Both stages had power losses and the integrated circuits generate heat. The solution was to get a big enough heat-sink to cope at full load. As the MOSFET's are the main heat-generators they were looked at first. A typical thermal dissipation network was set up as follows (Microchip, 2007).

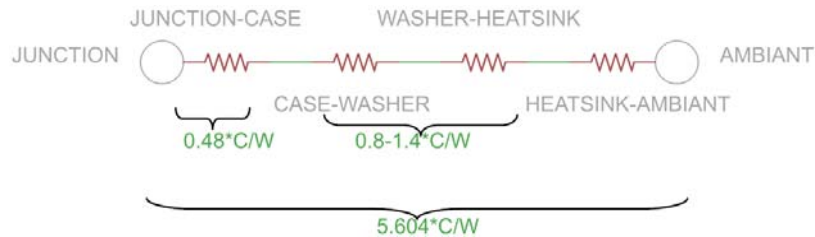


Figure 4.39: Thermal dissipation network (Microchip, 2007).

The maximum junction-ambient thermal resistance ($R_{\theta_{ja}}$) had to be calculated first (Texas Instruments, 2011).

Maximum junction temperature:	T_{j-max}	=	175 °C
Maximum ambient temperature:	$Ambient_{max}$	=	50 °C
Total switching losses for the twelve MOSFETS:	P_{MOSFET}	=	23.196 W

$$Max R_{\theta_{ja}} = \frac{T_{j-max} - Ambient_{max}}{P_{MOSFET}} \quad (39)$$

$$\therefore Max R_{\theta_{ja}} = 5.389 \frac{^{\circ}C}{W}$$

After the maximum junction-ambient thermal resistance was calculated, by the power of deduction, the heat-sink value ($R_{\theta_{ha}}$) could be calculated (Texas Instruments, 2011).

Maximum junction-ambient thermal resistance:	$Max R_{\theta_{ja}}$	=	$5.389 \frac{^{\circ}C}{W}$
--	-----------------------	---	-----------------------------

Thermal resistance of the interface compound used:	$R_{\theta_{ch}}$	=	$1.1 \frac{^{\circ}C}{W}$
--	-------------------	---	---------------------------

Thermal resistance inside the device package:	$R_{\theta_{jc}}$	=	$0.48 \frac{^{\circ}C}{W}$
---	-------------------	---	----------------------------

$$R_{\theta_{ha}} = Max R_{\theta_{ja}} - R_{\theta_{ch}} - R_{\theta_{jc}} \quad (40)$$

$$\therefore R_{\theta_{ha}} = 3.809 \frac{^{\circ}C}{W}$$

This means that the maximum heat-sink-ambient thermal resistance had to be lower than $4.024 \frac{C}{W}$. A heat-sink with a thermal resistance of $0.51 \text{ }^{\circ}\text{C}/\text{W}/200\text{mm}$ was chosen. To test if this heat-sink would suffice the following calculation had to be completed and the answer had to be lower than $R_{\theta_{ha}}$ (Texas Instruments, 2011).

$$\begin{aligned} \text{Thermal resistance of the heatsink: } R_{\theta_{ha}} &= 0.51 \frac{^{\circ}\text{C}}{\text{W}} \\ \text{Thermal resistance of the interface compound used: } R_{\theta_{ch}} &= 1.1 \frac{^{\circ}\text{C}}{\text{W}} \\ \text{Thermal resistance inside the device package: } R_{\theta_{jc}} &= 0.48 \frac{^{\circ}\text{C}}{\text{W}} \end{aligned}$$

$$\begin{aligned} R_{\theta_{ja}} &= R_{\theta_{ha}} + R_{\theta_{ch}} + R_{\theta_{jc}} & (41) \\ \therefore R_{\theta_{ja}} &= 0.208 \frac{^{\circ}\text{C}}{\text{W}} \end{aligned}$$

The heat-sink chosen was more than enough for this application. The final calculation was for the total efficiency.

$$\begin{aligned} \text{EFFICIENCY} &= \frac{P_{OUT} - P_{TOTAL}}{P_{OUT}} \times 100 & (42) \\ \therefore \text{EFFICIENCY} &= 96.911 \% \end{aligned}$$

4.2.4 The gate drivers (line drivers)

The last part in the control stage was the gate drivers, or line drivers. A gate driver is a chip that amplifies the signal from the dsPIC. It ensures that there is enough current to charge and discharge the gate capacitors of the MOSFET's for rapid response.

As International Rectifiers are one of the leaders in cost effective and efficient solutions in gate drivers, their IR2110 gate drivers were used. The application note AN-978 was consulted and a recommended circuit setup was derived and values calculated to drive a three phase induction motor. The three phase inverter uses three IRS2110 devices to drive six IGBTs as seen in Figure 4-40 (International Rectifier, 2016).

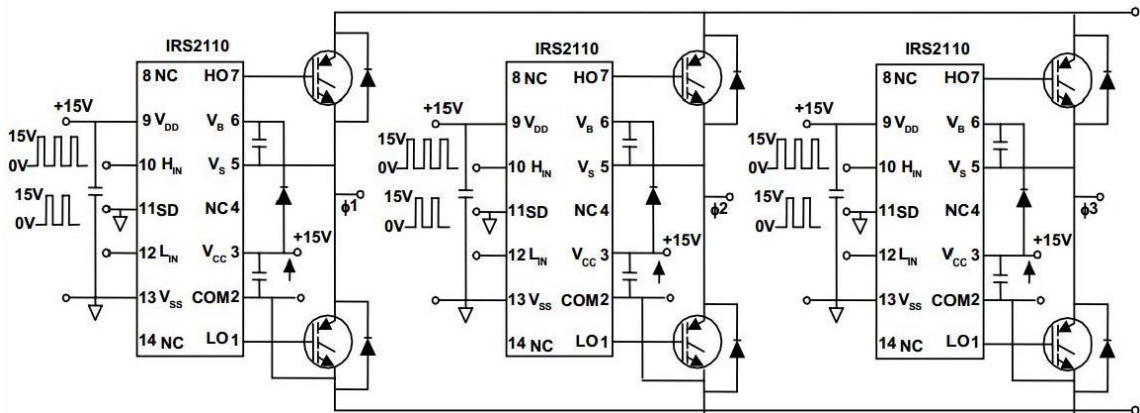


Figure 4-40: Minimum circuit connection for three phase inverters using three IRS2110 devices to drive six IGBTs (International Rectifier, 2016)

This setup proved to be the effective solution for this application. The only requirement was that a proper bootstrap capacitor and diode needed to be calculated. This was done using the following formula (Adams, 2008).

$$C \geq \frac{2 \left[2Q_g + \frac{I_{qbs(max)}}{f} + Q_{ls} + \frac{I_{cbs(leak)}}{f} \right]}{V_{cc} - V_f - V_{LS} - V_{min}} \quad (24)$$

where:

- Q_g = Gate charge of high-side FET (nC)
- f = frequency of operation (Hz)
- $I_{cbs(leak)}$ = bootstrap capacitor leakage current (only applicable on electrolytic capacitors) (A)
- $I_{qbs(max)}$ = Maximum V_{BS} quiescent current (A)
- V_{cc} = Logic section voltage source (V)
- V_f = Forward voltage drop across the bootstrap diode (V)
- V_{LS} = Voltage drop across the low-side FET (V)
- V_{min} = Minimum voltage between V_B and V_S (V)
- Q_{ls} = level shift charge required per cycle (typically 5 nC for 500 V/600 V MGDs and 20 nC for 1200 V MGDs) (Adams, 2008) (C)

The following values were selected and calculated before calculating the bootstrap capacitor value.

Table 4-6: Bootstrap capacitor values

Variable	Description	Value
Q_g	Gate Charge of High-Side FET	84 nC
f	Operating Frequency	16 kHz
$I_{cbs(leak)}$	Bootstrap Cap Leakage Current (Only applicable on Electrolytic capacitors)	0 A
$I_{qbs(max)}$	Max V _{BS} Quiescent Current	230 μA
V_{cc}	Logic section voltage source	15 V

V_f	Forward voltage drop across bootstrap diode	1.3 V
V_{LS}	Voltage drop across Low-Side FET	1.5 V
V_{min}	Minimum voltage between V_B and V_S	4 V
Q_{LS}	Level shift charge per cycle	5 nC

From the values above the capacitor bootstrap value was calculated (Adams, 2008).

$$C \geq \frac{2[(2 \times 84 \times 10^{-9}) + \frac{(230 \times 10^{-6})}{(16 \times 10^3)} + (5 \times 10^{-9}) + \frac{0}{(16 \times 10^3)}]}{[15 - 1.3 - 1.5 - 4]}$$

$$\therefore C \geq 45.7 \text{ nF}$$

The equation for the diode is a little less complicated and is calculated by (Adams, 2008):

$$Q_{BS} = 2 \times Q_g + \frac{I_{qbs(max)}}{F} + Q_{LS} + \frac{I_{Cbs(leak)}}{F} \quad (25)$$

$$= 187.375 \times 10^{-9}$$

$$I_F = Q_{BS} \times F \quad (26)$$

$$= (187.375 \times 10^{-9}) \times (16 \times 10^3)$$

$$= 2.998 \times 10^{-3}$$

$$= 3 \text{ mA}$$

Chapter Five

The battery pack and battery management system design

5.1 The battery pack

The Lithium-Ion polymer pouch cells available at the CPUT required a high degree of protection and secure inter-cell connections since the battery pack was intended for use in an EV, which placed demanding current requirements on it. The cells had to be continually monitored to provide a full picture of the available power.

5.1.1 Electrical requirements of the battery pack

The limitations for the Shell Eco-marathon state that the voltage in the vehicle can at no point exceed 60 V maximum and 52 V nominal (Shell, 2014). The available BMS supports six to ten series cells, and the three phase motor driver was designed for a nominal voltage of 38 V. Therefore the pack was composed of a maximum of ten series elements.

5.1.2 Lithium polymer pouch cell operating conditions

The Lithium polymer pouch cells had several critical parameters which had to be maintained in order to ensure safe operation and maximum battery lifespan. They were as follows (Shell, 2013):

- The cell's temperature should not have exceeded the safe values as listed in the datasheet.
- The pouch cells were clamped in such a manner that it was not possible for them to expand beyond their manufactured tolerance.
- The electrical tabs were clamped to each other or a contact with sufficient force to prevent arcing during high current discharge.
- The cells were protected from mechanical damage that could cause a short circuit and a fire.
- Both terminals of each cell were externally available in order to connect the battery management system.
- At this development stage it was necessary that the cells be individually accessible and replaceable since the cells were at different ages (used and from storage), and the pack was subjected to damaging electrical conditions during testing.
- Finally and most critically, the enclosure had to be fireproof. When Lithium cells burn the fire is extremely hot and impossible to extinguish by conventional methods. The only way to quench them is in Mica flakes, and then it is just to hold the burning cell until the fire has consumed its stored chemical energy.

The Lithium-Ion polymer cells available at CPUT for this project were the Lithium Manganese Oxide cells. This was determined by comparing the cell's specifications (Table 5-1) with typical specifications for different Lithium-Ion chemistries (necessary because the datasheet does not supply the cell chemistry, only stating "Lithium-Ion Polymer") (Battery University, 2016).

Table 5-1: Comparison of typical Lithium Manganese oxide batteries and the Lithium-ion batteries available at CPUT

Lithium Manganese Oxide: LiMn_2O_4 cathode Graphite anode, (Typical specifications)		Enertech SPB9345136UH1
Voltage, nominal	3.70 V	3.70 V
Specific energy (capacity)	100 –150 Wh/kg	135 Wh/kg
Charge (C-rate)	0.7 – 1 C typical, 3 C maximum, charges to 4.20 V (most cells)	1 C typical 2 C Maximum. 4.2 V charge voltage.
Discharge (C-rate)	1 C – 10 C, 30 C pulse (5 s), 2.50 V cut-off	Up to 30 C continuous, 50 C pulse
Cycle life	300 – 700	-
Thermal runaway	250 °C (482 °F)	-
Applications	Power tools, medical devices, electric powertrains	-
Comments	High power but less capacity; safer than Li-cobalt; commonly mixed with NMC to improve performance.	-

For these reasons, the Enertech SPB9345136UH1 Lithium-Ion polymer battery cells (LiPO) were chosen for this project. Appendix E contains the specifications for these battery cells.

These LiPO batteries were purchased from Enertech CC (Enertech, 2018) and for the purpose of this EV, the LiPO model type SPB9345136UH1 was selected. These batteries have a 4.4 Ah rating and a nominal voltage of 3.7 V.

They also provide a good current discharge C-rating of 132 A at 30 C (Solanki, 2011). The energy density of these batteries is approximately 135.6 Wh/Kg, which is very good. Li-Polymer energy density is about three times more than that of Lead Acid batteries and more or less twice that of NiCd batteries (Imanishi, et al., 2014).

In designing the battery pack, there were various factors that needed to be considered. For the EV to have been at an optimal efficiency, it was recommended that the EV run at a speed of 25 km/h (Shell, 2015).

It was determined that in order for the EV to have completed a single track length of 2.40 km, the vehicle would have needed to run continuously at 25 km/h for five minutes and forty six seconds.

A motor was developed for the CPUT EV to deliver approximately 23 V AC RMS, with a maximum current of approximately 35 A, at a power of 750 W each. A motor drive was developed with an input voltage of 38 V DC and an output power of 750 W, with a maximum current of 40 A per phase, in order to drive the motors.

For this reason, the Lithium-Ion batteries, which have a nominal voltage rating of 3.7 V each and a discharge current of 132.0 A at 30 C was incorporated. Ten cells were connected in series to deliver approximately 38 V DC to the BMS, which works in conjunction with the motor drive. Four stacks of the ten cell in series were also connected in parallel to deliver a continuous discharge current of 17.6 Ah to the BMS.

The provided LiPO pouch cells were assembled into a safe and robust “ten batteries in series and four stacks in parallel” combination (10S4P) battery pack utilizing 3D printing to perform the bulk of the manufacturing tasks. The battery pack was tested to ensure thermal and mechanical stability. The cells are housed in a robust Perspex enclosure that protects it in the event of a crash. The electrical connections are insulated by specifically designed 3D printed parts. Each set of ten series cells are monitored and each cell will have its own monitoring system for cell balancing purposes.

The battery specifications are as follows (Appendix E):

Table 5-2: Battery pack characteristics

Battery Aspect	Rating
Output voltage	38 V DC
Amp hour rating	17.6 Ah
Watt hour rating	668.8 Wh
Cell technology	Lithium-Ion
Amount of cells	40

5.1.3 Terminal connections of the battery pack

The electrical terminals were split into two types of outputs; the high current output terminals and the battery cell sense outputs. This is for the BMS which will carry small balancing currents and voltage sense signals.

The high current terminals are Aluminum bus bars, and the low current sense/balancing terminals are wired to an automotive specification plug on the side of the battery pack. This allows the BMS to be easily removed and different BMS' solutions may be tested without extensive rewiring.

There are three ways to interconnect the terminals of batteries.

- Soldering
- Spot welding
- Clamping

Each of these has unique advantages and disadvantages, however, only the third option (clamping the terminals together) provides the ability to easily remove and replace or test individual cells in the pack. It was thus selected.

The terminals of the pouch cells needed to be securely clamped. There are several factors to consider here:

- Ease of assembly.
- Ease of manufacture.
- Mechanical (and thus electrical) stability.
- Ability to modify design further after construction.

The traditional clamping methods available commercially, utilize a PCB with metal or plastic clamps that screw into it from above, with the cell's terminals inserted through slots in the PCB. This was an appealing option, however it would have been time consuming and difficult to manufacture since it required custom PCB's and numerous metal parts and screws.

An innovative pouch cell contact assembly mechanism was found (Maiser, 2014) was selected as a viable option since it is space efficient, easy to assemble and manufacture. The mechanical and electrical stability was dependent on the material used for the clamping bars and further modifications to the design. The clamping bars needed to be made of non-conductive non-flammable material, thus plastic was the only option.

Perspex has good mechanical stability but is easy to break as well as having demanding machining requirements (Ellse & Honeywell, 2004). Other common plastics that are not flammable include Acrylonitrile Butadiene Styrene (ABS) and Silicon composites such as Tufnol. In order to minimize construction time ABS was selected since it is a durable material which could easily be glued or welded by ultrasonic methods, and it is one of the two primary materials used in desktop three dimensional (3D) printers (Ram, 1997).

The design was modified to take advantage of 3D printing and other available materials. A 3D model was constructed using AutoCAD which provides slots for Aluminium or Copper contact bars as well as built in bolts which can be used to affix output wires to increase ease of assembly. This 3D iteration of the design (Figure 5-1) provides additional supports to keep the pouch cells lined up and the terminals isolated from external elements.

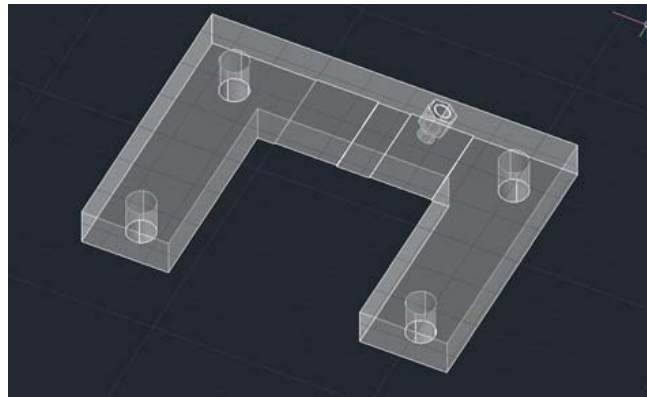


Figure 5-1: 3D model of cell clamping mechanism designed in AutoCad

The clamps were printed in sets of three on a Prusa i3 3D printer using black fire resistant ABS plastic. As a contact material between individual batteries, Aluminium was chosen due to it being available. As described in section 4.3.2, the battery pack's enclosure was made of a fireproof material (Shell, 2013). There was also a moderate amount of clamping force applied to the battery pack, in which metal being the best material for the body of the battery pack. Aluminium was selected for its ease of use and availability. The body of the battery pack was cut from an Aluminium sheet and drilled to provide slots for the threaded rods. The sheet was folded using a press.

The clamping force was provided by five millimetres threaded rods and 5 mm nuts which provide additional mechanical stability and prevents the cells from swelling during charging. The cells, clamps and casing were assembled as seen in Figures 5-2.



Figure 5-2: Assembly of aluminium enclosure for the battery pack

Figure 5-3 shows the assembly of the Lithium-Ion polymer cells and the 3D generated pouch cell. The terminal connectors can be seen at the top of each pouch.



Figure 5-3: The assembly of one stack of ten cells

Figure 5-4 shows the completed battery pack together with all the terminal connections for one stack of ten cells.



Figure 5-4: The assembled battery pack

A decision was made that the EV's power source should be electrically isolated from the remaining circuitries in the EV in case of a fault or short circuit in order to fulfil the completion rules (Shell, 2014). Fuses and a circuit breaker was the logical and cheap option in protecting the battery pack.

A 63 A circuit breaker was used to provide additional isolation of the battery pack from the EV's remaining circuitry in case of a fault. In addition, a metal bracket was built to support ten 0.5 A fuses that were placed in series with each cell to provide protection of each cell in case of a short circuit due to a fault in the BMS system.

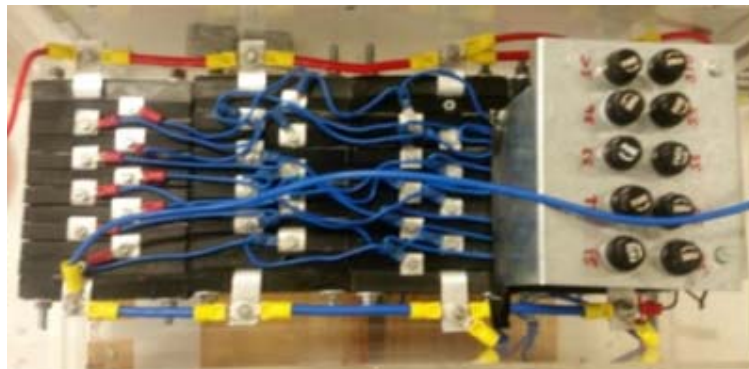


Figure 5-5: The completed battery pack together with fuse protection

A further decision was made to enclose the battery pack in a Perspex enclosure. This was also to meet the requirements of the Shell Eco Marathon (Shell, 2014).

A Perspex box was assembled and additional screws were fitted to secure the structure to the vehicle chassis. A partition was also built to separate the sections containing the battery pack from the main fuse.

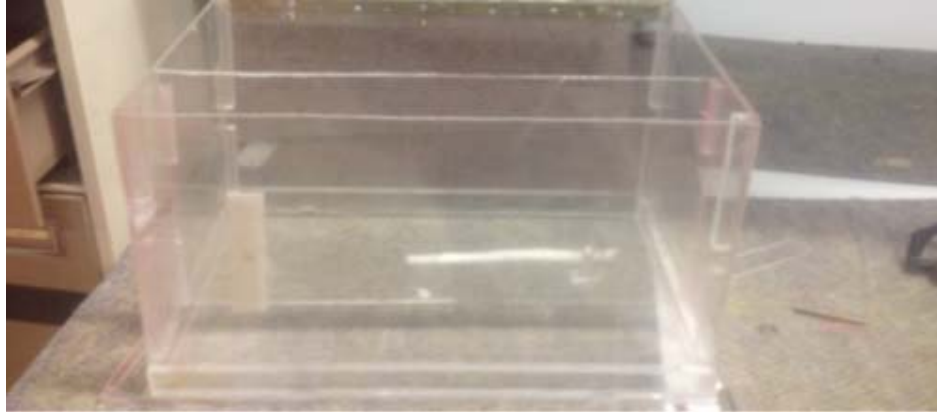


Figure 5-6: Battery pack enclosure

5.1.4 Test results for the battery pack

The individual stack of ten series cells, were charged and discharged several times to obtain data about their state of health and these tests were also done to ensure that the BMS is actually protecting the battery stack.

5.1.4.1 Cell balancing

In determining the efficiency of the cell balancing mechanism a set of unbalanced cells were charged with the cell voltages recorded before and after the test. The results of these tests can be seen in the figures to follow.

At the end of the charge cycle the charge current switched on and off rapidly as the BMS stopped charging, discharged the cells that were in overvoltage and then resumed charging. The small number of charge cycles shown between balancing cycles was a result of the logging data rate which was three times per minute.

Before charging, the cell voltages were spread over 1 V, ranging from 2.5 V up to 3.5 V. After charging and passive balancing, the cell voltages were all within 0.1 V of each other at 4 V. Although the battery cells had a recommended charge voltage of 4.2 V the BMS's threshold was set slightly lower than this to enable effective (time efficient) balancing at the top of the charge.

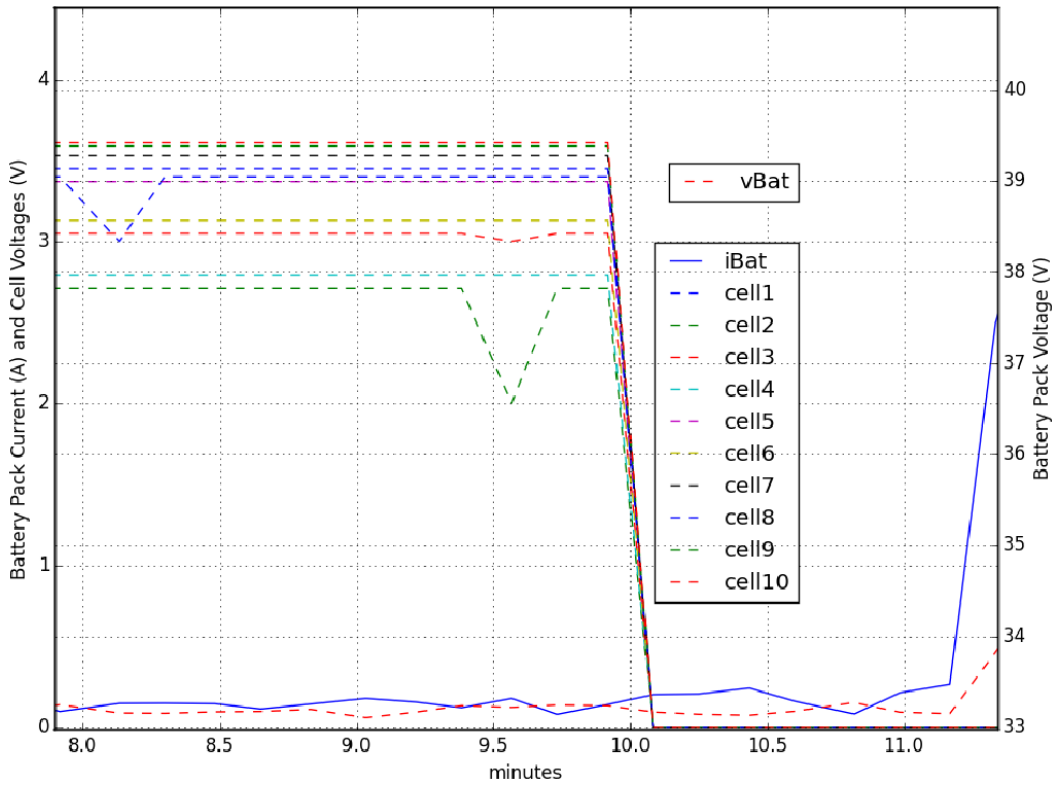


Figure 5-7: The battery cell voltages before charging and balancing

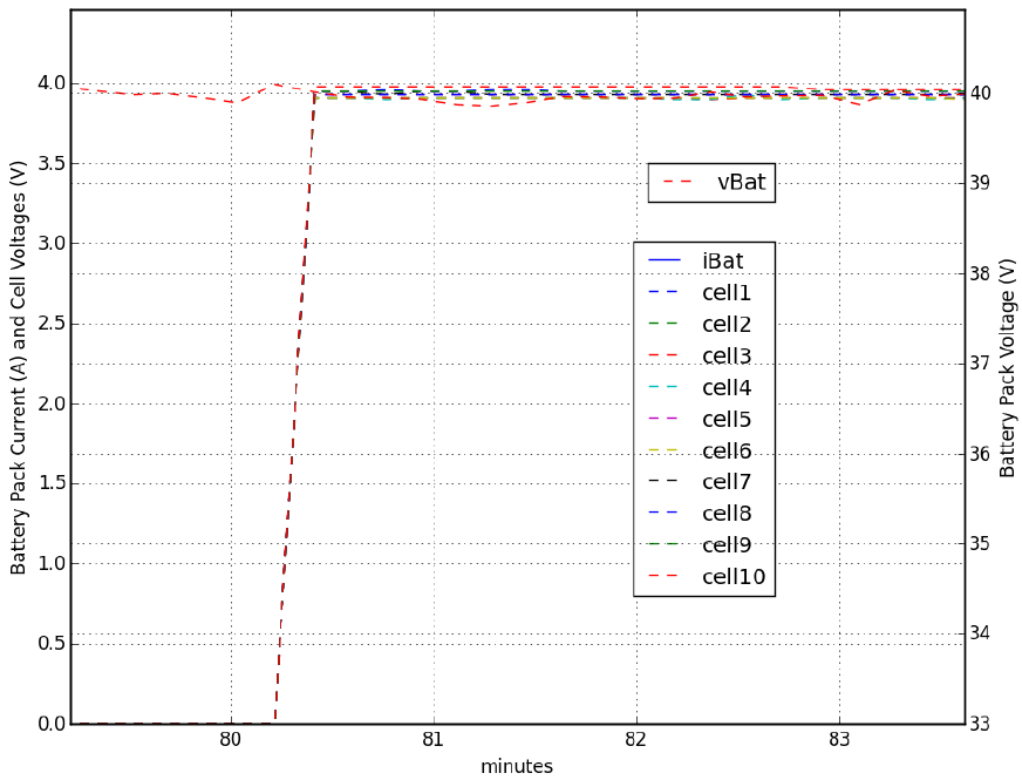


Figure 5-8: The battery cell voltages after charging and balancing

5.1.4.2 Battery capacity

It can be seen in Figure 5-9 that the cells voltages began to diverge rapidly when the pack's capacity was reduced below 0.5 Ah. The maximum capacity achieved with these cells using over-voltage at 4.0 V and under-voltage set to 3.0 V was 3.67 Ah during the second discharge test.

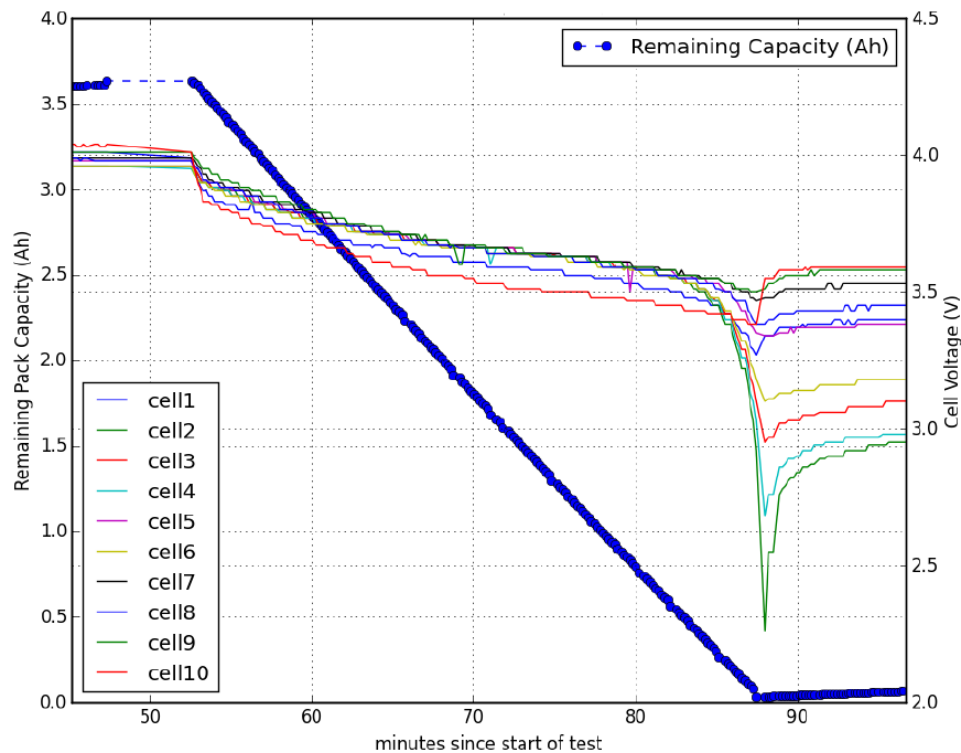


Figure 5-9: The battery capacity and cell voltages during discharging

Once all the above tests were completed the cell configuration was adjusted to provide 17.6 Ah maximum capacity, so that the EV endures 43 min (max) in a total track race length of 9 laps of 2.40 km each in length, when powering the 1.5 kW motors.

5.2 The battery management system (BMS)

Selection of the BMS came down to two options, namely the BQ77PL900 which can perform top of the battery pack balancing during charging. It also provides battery pack monitoring features for protection, health and SOC monitoring (Appendix D).

The other option of BMS was the BQ769X0 which supports all of the same functions as the B77PL900.

However one version can support up to fifteen cells and all versions provide more accurate pack current and cell voltage measurements than the BQ77PL900 (Texas Instruments, 2013).

Both required hosting a microcontroller unit (MCU) and an Inter-Integrated circuit (I²C) multiplexer to operate in parallel with other modules. This was required in order to support sets of parallel cells. The BQ77910AEVM and the BQ77PL900 both have stand-alone features but the BQ77PL900 was more suited for communicating with a MCU (Texas Instruments, 2013).

The BQ77PL900 is a system available intended to provide self-contained active balancing, overcharge and undercharge prevention on the Lithium battery pack. The control registers in the internal electrically erasable programmable read-only memory EEPROM were programmed with the threshold values that would trigger the internal FET drive controlling the charge or discharge cycles of the battery. The evaluation module mainly consists of the BQ77PL900 IC that operated in stand-alone mode or controlled by a host microcontroller using the IC's analogue front end. Two paired high current FET's located at the pack side are dedicated for charging and discharging and driven ON or OFF accordingly to an unsafe condition (Texas Instruments, 2013).

The BQ77PL900 (BQ) was also selected because of its availability and suitability for monitoring and balancing ten series cells. An evaluation module from Texas Instruments required some repairs. It had a damaged reverse voltage protection diode which resulted in a failure during initial testing with a power supply. The primary IC in the BQ was replaced along with several other passive components (Shell, 2017).

Initially also, the resistor R5 in the board's input was soldered into the BQ due to its prior inexistence which made impossible to fully connect the ten series cell battery pack available. A damaged resistor R1 was generating a permanent overcharge condition monitored using the XALERT pin which was also replaced.

The BQ77910AEVM was selected due to cost constraints of the project and will be implemented in order to monitor and protect the batteries. Each integrated circuit in the BQ77910AEVM provides protection and monitoring of up to ten cells. To monitor all the cells for the EV, four modules were required to operate in parallel. The reason for selecting this BMS was mainly because of the cost of the unit and also the fact that it could monitor ten cells at a time (Texas Instruments, 2013). The expected efficiency of the BQ77910AEVM was above ninety percent.

5.2.1 Setup procedure

The BQ77PL900 BMS was programmed using the EV2300 driver that uses I²C communication protocol to interface the board to Windows based software. This method allowed setting up the IC protection limits and assessing the overall functionality of the BQ board.

A 63 A circuit breaker and fuses were installed to the battery pack as an extra precautionary measure. Once the fuses and circuit breaker were in place and operational, a “load” was then connected to the BQ board using the circuit breaker with the current off to prevent arcing or transients that could potentially emerge during connectivity. A heat sink was also installed to prevent damaging temperatures imposed on the FET’s if the enclosed thermal sensor that is set to trip at sixty degrees, failed to respond.

The input to the board consisted of the Lithium-Ion battery pack and load banks to simulate normal load conditions. Heavy gauge wires were also used for the high current connections and the wires were positioned as close as possible to minimize inductance. On-board shunts were used to set cell count to ten in series and set to 5 V for the logic level voltage for EEPROM programming. The configuration used during tests is shown in Figure 5-10 (Texas instruments, 2008).

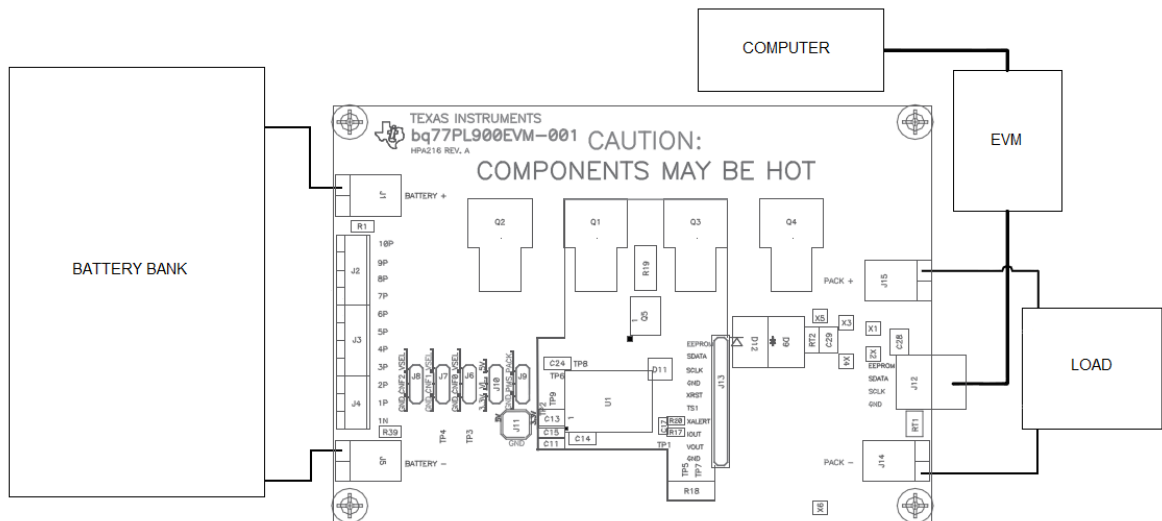


Figure 5-10: Hardware connections to the BMS

Additionally, the following procedure should be followed to connect the cells to the board.

- The cells should be connected in order from the lowest to the highest voltage rated starting by connecting the lowest cell negative terminal to the EVM BATTERY- terminal.

- Each cell should then be connected in ascending order, taking their voltage level into consideration.
- The most positive cell or the cell with the highest voltage should only be connected to the module's Battery+ terminal last after all the cells with the lower voltages have being connected.
- To disconnect the board from the pack, the cells should be disconnected from the highest voltage rated cell to the lowest rated voltage cell i.e. they must be disconnected in reverse order.

5.2.2 Software configuration initialization

I²C communication was established between the IC and the electric vehicle motor (EVM) module when $V_{STARTUP}$ was applied to the battery pack, causing the BQ device to wake up in standalone mode. This connection was provided by a toggle switch to prevent the FET's from being bypassed by a resistor while an enabled load was connected to the output of the BQ board ("PACK" terminals), which caused a current to flow through the resistor causing a short circuit, thereby disabling this part.

This start up voltage enabled the regulators "REG 1" and "REG 2" to power the IC and external circuitry. Once the operation of those regulators were stable, the power source was switched to "BAT" as long as the "BATTERY" voltage was within operating range, which is from 7 V to 50 V (Texas instruments, 2018). If the battery input was below this range the IC did not operate until a charger was applied at the "PACK" terminals. If the voltage at the regulators fell the IC FET's and all controllable functions were disabled. The EVM module gave access to the IC addressable registers, that provided status, control and configuration information for the protection system. Table 5-3 is a table of the BMS addressable registers (Texas instruments, 2018).

Table 5-3: BQ77PL900 addressable registers

Name	R/W	Description
Status	R	Status Register
Output control	R/W	Output pin control from system host and external pin
State control	R/W	State control from system host
Function control	R/W	Function control from system host and external pin
Cell Balance	R/W	Battery cell selection for balancing

Cell_Sel	R/W	Battery cell selection for balancing and voltage monitoring
OV_CFG	R/W	Overvoltage level register
UV_Level	R/W	Undervoltage level register
OCDelay	R/W	Delay time register

The registers were accessed in the registers tab of the module (Texas instruments, 2018).



Figure 5-11: Interface of addressable registers (Texas instruments, 2018).

5.2.3 Setup of overvoltage and under voltage settings

To adjust the detection voltages, the variables were written into the “OV_CFG” and “UV_Level” registers. A “CHG FET” and “DSG FET” in standalone mode was controlled by these registers which switched on and off by a fixed algorithm and the overall protection system operated as summarized in Figure 5-12 (Texas Instruments, 2009).

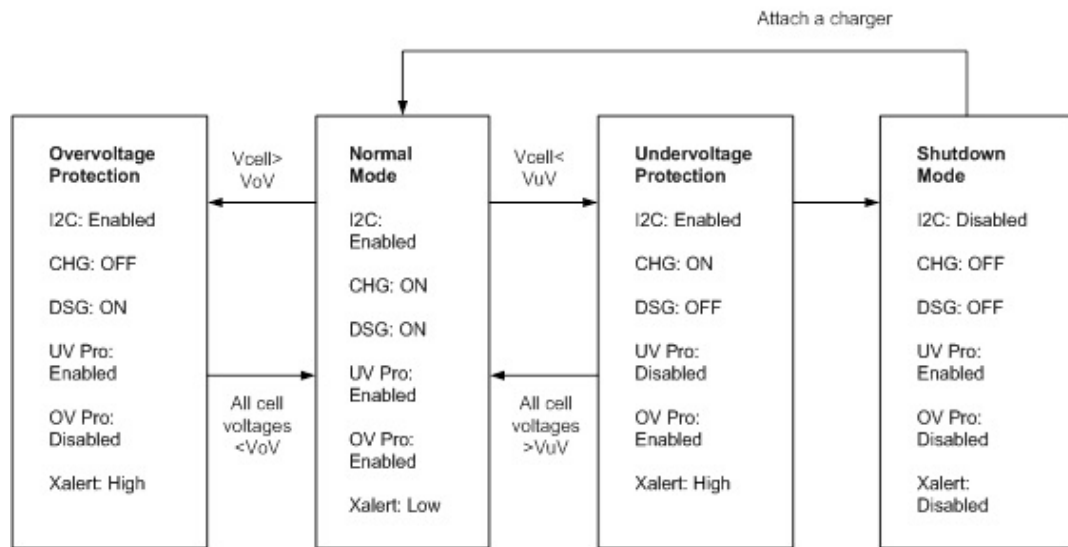


Figure 5-12: A safety overview in standalone mode

The IC monitored the voltage difference between the “Pack +” and “BAT”. If a difference higher than 0.4 V (typical) was detected the IC interpreted that a charger was connected. In obtaining battery information without an external microcontroller the operation mode was switched by “STATE_CONTROL [HOST]”. In this mode the IC still detected thresholds limits but recovery control was obtained by writing the command into the “CONTROL” register. The “XAlert” pin notified an external circuitry of an alert condition (Texas Instruments, 2009).

5.2.4 Cell balancing

The “CBEN” bit in the “OCDELAY” register was set to “1” to enable the IC’s bypass balancing method, a fixed algorithm which enables a NMOS switch across a cell thus providing a bypass path for a charging current from a cell that has reached the overvoltage threshold.

The operation worked as described in the following figures. The balancing was accomplished by opening a bypass path around the cell which reached overvoltage status (the BQ contains internal cell balancing FET’s). The bypass path included two resistors and dissipated power until the cell was within a safe range (V_{max}) minus hysteresis voltage. This is shown in Figure 5-13.

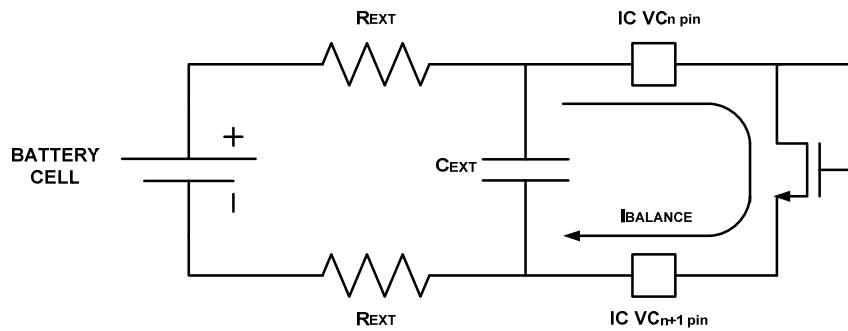


Figure 5-13: The configuration of a cell when balancing with the internal NMOS activated

During testing it was found that utilizing the internal FET's with the default external resistor values, resulted in extremely slow balancing. This was sufficient for normal usage; however, initially the cells were severely unbalanced due to their varied origins (some had been in storage in a fridge while others were in use by previous students). In providing a balanced starting point an external passive balancing connector was made up utilizing 1 Ω resistors, connecting two stacks of ten series cells in a "2P10S" configuration (the connections between parallel cells was the resistors) (Texas Instruments, 2009).

Figure 5-13 and Figure 5-14 show the cell configuration, when balancing of a cell was enabled and disabled.

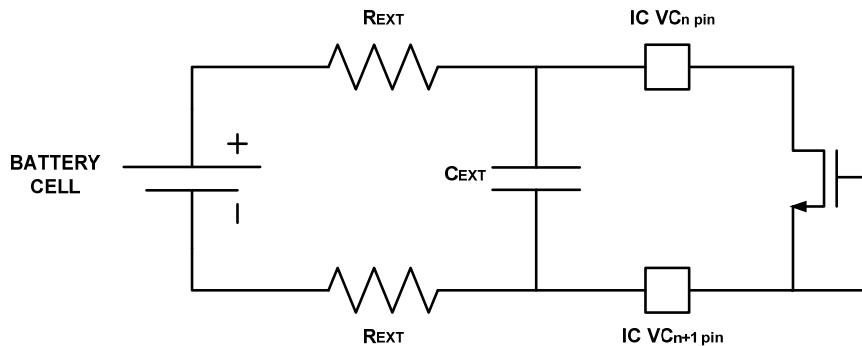


Figure 5-14: The configuration of a cell when not balancing with the internal NMOS deactivated

It is recommended that the values of 500 Ω and 0,1 μF are used for "R_{ext}" and "C_{ext}", to provide the amount of voltage necessary to activate the FET's and limit the balancing switch. Cell balancing lasted approximately 50 ms, within which 10 ms were used to monitor the voltage of the cell and the remaining 40 ms of the period in providing a bypass path.

Figure 5-15 and Figure 5-16 shows how external FET's were connected to the BQ with lower value resistors in enabling higher balancing current (Texas Instruments, 2009).

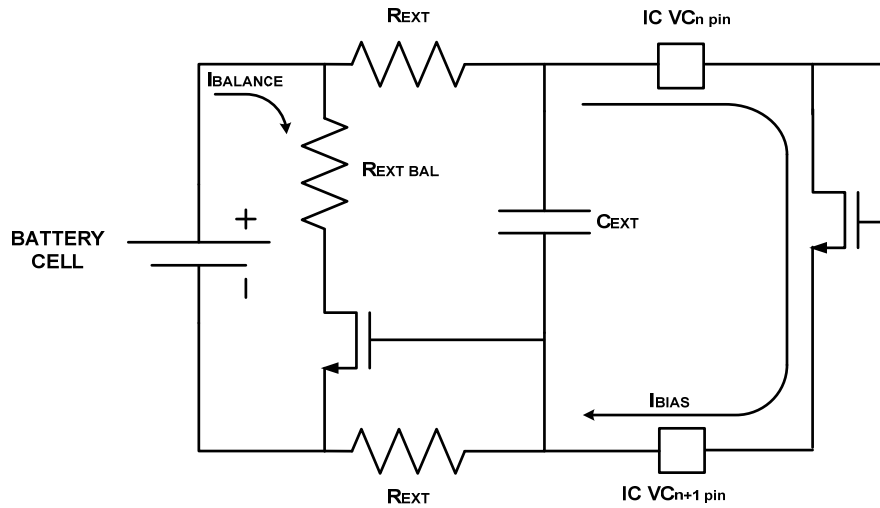


Figure 5-15: The configuration of a cell with external balancing and the internal NMOS activated

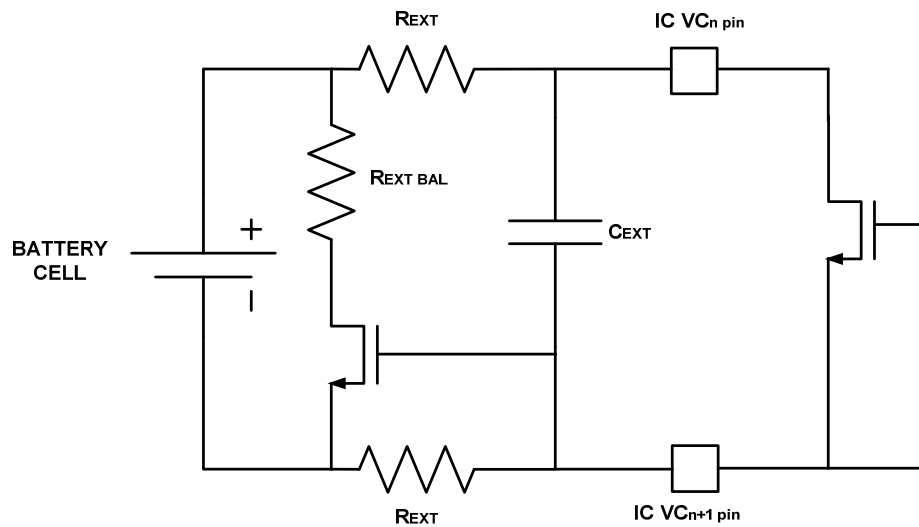


Figure 5-16: The configuration of a cell with external balancing and the internal NMOS deactivated

For the overall test procedure, the BMS voltage threshold limits were set to:

- Cell over voltage level: 4.15 V
- Cell under-voltage level: 1.40 V

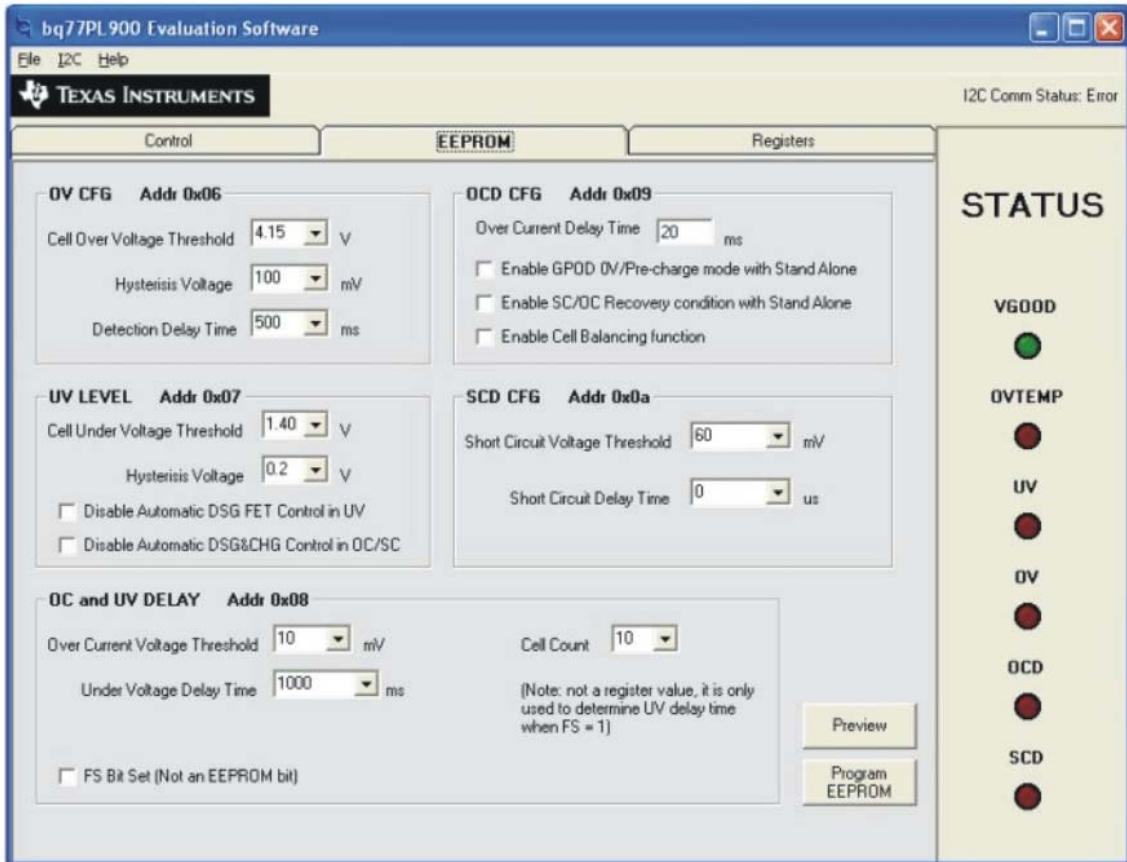


Figure 5-17: Setting up of cell overvoltage and under-voltage threshold limits (Texas instruments, 2018).

To test the overall functionality of the BMS, the battery bank was subsequently charged at no load to the limits established, so that the under-voltage (UV) and overvoltage (OV) indicators as well as the response were observed. The results obtained will be discussed in detail in Chapter 8.

Chapter Six

The EV display panel and user interface design

6.1 Microcontrollers interface

6.1.1 Arduino

Arduino is a relatively inexpensive board based on the Atmega eight-bit microcontroller, with features such as native I/O analogue commands that adds simplicity in developing code to interface with a variety of sensors and chips. Also there are a large number of compatible boards that can provide extra functionality to the microcontroller thus facilitating easy redevelopment or upgrades on the hardware controlled. Most MCU's are equipped with six analogue input channels and thirteen digital pins although some versions support eight to sixteen analogue pins and twenty to fifty three digital pins. The board responds well in battery powered circuits not being susceptible to abrupt power shortage but it is limited in terms of peripheral interfaces and associated high speed processors to provide capabilities for more elaborated HMI functionalities (Banzi & Shiloh, 2014)

6.1.2 Raspberry pi

Raspberry pi is a general-purpose computer based on Linux operating system, supporting two USB ports, connecting wirelessly to the internet, multitasking and functioning as a personal computer, although supporting forty general purpose input and/or output pins. It is best suitable for software applications; to use features like reading an analogue sensor requires additional hardware and development of code libraries. Also it requires a proper shutdown to avoid damage of its setup making it unsuitable to use in battery powered circuits (Monk, 2016).

6.1.3 Microchip

Upgrades can become a challenge using a device from the Microchip's bewilderingly large line of programmable interface controller (PIC) microcontrollers' given the fact that the architecture between line changes considerably (Barnett, et al., 2004).

6.1.4 Selection of microcontroller

For this application the Arduino will be used given the simplicity provided by the board and possibilities of implementing easier upgrades for the vehicle (Banzi & Shiloh, 2014).

An "Arduino Uno" (MCU1) and the "MEGA" (MCU2) were powered using an LM317 that regulated the voltage from the battery pack to 5 V and provided enough current to supply the MCU's and the dashboard.

The “Arduino Uno” interfaced with a temperature sensor and a power sensor that was built using a shunt current sensor and a voltage divider. The digital fault flag “XALERT”, from the BMS that alerted the host if the BMS exited the normal operational mode, was monitored by the “UNO”, and the processed data results were displayed by the “MEGA” (Mantech, 2010) (Arduino, 2017).

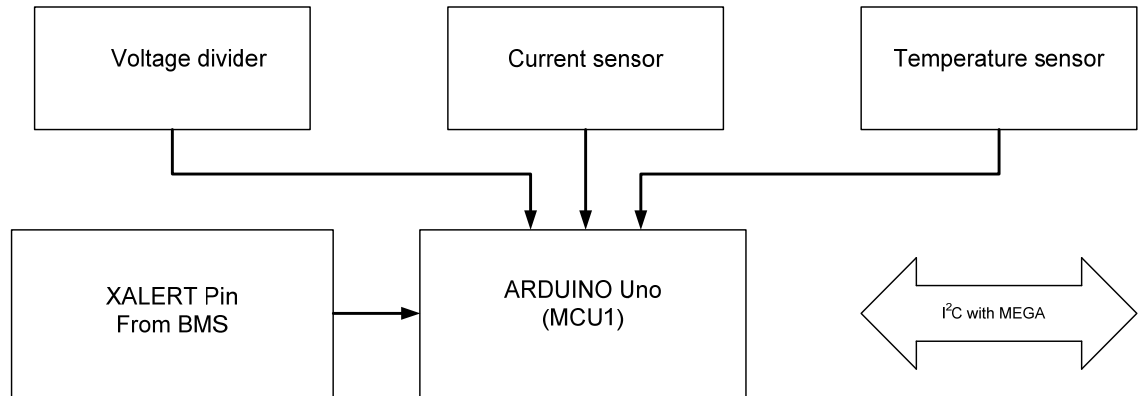


Figure 6-1: Arduino Uno complete connectivity diagram (Mantech, 2010)

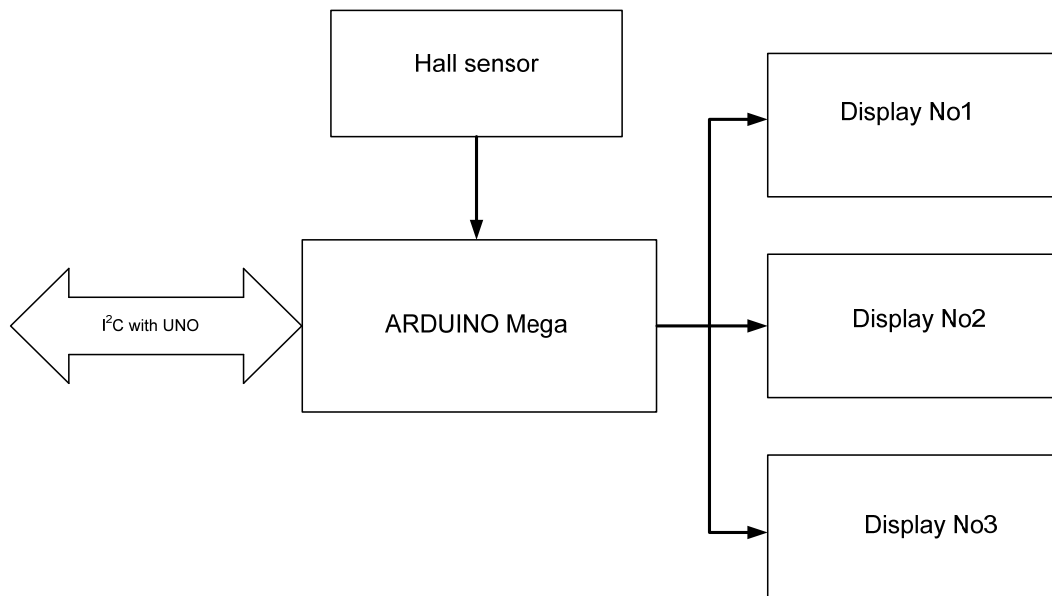


Figure 6-2: Arduino Mega complete connectivity diagram (Mantech, 2010)

6.1.5 Communication protocol

Available options included (Elahi, 2001)(Heath, 1999):

- I²C: requires two signal wires, data (SDA) and clock (SCL). The protocol allows a master to address individual slaves using a seven-bit or ten-bit address with speed ranging from slow (under 100 Kbps), fast (400 Kbps) to high (3.4 Mbps) (Elahi, 2001), (Heath, 1999).
- Serial Peripheral Interface (SPI): requires four signals, serial clock (SCL), master in slave out (MISO), master out slave in (MOSI) and an active low slave select (/SS) for each slave; unless extra I/O pins are available or space for a de-multiplexer IC is provided. The bus might not be a viable solution for low-pin count microcontrollers (Elahi, 2001) (Heath, 1999).
- Microwire: It has equivalent signals to the SPI, signal clock (SK), serial data in to master (SI) and serial data out of the master (SO). Both buses are restricted to distances no longer than half a meter, although higher lengths, approximately three meters can be achieved by adjusting bus capacitance and lower bit rates (Elahi, 2001) (Heath, 1999).
- 1-Wire: A single master asynchronous bus, allows it data wire to transfer power to slave devices with a limited speed of 16 kbps. (Elahi, 2001) (Heath, 1999).
- RS-232: It enables full-duplex communication between two receiver/transmitter pairs, the data terminal equipment (DTE) and data communication equipment (DCE). A driver/receiver IC or equivalent shield is required to use this protocol with an Arduino board (Elahi, 2001) (Heath, 1999).

A comparison among the serial protocols discussed is summarized in Table 6-1 (Elahi, 2001):

Table 6-1: Comparison of serial protocols

Protocol	Timing clock	Type	Duplex	Maximum Speed (Kbps)	Maximum cable length	Pins Count
I ² C	Synchronous	Multi-master	Half	3400	>3 m	2
SPI	Synchronous	Multi-master	Full	>1000	1 m	3+1 ²
Microwire	Synchronous	Master/slave	Full	>625	1 m	3+1
1-wire	Asynchronous	Master/slave	Half	16	1 m	1
RS-232	Asynchronous	Peer	Full	20	>9 m	2 to 4

Other communication protocols include:

- Can Protocol (Controller Area Network): It is the standard for commercial vehicles, however it requires additional shield like the Multiprotocol Radio shield to enable its usage with the Arduino (Shahan, 2015).
- Wireless communication: It is preferably implemented in situations where it is not feasible to use hardwired communication. At least two wireless modules are needed for transmission and the communication is susceptible to obstruction (Heath, 1999).

A suitable protocol for the CPUT EV should provide at least a maximum cable length capability of more than two meters, in order to cover the length of the chassis of the EV. The I²C protocol was chosen due to its clock and data pin outputs which are supported by Arduino without the need of using general I/O pins and making use of additional coding to implement the protocol.

6.1.5.1 Serial communication selection

The Arduino Uno localized in the boot communicated via I²C with an Arduino Mega localized in the header panel over a two meter RS232 port based cable that was built to interlink the systems.

In the I²C communication the Uno acted as the master by initiating the communication and sending to the slave namely the Mega, the values for the EV's performance rating, the slave, and the interfaces with a hall sensor for RPM measurements and wrote the overall data received into the dashboard. The RS232 output pins is illustrated in Figure 6-3 (Arduino, 2017)

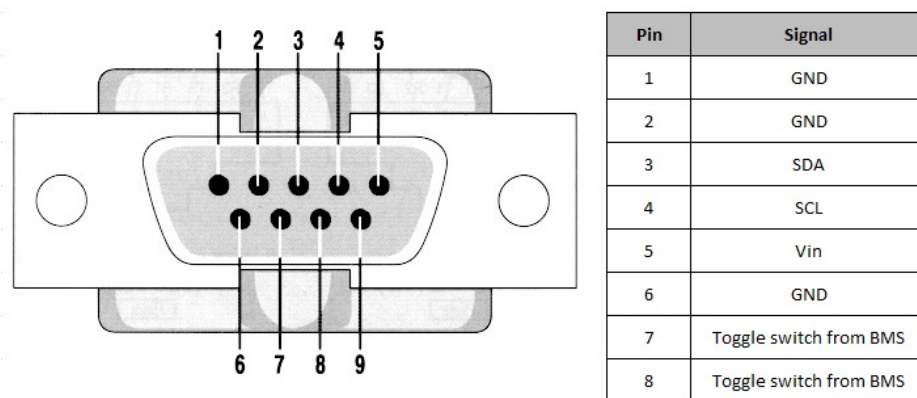


Figure 6-3: RS232 output pins interface connections

In Figure 6-4, is the interface connections when connecting the Arduino Uno via the RS232 cable to the Arduino Mega (Arduino, 2017).

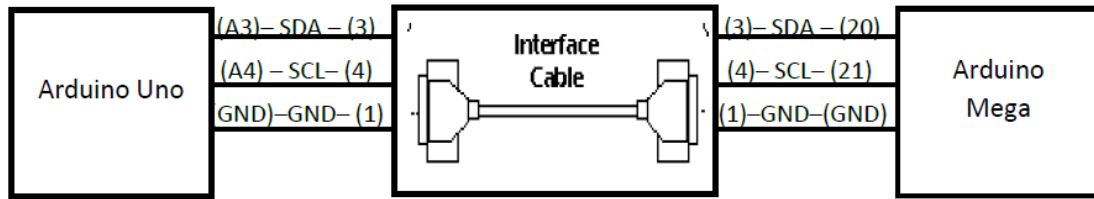


Figure 6-4: Connections between Arduino Uno and Mega via RS232 cable.

The serial data line (SDA), serial clock line (SCL) and ground (GND) from the Arduino Uno connected to the DB9 male pins 3, 4, and 1 respectively of the interface cable. The same signal from the Arduino Mega connected the female header of the interface cable to pins 3, 4 and 1. The remaining connections follow the same order logic. The toggle switch nodes from the boot connected to the start switch in the dashboard via interface cable pins 7 and 8 (Arduino, 2017).

6.1.6 Software flow charts

The battery monitoring system was done by the master; the slave performed speed measurements and controlled the operation of the dashboard by displaying the overall collected data. The flow charts describing the software utilized by Arduino Uno is described in Figure 6-5 (Arduino, 2017).

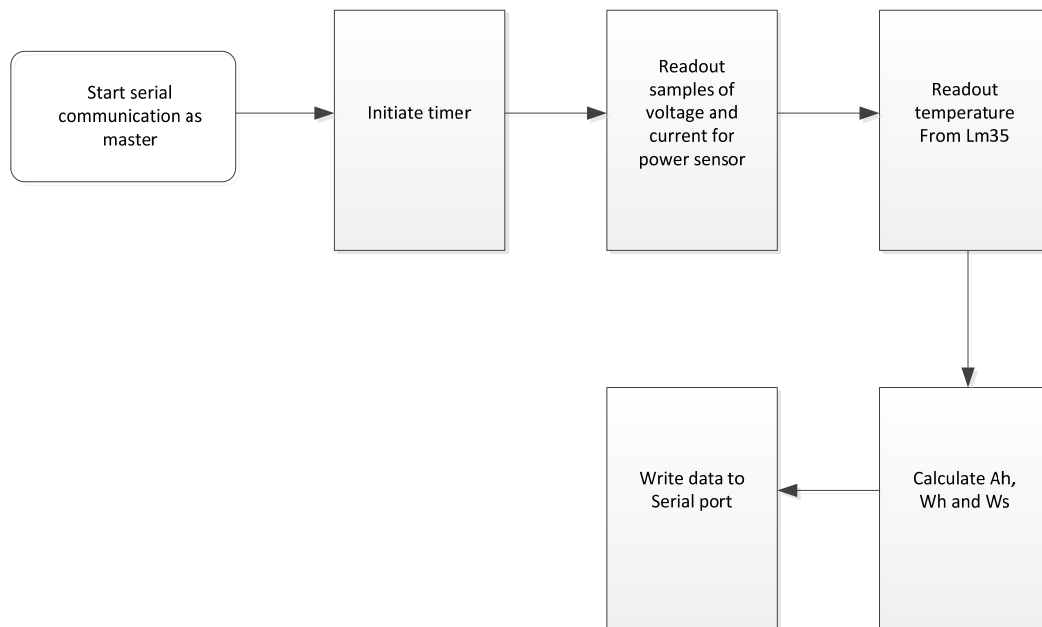


Figure 6-5: Flow chart of software for Arduino Uno

The flow charts describing the software utilized by Arduino Mega, the slave device is described in Figure 6-6 (Arduino, 2017) and are high level flow diagrams.

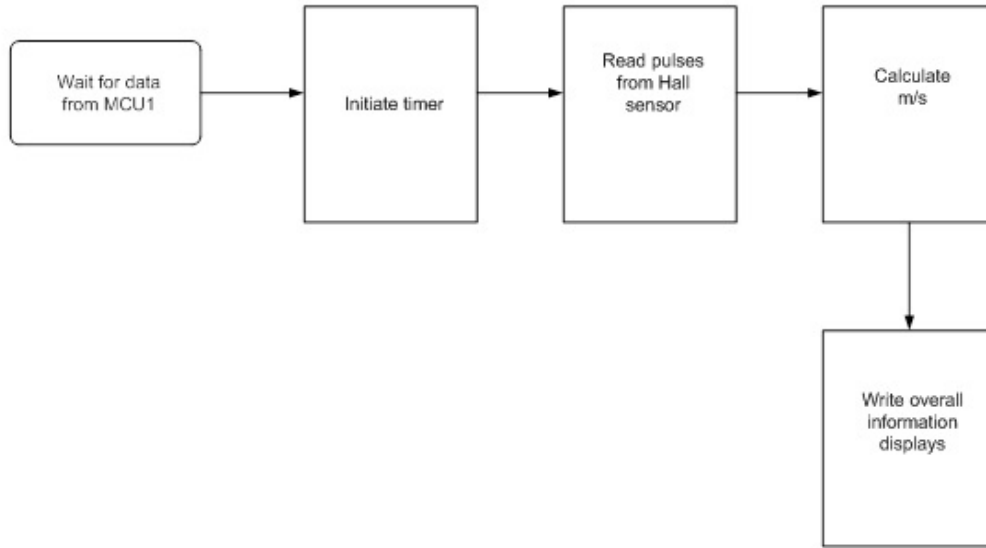


Figure 6-6: Flow chart for slave device

6.1.7 Sensors

Arduino compatible sensors were used to provide the EV's driver with the following information.

- The power rating of the battery pack in terms of ampere-hours (Ah), watts-hours (Wh) and Energy (Ws)
- The temperature of the Lithium battery bank.
- The speed of the EV throughout the race.

There are five basic sensors required for the EV in providing the driver with information needed. They are namely power monitoring sensors, current sensors, voltage sensors, temperature sensors and angular velocity (speed) sensors. These are all essential sensors and the following characteristics were looked at before selection of the sensors occurred (Erjavec, 2012).

6.1.7.1 Power monitoring sensors

To obtain the values of power and state of charge of the battery, a power sensor was built using voltage and current measurements from the battery pack.

6.1.7.2 Current sensors

Some current sensing techniques are:

- Current Shunt: Measures the voltage drop across a low value, high precision sense resistor between the battery and the load and causes power loss, heats up the battery and has a lower accuracy in low currents and also require additional isolation amplifiers (Bartelt, 2006).
- Hall Effect transducers: These transducers provide good accuracy over the entire range of measurement while preventing drift in high side current measurements. Also they do not require electrical isolation techniques (Bartelt, 2006).
- Current Transformers: These transformers can only measure AC currents, saturating in the presence of DC components on AC currents. Larger current sensors are bulky when compared to Hall sensors with the same range (Scrosati, et al., 2015) (Bartelt, 2006).

The current sensor incorporated in the EV consists of a breakout board based on the Hall Effect, being a ACS758 current sensor. This sensor is capable of measuring AC or DC currents outputting a precise voltage that is proportional to the current measured. This sensor was chosen due to its ability of providing highly reliable measurements, a wide current range and a high isolation from the electrically conductive paths and the signal leads. Additional characteristics of the ACS758 and the setting of the device in the system can be viewed in Table 6-2 (Allegro MicroSystems, Inc., 2010).

Table 6-2: ACS758 current sensor (Allegro MicroSystems, Inc., 2010).

Cost	R350
Supply Voltage	3 V to 5.5 V
Supply Current	10 mA to 13.5 mA
Operational Temperature	-40 °C to 150 °C
Current Directionality	Bidirectional
Current Measuring Range	-50 A to 50 A
Sensitivity	40 mV/A
Primary Conductor Resistance	100 $\mu\Omega$
Full Scale Nonlinearity	-1% to 1%
Full scale Total Output Error	2%

The setting of the ACS758 current sensor is described in the block diagram in Figure 6-7.

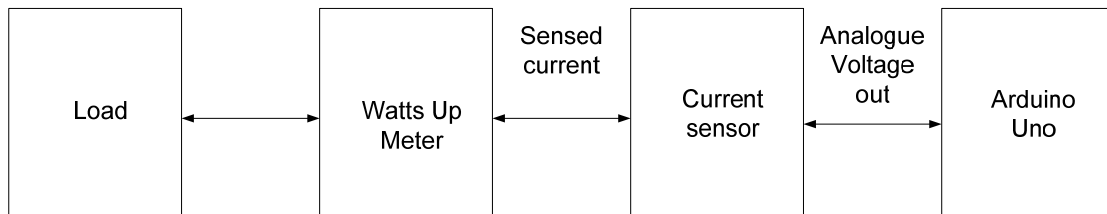


Figure 6-7: Block diagram of current sensing

The voltage from the V_{OUT} pin of the ACS758 was translated into a current using the analogue to digital converter of the Arduino UNO (License, 2017) (DFRobot, 2017).

$$\text{AnalogRead}[\text{index}] = (\text{AnalogRead}[\text{index}] - 510) * 5 / 1024 / 0.04 - \text{offsetValue} \quad (43)$$

Equation 43 describes the conversion of the varying output voltage of the sensor from analogue 0 V to 5 V to a digital value from 0 to 1023 for an accurate reference point (0 A). At no input the measured offset value at first measurement was used instead of the predetermined value on the datasheet (DFRobot, 2017).

The sensor was tested using load banks with a parallel current combination capable of 20 A. The results processed by the MCU was calibrated against a commercial E-bike power meter and the obtained data initially was viewed using the built in serial port viewer in Arduino IDE.

The percentage error against the standard was calculated using equation 44 (Wilson & Hernandez-Hall, 2015):

$$\text{Error} = \frac{\text{Measured value} - \text{Standard value}}{\text{Standard value}} \times 100\% \quad (44)$$

The overall linear relationship described is summarized in Figure 6-8.

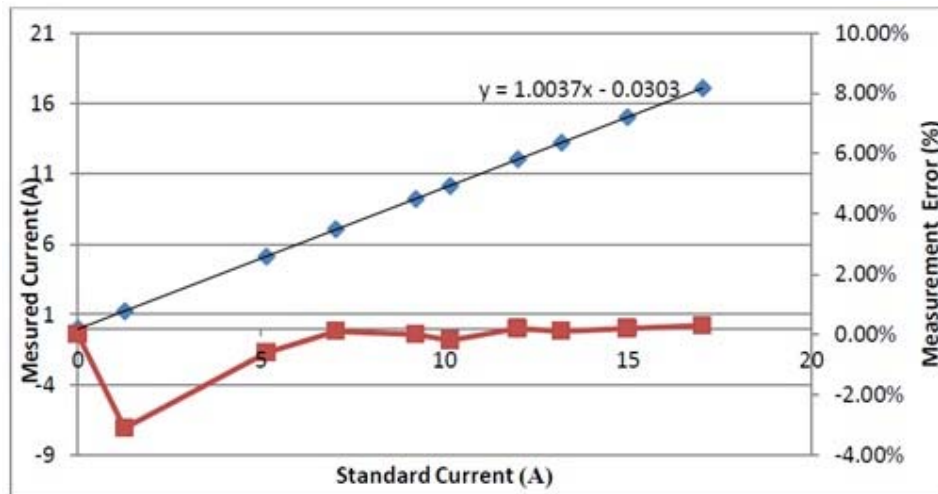


Figure 6-8: Linearity relationship of calibrated data and standard current value

The results obtained were linear to the standard measurement instrument chosen and a maximum error of 3.14 % was measured over the full measurement range. The complete results are described in the Appendix H.

6.1.7.3 Voltage sensors

A voltage divider was used to provide 5 V at 42 V battery voltages according to the battery operational limits. The device was calibrated using a laboratory power supply. The method used to calculate the error in the current sensor γ was applied to the sample obtained.

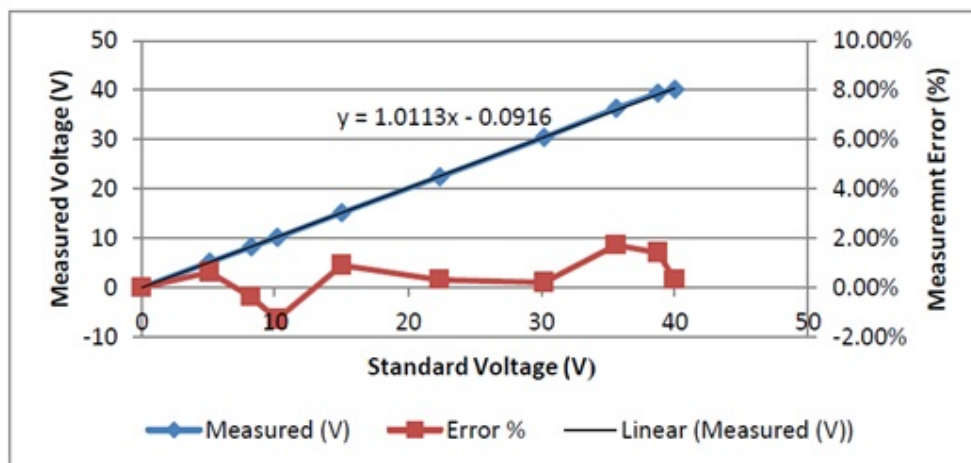


Figure 6-9: Data obtained from voltage meter evaluation

Figure 6-9 shows a linear response from the calibrated meter with a maximum error less than 2 % over the full range of measurement. The complete sampling is attached in Appendix H of this document.

6.1.7.4 Temperature sensors

There are many temperature sensors available on the market. Due to cost and availability, the following temperature sensors were evaluated and their features are tabulated (National Semiconductor, 2000), (Maxim Integrated, 2016):

Table 6-3: Comparison of different temperature sensors

	LM35	DS18B20+	100k NTC
Interface type	Analogue	Digital	Analog
Requirements	Vcc, Gnd, ADC	One MCU pin, Gnd (Vcc not required)	Vcc, Gnd, resistors, ADC.
Accuracy	±0.5 °C and dependent on ADC	±0.5 °C	Dependent on ADC and amplifiers
Resolution	Dependent on ADC	User selectable from 9 to 12 bits	Dependent on ADC
Cost (including measurement electronics)	Medium	Low	High

The sensors discussed can measure the desired range to be monitored but the LM35 was chosen given the fact that it featured the need of using the microcontroller I²C port that was intended for the communication protocol.

The LM35 was used to monitor the battery pack temperature calibrated directly in Celsius. It did not require external calibration to provide typical accuracies of ± ¼ °C to ± ¾ °C, over a full range from -55 °C to 150 °C. The output voltage from the sensor was linearly proportional to the centigrade temperature with a 10 mV scale factor; the conversion using the MCU1 was done in this section of the code (Texas Instruments, 2016):

$$Temperature = \frac{\frac{(float \times Analogue\ Read\ (Output\ Lm35) \times 5)}{1023}}{0.01} \quad (45)$$

6.1.7.5 Speed sensors

Optical sensors were used for speed detection by having features on a rotating target either interrupt or reflect a beam of light passing from an emitter (LED or laser) to a detector (phototransistor). They exist over a wide spectrum of forms and prices (Ramsden, 2006).

Variable reluctance sensors operate magnetically and consist of a coil of wire wound around a magnet. As ferrous targets pass the face of the sensor, they induce flux changes within the magnet, which are then converted into a voltage in the coil. They have the advantage of being inexpensive and rugged (Ramsden, 2006).

Inductive proximity sensors are also known as eddy-current killed oscillator sensors. These sensors work by sustaining an oscillation in a high-Q LC circuit formed from a capacitor and sensing inductor. The magnetic flux from the sensing inductor is allowed to pass to the outside of the sensor, through a detecting surface. When a conductive target is brought near the detecting surface, it absorbs energy from the magnetic field and damps the oscillation. Subsequent circuitry then reports target presence or absence based on the status of the oscillation. Table 6-4 summarizes a few of the advantages and disadvantages of each of these technologies (Ramsden, 2006).

Table 6-4: Speed sensing technology comparison

Technology	Advantages	Disadvantages
Optical	Fine spatial resolution. Inexpensive. Very fast (>100 kHz) Digital output.	Susceptible to contamination. Limited temperature range.
Variable reluctance	Inexpensive. Hot, dirty environments. Fast (>10 kHz)	Requires ferrous targets. Minimum sensing speed. Additional signal processing needed.
Inductive proximity	Hot, dirty environments. Non-ferrous metal targets. Digital outputs.	Slow (<1 kHz) Low spatial resolution.

Typical speed sensing devices are simple to use, reliable and inexpensive (Martínez, et al., 2013).

- Revolutions per minute (RPM) sensors: These devices send speed data as electrical pulses without direct contact. Once positioned near a moving device, the generated pulse is then fed into a digital counter depending on the processing device. Mechanisms include shaft encoders with a resolution of 1-5000 pulses per revolution; proximity sensors that provide low to medium resolution (which is dependent on the number of pulses measured per revolutions); magnetic rotational speed motor (proximity type) offering a range between 0 to 30000 rpm; and photoelectric sensors (Martínez, et al., 2013).

- Tachometers: Measure rotational or surface speed with resolutions ranging between 20 to 20000 rpm. Mechanical and optical versions allow the measurement to be done with or without contact with the rotating mechanism (Martínez, et al., 2013).

The speed monitoring of the project was done using an RPM sensor so that its result could be easily displayed in the vehicle dashboard and enable easier upgrades, if required. For determining angular velocity, three options of sensors were looked at in industry. They were namely an analogue voltage generator sensor, a digital Hall Effect sensor and a digital optical sensor (Hatch, 2016). The Hall Effect sensor was selected because it is non-contact and can be implemented with the addition of a small magnet on the motor's shaft (Hatch, 2016).

A speedometer was built using an LM393 Hall Effect sensor. The non-latching device generated an output "LOW" when a magnet was attached in the frame of the wheel of the vehicle and an output "HIGH" whenever the magnet was pulled away from the frame of the wheel of the vehicle.

The number of times that the sensor detected the magnet was fed into a counter, pulsed, and the time was obtained from adjusting an existing Arduino function that counted milliseconds. The formula below was used to calculate the rotational speed of the vehicle (Beaty & Santos, 2015).

$$rpm = \frac{3.141592654 \times 0.5 \times pulses}{time (s)} \quad (46)$$

6.2 EV Dashboard panel

The panel for the dashboard was built using a metal sheet that was drilled to fit the emergency button, an ignition switch and to secure the displays. It was the sheet to provide slots to fit the LCD displays into the panel.

6.3 User interface

The RS232 cable from the MCU1 in the "boot" of the EV was connected to the MCU2 with the Arduino Mega mounted in the back of the Dashboard of the vehicle. The board controls the operation of the LCD displays in front of the panel alongside the Hall Effect sensor connected to it. The Arduino LCD library was used to operate the LCD, but the default connections and code had to be adjusted to cater the LCD displays. Figure 6-10 shows testing of the functionality of three LCD displays with the Arduino Mega.



Figure 6-10: Testing the LCD functionality with the microcontroller

The overall connection of the LCD to the Arduino Mega and the switches to the RS232 port were soldered onto vari-board which was secured to the back of the Dashboard. On the display side of the Dashboard were mounted the following:

- An ignition switch: This was connected in parallel to an additional toggle switch in the battery enclosure. When triggered the switch connected the “BATT” terminal to the “PACK+” terminal of the BMS thereby consequently supplying the EV load.
- An Emergency button: Triggering this button disabled all electrical operations of the EV.
- LCD displays: Three 16x2 inch LCD displays were used to display the battery pack’s temperatures; speed that the motor was being driven at and overall performance rating in terms of ampere-hours, watt-hours and watt-seconds for the EV. An additional battery was added to power the LCD’s to eliminate dependency of the HMI to the BMS. The device should be replaced by low power rechargeable batteries in the future.



Figure 6-11: LCD configuration adjusted to fit into the EV dashboard

Figure 6-12 is the template for the display of the dashboard being designed for the CPU's EV.

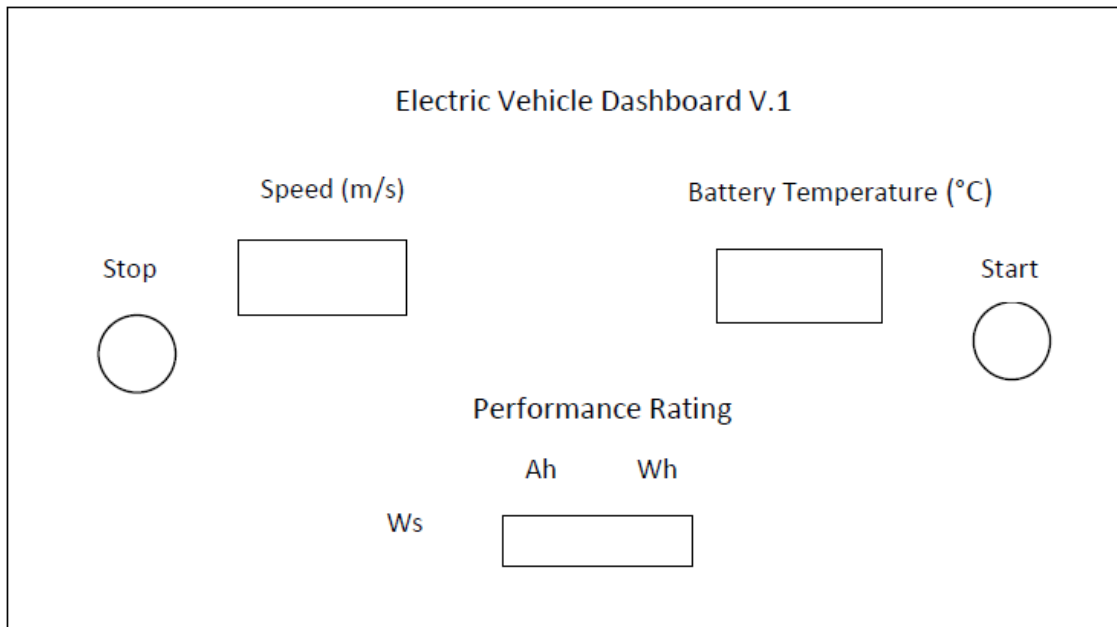


Figure 6-12: EV dashboard display template

Chapter Seven

Testing and evaluation of the EV motors and motor drive

The various tests of the EV components are concluded in chapter seven and chapter eight. Tests for the motors and motor drive are extensively examined in chapter seven and in chapter eight, the battery pack and BMS are also covered. Upon completion of these chapters, the efficiencies of each component will be determined and the overall efficiency of the EV will be calculated. A race simulation will be concluded to determine whether or not the EV will complete the race. The following research questions are particularly reviewed and answered:

- Can an efficient power train be developed for this car?
 - The motor needs to be rebuilt to comply with the Shell-eco rules without sacrificing efficiency.
 - An efficient motor drive needs to be developed.
- Can an effective power source be developed for this vehicle?
 - The battery needs to be sized to complete the race.
 - The BMS needs to comply with the competition rules.
- Will the total system:
 - Fulfil all the safety aspects of the vehicle for the competition?
 - As the chassis is not available for the EV yet, the vehicle is designed according to the safety requirements of the competition.
 - Allow the vehicle to complete the race?

7.1 Power train evaluation

In order to calculate any dynamics of the EV, it was critical to first calculate or determine the average speed of the EV to cover the entire distance of the track. From previous Europe Shell Eco-Marathons it was determined that an average speed of 25 km/h was optimal for the race to cover a track length of 1.626 km per lap (Shell, 2015). This was based on the Shell Eco-Marathon Europe race.

The first Shell Eco-Marathon South Africa was hosted in 2016 at the Zwartkop Raceway in Johannesburg and this track has a total distance of 2.40 km. This can be seen in Figure 7-1.



Figure 7-1: The Zwartkop Raceway track for the South African Shell Eco-marathon

The Zwartkops raceway is 2.40 km in length and a decision was made that an average speed of 25 km/h needs to be maintained for the CPUT EV, which would take the electric vehicle 5 minutes 46 seconds to complete a single lap. This is however assuming that the track is flat and that the weather conditions are perfect.

With an average speed of 25 km/h, the EV would require a velocity of 6.925 m/s. The EV would require an acceleration of 0.02 m/s². This would result in a climbing force of 0 N (as the track is assumed to be flat); an aerodynamic drag of 0.542 N; a rolling resistance of 26.969 N and an acceleration force of 5.44 N.

The respective power losses would be 0 W for the climbing power losses; 3.759 W for the aerodynamic power losses; 185.023 W for the rolling power and 5.44 W for the acceleration power losses. These values are all based from the theory in chapter 2 and these losses are based on one completed track length.

7.2 Motor efficiency

The purpose of this test was to determine if the off the shelf motor was successfully adapted for the CPUT EV application, and how efficient the re-wound motor was compared to the original motor. The original motor (measured) and re-wound motor (expected) efficiencies can be seen in Figure 7-2.

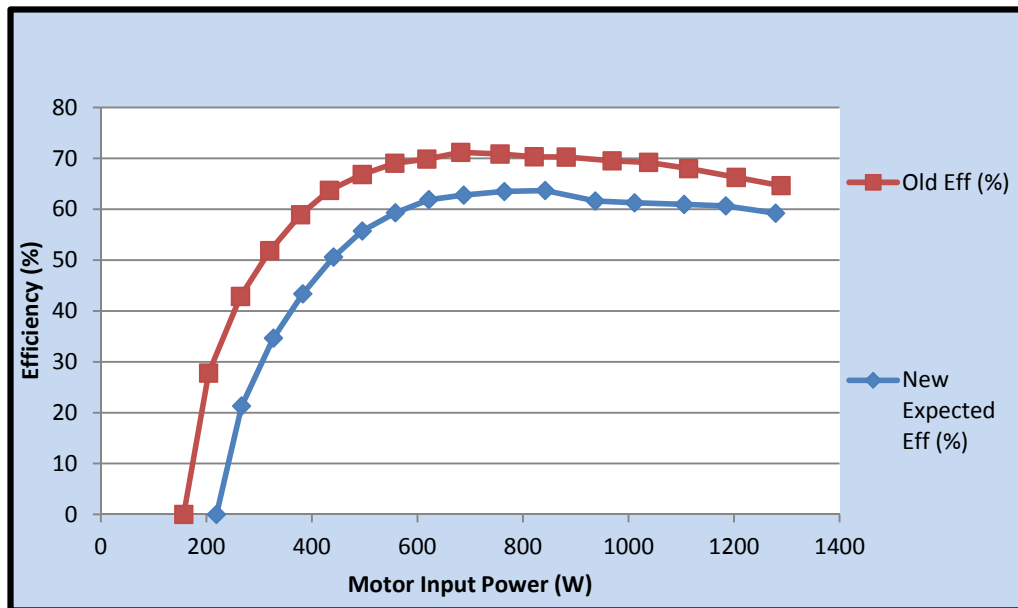


Figure 7-2: Efficiencies of the original motor (measured) and the new motor (expected)

The original motor had a peak efficiency of 71.177 %. The re-wound motor was expected to produce the same output power, but at a substantially lower input voltage (23 V as opposed to 380 V - less than a 16th of the original voltage). This means that the current increased drastically, and along with it, the copper losses should have increased as well, which subsequently would lead to a poorer efficiency. Therefore, the re-wound motor's efficiency was expected to be around 65 %. An efficiency of less than 50 % would render the motor unsuitable for this application.

7.2.1 Motor losses

In order to perform the track physics calculations, the ideal acceleration force (with no losses) was determined. This was done by assuming that two 750 W motors are used and that the EV has a maximum speed of 50 km/h. The acceleration force calculation is:

$$\begin{aligned} \text{Power (Assuming that } 2 \times 750 \text{ W motors will be used): } P &= 1.5 \text{ kW} \\ \text{Velocity (Assuming a } 50 \text{ km/h} = 13.889 \text{ m/s top speed) } v &= 13.889 \text{ m/s} \end{aligned}$$

$$P = F \times v \quad (10)$$

Therefore:
$$F = \frac{P}{v} = \frac{1500}{13.889} = 108 \text{ N}$$

The acceleration force is (Grunditz & Jansson, 2009):

$$\text{Total mass of vehicle and driver: } m = 275 \text{ kg}$$

$$\text{Acceleration force of the vehicle: } F_{acc} = 108 \text{ N}$$

$$F_{acc} = m \times a \quad (6)$$

Therefore:

$$a = \frac{F_{acc}}{m} = \frac{108}{275} = 0.3927 \text{ m/s}^2$$

7.2.2 Motor efficiency testing

The block diagram shown in Figure 7-3 graphically illustrates the test setup. Pictures of the setup can also be seen in Figure 7-4, Figure 7-5 and Figure 7-6.

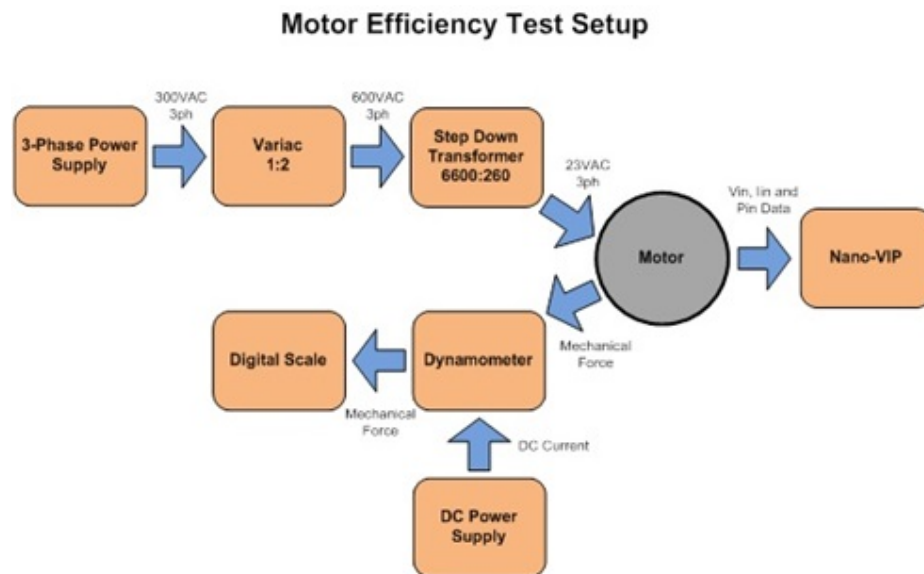


Figure 7-3: The EV motor efficiency test block diagram

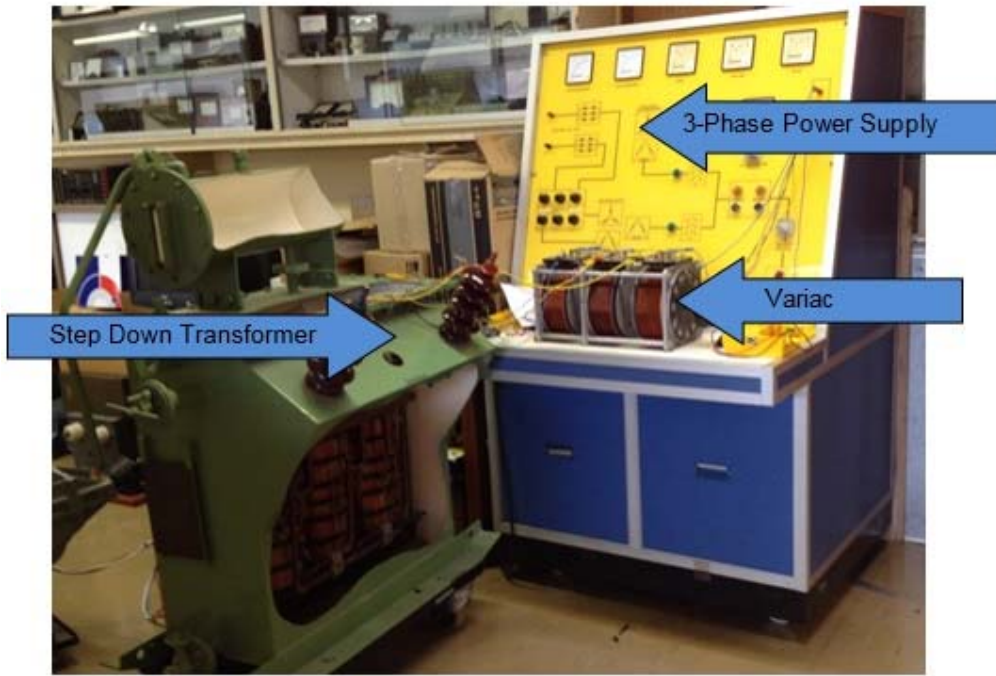


Figure 7-4: The EV motor three phase power supply

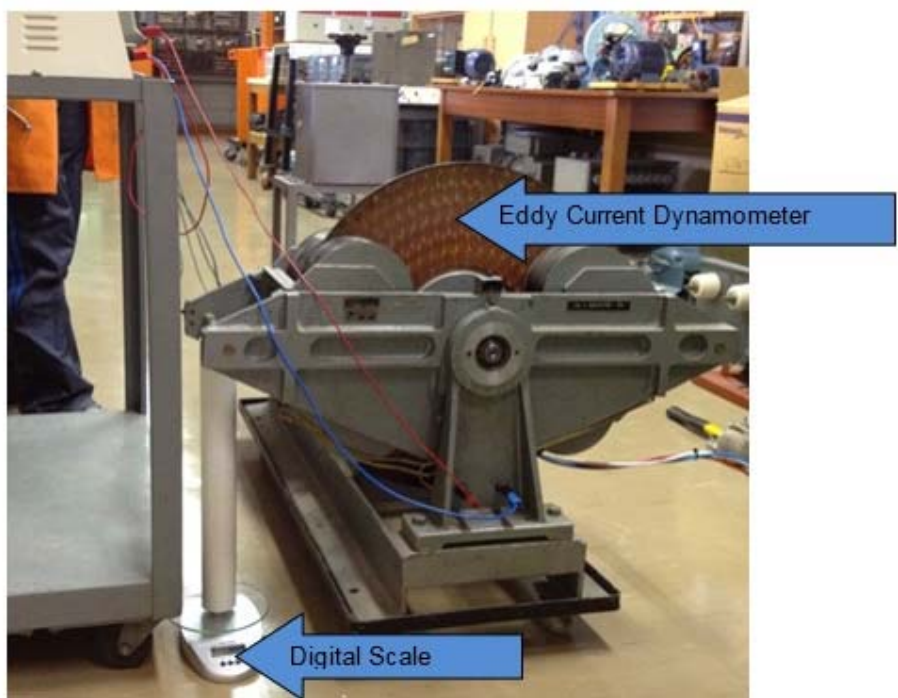


Figure 7-5: The eddy current dynamometer/brake and digital scale

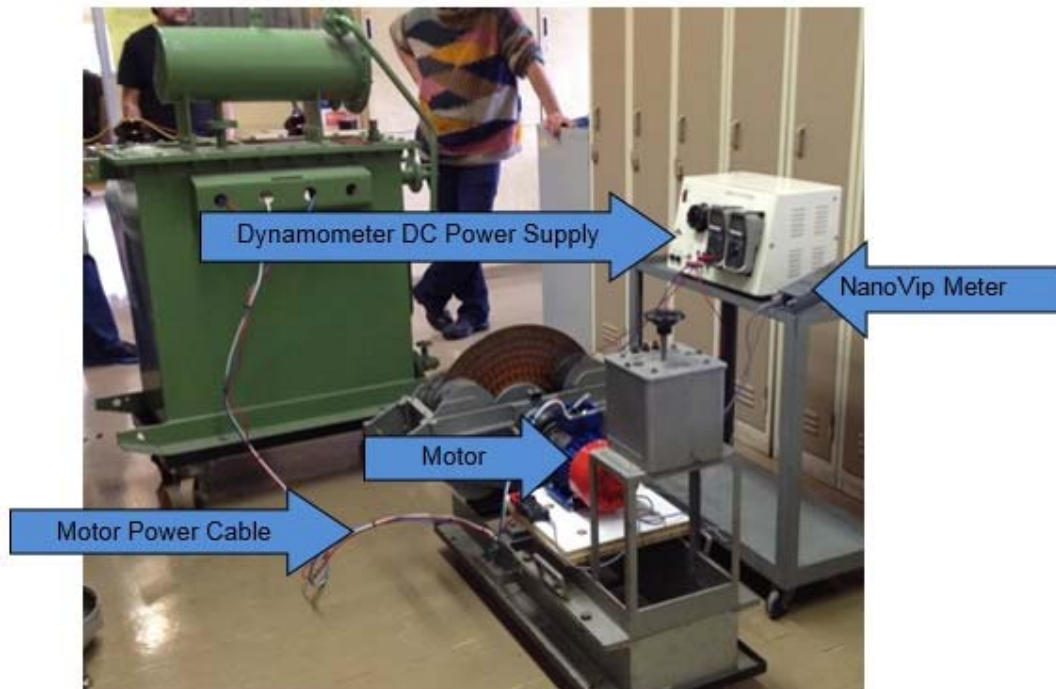


Figure 7-6: The complete test setup for the testing of the EV motor

Before the test procedure for the motor could commence a pre-test had to be done to ensure that the motor could not be damaged during the testing stage. The procedure involved for the pre-test is as follows.

- The three phase power supply was set up to produce three phase voltage of 300 V AC.
- The variable transformer (variac) was then connected to the power supply.
- The 1:2 tap setting on the transformer was selected and the output voltage of the transformer was measured giving a three phase voltage of 600 V AC.
- The variac was then connected to the step down transformer.
- The following step was to ensure that the 6600:260 tap setting was selected, so that a three phase output voltage of 23 V AC could be measured.
- The transformer was then connected to the motor terminal box, in star configuration.
- The motor was secured to the dynamometer and connected to the shaft, etc.
- On the input side of the dynamometer, the DC power supply was connected.
- The digital scale was calibrated (to ignore the mass of the dyno-scale spacer).
- The NanoVip Plus power meter was connected to the motor terminal box.

The reason for using the step down transformer is due to the fact that the CPUT Heavy Current Laboratory's three phase power supply was rated at 25 A. A current value of 35 A was required for the purpose of testing the full potential of the motor. Using the most ideal tap setting, meant an input of 600 V was required and for that reason a variac was also utilised.

After completion of the pre-testing of the motor, the testing of the motor was completed. This procedure followed the following steps.

- The three phase power supply was switched on from 0 V, 0 A.
- The input voltage was slowly increased until the motor started turning and being allowed to speed up.
- Once the motor was running at nominal speed, the input line-to-line voltage (V_{IN-L-L}), the input line-to-line current (I_{IN-L-L}) and the power factor were measured and recorded using the NanoVip power meter.
- Thereafter a DC current was injected into the dynamometer and the current was adjusted, until the desired mass was displayed on the digital scale. The DC current injected into the dynamometer, created an eddy current, which opposed the rotation of the dynamometer disc, and subsequently loaded the motor. The braking force applied to the motor caused the dynamometer axis to tilt, thereby exerting a force on the dynamometer scale spacer and thus on the scale as well. The mass component of this braking force could then be measured on the digital scale.
- Once again the input line-to-line voltage (V_{IN-L-L}), the input line-to-line current (I_{IN-L-L}) and the power factor were measured and recorded using the NanoVip power meter. The exact mass measured on the scale was also recorded.
- Steps four to five above were then repeated for weights of 0.1 kg to 1.5 kg.
- This was completed for various masses starting at 0.1 kg and going up in increments of 0.1 kg all the way to 1.5 kg.

The test results are graphically illustrated in Figure 7-7 and figure 7-8. The tabulated results are also available in Appendix G.

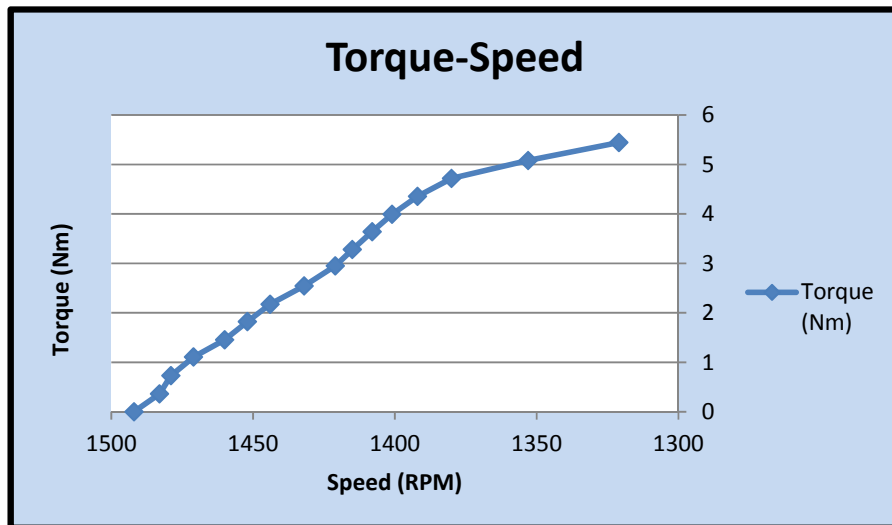


Figure 7-7: The re-wound motors torque versus speed curve

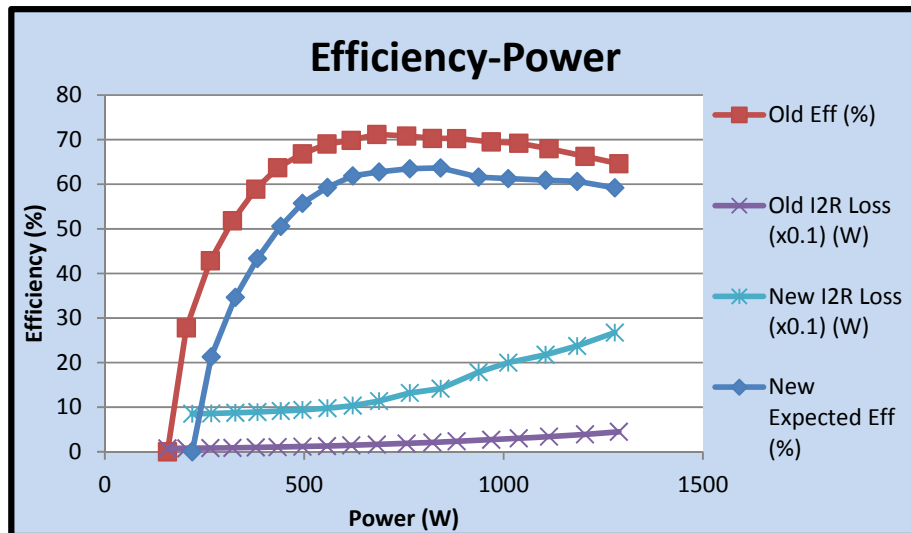


Figure 7-8: The old motor (measured), the new motor (expected), and the new motor (measured) efficiencies and I²R Losses

As can be seen in Figure 7-8, the re-wound motor has a peak efficiency of about 63 %, and the measured efficiency curve is very similar to the expected curve. The reason for the minute difference is due to the fact that the actual (measured) winding resistance was slightly more than the calculated, hence, leading to a slightly worse efficiency than expected. The rewind motor maintained an efficiency (above 50 %) from 623 W to 1.34 kW, which is ideal for the varying load (acceleration/deceleration) to be applied during the race. It can thus be concluded that the motor was successfully adapted for the application.

7.3 Motor drive testing and evaluation

7.3.1 Initial motor drive testing

The initial test needed to be completed on the motor drive was a load test. A test bench was developed (Figure 7-9) in order to determine the efficiency of the motor drive. Various measuring equipment was used. As damage to the developed battery pack might have occurred, the option of using three 12 V, 33 Ah car batteries was decided upon as a better option for testing purposes of the motor drive. These were connected in series to sum up the voltages to 36 V. The resultant energy of the source was then 36 V, 33 Ah. The power supply line of the electric vehicle power train was first passed through a 63 A circuit breaker for short circuit protection.

From the circuit breaker, the input power metering equipment were interfaced prior to the inverter. The output power metering equipment were interfaced along the power line between the inverter and the load. This was done so that the input and output power of the inverter could be measured and the efficiency calculated from these values.

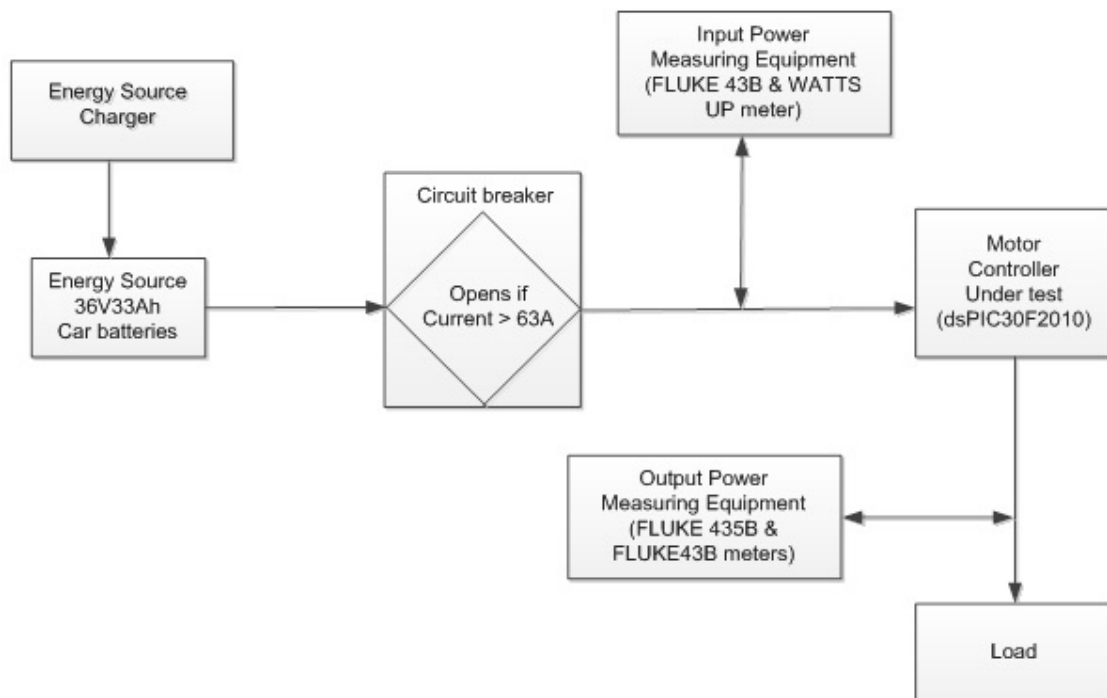


Figure 7-9: Test bench for initial load testing of dsPIC30F2010 motor controller.

On the input side of the motor controller, a decision was made to connect up a single phase Fluke 43B power analyser with data logging capabilities as well as a “Watts Up” single phase power analyser.

This was done to ensure that the measurements completed were similar to each other. The “Watts Up” meter was connected in series with the power cables by means of terminal connectors and the Fluke 43B meter was connected across the incoming power cables by means of banana sockets. A Fluke DC current clamp was clamped around the live incoming power cable and set to a 10 mV/A signal multiplication setting. The Fluke 43B was also set to the same measuring capability to ensure correct measurements. Care was taken in observing that the Fluke 80i-110s AC/DC current probe is a directional current clamp and had to be connected in the correct manner. Figure 7-10 and Figure 7-11 are of the test bench showing the meters connected to the input side of the motor drive as well as the current clamp employed and the display settings on the Fluke 43B.



Figure 7-10: The input side to the motor drive together with the metering equipment.

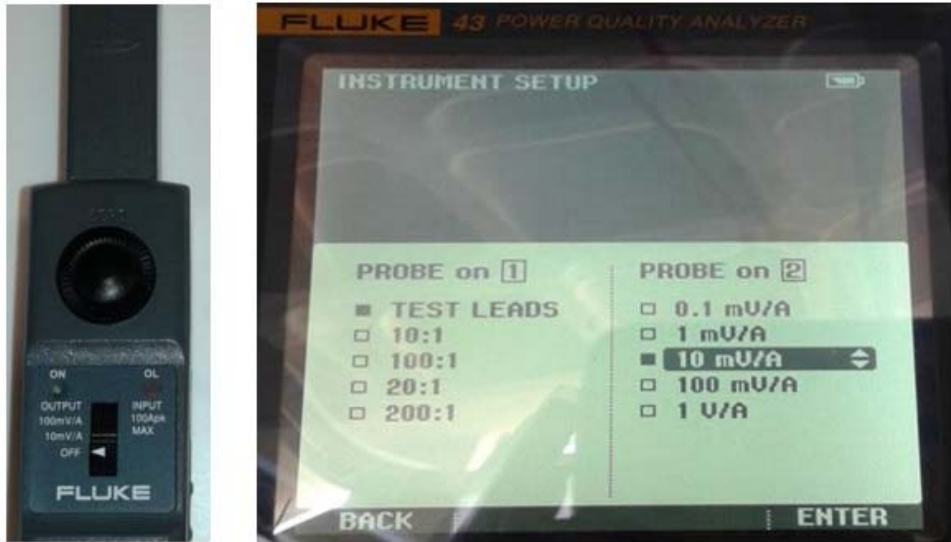


Figure 7-11: (a) The Fluke 80i-110s AC/DC current probe (b) The display of the Fluke 43B being setup correctly.

On the output side of the motor drive a three phase Fluke 435B, with data logging capabilities was connected across the three phase output terminals. The Fluke 80i-500S AC current clamps were also clamped around each of the three phase cables. This was completed so that three phase output power could be measured.

A single phase Fluke 43B was also connected across the output terminals so that the AC frequency could be monitored. This was done yet by connecting the meter's probes across any two lines of the three AC lines and a Fluke current clamp connected around the third power cable. Figure 7-12 illustrates the measuring equipment on the output side of the motor drive.



Figure 7-12: The Fluke 43B and Fluke 435B connections on the output side of the motor drive.

The current clamps incorporated for testing was the Fluke 80i-500S current clamps. These current clamps can measure up to 500 A and the power cable that went through each current clamp needed to be wound ten times around each current clamp. This was done to boost the sensitivity of the current clamps as the reading expected were quite low. This meant that the current clamps ratings were now modified to 10 mV/A. To compensate for this the Fluke 435B meter scale was set to 10 mV/A so that the correct measurement readings could take place. Figure 7-13 is a picture of the Fluke 435B being set to the correct scale.

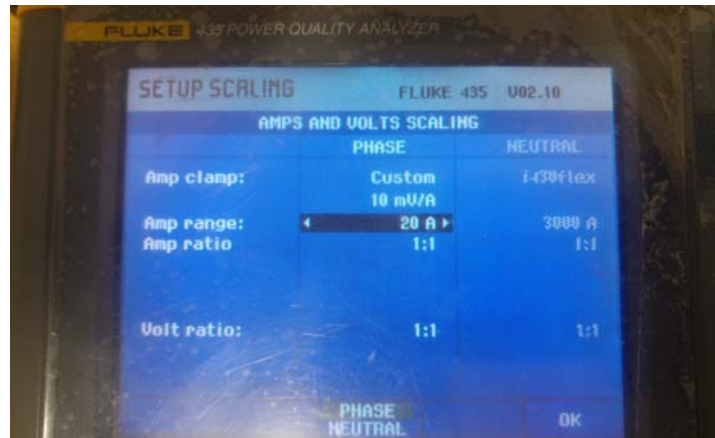


Figure 7-13: The Fluke 435B being set to 10mV/A scale.

In order to ensure that the load testing of the motor drive was successful, it was required that the initial testing of the motor drive first completed on a high-voltage resistive element bank. Figure 7-14 is a picture of the resistive element bank that was used for this initial testing purpose.



Figure 7-14: The resistive, high voltage, element bank used for initial load testing.

The motor drive inverter efficiency tests that was carried out was completed in two stages; firstly with just a 100 W and then secondly with a 600 W load. This was done this way in order to affirm the VSD's power capability.

Tremendous care was taken as serious damage could have been done to the motor drive as well as the car batteries and metering equipment.

7.3.1.1 Motor drive testing using a 100 W load

For the 100 W test, a resistive element bank containing twelve resistive elements of 52 Ω each was configured into a delta connected load of 13 Ω each per phase. In order to do so, the twelve resistive elements were grouped into three groups of four series resistive elements. Each group of series elements were connected in a parallel connection resulting in 13 Ω per phase as shown in Figure 7-15 (a). The phase resistances were then connected into a delta configuration as shown in Figure 7-15 (b).



Figure 7-15: (a) The load resistances connected in parallel. (b) The phase resistances connected in a delta configuration.

The equations and formulae to follow were used to calculate the 13 Ω per phase of the delta load (Bakshi & Bakshi, 2008):

$$P_T = \sqrt{3} \times V_L \times I_L \times \cos \phi \quad (47)$$

$$\therefore P_T = 100 \text{ W}$$

But $V_L = V_{PH} = 17.3 \text{ V}$ and $\cos \phi = 1$ (for a pure resistive load):

$$\therefore 100 \text{ W} = \sqrt{3} \times V_L \times I_L$$

But $I_L = \sqrt{3} \times I_{PH}$:

$$\therefore 100 \text{ W} = \sqrt{3} \times V_L \times (\sqrt{3} \times I_{PH})$$

$$\begin{aligned} \therefore 100 \text{ W} &= \sqrt{3} \times V_L \times \frac{V_{PH}}{R_{PH}} \\ \therefore R_{PH} &= \frac{(3 \times V_L \times V_{PH})}{100} = \frac{(3 \times 17.3 \text{ V} \times 17.3 \text{ V})}{100} \\ \therefore R_{PH} &= 8.98 \Omega \approx 8.67 \Omega = [13 \Omega // (13 \Omega + 13 \Omega)] \end{aligned}$$

For 13 Ω resistors in delta connection, the total resistance across each phase is 8.67 Ω , which is equivalent to 13 Ω in parallel to the addition of two 13 Ω resistors. A complete picture of the entire system to measure a load of 100 W can be seen in Figure 7-16.

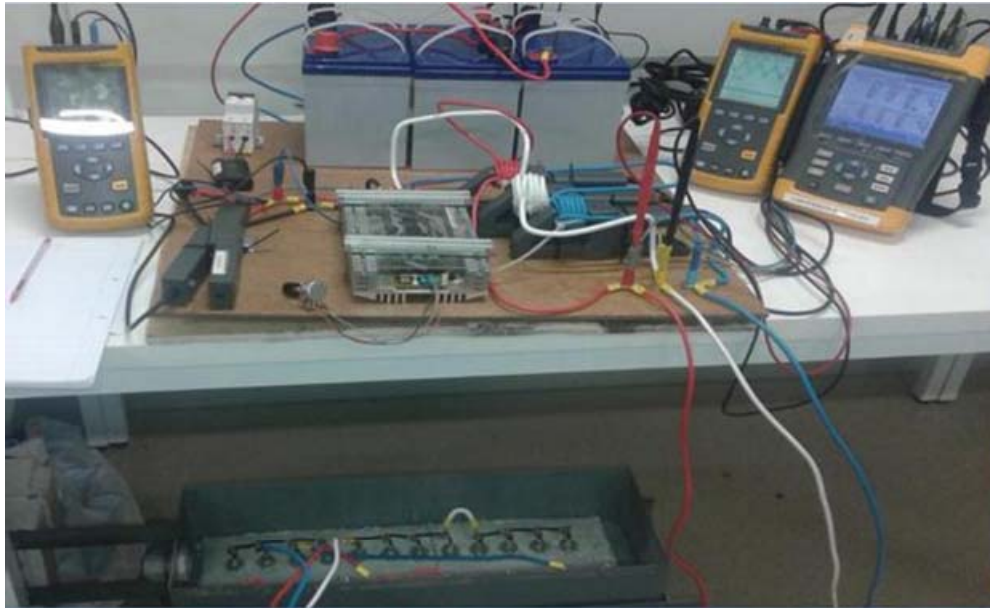


Figure 7-16: Complete test bench for the inverter to measure a 100W load.

The charged car batteries were connected directly to the inverter by switching the circuit breaker on. The inverter was then tuned by increasing its three-phase output frequency at constant intervals.

At every set frequency as monitored on the Fluke 43B, connected at the output of the inverter, the input and output voltages and currents were measured and recorded from the respective power analysers as shown in Figure 7-17. The data was then recorded and the input power was then calculated as $P = IV$ and the output power as $P_T = \sqrt{3} \times V_L \times I_L \times \cos \emptyset$ where $\cos \emptyset$ is the power factor, equal to unity for pure resistive loads.

Output line voltages (2.53 Vrms) and current (0.4 A)



Frequency (10.4 Hz)



Input voltage (38.10 V) and current (0.420 A)

Figure 7-17: Measurements of input and output power for the 100W load.

After completion of this test, the batteries were disconnected from the inverter by switching off the circuit breaker and then allowing the batteries to charge for a full eight hours again.

Figure 7-18 shows that the inverter efficiency and the output power were both linear with changes in the inverter frequency which becomes saturated at 50 Hz. In other words, the input power and the output power remained constant at frequencies greater than 50 Hz. Figure 7-18 also shows that the linearity of the efficiency was up to about 70 % and the output power was up to about 80 % for the 100 W power load. More importantly noted was that the meter started measurements of the output power only at frequencies greater than 10 Hz.

For a fixed load and VF control, the power was expected to change with the square of the voltage which is linked to the frequency as voltage and frequency is proportional.

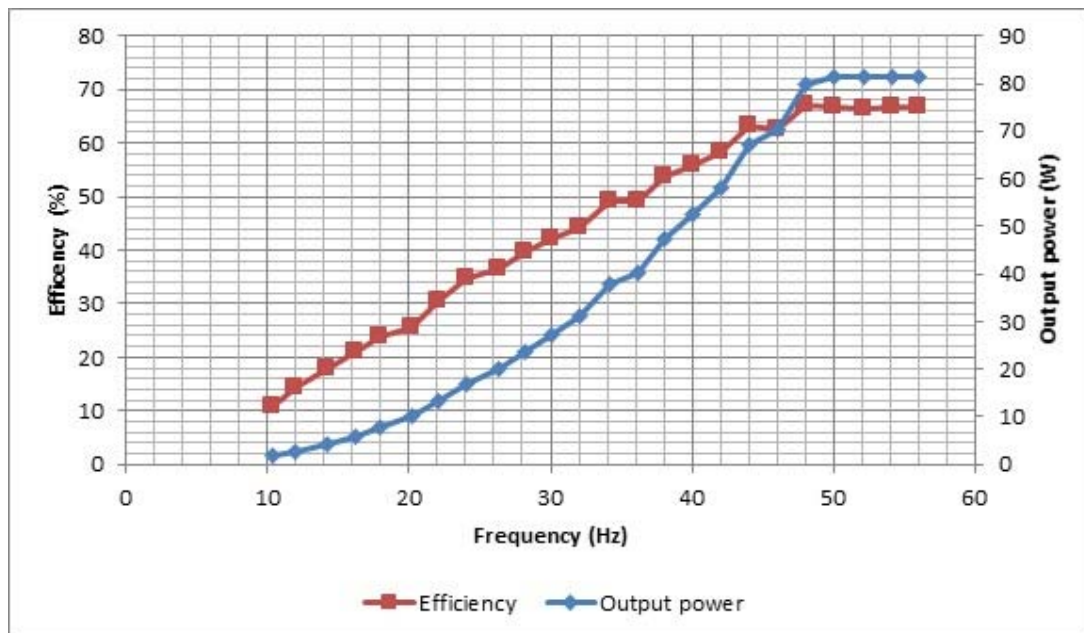


Figure 7-18: Graph of efficiency versus the output power and frequency for the inverter for 100 W load.

7.3.1.2 Motor drive testing using a 600 W load

After completion of this experiment and testing with a 100 W load, the 100 W load was disconnected and a 600 W load replaced the previous load. For the 600 W load test, a 600 W load was needed in order to load the inverter close to the maximum power (750 W) of the motor thereby verifying the reliability of the inverter. Finding such a load was really cumbersome since such a load has to be of a very low resistance and high temperature tolerance. The following resistance value was calculated for a load of six hundred watts (Bakshi & Bakshi, 2008):

$$P_T = \sqrt{3} \times V_L \times I_L \times \cos \phi \quad (47)$$

$$\therefore P_T = 600 \text{ W}$$

For a star load: $I_L = I_{PH} = V_{PH}/R_{PH}$ and $\cos \emptyset = 1$ (for a pure resistive load):

$$\therefore 600 \text{ W} = \sqrt{3} \times V_L \times V_{PH}/R_{PH}$$

But $V_{PH} = V_L/\sqrt{3}$

$$\therefore 600 \text{ W} = \sqrt{3} \times V_L^2/\sqrt{3} \times (1/R_{PH})$$

$$\therefore 600 \text{ W} = \frac{V_L^2}{R_{PH}}$$

$$\therefore R_{PH} = \frac{V_L^2}{600 \text{ W}}$$

$$\therefore R_{PH} = \frac{(17.3 \text{ V})^2}{600 \text{ W}}$$

$$\therefore R_{PH} = 0.5 \Omega$$

To make up this 0.5 Ω phase resistance, a decision was made to use a three core multi-strand, 2.5 mm² power extension code, which was 31 m long in length. This three core cable would be used in a star configuration. The three core cable was terminated at one end using terminal connectors, in order to create a star point. The other ends of the cables were connected to the three output terminals of the inverter. Using an LCR meter, the resistance of each length of cable before terminating them was found to be 0.7 Ω . Upon completion of this 100 W test for the inverter, the next step was to connect up the motor to the inverter and continue testing. The 100 W load would now be replaced by the 600 W load. Figure 7-19 shows the block diagram of the motor drive connected to the motor of the EV together with the measuring equipment.

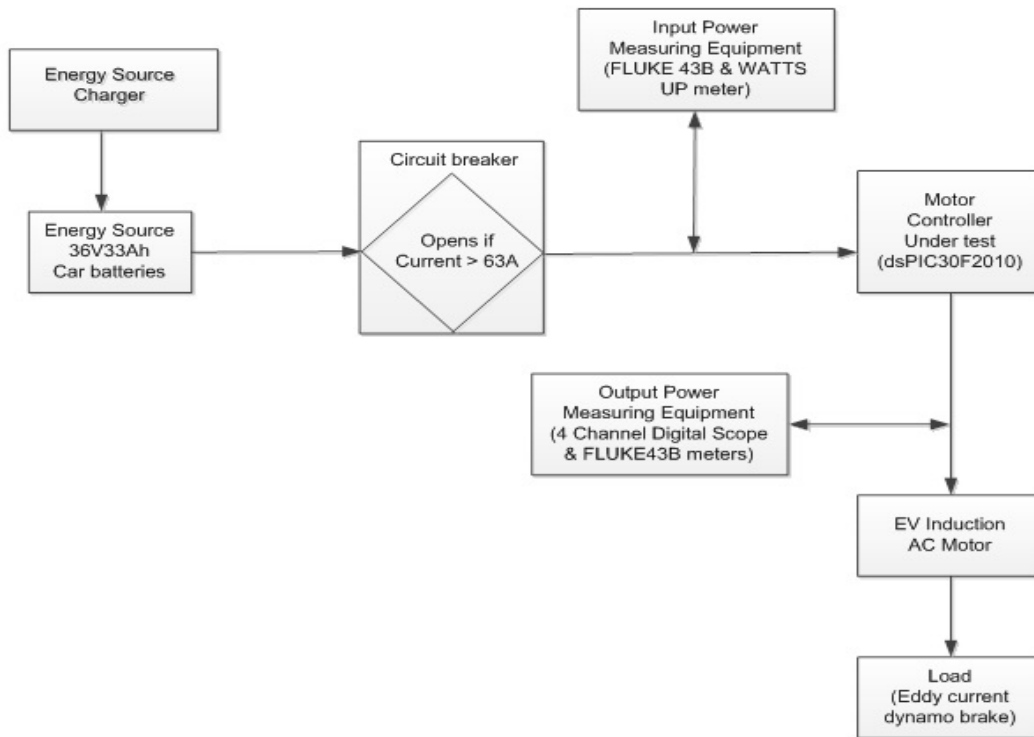


Figure 7-19: Test bench for load testing of dsPIC30F2010 motor controller and Motorelli motor.

By this design, the electric vehicle efficiency was simulated before carrying out the test on the actual EV prototype. This is done by monitoring the power drawn from the source and the mechanical power generated by the motor.

The Fluke 435B power analyser meter gives the possibility to store multiple readings with high resolution. The readings were observed during adjustable time intervals. At the end of the interval the min, max, and average values of all readings were stored in a long memory and the next observation interval started. This process continued for the duration of the observation.

The Fluke 435B set to 'Volts/Amps/Hertz' display mode

The metering equipment was connected in exactly the same fashion as the previous experiment whereby a 100 W load was measured. The charged batteries were disconnected from the charger (power supply).

The Fluke 435 power analysing option; 'Volts/Amps/Hertz' was selected for measuring purposes. The batteries were then connected to the inverter by switching the circuit breaker on again. This was the second part in testing the efficiency of the motor controller. The inverter was then tuned by increasing its three-phase output frequency at constant intervals.

Similarly as shown in Figure 7-17, the input current & voltage and output current & voltage were measured, and recorded on a spreadsheet after every frequency interval. The input and output powers were then calculated as previous discussed.

For safety reasons and to make sure the cable temperature did not exceed 50 °C the core temperature of the cable was observed as it increased with more power drawn from the inverter. The maximum temperature reached at maximum frequency of 55 Hz was 45 °C (using an APPA thermometer) as shown in Figure 7-20 (BrumBach, 2017).

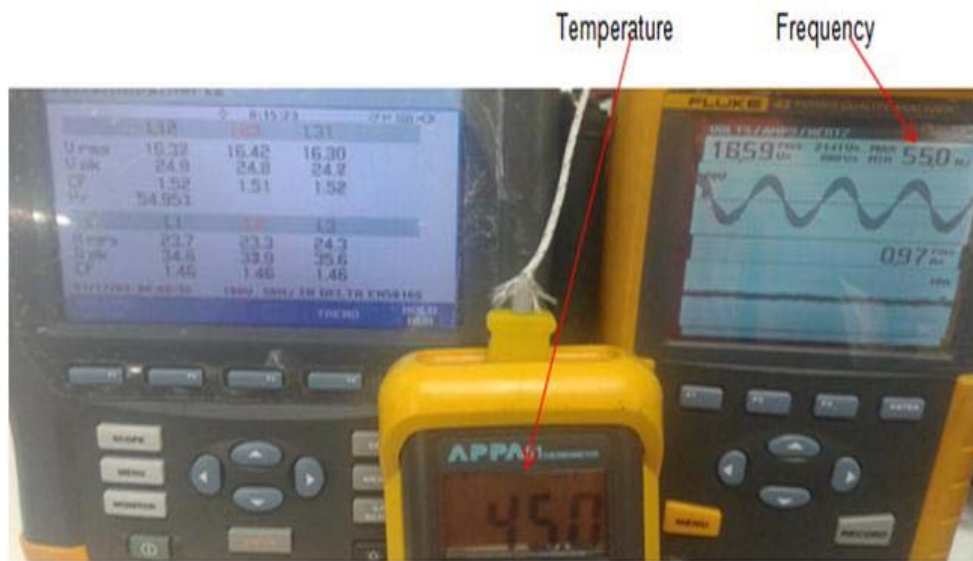


Figure 7-20: The 600W load testing of the motor drive measurements and temperature readings.

Figure 7.21 shows a graph of the motor drive efficiencies versus the output power and the output frequency.

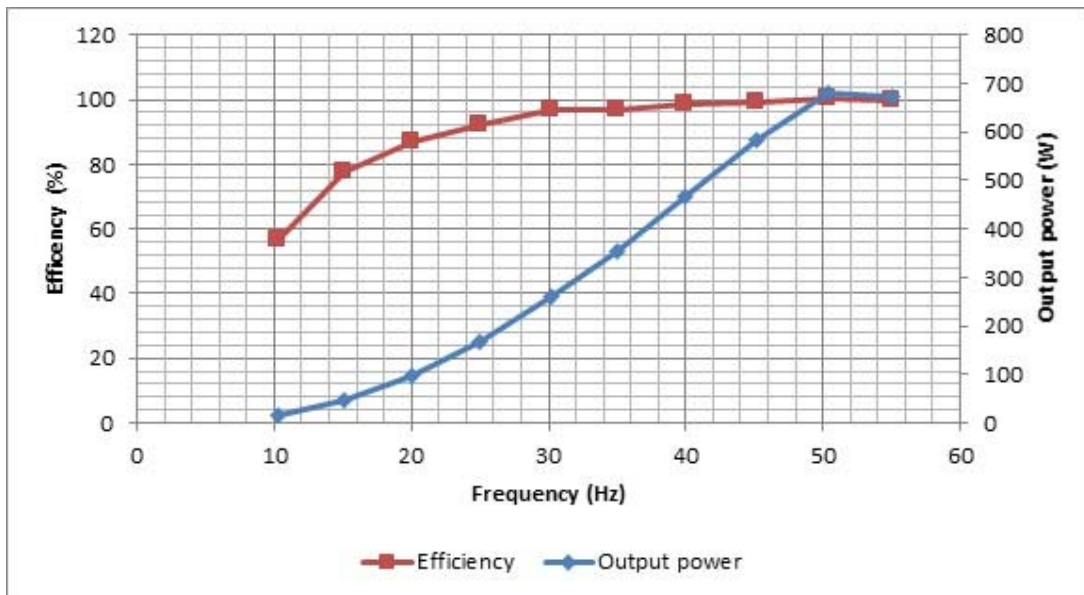


Figure 7-21: Graph of efficiency versus the output power and frequency for the inverter for 600 W load using the Volts/Amps/Hertz display option on the Fluke 435B.

Figure 7-21 shows that with a higher power demanding load (600 W), the efficiency was higher at lower frequencies than the previous 100 W load. This was because the 600 W load drew more power from the VSD which in turn drew more input power from the batteries at every set frequency than the 100 W load. This is why the efficiency curve was shifted 'up'. It could also be seen that the power output became constant at frequencies greater than 50 Hz. This was also true with experimental exercise-one, thus still indicating that the VSD became saturated at above 50 Hz. More so, the graph shows that the efficiency of the inverter was up to 100 % and above which was questionable. With this in mind, a decision was made to explore other measurement options other than the Fluke 435B power analyser.

The Fluke 435B set to 'Power and Energy' display mode

The Fluke 435B power analysing display option was now changed to 'Power and Energy'. The "load" was allowed to cool down for some time and the experiment repeated for the entire frequency range of the inverter. This was the third frequency test of the bridge inverter. The power input and output were recorded on an excel spreadsheet. A graph of the frequency vs output power and efficiency were plotted and can be seen in Figure 7-22.

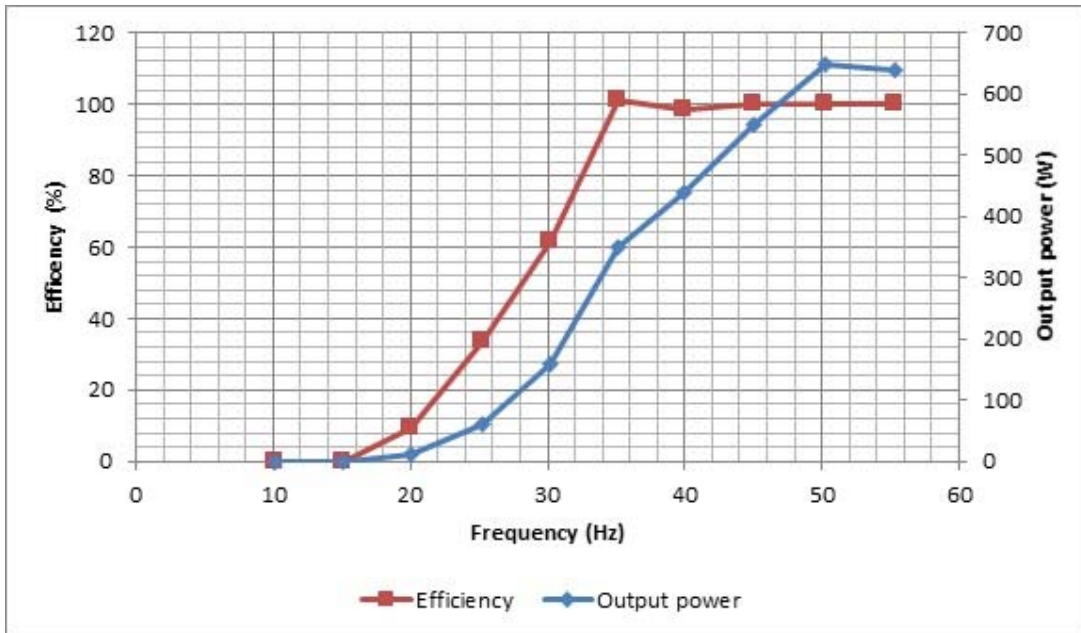


Figure 7-22: Graph of efficiency versus the output power and frequency for the inverter for 600 W load using the Power and Energy display option on the Fluke 435B.

By using this display option of the Fluke 435B, it could be seen in Figure 7-22, that at frequencies lower than 20 Hz, the output power was as low as zero, thus the efficiency is unlike that in Figure 7-21. The efficiency then increased abruptly and linear between a short frequency range of 20 Hz to 35 Hz. Here, the efficiency got close to a 100 % again, but at a much lower frequency of 35 Hz. The frequency then remained steady from 35 Hz to 55 Hz. This result was worse than the result in Figure 7.21. The picture in Figure 7-23 shows the maximum cable temperature reached at a maximum frequency of 55.3 Hz and an output power of 640 W.



Figure 7-23: Maximum cable temperature reached when using the Fluke 435B on the Power and Energy display option.

The Fluke 435B set to 'Logger' display mode

Lastly, the Fluke 435B power analyser meter option was again changed to 'Logger' display mode. The cable was once more allowed to cool down to 25 °C (room temperature) for a while and the experiment repeated for the entire frequency range of the inverter. This was the fourth and last efficiency test of the inverter by using the Fluke 435 power analyser. Figure 7-24(a) shows the set of variables selected to be logged while Figure 7-24(b) shows the output power being logged.

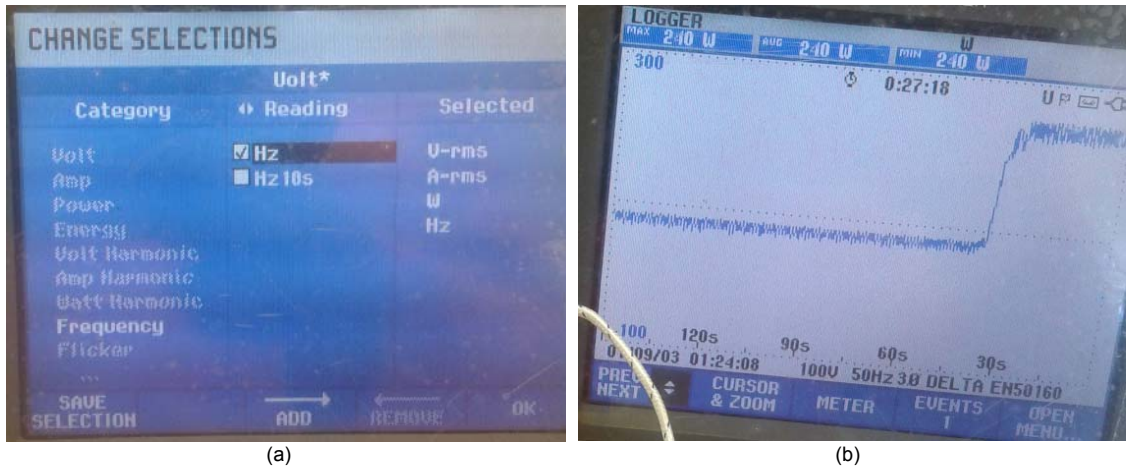


Figure 7-24: (a) Set of variables selected to be logged on Fluke 435B when in 'Logger' mode (b) The output power being logged by the Fluke 435B when in 'Logger' mode

The output voltage, current, power and frequency values were logged, as well as the input current and voltage values were also recorded. The batteries were once again disconnected from the rest of the circuit by switching off the circuit breaker. At the end of this experiment, the batteries were again put on charge for roughly eight hours.

The data recorded on a spreadsheet was plotted as in Figure 7-25.

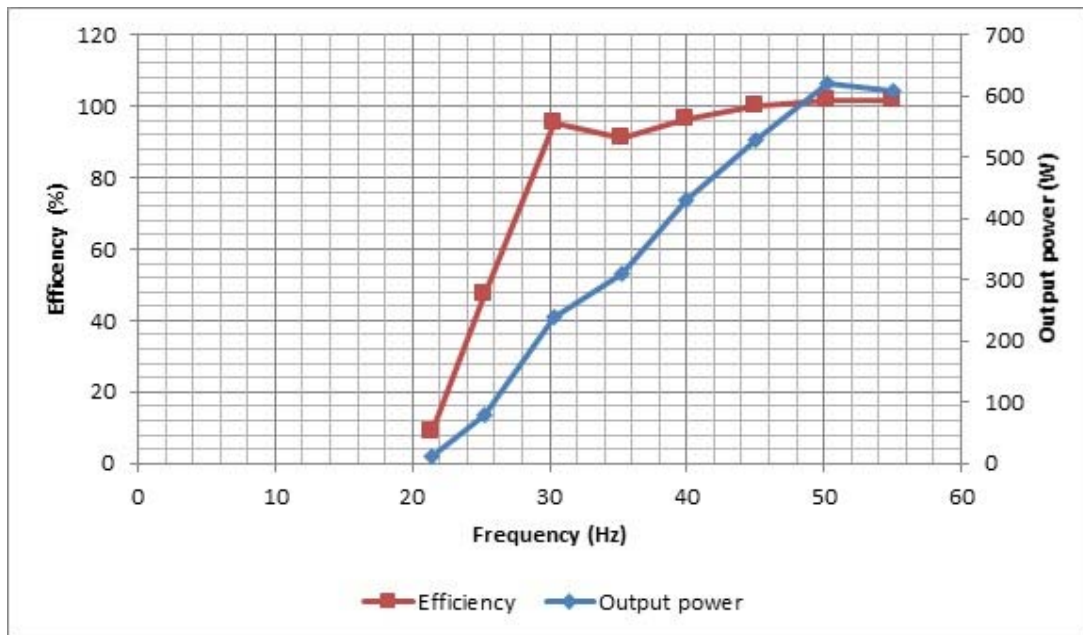


Figure 7-25: Graph of efficiency versus the output power and frequency for the inverter for 600 W load using the 'Logger' display option on the Fluke 435B.

The results seen in Figure 7-25 are the same as those seen in Figure 7-22. This lead to the conclusion that the Fluke 435B power analyser was not good for this inverter output wave which is a 'step by step' approximate sine wave with a high crest factor of 1.78 at 10 Hz. From the Fluke 435B data sheet, a crest factor of greater than 1.8 implies a high wave distortion, thus a high total harmonic distortion (THD). The power factor measurement by the meter may have been good but the true power measurement did cause the meter to have issues due to high harmonics from the inverter.

Using the Tektronix four channel data logger for power measurements

A proper measuring meter adopted in this experiment was the use of the digital method of power measurement namely, using a Blondel's four channel digital scope. The Fluke 435 power analyser was therefore replaced by the Blondel's digital scope and the scope was connected to the three-phase output of the inverter in a similar fashion as that of the Fluke 435B.

The test exercise using a 600 W load was repeated again as per the normal procedure of varying the frequency by intervals and recording the input and output data. An excel plot of the data was plotted as shown in Figure 7-26.

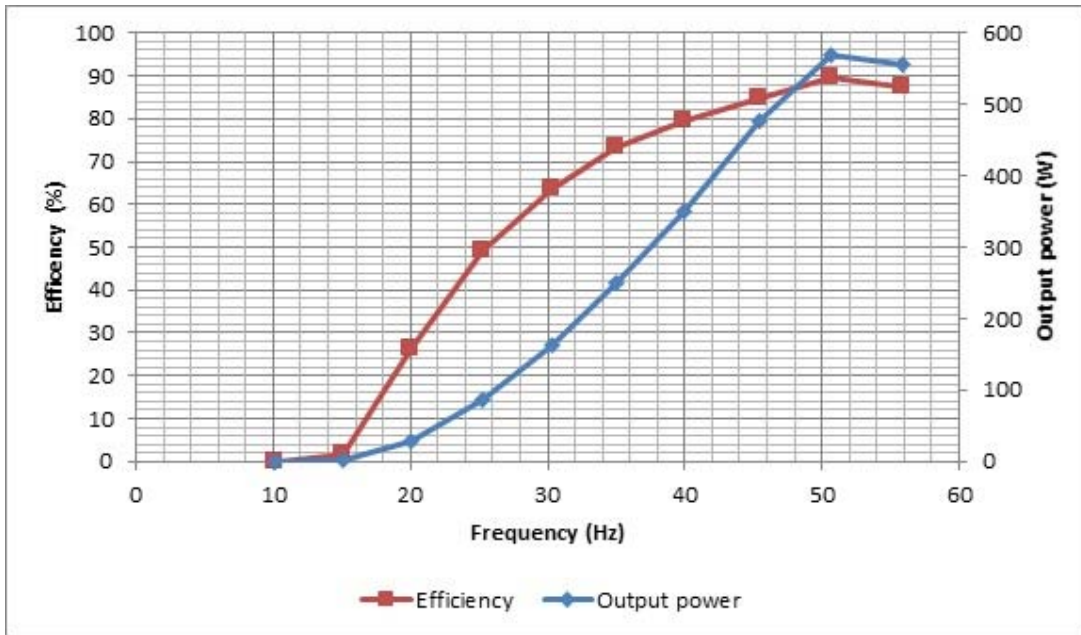


Figure 7-26: Graph of efficiency versus the output power and frequency for the inverter for 600 W load using the Blondel's four channel digital scope.

In Figure 7-26, as seen in Figure 7-22, it can be seen clearly that the efficiency remained zero at frequencies less than 20 Hz. This was because the power drawn from the supply was basically consumed by the active components of the bridge inverter (VSD) such as the metal oxide semiconductor field effect transistors (MOSFET) switches and filter capacitors, in becoming active. The power output then increased almost in a linear form from 20 Hz up to 50 Hz where the VSD saturated. The efficiency then remained constant (the input power and output power are equal) at this maximum of about 95 %. This result clearly confirms that the Fluke 435 was not a suitable meter for this bridge inverter output wave form.

7.3.1.3 Motor drive testing using the AC induction motor

The third experiment involved a few changes from the previous two experiments, namely using the 100 W and 600 W loads. Both loads were now removed and the developed AC motor was now inserted in the test bench. The changes to the test bench are as shown in the block diagram in Figure 7-27.

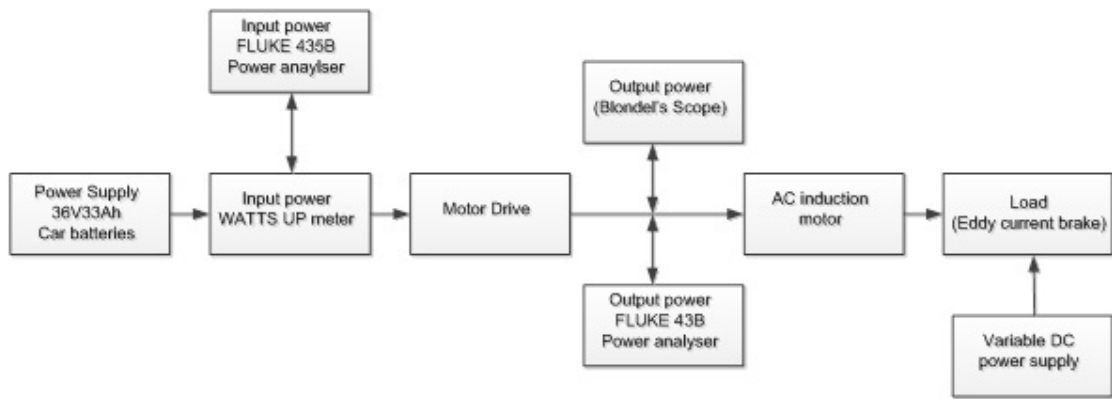


Figure 7-27: Block diagram for test bench with AC induction motor incorporated and metering equipment.

The Fluke 435 was discarded and replaced by a four channel digital oscilloscope, and the 600 W load was also discarded and replaced by the AC induction motor. The AC induction motor was then connected to the eddy current brake, used for loading. The eddy current brake was powered by a variable DC power supply. The set up was as shown in Figure 7-28.

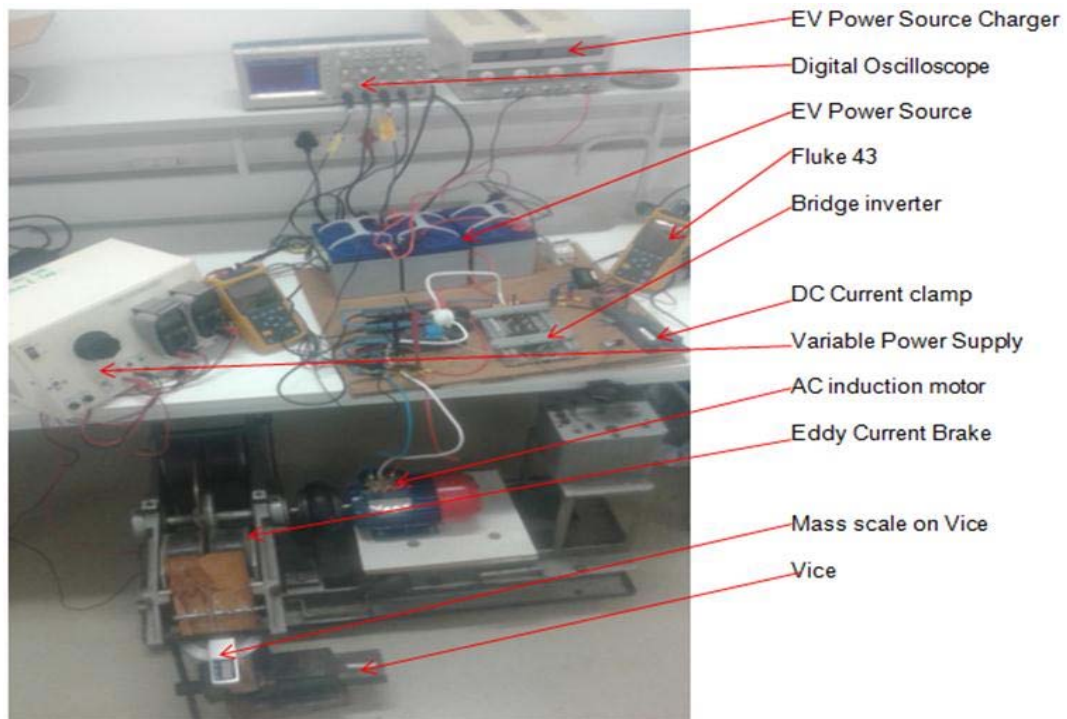


Figure 7-28: Complete test bench with AC induction motor incorporated with metering equipment and eddy current brake for loading purposes.

The charged batteries were disconnected from the charger. They were then connected to the power train by switching the circuit breaker on again. The three phase AC frequency of the inverter was varied at exactly or almost exact intervals as for the previous 600 W load exercise of the inverter efficiency test.

The motor started to rotate the eddy current brake disk at constant revolutions per minute (RPM) and there was a small power drawn into the inverter. This was the “no load” input power to the inverter-to-motor system. The power output of the inverter was negligible. This was the “no load” power to the motor.

The ‘mass scale’ was switched on to measure the weight drawn from the eddy current brake. The variable DC power supply to the eddy current brake was switched on and increased slowly until the power drawn to the inverter was the same or almost the same as the input power in the previous 600 W load exercise (at the same frequency). The eddy current brake opposed the rotation of the disk, thereby loading the motor and as well as exerting a force (torque) on the mass scale.

At constant RPM of the eddy current brake disk, the value on the mass scale, the RPM of the disk measured, the input power to the inverter, the input power to the motor and the output power of the inverter, were all recorded.

The variable DC power supply to the eddy current brake was then turned to zero and switched off. The inverter AC output frequency was then turned to the next frequency increment and the process repeated over the frequency range of the inverter.

An excel plot of the recorded data was plotted as shown on Figure 7-29.

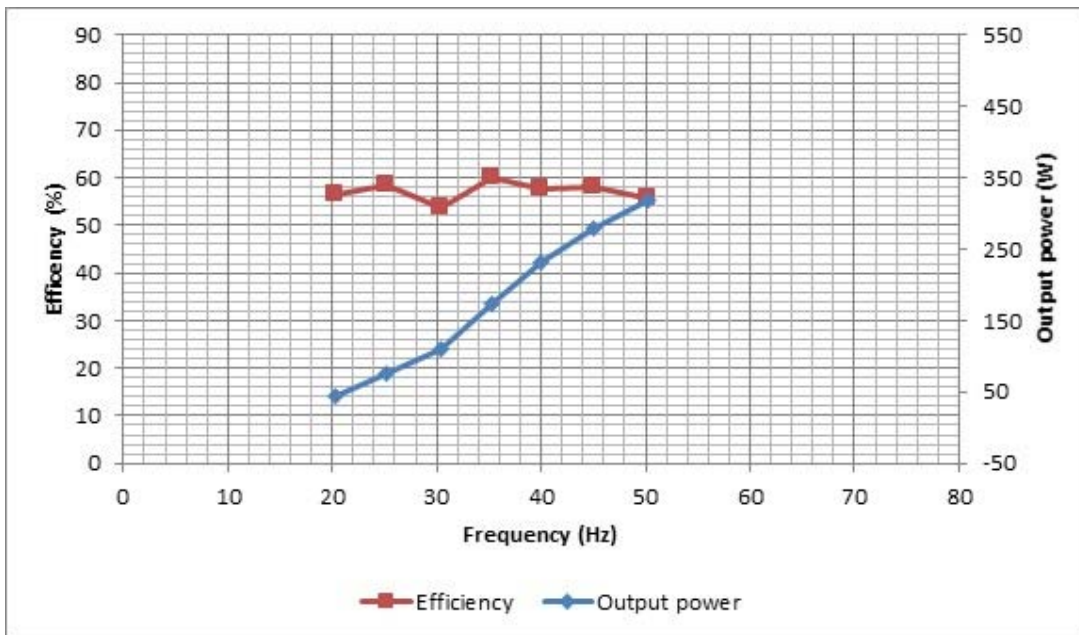


Figure 7-29: Graph of efficiency versus the output power and frequency for the inverter when the AC induction motor and eddy current brake are connected using the Blondel's four channel digital scope.

By the above plot, the motor could have sufficient rotation at the VSD output frequency of 20 Hz. A sufficient load on the motor showed that the motor was 56 % efficient at this frequency.

The efficiency of the motor then increased at higher VSD output frequencies (motor supply signal frequency) to 60 % at 35 Hz. It then dropped to 57 % and remained relatively constant from 40 Hz through 45 Hz to 50 Hz. This was because the motor's rotating magnetic field was not uniform enough. This low and nonlinear efficiency of the motor could also be attributed to the nature of the inverters output voltage signal. Figure 7-30 shows the data displayed by the respective meters used for measurement purposes.

Figure:

- 7-30 (a) shows the power (voltage & current) to the eddy current brake and VSD output frequency.
- 7-30 (b) shows the revolutions per minutes (RPM) of the motor after being loaded by the brake.
- 7-30 (c) shows the mass units generated by the torque from the motor, upon being loaded by the brake.
- 7-30 (d) shows power drawn from the batteries by the VSD-motor system.
- 7-30 (e) shows the AC motor input power measurement form the VSD output



Figure 7-30: Experimental Exercise 3 data display

After completing this section of the experiment, it was noticed that the VSD was getting very hot while its maximum power rating of 750 W was not yet reached. This was because of the regenerative energy of the motor. As the voltage on the motor was very low this caused the phase currents in the motor being quite high. This energy created was pushed back into the VSD and it created internal circulating currents in the VSD. The end product of these high currents generated heat. The regenerative power from the IM had a voltage amplitude of 9.91 V RMS and a current amplitude of 21.8 A RMS. Figure 7-31 shows the regenerative energy of the induction motor as negative power on the digital scope.

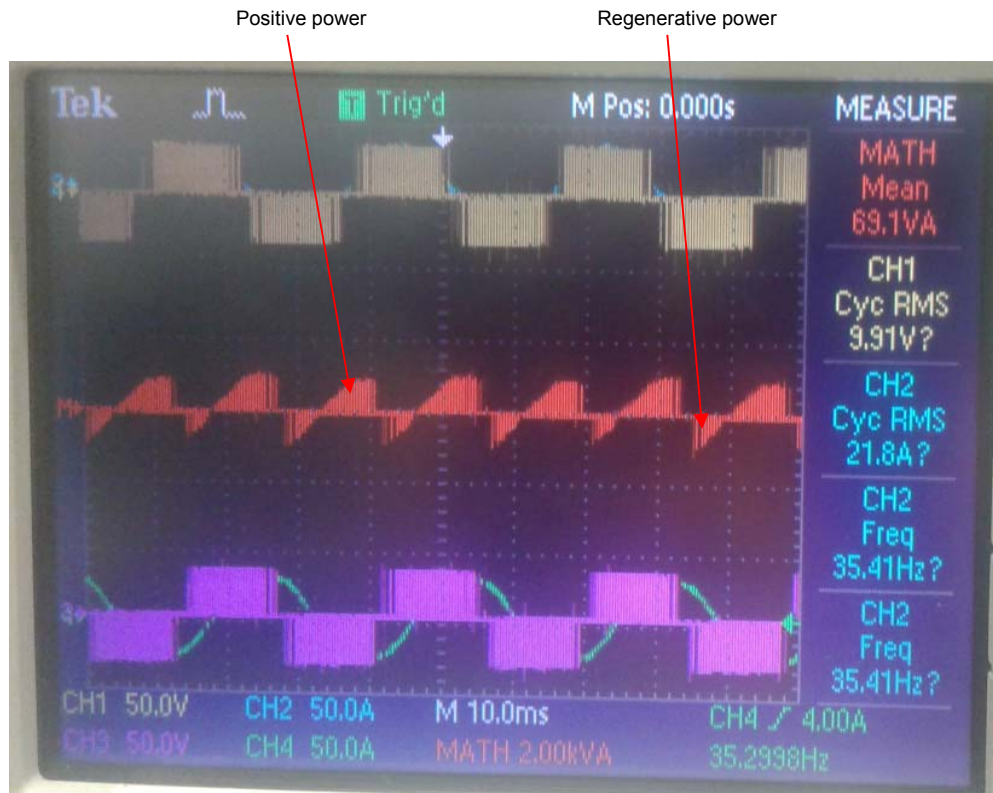


Figure 7-31: Induction motor Regenerative Power

This problem was reduced by connecting a 2 μF AC capacitor at the direct current input terminals of the VSD. This was a high frequency discharging capacitor. The supply line was also regulated by two power capacitors summed up by connecting them parallel together and then across the direct current power line as shown in Figure 7.32 (b).

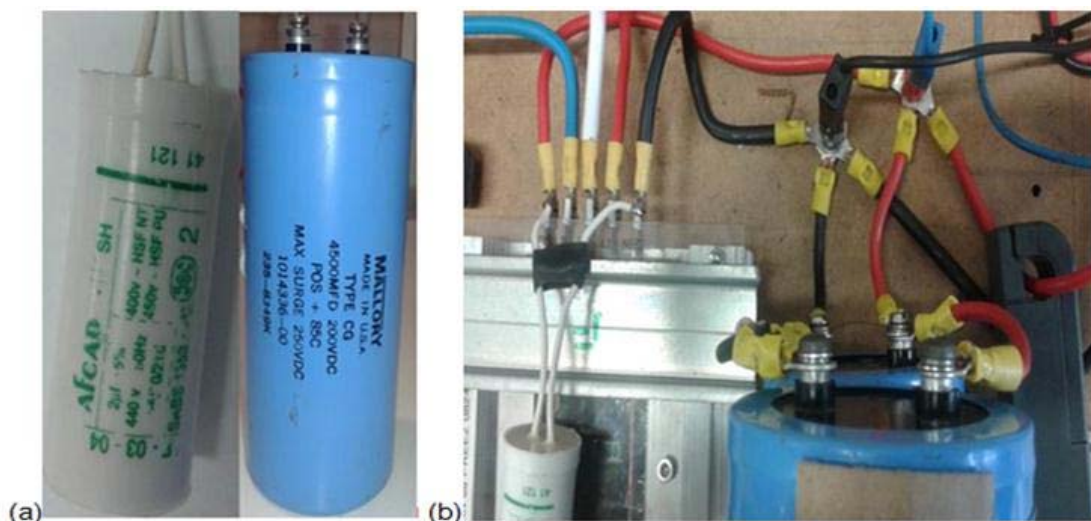


Figure 7.32: a) 2 μF AC & power capacitors b) Regenerative power protection

After connecting the capacitors to the circuit, the maximum motor power output reached was 174.027 W at 955.4 RPM, thus making the motor 60.2 % efficient. The best power measurements taken for the motor drive was an output power of 572 W with an input power of 593.135 W, making the motor drive 96.437 % efficient. Combining the motor drive and motor the highest efficiency obtained was 53.653 % (See Appendix I).

Chapter Eight

Testing and evaluation of the EV battery pack, the BMS and the display panel components

8.1 Evaluation of the battery pack

The charge profile in Figure 8-1 (Microchip, 2009) shows the balancing mechanism in effect at the end of the charge cycle; however the current remained constant throughout. This indicates the upper cell voltage limit was raised since the power supply did not enter constant voltage mode at the end to provide a trickle charge that tops up the battery pack. This lower cell voltage was chosen in order to preserve the cells lifespan since it is during the final trickle charge stage that Lithium-Ion cells swell the most significantly. Although the battery pack provided compression force to mitigate this swelling effect, it was decided to optimize battery lifespan over maximum charge levels.

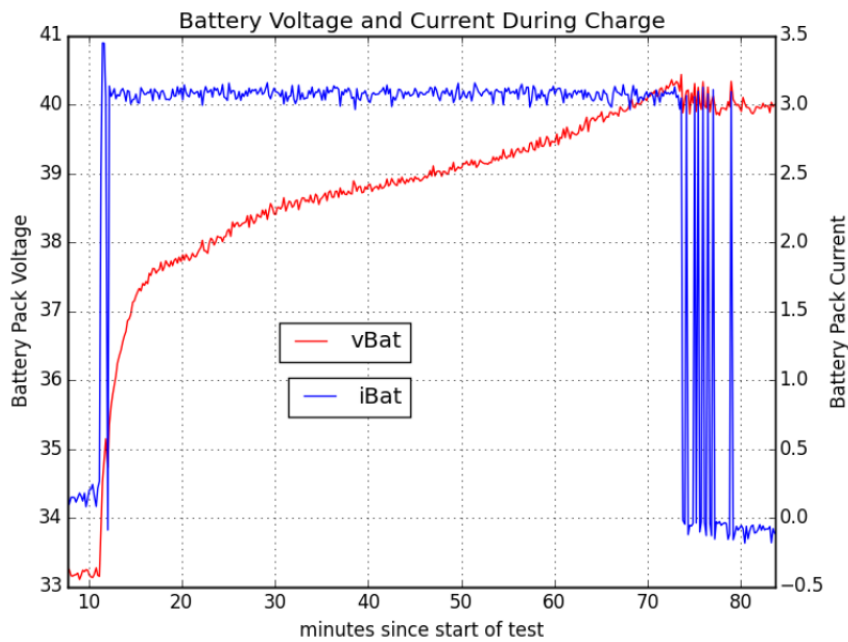


Figure 8-1: The battery pack voltage and current during charging

Unfortunately the large disparity in cell voltages at the end of the discharge cycle (or the beginning of the charge cycle seen in Figure 8-2) was a result of the BMS's inability to perform active balancing which allowed the cells to drift apart significantly if fully discharged. This was mitigated by never fully discharging the cells.

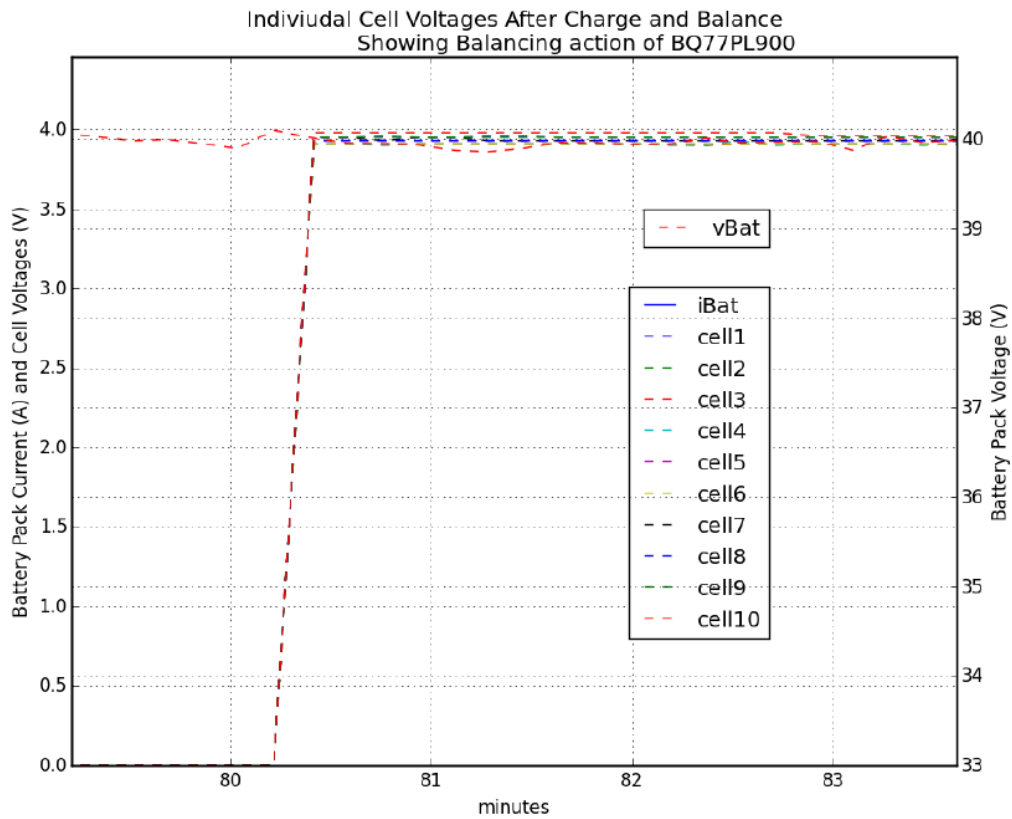


Figure 8-2: The battery cell voltages after charging and balancing

8.2 Evaluation of the BMS

Throughout the software configuration of the IC, it was observed that the device would trigger the overvoltage and under voltage alarms, disable the load and ultimately enter into shutdown mode. This condition emerged in standalone mode and host mode despite all cell voltage limits being within the values established in the EEPROM for voltage to overvoltage (VoV), voltage to undervoltage (VuV), the OV CFG and UV level registers. To recover from the shutdown mode, in standalone, the start-up voltage was applied at the IC pack terminal but the IC failed to recover automatically and communication between the IC and evaluation module was lost. Therefore the status control register was switched to host control.

Table 8-1: Recovery commands for the BMS

Mode Transition	Function and firmware procedure
Over voltage protection to normal	In the output register, toggle LTCR flag from 1 to 0. Read status bit to change XALERT status to HIGH. Set CHG FET on to enable normal operation.
Under voltage protection to normal	In the output register, set LTCR from 1 to 0. Set DSG FET on to enable normal operation. Read status but to change XALERT to HIGH.

8.2.1 Fault finding of the BMS

The recovery commands written in EEPROM failed to make the IC work in normal mode which indicated a possible hardware malfunction rather than failure from the standalone mode fixed algorithm or from the wrong host firmware command. Individual circuitries of the IC were checked.

8.2.1.1 Cell voltage measurement

The voltage monitoring done by the IC was checked using the V_{out} pin of the IC which, outputted the voltage measured from a series element of the battery according to the gain established by the host controller. The register CELL SEL enabled the host to select the series cell to be measured. The cell amplifier scale that varies from 0.15 to 0.20 was chosen. The bit State_Control [V_{gain}] was monitored using the following default equations (Texas Instruments, 2009):

$$V_{out_1} = 0.975 - [(cell\ voltage) \times 0.15] \quad (48)$$

or

$$V_{out_2} = 1.2 \times [(cell\ voltage) \times 0.20] \quad (49)$$

When $V_{gain} = 1$

For the total Pack Voltage measurement (Texas Instruments, 2009):

$$V_{out_3} = (Total\ pack\ voltage) \times 0.02 \text{ When register bit Pack} = 1 \quad (50)$$

$$V_{out_4} = (Total\ pack\ voltage) \times 0.02 \text{ When register bit BATT} = 1 \quad (51)$$

The pack voltage and the battery voltage was enabled and disabled by Function_Control [PACK] and Function_Control [BAT] respectively. During the experiment, the voltages obtained from the V_{out} pin differed completely from the actual cell value which was previously measured with a standard voltmeter indicating a fault in the IC's cell voltage monitoring circuit (Figure 8-3) (Texas Instruments, 2009):

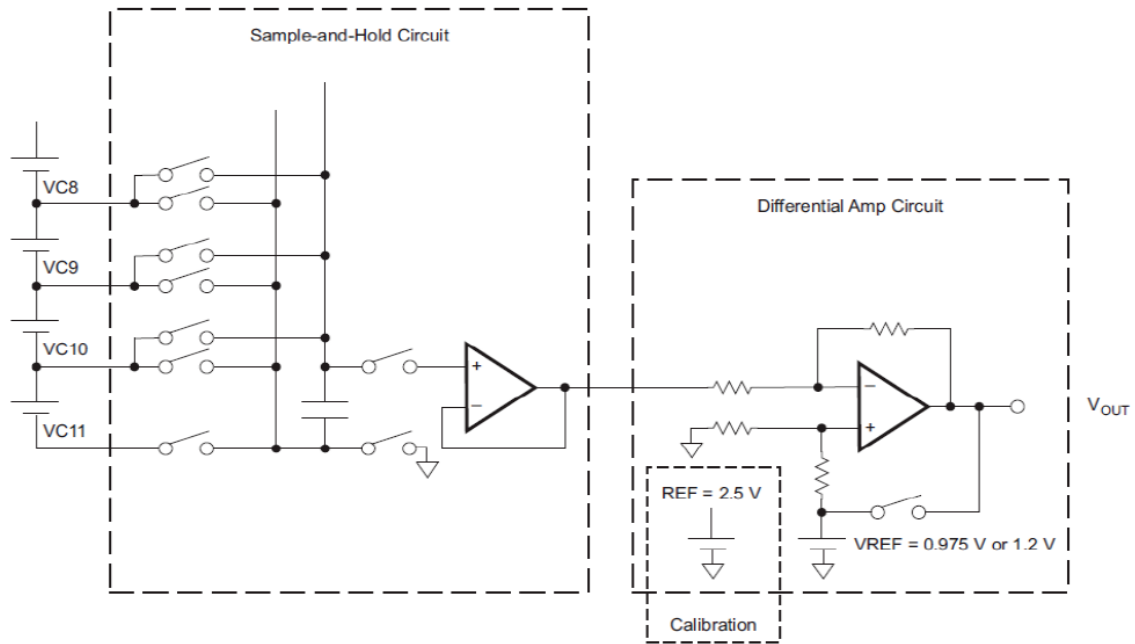


Figure 8-3: The cell monitoring circuit of the BMS

To check the operation of the differentiation amplifier the device was calibrated by programming the CELL_SEL registers bits and Function_Control [VAEN] bit to predetermine the inputs of differential amplifier and enable the predefined outputs. The steps taken into the amplifier calibration are summarized in Figure 8-4.

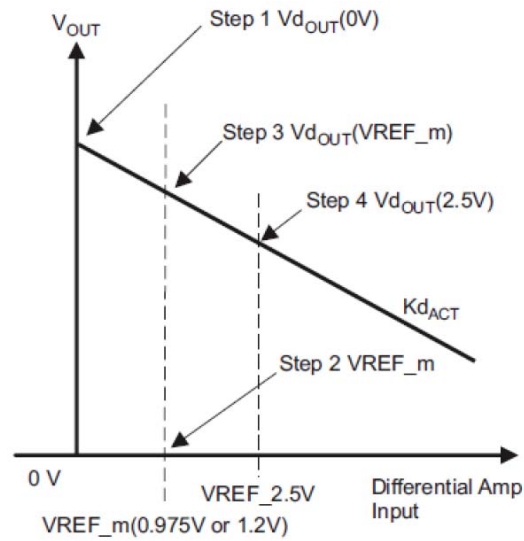


Figure 8-4: Calibration procedure of the BMS

The differential amplifier responded correctly which led to the conclusion that the sample-and hold (S/H) circuit was faulty. This caused the under voltage and overvoltage that are also driven by the S/H circuit, to fail.

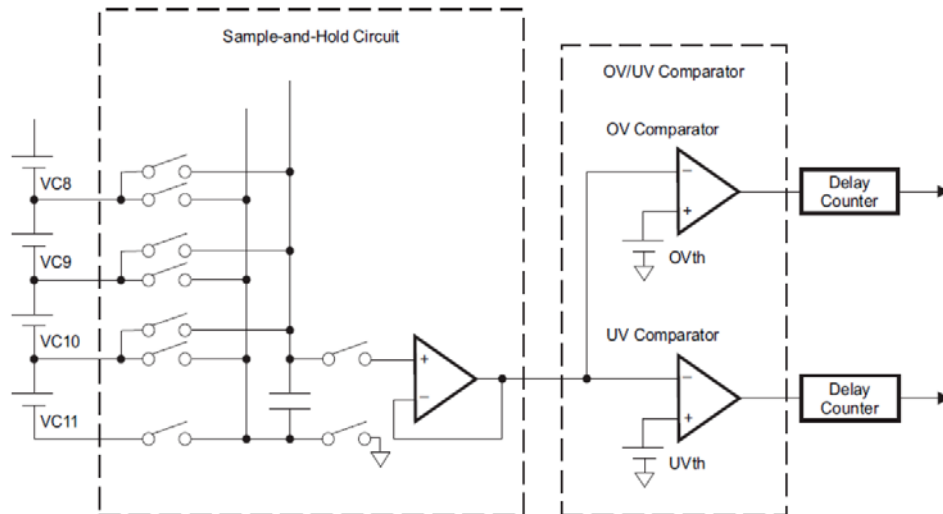


Figure 8-5 Faulty S/H circuit of the BMS

8.3 Dashboard metering equipment

The Shell marathon stipulates that the performance of the EV is judged on energy conservation rather than speed acquired. As such the assembled power sensor was used to build the following counters, which was calibrated.

8.3.1 Ampere hour (Ah) counter

The state of charge of the vehicle is represented in an amp-hour rate where 100 % is the equivalent of 17.6 Ah. This represents the actual configuration of the battery source.

8.3.2 Watt hour (Wh) and watt second (Ws) counter

The dashboard provides the amount of power used by the vehicle so that the associated cost in terms of electricity needed to fully charge the device can be obtained. The following formulas are used to calculate the power consumed (Beaty & Santoso, 2015):

$$P = V \times I \quad (52)$$

$$Wh = Ah \times \text{pack voltage} \quad (53)$$

$$Ws = Wh \times 3600 \quad (54)$$

The results obtained for the energy counter with a variable load of 20 A are recorded in the Appendix H.

8.3.3 Simulation of the race

To test the Wh and the Ah count, the battery bank at approximately 38 V was used to power a 30 A load that corresponds to at least 75 % of the EV motor power, assuming that the motor did not always run at its peak values. The experiment was conducted for forty-three minutes, which is the maximum time established by the Shell Eco-marathon rules for completion of the race. The results obtained are found in Appendix H. The calibrated data for the Ah counter against a commercial meter as well as the WH results are recorded below.

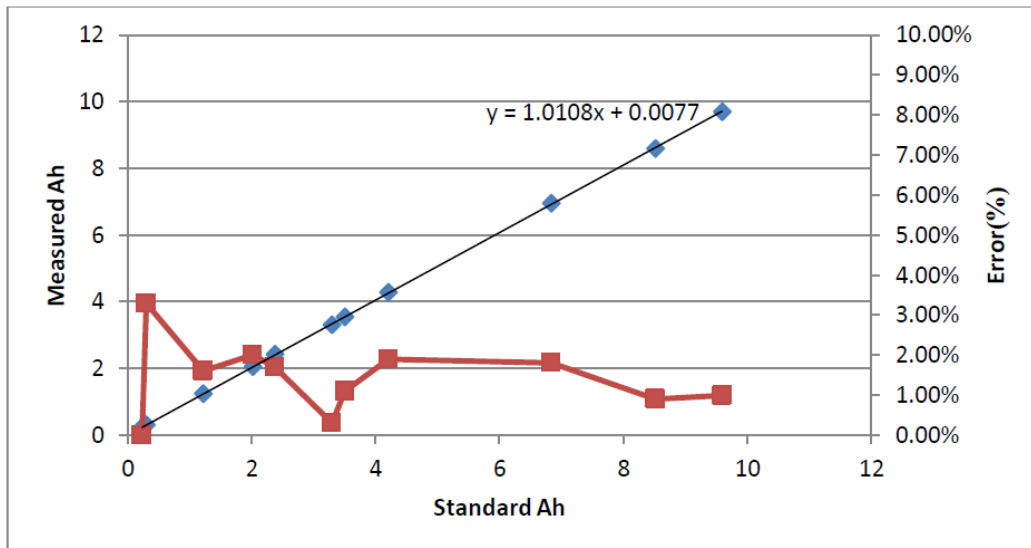


Figure 8-6: Calibrated data for the Ah counter

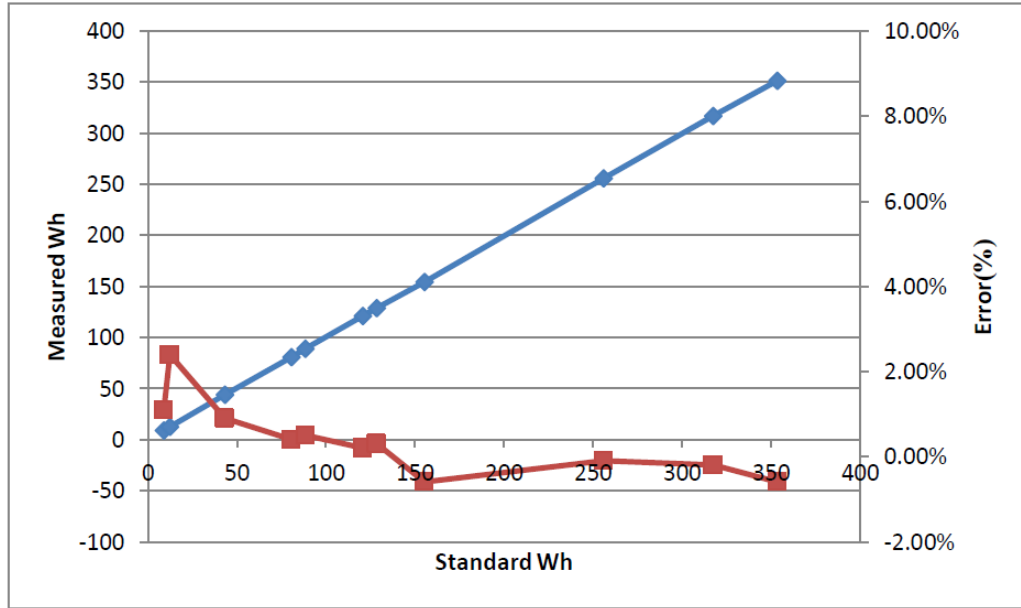


Figure 8-7: Calibrated data for the Wh counter

The graphs depicted in Figure 8-6 and Figure 8-7 shows a linear response from the calibrated meter for the ampere hour and watt hour counters. The error does not exceed 6 % for both meters in the measurements. The complete sampling is attached in Appendix H of this document. As can be viewed in Appendix H, it can be seen that the efficiency of the BMS under race simulated conditions, reached a measured power value of 351.31 W to a standard value of 353.4 W, making the BMS 99.4 % efficient.

8.4 Drive train system

For a highly efficient chain drive to be developed, three alternatives were looked at.

- A shaft and gearbox drive train system;
- A CVT belt system; and
- A chain and sprocket drive train.

The shaft and gearbox drain train system is used in most vehicles. It is the best method of delivering the highest torque from the engine to the wheels. However, this type of system is heavier than the other two systems looked at, which will make the overall system less efficient (Alshodokhi, et al., 2013).

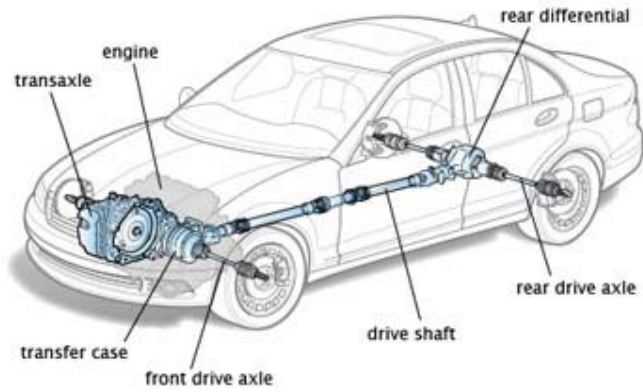


Figure 8-8: A shaft and gearbox drive train system (Visual Composer, 2016)

A CVT belt system has the advantage over the gearbox drive train in that the gear ratio can be controlled, which helps with the overall efficiency. This type of system also adds weight to the vehicle but not as much as the gearbox system. Installing this drive train also consumes more time (Alshodkhi, et al., 2013).

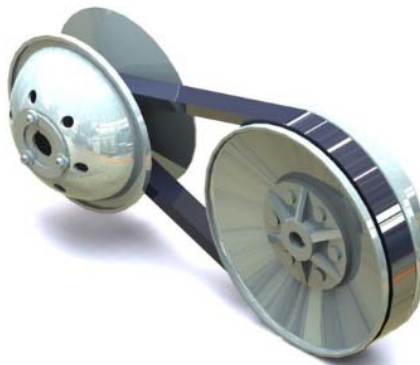


Figure 8-9: A Typical CVT belt system (Alshodkhi, et al., 2013).

The chain and sprocket drive train is the lightest of the three drive trains looked at and is also the simplest. These drive trains are commonly found on bicycles. In order to control the torque coming from the engine to the rear wheel a small transmission will be incorporated to increase or decrease the speed on the rear wheel, keeping in mind that the maximum speed and average speed needed to be achieved is 50 km/h and 25 km/h respectively.

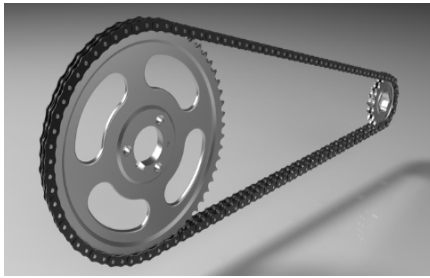


Figure 8-10: A typical chain and sprocket drive train (Alshodokhi, et al., 2013).

Belt drives can produce an efficiency of up to ninety eight percent if designed correctly whilst a chain drive produces a similarly high efficiency. Table 8-2 is a comparison of the advantages and the disadvantages of each type of drive (Rashid, 2007).

Table 8-2: The advantages and disadvantages of a shaft and gearbox; a belt drive and a chain drive (Rashid, 2007) (Alshodokhi, et al., 2013) (Gears Educational Systems, LLC, 2014)

	Advantages	Disadvantages
Shaft and gearbox drive	<ul style="list-style-type: none"> • High reliability 	<ul style="list-style-type: none"> • Highest in weight. • Complicated in construction • Higher in cost than a chain drive • Centre-to-centre distances are restricted to specific dimensions for a given set of gear. • Assembly tolerances are restricted
Belt drive	<ul style="list-style-type: none"> • Light in weight. • Simplicity in design. • Has a low moment of inertia • Not as noisy as chain or gearbox drives. • Belt drives can operate over longer centre distances than chain drives • Belts are better suited for extremely high-speed ratios. 	<ul style="list-style-type: none"> • Average in reliability • Higher in cost than a chain drive
Chain drive	<ul style="list-style-type: none"> • Shaft centre distances are relatively unrestricted • By using a chain, light weight sprockets can be manufactured • This reduces the overall weight of the car • Also produces a sprocket with a high moment of inertia • Lowest in cost • Easy to install • Assembly tolerances are not restricted • Can easily be redesigned and reconfigured. • Chain drives spread operating loads over many teeth. • They require less space for a given loading and speed condition than pulleys or belts. 	<ul style="list-style-type: none"> • Low in reliability

Based on the above advantages and disadvantages, a chain drive is a more practical and efficient solution. A few design considerations were looked at.

8.4.1 Sprocket size

In general, larger diameter sprockets are more efficient in transmitting power. The idea is that for the same gear ratio a pair of smaller sprockets will produce higher internal forces on the chain, which greatly increase friction losses in the chain (Rashid, 2007).

Ideally, the sprocket size should be closest to the rim dimension so as to allow for the largest possible diameter of the driver sprocket for any gear ratio (Rashid, 2007).

8.4.2 Chain speed

Another consideration would be the variation of the speed of the chain as it engages and disengages with the sprocket. This is due to the variation of the lever arm's length from the time the chain bush impacts the sprocket tooth till it gets seated on the sprocket. This speed variation increases with decreased number of teeth and causes increased chain noise and wear (Rashid, 2007).

8.4.3 Chain Pitch

One advantage of having a small chain pitch is reducing the angle of articulation. The angle of articulation is the angle that the chain makes when it is tangent to the pitch circle; it is the angle through which the chain rotates to mesh with the sprocket.

A larger angle of articulation will produce more wear and as a result increased elongation of the chain and thus it is advantageous to have a larger number of teeth for a given sprocket size to reduce this angle. It is therefore advisable to find the smallest chain possible as the smallest pitch chains can withstand more than 1000 N of force (Rashid, 2007).

Chapter Nine

Conclusion and recommendations

9.1 Simulated race results

As the installation of the peripherals for the car is not completed as yet, only a simulation of the various components together with the race results was simulated. Figure 9-1 shows the simulation of the various components of the CPUT EV.


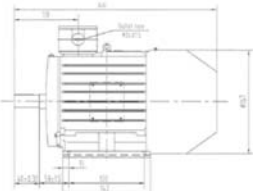
Car body information			Motor information			Tyre information																										
						<table border="1"> <tr><td>Mass</td><td>7</td><td>kg</td></tr> <tr><td>Rim Diameter</td><td>17</td><td>inch</td></tr> <tr><td>Outer Diameter</td><td>22</td><td>inch</td></tr> <tr><td>Outer Diameter</td><td>0.56</td><td>m</td></tr> <tr><td>Circumference</td><td>1.76</td><td>m</td></tr> <tr><td>Torque at wheel</td><td>37.7</td><td>N.m</td></tr> <tr><td>Wheel/road force</td><td>135</td><td>N</td></tr> <tr><td>Crusing Whl/Rd Force</td><td>48.5</td><td>N</td></tr> </table>			Mass	7	kg	Rim Diameter	17	inch	Outer Diameter	22	inch	Outer Diameter	0.56	m	Circumference	1.76	m	Torque at wheel	37.7	N.m	Wheel/road force	135	N	Crusing Whl/Rd Force	48.5	N
Mass	7	kg																														
Rim Diameter	17	inch																														
Outer Diameter	22	inch																														
Outer Diameter	0.56	m																														
Circumference	1.76	m																														
Torque at wheel	37.7	N.m																														
Wheel/road force	135	N																														
Crusing Whl/Rd Force	48.5	N																														
Mass			Mass			Gearbox information																										
Mass car	205	kg	Motor mass	8	kg	Desire top speed	40	km/h																								
Mass driver	70	kg	Power	750	W	Desire top speed	11.1	m/s																								
Total mass	275	kg	Efficiency	82.2	%	Ratio	3.77																									
			Speed	1430	rpm	Efficiency	98	%																								
Simulation data			Speed	23.83	rps	Inverter																										
Front Area	1.15	m ²	Torque	5	N.m	Effeciency	90	%																								
Drag coeff	0.4					Battery																										
			No. of motors	2		Efficiency	95	%																								
Contants			Total Tourque	10	N.m	Enegy Density	136	Wh/kg																								
Rolling resistance coeff (crr)	0.01	tires on tar				Enegy Density	286	Wh/L																								
Rolling resistance force	26.98	N	Crusing Torque	3.6	N.m	System Efficiency	68.9	%																								
Air density	1.225	kg/m ³																														

Figure 9-1: Simulated efficiency results for CPUT EV

A simulation was also completed of all the forces acting on the EV, the speed the EV would be doing as well as the power required and loss by the motor and the battery pack, for every meter covered during the race (Figure 9-2).

Total length	21600	m	Total time allowed			34	min	Start acceleration		0	m		
Laps	9		Time per lap			3.78	min	Stop acceleration		110	m		
Length / lap	2400	m	Avg Speed			10.58	m/s	Start de-acceleration		1552	m		
			Avg Speed			38.12	km/h	Stop de-acceleration		1612	m		
Dist. (m)	Ac c/ Brk	Wheel (N)	Roll. (N)	Drag (N)	Avail. (N)	Acc. (m/s ²)	Speed (m/s)	Speed (km/h)	Time (s)	Motor rpm	Motor (W)	Batt (W)	Energy (J)
0	1	134.7	-26.98	0.00	107.8	0.39	0.00	0.00	0.00	0.00	0.00	0.00	0.00
1	1	134.7	-26.98	-0.22	107.5	0.39	0.89	3.19	1.13	113.9	119.3	173.2	195.64
2	1	134.7	-26.98	-0.44	107.3	0.39	1.25	4.51	0.80	161.0	168.6	244.8	195.64
3	1	134.7	-26.98	-0.66	107.1	0.39	1.53	5.52	0.65	197.1	206.4	299.7	195.64
4	1	134.7	-26.98	-0.88	106.9	0.39	1.77	6.37	0.57	227.5	238.2	345.9	195.64
5	1	134.7	-26.98	-1.10	106.7	0.39	1.98	7.11	0.51	254.2	266.2	386.5	195.64
6	1	134.7	-26.98	-1.32	106.4	0.39	2.16	7.79	0.46	278.4	291.5	423.2	195.64
7	1	134.7	-26.98	-1.54	106.2	0.39	2.34	8.41	0.43	300.5	314.7	456.9	195.64
8	1	134.7	-26.98	-1.75	106.0	0.39	2.50	8.98	0.40	321.1	336.2	488.2	195.64
9	1	134.7	-26.98	-1.97	105.8	0.38	2.65	9.52	0.38	340.4	356.4	517.5	195.64
10	1	134.7	-26.98	-2.19	105.6	0.38	2.79	10.03	0.36	358.7	375.5	545.2	195.64
11	1	134.7	-26.98	-2.40	105.3	0.38	2.92	10.52	0.34	376.0	393.6	571.5	195.64
12	1	134.7	-26.98	-2.62	105.1	0.38	3.05	10.98	0.33	392.5	410.9	596.7	195.64
13	1	134.7	-26.98	-2.84	104.9	0.38	3.17	11.42	0.32	408.3	427.5	620.7	195.64
14	1	134.7	-26.98	-3.05	104.7	0.38	3.29	11.85	0.30	423.5	443.4	643.8	195.64
15	1	134.7	-26.98	-3.27	104.5	0.38	3.40	12.26	0.29	438.1	458.7	666.1	195.64
16	1	134.7	-26.98	-3.48	104.3	0.38	3.51	12.65	0.28	452.3	473.5	687.6	195.64
17	1	134.7	-26.98	-3.69	104.1	0.38	3.62	13.04	0.28	466.0	487.9	708.4	195.64

Figure 9-2: Simulated results for forces acting on the EV.

The final simulation is a graph of the EV performance for one single track of 2.40km in length. It shows the average speed maintained of the EV as well as the power consumption of the vehicle for the duration of the single lap.

Accelerate for	110	m	Energy	123011.6	J	Battery Volt	3.8	V
Brake for	60	m	Energy	0.03417	kWh/lap	Battery Amp	4.4	Ah
Cruising torque	3.6	N	Energy	0.341702	kWh	Battery Energy	16.72	Wh
Max Speed =	31.77509	km/h	Energy	341.7017	Wh			
Avg. Speed =	30.48043	km/h	Battery Mass	2.519924	kg	Need	342	Wh
Min Speed =	0	km/h	Battery volume	1.194761	L	No. Battery	20.45455	
			No Batteries	20.99937	Approx.			

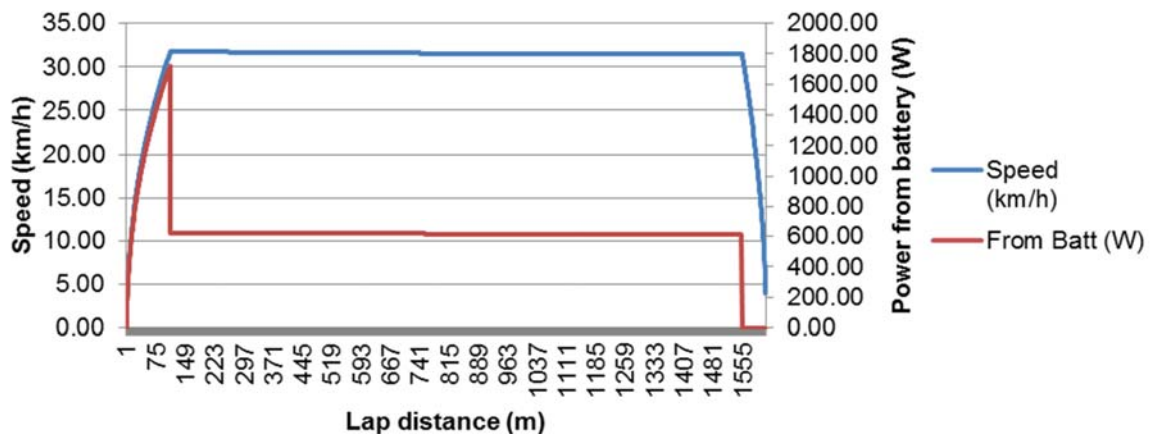


Figure 9-3: Simulated results of the EV completing one track length

9.2 Efficiency diagram

As the installation of the peripherals for the car is not completed as yet, it is difficult to measure the overall efficiency of the entire power train mounted in the vehicle. For this reason the following assumptions were concluded.

Based on previous research completed, the assumption was made that the gear transmission is 98 % efficient. Figure 9-4 shows a typical drive train power demands and efficiencies expected from a battery EV (Gustafsson & Johansson, 2015).

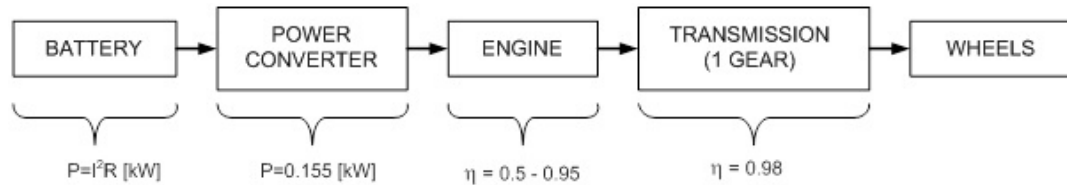


Figure 9-4: A typical power train of a battery EV

Based on these typical efficiencies of the electric EV above, the following efficiencies for the CPUT battery EV were developed. As the battery pack is the main source of energy it has no losses and delivers a total power of 1.2 kW. As previously discussed, the battery management has an over efficiency of 99.4 %, the motor drive has an efficiency of 96.43 %, the motor has an overall efficiency of 60.2 % and the gear transmission we assumed to be 98 %. The complete overall efficiency expected from the CPUT EV is 56.896 %. Figure 9-5 shows the efficiency diagram of each component and the overall system.

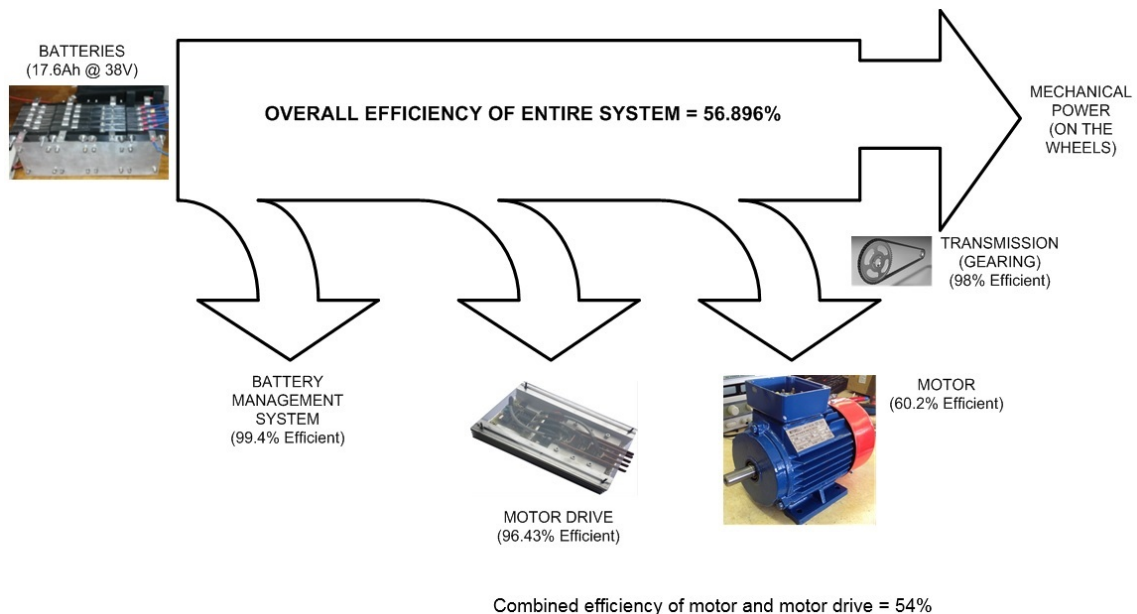


Figure 9-5: Efficiency diagram for overall system

9.3 Conclusion

In conclusion, the following questions were asked in the research proposal and have been summarised as follows:

Table 9-1: Research questions answered

Research question	Yes/No
Is the motor that was rebuilt efficient enough and complies with the Shell Eco-marathon rules and regulations?	Yes
Is the motor drive developed efficient for the power train?	Yes
Is the battery sized correctly in order to complete the race?	Yes
Does the BMS comply with the competition rules?	Yes
Does the EV power train fulfil all the safety aspects for the Shell Eco-marathon competition?	Yes
Is the EV able to complete the entire race?	Yes

The following aims were reviewed and headed the following results:

Table 9-2: Aims questions answered

Aims	Aims obtained
The EV must be able to complete a complete single track length of 2.40 km (for the Zwartkops Raceway) without stopping.	Yes. This EV will complete a single track of 2.40 km in length without stopping in approximately 3 minutes 47 seconds.
As the EV developed is a battery electric vehicle, it must produce at least 60 km/kWh in completing a single track length.	Yes. This EV produces 70.237 km/kWh in completing a single track length of 2.40 km.
The overall efficiency of the electric drive train was expected to be above 80%.	No. Due to the in efficient motors developed the overall efficiency of the power train is 56.896 %
The following most important safety standards of the EV will also be fulfilled: <ul style="list-style-type: none"> - A bulkhead separating the driver from the energy storage system, in order to protect the driver from an open flame in the energy compartment, will be implemented. - A safety harness with five mounting points for the driver will be incorporated in the EV. - The driver will be able to vacate the EV within ten seconds at any time. <ul style="list-style-type: none"> - An emergency shutdown switch to disable the propulsion system of the EV will be implemented. 	<ul style="list-style-type: none"> - Yes. A bulkhead has been installed. - A five mounting point safety harness is in the EV. - The driver is able to vacate the EV within ten seconds. - An emergency switch to disable the propulsion system is installed on the EV.

The motors employed and designed for this EV could be replaced by more efficient motors. The three phase AC IM motors were found to be quite heavy as well thereby adding extra weight to the vehicle. In the future, synchronous machines or hub motors should be considered, which are lighter and more efficient.

Regarding the BMS, the FET driver of the BQ77PL900 is responsible for the isolation and connection of the Lithium battery between the load and the charger, and the response of the driver is dictated by the IC battery cell voltage monitor circuitry. However, during configuration of the IC it was observed that this circuitry was faulty which rendered the available BMS unable of providing the protection required and control of the battery for the electric vehicle. Therefore the board should be replaced to provide such features.

The implemented monitoring system responded with a maximum error less than 5 % for all sensing devices assembled. The key parameters that dictated the operation of the vehicle were successfully obtained and sent to the microcontroller that drives the dashboard which provides relevant real time data obtained from the previous system.

To provide extra functionality and modernization of the dashboard in the future, a high speed processor with advanced HMI capabilities should collect data from the Arduino responsible for data monitoring and control the operation of the user interface. A creation of a database with the overall readings throughout the race will help build a profile to monitor the lifecycle of the battery and its overall performance during operation. Finally, the necessary support was provided so that the electronics implemented can be placed in the chassis of the vehicle and be promptly used. The following objectives and the results obtained are tabulated below.

Table 9-3: Objective questions answered

Objective	Was the objective obtained?
<ul style="list-style-type: none"> Two "currently off the shelf" (COTS) motors will be taken apart and reconstructed to deliver 750 W of mechanical power at 23 V AC. Calculations to carry 50 A for the motor wiring thicknesses, will be performed. 	Yes. The motors have an efficiency of 60.2 % from and can deliver 1.34 kW mechanical power at 23V AC. The motors could comfortably carry 35A, which was above the optimal running current of 30 A.
<ul style="list-style-type: none"> A battery pack containing Lithium-Ion batteries providing at least 40 A at 38 V DC (nominal), will be developed together with an effective BMS for this EV. 	Yes. The battery pack comfortably handled 40V DC providing 40 A consistently for 73 minutes. The BMS has an over efficiency of 99.4 %.

<ul style="list-style-type: none"> A 23 V AC motor drive for the vehicle will be developed. This motor drive will produce an output power of 1200W electrical power and a minimum of 30 A AC. 	<p>Yes. A 23V AC motor drive with an efficiency of 96.43 % was developed. The best output power developed was 572 W mechanical power.</p>
<ul style="list-style-type: none"> The efficiency of the power train will be above 80 %. 	<p>No. Due to the in efficient motors developed the overall efficiency of the power train is 56.896 %</p>
<ul style="list-style-type: none"> The vehicle electrical subsystems will be designed and developed. 	<p>Yes.</p>
<ul style="list-style-type: none"> Monitoring and measurement parameters will be implemented to ensure that the objectives are met. 	<p>Yes.</p>
<ul style="list-style-type: none"> All electrical peripherals will be installed and comply with the competition rules. 	<p>Yes.</p>

9.4 Future work

For future work, this electric vehicle was developed as an educational platform as it is the first prototype of its type developed by the CPUT. Future developments can be made in getting more efficient motors for the EV as there were budget constraints in purchasing an efficient motor. It is recommended that synchronous motors would be a better option to induction motors as they provide a much higher efficiency and are lighter than induction motors.

The batteries purchased for this EV were purchased a few years ago and there has been significant developments in battery technology with Aluminium batteries being the newer technology compared to Lithium Ion batteries. They are however a lot more expensive but are a lot more compact providing the same amount of energy.

The material also used to construct the chassis of the vehicle is heavy and the EV chassis could be made of a lighter material resulting in the overall efficiency being improved. For future work an aluminium chassis should be considered as opposed to mild steel.

If this research was to be completed again, induction motors would not be considered as they are not very efficient for this research purpose. Careful selection of the motor drive microchip would also be reviewed as the IRAM 136-3023B by International Rectifier was not the correct microprocessor and had to be replaced by the dsPIC30F2010 by Microchip. The design and development of the motor controller was time consuming as the incorrect microprocessor was selected and tested. In repeating this research, a local battery supplier would also be considered as quite a few batteries were rendered obsolete as they could not be charged and were purchased overseas.

References

ABB Webinar, 2014. *ABB Automation & Power World: April 23-26, 2012; E195C; Drives 101; Basic Features of AC drives*. s.l., ABB Webinar.

Adams, J., 2008. *Bootstrap Component Selection For Control IC's*. [Online]

Available at: <http://www.irf.com/technical-info/design/tp/dt98-2.pdf>

[Accessed 13 December 2016].

Alber, G. & Leissle, B., 2000. *Battery Monitoring: Why not do it right?*. Florida, Albercorp.

Allegro MicroSystems, Inc., 2010. *ACS758_Bi.indd - ACS758XCB.pdf*. [Online]

Available at: <http://www.mantech.co.za/datasheets/products/ACS758XCB.pdf>

[Accessed 11 May 2017].

Alshodokhi, A., Gamble, J., Glassy, N. & Moore, T., 2013. *Shell Eco-Marathon Concept Generation and Selection Document*. [Online]

Available at:

<https://www.cefn.s.nau.edu/capstone/projects/ME/2014/ShellEcoMarathon/Downloads/ConceptGenerationandSelectionReportTeam14B.pdf>

[Accessed 08 December 2016].

Altera, n.d. *What is an FPGA?*. [Online]

Available at: <http://www.altera.com/products/fpga.html>

[Accessed 15 May 2014].

Andrea, D., 2010. *Battery Management Systems for Large Lithium-Ion Battery Packs*.

Norwood: Artech House.

Anon., 2015. *Unexplained torque output from large VFDs*. [Online]

Available at: <http://www.eng-tips.com/viewthread.cfm?qid=343171>

[Accessed 16 July 2015].

APOGEE interactive, n.d. *Voltage Source Inverter (VSI)*. [Online]

Available at: <http://smud.apogee.net/comsuite/content/ces/?utilid=s&id=1208>

[Accessed 15 May 2014].

Arduino, 2016. *Arduino - IntelGalileo*. [Online]

Available at: <https://www.arduino.cc/en/ArduinoCertified/IntelGalileo>

[Accessed 06 July 2016].

- Arduino, 2017. *Arduino - ArduinoBoardUno*. [Online]
Available at: <https://www.arduino.cc/en/main/arduinoBoardUno>
[Accessed 13 April 2017].
- Arduino, 2017. *Arduino - ArduinoSoftwareRS232*. [Online]
Available at: <https://www.arduino.cc/en/Tutorial/ArduinoSoftwareRS232>
[Accessed 11 May 2017].
- Arendarik, S., 2012. *Active Cell Balancing in Battery Packs*, Rožnov pod Radhoštěm: Freescale Semiconductor.
- Arendarik, S., 2016. *Active Cell Balancing in Battery Packs*. [Online]
Available at: <http://www.nxp.com/assets/documents/data/en/application-notes/AN4428.pdf>
[Accessed 06 December 2016].
- Arsie, I., Rizzo, G. & Sorrentino, M., 2007. *A Model for the Optimum Design of a Hybrid Solar Vehicle*. Fisciano , JSAE.
- Atmel, 2016. *8-bit Atmel Microcontroller with 8K Bytes In-System Programmable Flash AT90PWM2 AT90PWM3 AT90PWM2B AT90PWM3B*. [Online]
Available at: http://www.atmel.com/Images/Atmel-4317-8-bit-AVR-Flash_Microcontroller-AT90PWM2-3-2B-3B_datasheet.pdf
[Accessed 18 September 2017].
- Bajpai, R. P. & Chandrasekhar, U., 2016. *Innovative Design and Development Practices in Aerospace and Automotive Engineering*. Singapore: Springer.
- Bakker, D., 2010. *Battery Electric Vehicles: Performance, CO2 emissions, lifecycle costs*, Utrecht: Copernicus institute University of Utrecht.
- Bakshi, U. & Bakshi, A., 2008. *Basic Circuit Analysis*. First ed. Pune: Technical Publications Pune.
- Banzi, M. & Shiloh, M., 2014. *Getting Started with Arduino*. 3rd ed. Sebastopol: Maker Media, Inc..
- Barnett, R., O'Cull, L. & Cox, S., 2004. *Embedded C Programming with the Microchip PIC*. Clifton Park: Delmar Learning.

Barry Davies, B., 2016. *Build a Drone: A Step-by-step guide to designing, constructing, and flying your very own drone*. New York: Skyhorse.

Bartelt, T., 2006. *Industrial Control Electronics: Devices, Systems, and Applications*. 3rd ed. Clifton Park: Cengage Learning .

Batson, J., Chin Fatt, G. & Wolff, M., 2012. *Electric PI: Urban Concept Plug-In Electric Vehicle for Shell Eco-marathon Americas 2012*. Florida, Florida International University.

Battery University, 2016. *Types of Lithium-ion Batteries – Battery University*. [Online] Available at: http://batteryuniversity.com/learn/article/types_of_lithium_ion [Accessed 05 October 2016].

Beaty, H. W. & Santoso, S., 2015. *Handbook of Electric Power Calculations*. Fourth ed. New York: McGraw Hill professional.

Benenson, W. et al., 2000. *Handbook of Physics*. Fourth ed. Frankfurt: Springer.

Benmore, 2011. *Benmore.net*. [Online] Available at: <http://www.benmore.net/Portable-Appliance-Equipment-testing.pdf> [Accessed 09 04 2014].

Bergveld, H., 2001. *Battery Management Systems - Design by Modelling*. Eindhoven, Philips Research Laboratories.

Bird, J., 1995. *Electrical Principles & Technology for Engineering*. First ed. Oxford: Butterworth- Heinemann Ltd.

Brain, M., 2001. *How Stuff Works*. New York: Hungry Minds, Inc.

BrumBach, M. E., 2017. *Industrial Elcetricity*. 9th ed. Boston: Cengage Learning.

Buchmann, I., 2014. *Batteries in a Portable World: A handbook on rechargeable batteries for non-engineers*. Second Edition ed. Richmond: Cadex Electronics Inc..

Burroughs, J., 2009. *Controlling 3-Phase AC induction Motors Using the PIC18F4431*. [Online] Available at: <http://ww1.microchip.com/downloads/cn/AppNotes/cn020394.pdf> [Accessed 17 June 2016].

- Cabrera, R., Francisque, C. & Synalovski, L., 2015. *Shell Eco-Marathon: Electric Car Prototype*. [Online]
Available at:
<http://www.eng.fiu.edu/mme/robotics/EML4905SeniorDesignProject/SeniorDesignProjects/2015Spring/11-2015spr-ShellEco-ElectricCarPrototype.pdf>
[Accessed 05 July 2017].
- Ceraolo, M. & Poli, D., 2014. *Fundamentals of Electric Power Engineering*. New Jersey: John Wiley & Sons, Inc..
- Chan, C. & Chau, K., 2001. *Modern Electric Vehicle Technology*. 1st ed. Oxford: Oxford Science Publications.
- CMI, 2009. *VFD Motor Control for Dryers; AB Power Flex 755 Adjustable Speed Drive*. [Online]
Available at: <http://carwashcmi.com/wp-content/uploads/2009/03/vfd-dryer-brochure.pdf>
[Accessed 18 October 2016].
- Cogan, D. (., 2014. *CPUT Shell-Eco Marathon Vehicle Simulation*, Cape Town: s.n.
- Cohen V, 1997. *Application Guide for the protection of LV Distribution system*. South Africa: ISB 0 620 20741 8.
- Council, B. o. A. S. a. T. C. o. E. a. T. S. N. R., 1993. *Star 21: Technology Forecast Assessments: Strategic Technologies for the Army of the Twenty-First Century*, Washington D.C.: National Academy Press.
- Curtis Instruments, Inc., 2015. *Model 1204/5 Motor Controllers*. [Online]
Available at: <http://e-kart.fr/images/stories/technique/curtis/curtis-controlers-1204.pdf>
[Accessed 07 December 2016].
- D.Rozhdestvenskiy, et al., 2015. *Dynamic Human-Machine Interface for Electrical Vehicle design guidelines*. [Online]
Available at: <http://ieeexplore.ieee.org/stamp/stamp.jsp?arnumber=7181573>
[Accessed 31 May 2017].
- DFRobot, 2017. *50A Current Sensor(SKU:SEN0098) - DFRobot Electronic Product Wiki and Tutorial: Arduino and Robot Wiki-DFRobot.com*. [Online]

Available at: [https://www.dfrobot.com/wiki/index.php/50A_Current_Sensor\(SKU:SEN0098\)](https://www.dfrobot.com/wiki/index.php/50A_Current_Sensor(SKU:SEN0098))
[Accessed 31 May 2017].

Digital Trends, 2015. *First Drive: 2014 Chevy Spark EV* | *Digital Trends*. [Online]

Available at: <https://www.digitaltrends.com/cars/2014-chevy-spark-ev-review>

[Accessed 10 December 2017]

Dobkin, B. & Williams, J., 2013. *Analog Circuit Design: Volume 2 Immersion in the Black Art of Analog Design*. Volume 2 ed. Oxford: Newnes Elsevier.

EATON, 2011. *Smart solutions for electrical distribution in commercial and industrial applications*. [Online]

Available at: file:///C:/Users/210012749.ADS.012/Downloads/PG01414001U_Oct11v2.pdf

[Accessed 26 4 2014].

EE Publishers, 2014. *Domestic Use of Energy conference focuses on DC grids*. Cape Town, 2014.

Ehsani, M., Gao, Y. & Miller, J., 2007. *Hybrid Electric Vehicles: Architecture and Motor Drives*. s.l., IEEE.

Elahi, A., 2001. *Network Communications Technology*. Albany: Delmar Thomson Learning.

Electrical Apparatus Service Association, Inc., 2003. *The effect of Repairing/rewinding on Motor Efficiency: EASA/AEMT Rewind Study and Good Practice Guide To Maintain Motor Efficiency*, Missouri: Electrical Apparatus Service Association, Inc..

Electrical Engineering portal, 2012. *Measurement of insulation resistance (IR) - Part 2*.

[Online]

Available at: <http://electrical-engineering-portal.com/measurement-of-insulation-resistance-2>

[Accessed 12 December 2016].

Electronics stack exchange, n.d. *FPGA's vs Microcontrollers*. [Online]

Available at: <http://electronics.stackexchange.com/questions/4382/fpgas-vs-microcontrollers>

[Accessed 15 May 2014].

Electropaedia, 2015. *Battery Management and Monitoring Systems BMS*. [Online]

Available at: <http://www.mpoweruk.com/bms.htm>

[Accessed 18 October 2016].

Else, M. & Honeywell, C., 2004. *Electricity and Thermal Physics*. Revised Edition ed. Cheltenham: Nelson Thomas Ltd.

Ellyard, D., 2005. *Who Discovered What When*. Sydney: New Holland Publishers (Australia) Pty Ltd.

Emadi, A. 2005. *Handbook of Automotive Power Electronics and Motor Drives*. Boca Raton: CRC Press.

Emadi, A., 2015. *Advanced Electric Drive Vehicles*. Boca Raton: CRC Press.

Energizer Battery Manufacturing Inc., 2014. *Alkaline Manganese Dioxide: Handbook and Application Manual*. [Online]

Available at: http://data.energizer.com/PDFs/alkaline_appman.pdf

[Accessed 23 June 2014].

Enertech International., 2018. *Home - Enertech int*. [Online]

Available at: <http://enertechint.com/>

[Accessed 12 December 2018].

Enviromental Transport Association, 2011. *Transparent solar panels for car windscreens | ETA*. [Online]

Available at: <https://www.eta.co.uk/2011/10/07/transparent-solar-panels-for-car-windscreens/>

[Accessed 03 November 2016].

Erjavec, J., 2012. *Hybrid, Electric and Fuel-Cell Vehicles*. Second Edition ed. Columbus: Cengage Learning.

Erjavec, J. & Pickerill, k., 2015. *Electrical and Electronic Systems NATEF Standards Job Sheets*. Fourth Edition ed. Stamford: Cengage Learning.

European Commission, 2010. *European Statement on Principles on Human Machine Interface for In-Vehicle Information and Communication Systems*. [Online]

Available at: http://cordis.europa.eu/pub/telematics/docs/tap_transport/hmi.pdf

[Accessed 07 December 2016].

Fairchild, 2016. *AN-558 Introduction to Power MOSFETS and their Applications*. [Online]
Available at: <https://www.fairchildsemi.com/application-notes/AN/AN-558.pdf>
[Accessed 13 December 2016].

Fawkes, H., 2008. *Mechanics for Engineering*. Third ed. Cape Town: Juta & Co.

Freescale semiconductor, 2016. *Motor Control Technologies*. [Online]
Available at:
https://www.nxp.com/files/motor_control/doc/brochure/BRMOTORCONTROL.pdf
[Accessed 18 October 2016].

Freescale, 2016. *MC33771 Battery Cell Controller and MC33664 Transformer Physical Layer*. [Online]
Available at: <http://www.mouser.com/ds/2/161/MC33664FS-596416.pdf>
[Accessed 07 December 2016].

Freescale, 2016. *Motor Control Technologies*. [Online]
Available at:
https://www.nxp.com/files/motor_control/doc/brochure/BRMOTORCONTROL.pdf
[Accessed 16 June 2016].

Fuhs, A. E., 2008. *Hybrid Vehicles and the Future of Personal Transportation*. First Edition ed. Boca Raton: CRC Press.

Gears Educational Systems, LLC, 2014. *Chain Drive Systems*. [Online]
Available at:
http://gearseds.com/documentation/deb%20holmes/2.5_Chain_drive_systems.pdf
[Accessed 08 December 2016].

Gieras, J. F., 2010. *Permanent Magnet Motors Technology: Design and Applications*. 3rd edition revised ed. New York: Taylor and Francis (CRC Pres) Boca Raton.

Giordani, N.J., 2009. *College Physics: Reasoning and Relationships*. First Edition ed. Belmont: Mary Finch.

Graphenomenon, 2015. *Graphene Properties, Structure, and Potential Applications*. [Online]
Available at: <http://www.graphenomenon.com/>
[Accessed 07 December 2016].

Grassmann, P., 1971. *Physics Principles of Chemical Engineering*. Volume 12 ed. Zürich: Pergamon Press.

Greyling & Carin, 2009. *The RDP house system in South Africa*. [Online]

Available at:

https://www.google.co.za/search?q=www.lowcosthousing.co.za+448+%C3%97+249+Search+by+image.&es_sm=93&source=lnms&tbn=isch&sa=X&ei=9yR7U5y1N-_Y7AbdqpCgBg&ved=0CAcQ_AUoAg&biw=1600&bih=1056#q=south+africa+rdp+houses&tbn=isch&facrc=_&imgdii=_&imgrc=hjrFcaNATyi

[Accessed 06 05 2014].

Gross, O. & Clark, S., 2011. *Optimizing Electric Vehicle Battery Life through Battery Thermal Management*. [Online]

Available at: <http://papers.sae.org/2011-01-1370/>

[Accessed 31 May 2017].

Grudic, E., 2008. *Electric Propulsion System for the Shell Eco-marathon Purechoice Vehicle*. Trondheim, Norwegian University of Science and Technology.

Grunditz, E. & Jansson, E., 2009. *Modelling and Simulation of a Hybrid Electric Vehicle for Shell Eco-marathon and an Electric Go-kart*. Göteborg: Chalmers.

Gupta, A., 2010. *Summer Automotive Engineering Project 2009: Reconfigurable Electric Vehicle*. Michigan: Dearborn.

Gustafsson, T. & Johansson, A., 2015. *Comparison between Battery Electric Vehicles and Internal Combustion Engine Vehicles fueled by Electrofuels*. [Online]

Available at: <http://publications.lib.chalmers.se/records/fulltext/218621/218621.pdf>

[Accessed 11 May 2017].

Hashernnia, N. & Asaei, B., 2008. *Comparative Study of Using Different Electric Motors in the Electric Vehicles*. Vilamoura, Electrical Machines, 2008. ICEM 2008. 18th International Conference on Electrical Machines.

Hatch, S. V., 2016. *Computerized Engine Controls*. Tenth ed. Boston: Cengage Learning.

Heath, S., 1999. *Multimedia and Communications Technology*. 2nd ed. New York: Routledge.

Hermann, Dave & Ajinder Singh, 2014. *EDN Network; Power line communication implementation for DC applications*. [Online]
Available at: <http://edn.com/design/power-management/4427860/Power-line-communication-implementation-for-DC-applications>
[Accessed 29 04 2014].

Hill Publishing Company, 1945. Power and the Engineer, Volume 89, Issue 2. *Power and the Engineer*, 89(2), p. 189.

Hossain, E., Han, Z. & Poor, h. V., 2012. *Smart grid Communications and Networking*. Cambridge: Cambridge University Press.

Husain, I., 2011. *Electric and Hybrid Vehicles Design Fundamentals*. Second Edition ed. Boca Raton: CRC Press.

HussainZuberi & Khurram, 2003. *Powerline Carrier (PLC) Communication System*, Sweden: Royale Institute of Technology.

IEEE Smart Grid Round up AC vs DC, 2014. *IEEE Smart Grid Experts Roundup: Ac vs DC*. Piscataway, New Jersey: IEEE.

IUM research, Innovation & Invention Exhibition 2010 (IRIIE 2010), 2010. *Enhancing Quality Research & Innovation for Social Development*. Selangor, IRIIE 2010.

Imanishi, N., Luntz, A. & Bruce, P., 2014. *The Lithium Air Battery: Fundamentals*. New York: Springer.

Inderwildi, O. & King, S. D., 2012. *Energy, Transport, & the Environment: Addressing the Sustainable Mobility Paradigm*. London: Springer.

Intel®, 2016. *Intel® Galileo Gen 2 Development Board: Datasheet*. [Online]
Available at: <http://www.intel.com/content/www/us/en/embedded/products/galileo/galileo-g2-datasheet.html>
[Accessed 06 July 2016].

International Rectifier, 2016. *Application Note AN-978: HV Floating MOS-Gate Driver ICs*. [Online]

Available at: <http://www.infineon.com/dgdl/an-978.pdf?fileId=5546d462533600a40153559f7cf21200>

[Accessed 20 June 2016].

Interview with Thought Leaders on Intelligent Energy Use Energy Use. 2008. [Film] Directed by John McDonald. s.l.: IEEE energy .

ISPE, 2009. *Research and Development on Renewable Energies*, s.l.: International Science Panel on Renewable.

J.Duncan Glove, Sarma S. Mulukutla & Overbye Thoma, 2010. *Power System. Analysis and Design*. 4 ed. USA: 2010.

Jessica E. Chaidez, 2011. *DC House Modeling and System Design*, California: s.n.

John Åkerlund & Christer Boije af Gennäs, 2007. *Comparison of the AC UPS and the DC UPS solutions for critical loads*, Sweden: IEEE.

Jowett, C., 1972. *Compatibility & Testing of Electronic Components*. First ed. London: Butterworth & Co (Publishers) Ltd.

Kamath D, K R Jagadisha & S K Girish, 2012. Smart DC micro-grid for effective utilization of solar energy. *International Journal of Scientific and Engineering Resaerch*, 3(12).

Kazanbas, M.C., 2014. *Analysis and Comparison of Power Electronic Converters with Electronic Isolation*. Kassel: Kassel University Press.

Kersting & H.William, 2002. *Distribution System Modeling and Analysis*. USA: s.n.

Kharagpur, T., 2014. *INVERTERS - Introduction_to_Voltage_Source_Inverters.pdf*. [Online] Available at: http://www.idc-online.com/technical_references/pdfs/electrical_engineering/Introduction_to_Voltage_Source_Inverters.pdf

[Accessed 03 November 2016].

Kharagpur, T., 2015. *Module 5: DC to AC converters: Lesson 33: Introduction to Voltage Source Inverters*. [Online]

Available at: <http://www.nptel.ac.in/courses/Webcourse->

[contents/IIT%20Kharagpur/Power%20Electronics/PDF/L-33\(DP\)\(PE\)%20\(\(EE\)NPTEL\).pdf](http://www.nptel.ac.in/courses/Webcourse-contents/IIT%20Kharagpur/Power%20Electronics/PDF/L-33(DP)(PE)%20((EE)NPTEL).pdf)
[Accessed 19 October 2016].

Kharagpur, T., n.d. *Current Source Inverter*. [Online]
Available at: [http://www.nptel.ac.in/courses/Webcourse-contents/IIT%20Kharagpur/Power%20Electronics/PDF/L-39\(NKD\)\(PE\)%20\(\(EE\)NPTEL\)%20.pdf](http://www.nptel.ac.in/courses/Webcourse-contents/IIT%20Kharagpur/Power%20Electronics/PDF/L-39(NKD)(PE)%20((EE)NPTEL)%20.pdf)
[Accessed 15 May 2014].

Kharagpur, T., n.d. *Introduction to Voltage Source Inverters*. [Online]
Available at: [http://www.nptel.ac.in/courses/Webcourse-contents/IIT%20Kharagpur/Power%20Electronics/PDF/L-33\(DP\)\(PE\)%20\(\(EE\)NPTEL\).pdf](http://www.nptel.ac.in/courses/Webcourse-contents/IIT%20Kharagpur/Power%20Electronics/PDF/L-33(DP)(PE)%20((EE)NPTEL).pdf)
[Accessed 15 May 2014].

KirkPatrick, L. & Francis, G., 2010. *Physics A Conceptual World View*. Seventh Edition ed. Belmont: Mary Finch.

Klauke, 2002. *Technical reports: Accurately connecting copper and aluminium*. [Online]
Available at: <http://www.klauke.com/electrical/technical-reports/accurately-connecting-copper-and-aluminium/>
[Accessed 11 October 2016].

Kreith, F. & Yogi Goswami, D., 2007. *Handbook of Energy Efficiency and Renewable Energy*. Boca Raton: CRC Press.

Kulkani, S. & Khaparde, S., 2013. *Transformer Engineering. Design, Technology and Dianostics..* 2 ed. USA: 2013.

Kumar, A. A., 2014. *Fundamentals of Digital Circuits*. Third Edition ed. New Delhi: Asoke K. Ghosh, PHI Learning Private Limited.

Larminie, J. & Lowry, J., 2012. *Electric Vehicle Technology Explained*. Second Edition ed. West Sussex: John Wiley & Sons.

Levy, S. C. & Bro, P., 1994. *Battery Hazards and Accident Prevention*. Santa Fe: Springer Science+Business media, LLC.

License, G. F. D., 2017. *50A Current Sensor(SKU:SEN0098) - Robot Wiki*. [Online]
Available at: [https://www.dfrobot.com/wiki/index.php/50A_Current_Sensor\(SKU:SEN0098\)](https://www.dfrobot.com/wiki/index.php/50A_Current_Sensor(SKU:SEN0098))
[Accessed 23 March 2017].

Linear Technology Corporation, 2014. *LTC3300-1 High Efficiency Bidirectional Multicell Battery Balancer*. [Online]
Available at: <http://cds.linear.com/docs/en/datasheet/33001fb.pdf>
[Accessed 06 July 2016].

Linear Technology, 2013. *High Efficiency Bidirectional Multicell Battery Balancer*, Milpitas:
Linear Technology Corporation.

Linear Technology, 2016. *Battery Management - Linear Technology*. [Online]
Available at: http://www.linear.com/products/battery_management
[Accessed 18 October 2016].

Linear Technology, n.d. *LT1074 - Step-Down Switching Regulator*. [Online]
Available at: <http://www.linear.com/product/LT1074>
[Accessed 22 April 2017].

Liu, C. et al., 2010. Graphene-Based Supercapacitor with an Ultrahigh Energy Density. *Nano Lett*, 10(12), pp. 4863-4868.

Liu, H.-C., Sung, W.-e. & Wenli-Yao, 2015. *Information, Computer and Application Engineering*. Leiden: CRC Press/Balkema.

Lund, M., 2016. *American Wire Gauge table and AWG Electrical Current Load Limits with skin depth frequencies and wire breaking strength*. [Online]
Available at: http://www.powerstream.com/Wire_Size.htm
[Accessed 12 December 2016].

Maiser, E., 2014. *Battery Packaging – Technology Review*, Frankfurt: American Institute of Physics.

Mantech, 2010. *Arduino Mega 2560*. [Online]
Available at: <http://www.mantech.co.za/datasheets/products/A000047.pdf>
[Accessed 13 April 2017].

Martínez, D. A., Poveda , J. D., Guáqueta , A. F. & Montenegro, D., 2013. *Electric Vehicle Instrumentation by Using HMI's*. Bogotá, IEEE.

Maxim Integrated, 2016. *DS18B20 Programmable Resolution 1-Wire Digital Thermometer*. [Online]

Available at: <https://datasheets.maximintegrated.com/en/ds/DS18B20.pdf>

[Accessed 6 July 2016].

Mi, C., Masrur, M. A. & Gao, D. W., 2011. *Hybrid Electric Vehicles: Principles and Applications with Practical Perspectives*. First Edition ed. West Sussex: John Wiley & Sons.

Microchip, 2007. *An Introduction to AC Induction Motor Control Using the dsPIC30F MCU*. [Online]

Available at:

[http://ww1.microchip.com/downloads/en/AppNotes/AC%20Induction%20Motor%2000984a.p
df](http://ww1.microchip.com/downloads/en/AppNotes/AC%20Induction%20Motor%2000984a.pdf)

[Accessed 12 December 2016].

Microchip, 2007. *dsPIC30F Family Reference Manual - Section 30 Power Supply PWM - 70270B.pdf*. [Online]

Available at: <http://ww1.microchip.com/downloads/en/DeviceDoc/70270B.pdf>

[Accessed 12 April 2017].

Microchip, 2009. *Getting Started with dsPIC30F Digital Signal Controllers User's Guide*. [Online]

Available at: <http://ww1.microchip.com/downloads/en/DeviceDoc/70151a.pdf>

[Accessed 24 January 2017].

Microchip, 2011. *dsPIC33FJ12MC201/202 Data Sheet: High Performance 16-bit Digital Singal Controllers*. [Online]

Available at: <http://ww1.microchip.com/downloads/en/DeviceDoc/70265E.pdf>

[Accessed 20 June 2016].

Microchip, 2013. *PIC16F7X7: 28/40/44-Pin, 8-Bit CMOS Flash Microcontrollers with 10-Bit A/D and nanoWatt Technology*. [Online]

Available at: <http://ww1.microchip.com/downloads/en/DeviceDoc/30498D.pdf>

[Accessed 2017 September 18].

Microchip, 2016. *AC Induction Motor (ACIM)*. [Online]
Available at: <http://www.microchip.com/design-centers/motor-control-and-drive/motor-types/acim>
[Accessed 16 June 2016].

Microchip, 2016. *AC Induction Motor (ACIM)*. [Online]
Available at: [http://www.microchip.com/design-centers/motor-control-and-drive/motor-types/ac-induction-motor-\(acim\)](http://www.microchip.com/design-centers/motor-control-and-drive/motor-types/ac-induction-motor-(acim))
[Accessed 16 June 2016].

Microchip, 2016. *Brushless DC (BLDC) Motor*. [Online]
Available at: <http://www.microchip.com/design-centers/motor-control-and-drive/motor-types/bldc>
[Accessed 13 December 2016].

Microchip, 2016. *PWM Edge and Center Aligned Modes*. [Online]
Available at: <http://microchip.wikidot.com/pwr3101:pwm-edge-center-aligned-modes>
[Accessed 13 December 2016].

Microchip, n.d. *00889b App Notes*. [Online]
Available at: <http://ww1.microchip.com/downloads/en/AppNotes/00889b.pdf>
[Accessed 30 April 2014].

Mohanty, A. R., 2015. *Machinery Condition Monitoring Principles and Practices*. West Bengal: CRC Press.

Monk, S., 2016. *Raspberry Pi Cookbook*. 2nd ed. Sebastopol: O'Reilly Media, Inc..

Moore, S. W. & Schneider, P. J., 2001. *A Review of Cell Equalization Methods for Lithium Ion and Lithium Polymer Battery Systems*. Detroit, Michigan, SAE Technical Paper Series.

Moshe Chaim Kinn, 2011. *Benefits of Direct Current Electricity Supply for Domestic Application*, USA: University of Manchester.

Moura, S. J., Steyn, J. L. & Fathy, H. K., 2013. *Battery-Health Conscious Power Management in Plug-In Hybrid Electric Vehicles via Electrochemical Modeling and Stochastic Control*. Michigan, IEEE.

Nasar, S., Boldea, I. & Unnewehr, L., 1993. *Permanent Magnet, Reluctance, and Self-synchronous Motors*. Florida: CRC Press.

National Semiconductor, 2000. *LM35 Precision Centigrade Temperature Sensors*. [Online] Available at: <http://www2.ece.ohio-state.edu/~passino/LM35.pdf> [Accessed 06 July 2016].

Newman, J., 2008. *Physics of the Life Sciences*. Schenectady: Springer.

NMB Technologies Corporation , 2014. *Permanent Magnet Motor Construction*. [Online] Available at: <http://www.nmbtc.com/pm-step-motors/engineering/construction.html> [Accessed 23 June 2014].

Novak, P., 2016. *The Basics of Variable-Frequency Drives*. [Online] Available at: <http://ecmweb.com/power-quality/basics-variable-frequency-drives> [Accessed 03 November 2016].

NXP Products, 2016. *MC33771: 14-Channel Li-ion Battery Cell Controller IC*. [Online] Available at: <http://www.nxp.com/products/power-management/battery-management/battery-cell-controllers/14-channel-li-ion-battery-cell-controller-ic:MC33771> [Accessed 06 July 2016].

Pappano, A. J. & Wier, W. G., 2013. *Cardiovascular Physiology*. 10th ed. Philadelphia: Elsevier Mosby.

Parekh, R., 2009. *VF Control of 3-Phase Induction Motors Using PIC16F7X7 Microcontrollers - 00889b.pdf*. [Online] Available at: <http://ww1.microchip.com/downloads/en/AppNotes/00889b.pdf> [Accessed 03 November 2016].

Paul Savage, Robert R. Nordhaus & Sean P Jamieson, n.d. s.l.: s.n.

Pay, S. & Baghzouz, Y., 2003. *Effectiveness of Battery-Supercapacitor Combination in Electric Vehicles*. Bologna, IEEE.

Pistoia, G., 2014. *Lithium-Ion Batteries: Advances and Applications*. First ed. Amsterdam: Elsevier.

- Plett, D. G., 2015. *ECE5720: Battery Management and Control*. [Online]
Available at: <http://mocha-java.uccs.edu/ECE5720/ECE5720-Notes05.pdf>
[Accessed 18 October 2016].
- Pop, V. et al., 2008. *Battery Management Systems: Accurate State-of-Charge Indication for Battery-Powered Applications*. Eindhoven: Springer Science & Business Media.
- PowerStream, n.d. *Wire Gauge and Current Limits Including Skin Depth and Strength*.
[Online]
Available at: http://www.powerstream.com/Wire_Size.htm
[Accessed 20 August 2014].
- Princeton University, n.d. *What is a microcontroller?*. [Online]
Available at: <https://www.princeton.edu/~achaney/tmve/wiki100k/docs/Microcontroller.html>
[Accessed 15 May 2014].
- Rae, A.I.M, 2005. *Quantum Physics: A Beginners Guide*. First Ed. London: Oneworld.
- Rajewski, J., 2017. *Learning FPGAs: Digital Design for Beginners with Mojo and Lucid HDL*. First ed. Sebastopol: O'Reilly Media, Inc..
- Rajput, R., 2005. *Basic Electrical and Electronics Engineering*. Jalandhar: Daryaganj, New Delhi : Laxmi Publications, 2006..
- Ram, A., 1997. *Fundamentals of Polymer Engineering*. Haifa: Springer Science+Business Media.
- Ramsden, E., 2006. *Hall-Effect Sensors Theory and Application*. Second Edition ed. Burlington: Newnes.
- Ranka, S. et al., 2010. *Contemporary Computing*. Noida: Springer.
- Rashid, K., 2007. *Chalmers University of Technology: Shell Eco-Marathon 2007: Drive-Train Design Report*, Gothenburg : Chalmers University of Technology.
- Rashid, M. H., 2011. *Power Electronics Handbook*. Third Edition ed. Burlington: Butterworth-Heinemann.
- Rich, V., 1994. *The International Lead Trade*. 1st ed. Cambridge: Woodhead Publishing Limited.

Rivers, R., 1999. *Traffic accident investigator's and reconstructionist's Book of Formulae and Tables*. Second Edition ed. Springfield: Charles C Thomas Publisher LTD.

Roger Dugan, Granaghan Mc, F Mark & Surya Santoso, 2002. *Electrical Power System Quality*. 2 ed. USA: 2002.

S. Rajamohamed & M.H. Shwehdi, 2012. *Imminent Smart DC Nano-Grid for Green Buildings — A Contemplative View*, Saudi Arabia: Recent Advances in Energy, Environment, Biology and Ecology; King Faisal University.

S.Chowdhury & P.Crossley, 2009. *Microgrids and Active Distribution Network..* United Kingdom: 2009.

SAE International, 2016. *Mazda introduces supercapacitor-type regenerative braking - SAE International*:. [Online]
Available at: <http://articles.sae.org/11845/>
[Accessed 26 October 2016].

Sajan, C., Kumar, T. P., Rajashekar, B. & Srilatha, K., 2013. A New Topology for High Level Inverter Motor Drive with Energy Storage and Power Distribution. *IOSR Journal of Electrical and Electronics Engineering (IOSR-JEEE)*, 8(4), pp. 75-83.

Satish Rajagopalan & Brian Fortenbery, 2011. *DC House. Realizing a cost-effective zero net energy building through direct current (DC) residential distribution*, USA: EC&M.

Savage Paul, Nordhaus Robert R & P Jamieson, 2009. *DC Microgrids:Benefits and Barriers*. s.l., s.n.

Saxena Ashutosh, Ray Supratim & Varma Rajiv K, 2008. *A Novel Electric Shock Protection System Based on Contact Currents on Skin Surface*. [Online]
Available at: <http://www.cs.cornell.edu/~asaxena/papers/IEEEPD-shock.pdf>
[Accessed 56 03 2014].

Scott, Willis H Lee & Walter G, 2002. *Distribution power Generation, Planning and Evaluation..* Swuizerlad: s.n.

Scrosati, B., Abraham, K., Van Schalkwijk, W. & Hassoun, J., 2013. *Lithium batteries Advanced Technologies and applications*. New Jersey: John Wiley and Sons, Inc., Hoboken, New Jersey.

Scrosati, B., Garche, J. & Tillmetz, W., 2015. *Advances in Battery Technologies for Electric Vehicles*. s.l.:Woodhead publishing.

SENCORE®, 2014. *Understanding ESR in Capacitors*. [Online]

Available at: http://slot-tech.com/interesting_stuff/sencore/LC103/TT104%20-%204416.pdf

[Accessed 06 December 2016].

Sengpielaudio, n.d. *Conversion and calculation – cross section < > diameter*. [Online]

Available at: <http://www.sengpielaudio.com/calculator-cross-section.htm>

[Accessed 20 August 2014].

Sengpiel, E., 2014. *Cross-sectional area to diameter conversion circle intersection cross section diameter electric cable conductor formula wire diameter and wiring*. [Online]

Available at: <http://www.sengpielaudio.com/calculator-cross-section.htm>

[Accessed 05 October 2016].

Shahan, Z., 2015. *10 Best Electric Cars*. [Online]

Available at: <https://evobsession.com/10-best-electric-cars/>

[Accessed 31 May 2017].

Shell Eco-marathon, 2016. *Shell Eco-Marathon: 2016 Official Rules Chapter 1*. s.l.:Shell.

Shell Global, 2014. *Location and Track*. [Online]

Available at: <http://www.shell.com/global/environment-society/ecomarathon/events/europe/location-and-track.html?url=/>

[Accessed 12 June 2014].

Shell Global, 2014. *Shell Eco-marathon Europe 2014: Drive around the equator with 12.5 litres of fuel*. [Online]

Available at: <http://www.shell.com/global/environment-society/ecomarathon/events/europe/press-centre/sem-close-18052014.html>

[Accessed 12 June 2014].

Shell Global, 2014. *What is the history?*. [Online]

Available at: <http://www.shell.com/global/environment-society/ecomarathon/about/history.html>

[Accessed 12 June 2014].

Shell, 2012. *Shell Eco-Marathon Legacy*. [Online]

Available at: <http://www.youtube.com/watch?v=2ImSHgBn2kA>

[Accessed 15 May 2012].

Shell, 2013. *Shell Eco- Marathon Official Rules 2014 - Chapter 1*. [Online]

Available at: [http://s01.static-shell.com/content/dam/shell-](http://s01.static-shell.com/content/dam/shell-new/local/corporate/ecomarathon/downloads/pdf/sem-global-official-rules-chapter-1-2014.pdf)

[new/local/corporate/ecomarathon/downloads/pdf/sem-global-official-rules-chapter-1-2014.pdf](http://s01.static-shell.com/content/dam/shell-new/local/corporate/ecomarathon/downloads/pdf/sem-global-official-rules-chapter-1-2014.pdf)

[Accessed 03 September 2013].

Shell, 2013. *Updated Rotterdam Track: New Race Direction in 2014*. [Online]

Available at: [http://s00.static-shell.com/content/dam/shell-](http://s00.static-shell.com/content/dam/shell-new/local/corporate/ecomarathon/downloads/pdf/europe/sem-europe-2014-QA-track-change-021213.pdf)

[new/local/corporate/ecomarathon/downloads/pdf/europe/sem-europe-2014-QA-track-change-021213.pdf](http://s00.static-shell.com/content/dam/shell-new/local/corporate/ecomarathon/downloads/pdf/europe/sem-europe-2014-QA-track-change-021213.pdf)

[Accessed 2015 December 2013].

Shell, 2014. *Shell Eco-Marathon Europe 2014 Official Rules, Chapter 2*. [Online]

Available at: [http://s03.static-shell.com/content/dam/shell-](http://s03.static-shell.com/content/dam/shell-new/local/corporate/ecomarathon/downloads/pdf/europe/sem-europe-rules-chapter-2-210214.pdf)

[new/local/corporate/ecomarathon/downloads/pdf/europe/sem-europe-rules-chapter-2-210214.pdf](http://s03.static-shell.com/content/dam/shell-new/local/corporate/ecomarathon/downloads/pdf/europe/sem-europe-rules-chapter-2-210214.pdf)

[Accessed 21 February 2014].

Shell, 2015. *Shell Eco-Marathon Europe 2014*. [Online]

Available at: [http://s00.static-shell.com/content/dam/shell-](http://s00.static-shell.com/content/dam/shell-new/local/country/deu/downloads/pdf/shell-ecomarathon-presskit-2014.pdf)

[new/local/country/deu/downloads/pdf/shell-ecomarathon-presskit-2014.pdf](http://s00.static-shell.com/content/dam/shell-new/local/country/deu/downloads/pdf/shell-ecomarathon-presskit-2014.pdf)

[Accessed 14 June 2016].

Shell, 2017. *Shell Eco-Marathon 2015 Official Rules – Chapter 2*. [Online]

Available at: [http://s02.static-shell.com/content/dam/shell-](http://s02.static-shell.com/content/dam/shell-new/local/corporate/ecomarathon/downloads/pdf/south-africa/sem-south-africa-chapter2-rules-18082015.pdf)

[new/local/corporate/ecomarathon/downloads/pdf/south-africa/sem-south-africa-chapter2-rules-18082015.pdf](http://s02.static-shell.com/content/dam/shell-new/local/corporate/ecomarathon/downloads/pdf/south-africa/sem-south-africa-chapter2-rules-18082015.pdf)

[Accessed 24 January 2017].

Shell, 2017. *Shell Eco-Marathon; Official Rules 2014; Chapter 1*. [Online]

Available at: [http://s01.static-shell.com/content/dam/shell-](http://s01.static-shell.com/content/dam/shell-new/local/corporate/ecomarathon/downloads/pdf/sem-global-official-rules-chapter-1-2014.pdf)

[new/local/corporate/ecomarathon/downloads/pdf/sem-global-official-rules-chapter-1-2014.pdf](http://s01.static-shell.com/content/dam/shell-new/local/corporate/ecomarathon/downloads/pdf/sem-global-official-rules-chapter-1-2014.pdf)

[Accessed 24 January 2017].

- Siddiqui, K. M., Sahay, K. & V.K.Giri, 2015. Modelling and Simulation of Variable Speed Squirrel Cage Induction Motor Drives. *International Journal of Advanced Research in Electrical, Electronics and Instrumentation Engineering*, 4(7), pp. 6720-6728.
- Singh, M. & Khanchandani, K., 2007. *Power Electronics*. Second Edition ed. New Delhi: Tata McGraw-Hill Publishing Company Limited.
- Sixto, V. et al., 2014. *Advanced co-simulation HMI Environment For Fully Electric Vehicles*. Vigo, IEEE.
- Smal, D., 2012. *Design of lithium ion power source for electric vehicle*. Cape Town, Cape Peninsula University of Technology.
- Solanki, C. S., 2011. *Solar Photovoltaics: Fundamentals, Technologies and Applications*. Second Edition ed. New Delhi: Asoke K. Ghosh, PHI Learning Private Limited.
- Solar Energy International, 2006. *Photovoltaics Design and Installation Manual*. Gabriola Island: Solar Energy International.
- Soni, H. & Shah, A., 2011. *Proceedings of the 2011 Multi-Conference 2nd International Conference on Signals, Systems and Automation 2011 (ICSSA 2011) and International Conference on Intelligent Systems and Data Processing 2011 (ICISD 2011)*. Boca Raton: Universal-Publishers.
- StackElectronix, 2016. *FPGA's vs Microcontrollers - Electrical Engineering Stack Exchange*. [Online]
Available at: <http://electronics.stackexchange.com/questions/4382/fpgas-vs-microcontrollers>
[Accessed 19 October 2016].
- Strang, G., 1991. *Calculus: Volume 1*. Wellesley: Wellesley-Cambridge Press.
- Strickland, K., 1993. *Advanced Components for Electric and Hybrid Electric Vehicles*. Maryland: National Institute of Standards and Technology.
- TECHNOLOGY), E. G. a. E. J. (. U. O., 2009. Modelling and Simulation of a Hybrid Electric Vehicle for Shell Eco-marathon and an Electric Go-kart. pp. 30-31.

Teja, D., 2014. *Squirrel cage Induction motor Advantages, Disadvantages and Applications*. [Online]

Available at: <http://electricalquestionsguide.blogspot.com/2011/11/squirrel-cage-induction-motor.html>

[Accessed 23 June 2014].

Texas instruments, 2008. *bq77PL900EVM-001 User's Guide SLUU324B*. [Online]

Available at: <file:///C:/Users/roseg/Desktop/slUU324b.pdf>

[Accessed 03 June 2018].

Texas Instruments, 2009. *Five to Ten Series Cell Lithium-Ion or lithium Polymer Battery protector and Analog Front End*. [Online]

Available at: <http://www.ti.com/lit/ds/symlink/bq77pl900.pdf>

[Accessed 13 April 2017].

Texas Instruments, 2011. *Understanding Thermal Dissipation and Design of a Heatsink*.

[Online]

Available at: <http://www.ti.com/lit/an/slva462/slva462.pdf>

[Accessed 2017 July 2017].

Texas Instruments, 2013. *User's Guide bq77PL900EVM-001*. [Online]

Available at: <http://www.ti.com/lit/ug/slUU324a/slUU324a.pdf>

[Accessed 24 January 2017].

Texas Instruments, 2015. *TMP10x Temperature Sensor with I2C and SMBus Interface with Alert Function in SOT-23 Package*. [Online]

Available at: <http://www.ti.com/lit/ds/symlink/tmp101.pdf>

[Accessed 31 May 2017].

Texas Instruments, 2016. *Battery Management IC BMS University | Battery Management IC Solutions | Power Management | TI.com*. [Online]

Available at: <http://www.ti.com/lit/ds/ti/power-management/battery-management-bms-university.page>

[Accessed 06 July 2016].

Texas Instruments, 2016. *LM35 Precision Centigrade Temperature Sensors*. [Online]

Available at: <http://www.ti.com/lit/ds/symlink/lm35.pdf>

[Accessed 17 May 2017].

Texas Instruments, 2016. *MOSFET power losses and how they affect power-supply efficiency - slyt664.pdf*. [Online]

Available at: <http://www.ti.com/lit/an/slyt664/slyt664.pdf>

[Accessed 7 July 2017].

Texas Instruments, 2017. *TMS320F2833x, TMS320F2823x digital Signal Controllers (DSCs)*. [Online]

Available at: <http://www.ti.com/lit/ds/symlink/tms320f28333.pdf>

[Accessed 18 September 2017].

Texas instruments, 2018. *User's Guide bq77PL900EVM-001*. [Online]

Available at: <http://www.ti.com/lit/ug/sl00324b/sl00324b.pdf>

[Accessed 20 April 2018].

The Carbon Trust, 2011. *Variable speed drives*. United Kingdom: The Carbon Trust 2011.

Theodore Bernstein, 1991. Electric Shock Hazards and safety Standard.. *IEEE Transaction on Education*, 34, no3(August 1991), pp. 216-222.

Totten, G. E., 2003. *Fuels and Lubricants Handbook: Technology, Properties, Performance, and Testing*. West Conshohocken: ASTM International.

Turkel, S., 2016. *Understanding Variable Speed Drives (Part 1)*:. [Online]

Available at: <http://ecmweb.com/content/understanding-variable-speed-drives-part-1>

[Accessed 03 November 2016].

UK Renewable Energy Roadmap, 2011. *UK Renewable Energy Roadmap*. [Online]

Available at:

https://www.gov.uk/government/uploads/system/uploads/attachment_data/file/48128/2167-uk-renewable-energy-roadmap.pdf

[Accessed 06 03 2014].

Union of Concerned Scientists, 2016. *How It Works: Electric Drive Vehicles | Catalyst Spring 2012*. [Online]

Available at: <http://www.ucsusa.org/publications/catalyst/sp12-how-it-works.html#.WBDqSzVIm70>

[Accessed 26 October 2016].

University of Kentucky - College of Engineering, n.d. *Computing the Power in a Three Phase Motor*. [Online]

Available at: www.engr.uky.edu/.../LectureNotes/PWMmotorVoltage.doc

[Accessed May 2014].

Visual Composer, 2016. *Transmission Repair*. [Online]

Available at: <http://pepservicecenter.com/index.php/transmission-repair/>

[Accessed 08 December 2016].

Wald, M., 2012. *The Convoluted Economics of Storing Energy*. New York: The New York Times.

Walsh, P. M., 2011. *Plug-in Hybrid Electric Vehicle Supervisory Control Strategy Considerations for Engine Exhaust Emissions and Fuel Use*. [Online]

[Online]

Available at: https://theses.lib.vt.edu/theses/available/etd-05102011-155420/unrestricted/Walsh_PM_T_2011.pdf

[Accessed 7 December 2016].

Warner, J., 2015. *the Handbook of Lithium-Ion Battery Pack Design*. Amsterdam: Elsevier.

What-When-How, 2016. *Polyphase Induction Motors Supplied by Adjustable-frequency power supplies (electric motors)*. [Online]

Available at: <http://what-when-how.com/electric-motors/polyphase-induction-motors-supplied-by-adjustable-frequency-power-supplies-electric-motor/>

[Accessed 12 December 2016].

Whitaker, J. C., 2005. *The Electronics Handbook*. Second Edition ed. Boca Raton: CRC Press; Taylor & Francis Group.

Wikipedia, 2017. *Snubber - Wikipedia*. [Online]

Available at: <https://en.wikipedia.org/wiki/Snubber>

[Accessed 04 July 2017].

Wilson, J. D. & Hernandez-Hall, C. A., 2015. *Physics Laboratory Experiments*. Eighth ed. Stamford: Cengage Learning.

Wiring Harness Manufacturers Assoc., 2010. *Requirements and Acceptance for Cable and Wire Harness Assemblies*. [Online]

Available at: <http://www.ipc.org/TOC/IPC-A-620.pdf>

[Accessed 12 December 2016].

WordPress.com, 2013. *Zagreb « A Fulbright Experience in Croatia...»*. [Online]

Available at: <https://zarocroatia.wordpress.com/2013/02/03/zagreb/>

[Accessed 26 October 2016].

WordPress, 2016. *Fuel Cell Electric Vehicles – No Mo Oil 100% electric vehicles.* [Online]

Available at: http://www.nomooil.org/?page_id=1198

[Accessed 26 October 2016 2016].

Yardley, E. & Stace, L., 2008. *Belt conveying of minerals*. Boca Raton: CRC Press.

Appendices

Appendix A – Motorelli motor dimensions and specifications

OUTLINE DIMENSIONS FOOT MOUNTED MOTORS				SHAFT EXT. DE ONLY		WEIGHT (kg)								
125	A	AA	AB	B	BB	C	H	HA	HB	HD	HE	HH	KK	L
34	AA	AB	AC	B	BB	C	H	HA	HB	HD	HE	HH	KK	L
160	AB	AC	B	BB	C	H	HA	HB	HD	HE	HH	KK	L	
156	AC	B	BB	C	H	HA	HB	HD	HE	HH	KK	L		
100	B	BB	C	H	HA	HB	HD	HE	HH	KK	L			
130	BB	C	H	HA	HB	HD	HE	HH	KK	L				
50	C	H	HA	HB	HD	HE	HH	KK	L					
80	H	HA	HB	HD	HE	HH	KK	L						
10	HA	HB	HD	HE	HH	KK	L							
195	HB	HD	HE	HH	KK	L								
225	HD	HE	HH	KK	L									
59	HE	HH	KK	L										
112	HH	KK	L											
10	KK	L												
1-M20x1.5	L													
296	L													
	D	DB	E	ED	F	G								
19	D	DB	E	ED	F	G								
M6X16	DB	E	ED	F	G									
40	E	ED	F	G										
25	ED	F	G											
6	F	G												
15.5	G													

CLIENT:	FRAME	KW	RPM
	80		

Appendix B – Motor Experimental Results

Original Motor Measurements						
Old Efficiency	Old Current	Old Resistance	Old Copper losses (I ² R)	Old Input Power	Old Rotor, Windage and friction losses	Output Power
0	1.01	7.6	23.25828	157.0235693	133.7652893	0
27.79586267	1.02	7.6	23.72112	204.2825756	180.5614556	56.78210417
42.83870127	1.05	7.6	25.137	264.5595025	239.4225025	113.333855
51.83950238	1.08	7.6	26.59392	320.0996169	293.5056969	165.9380486
58.92715703	1.13	7.6	29.11332	378.6041363	349.4908163	223.1006539
63.72313339	1.18	7.6	31.74672	433.3715828	401.6248628	276.1579518
66.81738853	1.24	7.6	35.05728	495.3554458	460.2981658	330.9835728
69.03099829	1.31	7.6	39.12708	557.0815797	517.9544997	384.5589757
69.85413155	1.39	7.6	44.05188	617.9700938	573.9182138	431.6776423
71.17772926	1.47	7.6	49.26852	681.9513578	632.6828378	485.3974912
70.84557594	1.57	7.6	56.19972	756.6507254	700.4510054	536.0535643
70.30317646	1.66	7.6	62.82768	821.359624	758.531944	577.4419058
70.25788471	1.76	7.6	70.62528	882.1487183	811.5234383	619.7790295
69.5099538	1.89	7.6	81.44388	968.9785038	887.5346238	673.5365103
69.20004431	2	7.6	91.2	1038.191254	946.9912541	718.4288078
67.97877339	2.12	7.6	102.47232	1114.068936	1011.596616	757.3303973
66.25596975	2.27	7.6	117.48612	1204.178706	1086.692586	797.8402791
64.61783657	2.43	7.6	134.63172	1289.054738	1154.423018	832.9592839

Re-wound Motor Measurements						
New Current (A)	New calculated resistance (Ω)	New Copper losses (I^2R)	Old Rotor, Windage and friction losses	New Input Power	Expected efficiency (%)	Output Power
22.6	0.055707848	85.36002133	133.7652893	219.1253106	0	0
22.7	0.055707848	86.11709099	180.5614556	266.6785466	21.2923405	56.78210417
22.9	0.055707848	87.64125771	239.4225025	327.0637602	34.65191463	113.333855
23.1	0.055707848	89.17879431	293.5056969	382.6844912	43.36158176	165.9380486
23.4	0.055707848	91.51016775	349.4908163	441.000984	50.58960455	223.1006539
23.7	0.055707848	93.87162343	401.6248628	495.4964862	55.73358428	276.1579518
24.2	0.055707848	97.87423231	460.2981658	558.1723981	59.29773202	330.9835728
24.9	0.055707848	103.6182685	517.9544997	621.5727682	61.8686975	384.5589757
26.1	0.055707848	113.8462294	573.9182138	687.7644432	62.76533289	431.6776423
28.1	0.055707848	131.9624216	632.6828378	764.6452594	63.480089	485.3974912
29.1	0.055707848	141.5218883	700.4510054	841.9728937	63.66636839	536.0535643
32.7	0.055707848	178.7035344	758.531944	937.2354783	61.61118728	577.4419058
34.6	0.055707848	200.0736219	811.5234383	1011.59706	61.26738143	619.7790295
36.1	0.055707848	217.7970738	887.5346238	1105.331698	60.93523888	673.5365103
37.7	0.055707848	237.5310219	946.9912541	1184.522276	60.65135476	718.4288078
40	0.055707848	267.3976704	1011.596616	1278.994286	59.21296174	757.3303973

RPM	Mass (g)	Force (N)	Torque (Nm)	Mechanical Output Power (W)	Input Voltage L-L (V)	Input Current L-L (A)	Power Factor	Power In (W)	Efficiency (%)
1492	0	0	0	0	22.9	22.6	0.33	295.814	0
1483	100	0.981	0.363	56.372	23	22.7	0.39	352.678	15.984
1479	201	1.978	0.730	113.002	22.9	22.9	0.44	399.654	28.275
1471	305	2.992	1.107	170.543	22.8	23.1	0.5	456.118	37.390
1460	401	3.933	1.456	222.546	22.7	23.4	0.55	506.017	43.980
1452	502	4.925	1.822	277.072	22.5	23.7	0.61	563.406	49.178
1444	599	5.876	2.174	328.788	22.2	24.2	0.67	623.453	52.737
1432	701	6.877	2.544	381.578	21.8	24.9	0.72	676.938	56.368
1421	813	7.976	2.951	439.144	21.2	26.1	0.78	747.535	58.746
1415	904	8.868	3.281	486.236	22.8	28.1	0.75	832.268	59.120
1408	1003	9.839	3.641	536.816	22.3	29.1	0.8	899.184	59.700
1401	1100	10.791	3.993	585.805	23	32.7	0.75	977.007	59.959
1392	1200	11.772	4.356	634.954	23.1	34.6	0.78	1079.800	58.803
1380	1300	12.753	4.719	681.937	23.1	36.1	0.8	1155.500	59.017
1353	1400	13.734	5.082	720.025	23.2	37.7	0.82	1242.235	57.962
1321	1500	14.715	5.445	753.210	23.1	40	0.84	1344.349	56.028

